Spectral Micro-CT Imaging of Ex Vivo Atherosclerotic Plaque

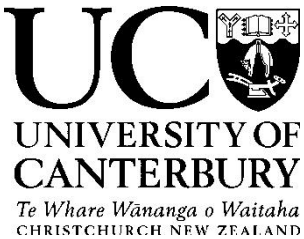

Rafidah Binti Zainon

A thesis submitted in partial fulfilment of the
requirements for the degree of
Doctor of Philosophy in Medical Physics
in the University of Canterbury, Christchurch, New Zealand

2012

Contents

Page

Contents i

Acknowledgements vii

Abstract ix

Abbreviations x

List of Figures xii

Academic Contribution xxiv

Chapter 1: Introduction to the thesis

1.1 Goals 1

1.1.1 The visionary goal 1

1.1.2 The thesis goal 1

1.2 Clinical and technical background 2

1.3 Motivation for using spectral CT 5

1.4 Clinical significance 7

1.5 Thesis organisation 7

1.6 Summary 11

Chapter 2: Interactions of x-rays with matter

2.1 Introduction 12

2.2 Photoelectric absorption 14

2.3 Rayleigh (coherent) scattering 15

2.4 Compton scattering 15

2.5 The energy dependence of x-ray attenuation 16

2.6 Summary 18

Chapter 3: Conventional CT imaging

3.1 Introduction 20

3.2 Basic principles of CT imaging 23

3.2.1 Image reconstruction in CT 26

3.2.2 CT image display 31
3.3 Evolution of spatial resolution in CT imaging 32
3.4 CT image quality 34
3.4.1 Image contrast 35
3.4.2 Spatial resolution 36
3.4.3 Image noise 37
3.4.4 Artifacts 38
3.5 Summary 39

Chapter 4: The Medipix photon-counting detector
4.1 Introduction 40
4.2 Medipix detectors 42
4.3 Summary 47

Chapter 5: Spectral CT
5.1 Introduction 49
5.2 Evolution of CT imaging 50
5.3 Developments of the MARS-CT systems 54
5.3.1 The MARS-CT systems 57
5.3.1.1 MARS scanning unit 57
5.3.1.2 MARS console 58
5.3.1.3 MARS workstation 58
5.3.2 The MARS-CT2 system 59
5.3.3 The MARS-CT3 system 61
5.4 Potential influencing factors on spectral CT imaging assessment 62
5.5 Summary 65

Chapter 6: Atherosclerosis imaging
6.1 Atherosclerosis 67
6.2 Characterisation of atherosclerotic lesions by various imaging modalities 71
6.2.1 Invasive techniques 72
6.2.2 Non-invasive techniques 74

6.3 The need for spectral CT imaging in characterisation of atherosclerotic plaque 76
6.4 Summary 78

Chapter 7: Preliminary studies on atherosclerotic plaque with the MARS-CT2 system

7.1 Introduction 80
7.2 Materials and Methods 82
7.2.1 Study design 82
7.2.2 Ex vivo MARS-CT2 scanning protocol 82
7.2.3 Ex vivo MRI scanning protocol 84
7.2.4 MARS-CT image processing 84
7.3 Results 85
7.4 Discussion 93
7.5 Conclusion 98
7.6 Summary 99

Chapter 8: Calibration of the MARS-CT3 system with Medipix3

8.1 Introduction 102
8.2 Materials and methods 103
8.2.1 Medipix3 configuration and calibration 103
8.2.2 Geometrical calibration of the MARS-CT scanner 104
8.2.2.1 Motor controller calibration 106
8.2.2.2 Centre of rotation 107
8.2.2.3 X-ray projection magnification 108
8.2.2.4 Vertical beam centre and gantry tilt 108
8.2.2.5 Detector translation skew 109
8.3 Results and discussion 110
8.3.1 Energy calibration of Medipix detector 110
8.3.2 Calibration of motor controller 111
8.3.3 Scanner geometry measurement 112
8.3.3.1 Centre of rotation 112
8.3.3.2 X-ray projection magnification 113
8.3.3.3 Vertical beam centre and gantry tilt 114

8.3.3.4 Detector translation skew 116
8.4 Conclusion 117
8.5 Summary 117

Chapter 9: Performance evaluation of the MARS-CT3 system
9.1 Introduction 119
9.2 Materials and methods 120
9.2.1 MARS-CT system 120
9.2.2 Scanning protocol and data processing 121
9.2.3 Performance evaluation 121
9.2.3.1 Spatial resolution 122
9.2.3.2 Image uniformity 122
9.2.3.3 Pixel noise 123
9.2.3.4 Linearity 123
9.2.3.5 Spectroscopic calibration 124
9.2.3.6 Dose measurement 124
9.2.4 Demonstration with biological specimens 124
9.3 Results 125
9.3.1 Spatial resolution 125
9.3.2 Image uniformity 126
9.3.3 Pixel noise 127
9.3.4 Linearity 128
9.3.5 Spectroscopic calibration 129
9.3.6 Dose measurement 130
9.3.7 Demonstration with biological specimens 131
9.4 Discussion 131
9.4.1 Spatial resolution 131
9.4.2 Image uniformity 132
9.4.3 Pixel noise 133
9.4.4 Linearity 134
9.4.5 Spectroscopic calibration 134
9.4.6 Dose measurement 135

9.5 Conclusion 136
9.6 Summary 137

Chapter 10: Material decomposition with spectral CT imaging

10.1 Introduction 138
10.2 Theory 141
10.3 Materials and methods 142
10.3.1 Spectral CT system 142
10.3.2 Linearity 143
10.3.3 Spectroscopy 144
10.3.4 Material Analysis 144
10.4 Results 145
10.4.1 Linearity 145
10.4.2 Spectroscopy 146
10.4.3 Material analysis 148
10.5 Discussion 150
10.6 Conclusion 152
10.7 Summary 153

Chapter 11: Characterising ex vivo human carotid arteries with the MARS-CT3

11.1 Introduction 154
11.2 Materials and methods 157
11.2.1 Evaluation of imaging parameters 157
11.2.2 Preparation of atherosclerotic plaque imaging 158
11.2.2.1 Ex vivo MARS-CT3 imaging protocol of the excise carotid atherosclerotic plaque 159
11.2.2.2 MARS-CT3 image processing 160
11.2.2.3 Image analysis 162
11.2.3 Ex vivo histological processing of carotid endarterectomy specimens 163
11.2.3.1 Postprocessing of ex vivo spectral micro-CT images and histological sections 164

11.3 Results 165
11.3.1 Phantom study 165
11.3.1.1 Determination of number of projections 165
11.3.1.2 Evaluation of tube voltage 166
11.3.1.3 Evaluation of sensitivity for differentiating of iron and calcium 169
11.3.1.4 Demonstration of spectral CT analysis with a multi-contrast phantom 170
11.3.2 Ex vivo atherosclerotic plaque images 171
11.4 Discussion 177
11.5 Limitations 182
11.6 Conclusion 182
11.7 Summary 183

Chapter 12: Conclusion and further work
12.1 Summary of conclusions 185
12.2 Future work 190

References 193

Acknowledgements

I would like to thank the following people and groups for their assistance, support and friendship during my doctoral study and make this research project possible. I wish to express my gratitude to my principal supervisor, Prof. Philip Butler for his advice, encouragement and support during my study. I would also like to acknowledge the advice and guidance of my co-supervisors, Dr Anthony Butler and Assoc. Prof. Steven Gieseg.

I also wish to express my sincere appreciation to Dr Juergen Meyer (Medical Physics Director) and Dr Jenni Adams (Postgraduate Coordinator) for their valuable advice and support as I started my Ph.D degree at University of Canterbury. I am grateful to Dr Nicholas Cook, a medical physicist at the Christchurch Hospital who assisted me to use MARS-CT2 scanner at the start of this research. I also like to convey thanks to MARS soft tissue imaging team members, particularly to the radiologists, Dr Nigel Anderson, Dr Michael Hurrell and Dr Damian Jiang for their informative discussions and continuous support in this research throughout the years. Many thanks go to biochemist and pathologists, Dr Nicola Scott, Prof. Robin Fraser and Dr Niel Lambert for their advice, help and guidance in plaque histology. I also wish to express my gratitude to my fellow colleague, J Paul Ronaldson, for valuable discussions, help and support, and for proofreading my thesis. Thanks to my colleague at Free Radical Biochemistry Lab, Tejraj Janmale, for his help in plaque histology.

Thanks to all involved in the plaque study at the Christchurch Hospital especially Prof. Tim Buckenham who is a Head of Radiology Department at Christchurch Medical School for his knowledge sharing. Prof. Justin Roake and his surgical team, and plaque donors for their contribution in this research.

Special thanks go to the former MARS lab managers, Alexandra Butler, Angela Moore and present MARS research facilitator, Peter Hilton for their great help and coordinating research activities. Thanks to Dr Judy Mohr for her knowledge sharing. I also would like to convey thanks to my colleagues, Robert Doesburg, Raja Aamir Mallal, Anas Sedayo, Syen Jien Nik, Michael Walsh and Niels de Ruiter for an inspiring and friendly environment.

I also wish my sincere appreciation to Dr Darin O'Keeffe, Annalie Ronaldson, Steven Muir and staff at the Medical Physics and Nuclear Medicine Department, Christchurch Hospital for their great help and support. Thanks to the technicians at Physics and Astronomy Department, University of Canterbury, especially Graeme Kershaw and Bob Flygenring, various technicians at Canterbury District Health Board bioengineering workshop and Maggie Tisch at School of Biological Sciences for helping me in fabrication of phantoms and cooling chambers for this study. Thanks to Matthew Walters, the technician at Biological Sciences Department for his help in photographing the plaques.

I wish to express my love and gratitude to my lovely parents, Zainon Ahmad and Rahela Bakar for their endless love, resolute support and encouragement in my life. My thanks are due to my siblings and Mohd Azzim A. Rani for their loving support. I would also like to extend my deepest gratitude to all my friends for their support and made my time here so enjoyable.

I am grateful for the financial support by the Ministry of Higher Education Malaysia and Universiti Sains Malaysia through the Academic Staff Training Scheme.

Abstract

The goal of this research was to demonstrate the potential of spectral CT for the discrimination of vulnerable atherosclerotic plaques. It was proposed that spectral CT has the potential to identify the presence of specific markers for vulnerable plaques: iron deposits and lipid core. A spectral micro-CT system incorporating the latest Medipix spectroscopic photon-counting detectors was commissioned for this purpose. Using spectroscopic methods developed with this system, it was possible to distinguish the presence of iron deposits and lipid core within ex vivo atherosclerotic plaques.

Atherosclerosis or hardening of arteries is a systemic disease of the vessel wall that occurs in the aorta, carotid, coronary and peripheral arteries. It is characterised by the deposition of calcified plaques on the innermost layer of the artery wall. Vulnerable plaques are unstable, prone to rupture and put the person at risk of cardiovascular events and strokes. Factors that may lead to plaque instability are lipid content and iron deposits. This preclinical study is a precursor to the development of a clinical technique that will enable vulnerable atherosclerotic plaques to be identified in vivo prior to treatment or removal.

Following a preliminary study on atherosclerotic plaques with a prototype system, the MARS-CT3 spectral micro-CT system incorporating Medipix3 was developed and commissioned for further plaque studies. The spectral CT data sets acquired by this system were assessed visually for morphology and analysed for material composition using a linear algebra method. The results were correlated with photography and histology (the histology is the current gold standard).

The presence of iron and lipid can be differentiated from the background soft-tissue using a linear algebra method. However the quantification of iron in the presence of calcium is not currently possible without additional data or constraints. Nevertheless the presence of iron deposits within the plaques can be distinguished in the high resolution MARS-CT images and has been correlated with photographic and histological evidence. Thus, using the high spatial resolution spectral data from MARS-CT, the discrimination of lipid core and iron deposits within ex vivo advanced human atherosclerotic plaques is feasible. This may provide the basis for the development of a clinical technique that will identify vulnerable plaques in vivo by high resolution spectral CT.

Abbreviations

2D	Two-dimensional
3D	Three-dimensional
Apo E-KO	Apolipoprotein E-knockout
ASIC	Application Specific Integrated Circuit
Au-HDL	A gold high-density lipoprotein nanoparticle contrast agent
CAT	Computerised Axial Tomography
CdTe	Cadmium Telluride
CERN	European Organisation for Nuclear Research
CMOS	Complementary Metal-Oxide-Semiconductor
CNR	Contrast-to-Noise Ratio
COR	Centre of Rotation
CT	Computed Tomography
DAC	Digital-to-Analog Converter
DICOM	Digital Imaging and Communications in Medicine
EBCT	Electron-Beam CT
FDK	Feldkamp-Davis-Kress
FIESTA	Fast Imaging with Steady-state Acquisition
FOV	Field Of View
fps	Frames Per Second
GaAs	Gallium Arsenide
GUI	Graphical User Interface
HU	Hounsfield Unit
IVUS	Intravascular Ultrasound
kV	Kilovoltage
kVp	Peak Kilovoltage
MARS	Medipix All Resolution System
mAs	Milliampere Second
MDCT	Multi-Detector Computed Tomography
MSCT	Multi-slice Spiral CT
MRI	Magnetic Resonance Imaging

MTF	Modulation Transfer Function
MUROS	Medipix Reusable Readout System
NEX	Number of Excitations
NIH	National Institutes of Health
NIRS	Near Infrared Spectroscopy
OCT	Optical Coherence Tomography
OECD	Organisation for Economic Co-operation and Development
PCA	Principal Component Analysis
PET	Positron Emission Tomography
PMMA	Polymethyl methacrylate
PSF	Point Spread Function
RFA	Request for Applications
ROI	Region of Interest
SDD	Source-to-Detector Distance
SEM	Standard error of the mean
Si	Silicon
SNR	Signal-to-Noise Ratio
SOD	Source-to-Object Distance
THH	High Threshold
THL	Lower Threshold
VBC	Vertical Beam Centre
Voxel	Volume element

List of Figures

		Page
Figure 2.1	The electromagnetic spectrum presented as a function of wavelength, frequency and energy. The x-rays are part of the high energy portion of the spectrum. Retrieved from Seibert (2004).	13
Figure 2.2	The three major x-ray interactions involved in the diagnostic x-ray energy range (10-150 keV): photoelectric absorption, Rayleigh (coherent) scattering and Compton scattering. Retrieved from Siebert et al. (2005).	14
Figure 2.3	(a) Rayleigh, photoelectric, Compton, pair production and total mass attenuation coefficients for soft tissue (Z=7) as a function of energy. (b) The linear attenuation coefficients of water, bone, iodine (K-edge at 33.2 keV), gadolinium (K-edge at 50.2 keV). Retrieved from Bushberg, (1998) and Wang et al. (2011b).	17
Figure 3.1	Bertha Roentgen's hand, the first x-ray image Roentgen ever published. Retrieved from Medcyclopaedia (2011).	21
Figure 3.2	The emission spectrum for a tungsten target x-ray tube operated at 150 kVp. Characteristic K x-ray emission occurs for tungsten whenever the tube voltage exceeds 60 kVp, corresponding to the K-shell binding energy for tungsten. The rising edge is due to the effect of the filtration. The purpose of the filtration is to enrich the beam with high energy photons by absorbing the lower energy component of the spectrum. The characteristic x-rays are seen as sharp peaks on top of the broad continuum from the bremsstrahlung. The area under the spectrum represents the total number of x-rays. Retrieved from OpenLearn LabSpace (2005).	24
Figure 3.3	(Left) The basic setup of CT imaging. The x-ray source and detector unit rotate synchronously around the patient. Data is essentially acquired continuously during rotation. (Right) An example of a single-slice CT image of the lung. Retrieved from U.S. Department of Health and Human Services (2010).	25

Figure 3.4 The coordinate systems for Radon transform. 27

Figure 3.5 A computer simulation of filtered back projection. Retrieved from AAPM (2010). 28

Figure 3.6 The geometry description and parameters for the FDK algorithm. Retrieved from Li et al. (2008). 29

Figure 3.7 The CT Hounsfield scale for various human organs at an effective energy of about 70 keV. The CT values show the attenuation coefficient of the tissues relative to the density of water. The typical HU range of compact bone is 300 HU to 1300 HU. Retrieved from Kachelrieß (2008). 32

Figure 3.8 The hierarchy of scales associated with different forms of CT. The CT technique can be used over the range of different resolutions, whilst using the same physical principles. In high resolution CT, normal x-ray tubes can be used as a source, whereas for micro-CT special microfocus x-ray tubes are required. The lower range of micro-CT as well as the nano-CT domain is currently best assessed using synchrotron radiation. The images show from left to right, human hand, trabecular bone structure, microcallus, murine cortical bone surface of a femur with internal vasculature and capillary in bone surrounded by osteocyte lacunae. Retrieved from Stauber et al. (2008). 33

Figure 4.1 Medipix detector assemblies. (a) The Medipix detection system and (b) the electronic circuitry of a Medipix2 pixel cell. The analog side contains a charge preamplifier with direct current leakage current compensation, a test capacitance and two branches of identical discriminators. The digital side contains the double discriminator logic and 13-bit shift register. 42

Figure 4.2 Absorption probabilities of different semiconductor materials with 300 µm thickness. The choice of sensor layer depends on the availability of the sensor layer for application. 44

For most energies Si has a lower absorption probability compared to GaAs and CdTe. The higher-*Z* materials like GaAs or CdTe, have better conversion efficiencies than Si for x-rays in the energy-range used for medical imaging (20-100 keV). Retrieved from Mitschke (2006).

Figure 4.3 (a) A single Medipix3 detector with 300 µm Si sensor layer has 256 x 256 pixels in a detection area of 14 mm × 14 mm. (b) A multi-detector board capable of carrying up to 2 × 3 Medipix3 detectors. A Peltier cooler (thermoelectric heat pump) was mounted onto the multi-chip board to maintain the Medipix detector at a constant temperature during scanning. 47

Figure 5.1 Differences between conventional CT, dual-energy CT and spectral CT. The conventional CT system measures the x-ray flux averaged over the entire spectrum, dual-energy CT measures the flux over two separate spectra and spectral CT detects the flux within multiple energy bands of a single spectrum. The multiple energies are measured by a photon-counting detector, (Medipix) allows a more complete attenuation curve to be reconstructed. Spectral CT can identify multiple materials simultaneously whereas conventional and dual-energy CT have insufficient information to differentiate these materials. This diagram has been used by other MARS team members in several published papers (Anderson et al., 2010; Zainon et al., 2010a) and talks. The diagram has been modified here to suit the thesis context. 52

Figure 5.2 The MARS-CT workflow. There are three different sub-systems involved in this process. The MARS scanning unit consists of the scanner gantry, the micro-focus x-ray tube and the Medipix readout system. The physical scanning processes are performed in this unit. The man-machine interface is implemented in the MARS Console that also temporarily caches the scan data. The image pre-processing, image reconstruction, 3D visualisation and analysis of images are performed in the MARS Workstation. 57

Figure 5.3 The object is placed in the centre of the rotating gantry carrying the Medipix detector and micro-focus x-ray source. The SOD and SDD are adjustable so that users can mechanically change the magnification. 58

Figure 5.4 (Left) The MARS-CT2 scanner with its main components labelled: (a) lead shielded box, (b) stepper motor, (c) gantry, (d) motor controller, (e) x-ray controller, (f) fan switch, (g) power supply and (h) MUROS power. (Right) The scanner gantry with its main components labelled: (a) Medipix detector, (b) sample (in this case a human atherosclerotic plaque fixed in resin), (c) sample holder and (d) micro focus x-ray tube. 60

Figure 5.5 (Left) The MARS-CT3 system. (a) A warning light (it illuminates when x-rays are on) and (b) the emergency stop button. (Right) The top view of the gantry. (a) The sample holder, (b) webcam, (c) Medipix3 detector box and (d) x-ray tube. 62

Figure 5.6 Factors potentially influencing spectral CT assessment. 63

Figure 6.1 The formation of a stable atherosclerotic plaque. (a) The human artery has three different layers: the intima (the innermost layer and site of plaque formation), the media (consisting of mostly smooth muscle cells) and the adventitia (the outer layer of the artery). Plaque builds up on the innermost layer of the arteries and is formed from cholesterol, fat, calcium and other substances in the blood. (b) The fatty streak develops inside the intima. (c) It can evolve into a stable plaque with a thick fibrous cap and a small fatty core. Retrieved from American Heart Association (2011). 69

Figure 6.2 The formation of an unstable atherosclerotic plaque. (a) Once the fatty streak develops inside the intima, it can develop into an unstable plaque with a thin fibrous cap and large fatty core. It is vulnerable to rupture. (b) The ruptured material from an unstable plaque protrudes into the artery, causing a partial or complete obstruction to blood flow. 70

(c) The blood clot can grow, leading to a sudden occlusion of the artery. This condition is called arterial thrombosis. Retrieved from American Heart Association (2011).

Figure 7.1 A single slice of femoral artery plaque fixed in resin. The complexity of the plaque structure is apparent. Large confluent dense areas (with a linear size >1000 μm) are seen peripherally, whereas the central densities tend to be punctate and much smaller (with a linear size from 100 μm to 1000 μm). Some ring artifacts are also visible. The plaque was imaged at 75 kVp with the detector threshold set at 14.5 keV. 85

Figure 7.2 Matching of multi-modality images. The femoral plaque images acquired from (a) high resolution of MARS-CT2 scanner, (b) clinical MDCT scanner, (c) MRI scanner with 1.5 T 3D FIESTA. The high resolution MARS-CT2 image shows the femoral plaque lesions and the structure within the plaque whereas the spatial resolution of the images from the other modalities is too poor to visualise these features. 86

Figure 7.3 A high resolution MARS-CT2 image (left) and a MDCT image (right) of slice 156 of the carotid artery plaque. 87

Figure 7.4 Excised femoral plaque (left) and carotid plaque (right). Both plaques were fixed in resin within a 25 mm internal diameter PMMA tube. The annotations give the slice location number of each image used in Figures 7.4 and 7.5. 87

Figure 7.5 Spectral images of femoral artery plaque (fixed in resin) obtained at several energies. These images were scaled to HU normalised using regions of air and resin. The colour coded images were obtained from

PCA. 89

Figure 7.6 Spectral images of cross sections through carotid artery plaque (fixed in resin). Several images were selected at different energies to display the progression of calcification in plaque and the response of absorption characteristics of dense and non-dense regions over the entire energy range. The colour coded images were obtained from PCA. 90

Figure 7.7 The low and high energy images of femoral artery plaque (fixed in resin). These images were scaled to HU normalised using regions of air and resin. The images in the final column are subtraction images showing the difference in HU between images obtained using the lowest and highest threshold energies. 91

Figure 7.8 The low and high energy images of cross sections through carotid artery plaque (fixed in resin). The images in the final column are subtraction images showing the difference in HU between images obtained using the lowest and highest threshold energies. 92

Figure 7.9 Spectral images, PCA images and photographs of 3 mm slices of a carotid artery plaque, snap frozen. The plaque was imaged using four energy thresholds: 14.0 keV, 20.0 keV, 25.0 keV and 34.5 keV. 93

Figure 8.1 The geometry of MARS-CT system. The view from positive *Z* shows 105 the COR and VBC sensor column and row locations. The view from positive *X* shows the relative locations of the source, gantry axis and optical axis. 105

Figure 8.2 X-ray detector and source motor drives of MARS-CT scanner. The view is of the bottom of the gantry and the blue box of the MARS camera is just visible between the movable x-ray and camera platforms. 107

Figure 8.3 The wire phantom used to find the centre of rotation. 107

Figure 8.4 (a) The magnification phantom and (b) a projection image of the phantom. 108

Figure 8.5 (a) The phantom used for measurement of the vertical beam centre and detector translation skew. A high contrast steel ball is mounted on the tip of the phantom. (b) A projection image of the phantom. 109

Figure 8.6 The spectra obtained with molybdenum and indium foils within the open beam. The peaks correspond to the molybdenum and indium K fluorescence lines at 17.5 keV and 22.5 keV respectively. 110

Figure 8.7 A linear regression fit of the threshold DAC values for the two fluorescence peaks and the noise floor against the corresponding energies is shown. The straight line relationship gives the threshold DAC value in terms of detector threshold energy *E*. 111

Figure 8.8 The x-ray detector (top) and x-ray source (bottom) displacements plotted as a function of index value. 112

Figure 8.9 The superimposed images of a wire phantom taken with the gantry rotated by 180°. The intersection of the images of the diagonal wire indicates the centre of rotation of the scanner. In this case the centre of rotation is at column 137. 112

Figure 8.10 The object magnification with detector position for four gantry angles 90° apart. In each case the SOD is obtained from the reciprocal of the gradient and the SDD by substitution into the equation for magnification. 113

Figure 8.11 The projections of the phantom were plotted and an ellipse was fitted to the data. 115

Figure 8.12 The ball position displacement is plotted for a series of detector translations. The image stitching vector is determined from the motor index coefficient and the sine of the angle $\theta = 89.05°$ of the fitted line with respect to the y-displacement axis. 116

Figure 9.1 The MTF phantom used in the measurement of spatial resolution of the system. The diameters of the three sections from top to bottom were 5, 10 and 15 mm respectively. 122

Figure 9.2 (Top) A reconstructed image of perspex phantom used for evaluation of spatial resolution. (Bottom left) The LSF and (bottom right) MTF measured at the edge of the perspex phantom. The MTF falls to 10% of its maximum value at a spatial frequency of 8.8 mm^{-1}. The phantom was scanned at 50 kVp with threshold energy of 9.8 keV. 125

Figure 9.3 (a) A reconstructed slice of a 15 mm diameter water-filled phantom with CT response uniformity (after beam hardening correction) measured at the centre and near the periphery. (b) The CT number profile through the centre of the phantom. The phantom was scanned at 50 kVp with a threshold energy of 9.8 keV. 126

Figure 9.4 CT slices of the water phantom obtained at different exposure times: 250 mAs, 100 mAs, 50 mAs and 25 mAs. The CT image noise depends on the number of x-ray photons contributing to the image. 127

Figure 9.5 Graph of noise variance, σ^2, against reciprocal exposure Q^{-1} from scans of a 15 mm diameter water phantom. The noise variance is approximately linear (R2 = 0.994) with reciprocal exposure. 128

Figure 9.6 (a) The reconstructed CT image of the phantom with air, water and calcium chloride at concentrations of 74.9, 147.0, 294.0 and 735.0 mg.ml^{-1} and (b) the measured CT numbers, *S*, as a function of calcium chloride concentration, C. The phantom was scanned at 50 kVp with a threshold energy of 12.3 keV. 129

Figure 9.7 (a)-(f) Spectral CT reconstructions of a perspex phantom containing Ca, Fe, I, oil, water and air at six different energies. The photoelectric and Compton effects that contribute to spectral response in attenuation are energy and material dependent. 129

Figure 9.8 The spectral dependence of the CT values of Ca, Fe, I, oil and water. Additional attenuation measurement obtained at different energies allowing the differentiation of materials. 130

Figure 9.9 The dose rate measured at the isocentre for different tube voltages as a function of current. 130

Figure 9.10 A single slice of femoral plaque in resin and the abdominal region of a euthanized mouse with kidneys enhanced using iodine contrast agent. 131

Figure 10.1 (a) A reconstructed CT image of the perspex phantom with solutions of different concentrations of calcium chloride acquired with a threshold energy of 12 keV and a tube voltage of 50 kVp. (b) The measured CT numbers as a function of concentration. There is a linear increase in attenuation with increasing calcium chloride concentration to ~300 mg.ml^{-1} corresponding to a CT number of ~2000 HU (R^2 = 0.997). The standard uncertainties for the measured data are in the range 10 HU. 146

Figure 10.2 Spectral CT reconstructions of a perspex phantom containing Ca, Fe, oil, water and air. Data were acquired with a tube voltage of 50 kVp and six threshold energies. 147

Figure 10.3 The material-specific CT numbers of materials tested (Ca, Fe, I, oil and water) plotted versus photon energy. The spectroscopic response to the materials tested is consistent with the energy dependent attenuation coefficients for those materials. The standard uncertainties for each data point are 10 HU. 147

Figure 10.4 (a) The cumulative information entropy (solid lines) and number of degrees of freedom (dashed lines) retrieved by a sequence of spectral CT measurements for an unconstrained system. (b) The cumulative information entropy and number of degrees of freedom for a system including volume constraints on oil and water. 149

Figure 10.5 Material-selective images obtained from the proposed technique. (a) Fe and Ca, (b) K-edge material (iodine), (c) water and (d) oil images. 150

Figure 11.1 Cooling chambers used for keeping the specimens cool during imaging. (Top) The first cooling chamber could be filled with 500 ml of liquid nitrogen and remained cold for approximately 45 min. (Bottom) The second design of cooling chamber also contained 500 ml of liquid nitrogen but remained cool for approximately 90 min. 160

Figure 11.2 The cutting edge of the plaque segment and the corresponding CT reconstructed slices. The surface 'slice' image (Slice C) shows the surface of the plaque exposed by the histological cutting C. 161

Figure 11.3 The perspex phantom images acquired on the same scanner with all the technical factors the same except the number of projection angles. The perspex phantom was scanned with 125, 250, 500 and 1000 projection angles to evaluate the image noise. 166

Figure 11.4 Standard deviation of pixel grey-scale value for the perspex phantom imaged with different numbers of projection angles. 166

Figure 11.5	The MARS-CT3 images of various solutions of contrast material within the calibration phantom, showing the effect of increasing tube voltage. (a) 35 kVp, (b) 50 kVp and (c) 80 kVp. This phantom was scanned at four threshold energies: 10, 16, 22 and 28 keV.	167
Figure 11.6	CNR in oil and aqueous solutions of iron and calcium in a multi-contrast phantom as a function of tube voltages (35, 50 and 80 kVp). These materials mimic iron, calcium deposits and lipid in atherosclerotic plaque.	168
Figure 11.7	The differences in dual-energy ratios for the combination of threshold energy pairs to discriminate iron and calcium at different tube voltages (a) 35 kVp, (b) 50 kVp and (c) 80 kVp.	170
Figure 11.8	A plot of CT number for different materials in the multi-contrast phantom evaluated against threshold energies at 50kVp. The standard uncertainties are in the range 4-15 HU. The CT number response is characteristic of the material.	171
Figure 11.9	Plaque A has been cut into small segments. A1-A3 and B1 corresponds to the cutting edges of the plaques which have been scanned with the MARS-CT3 scanner.	172
Figure 11.10	(Top row) The photograph of atherosclerotic plaque segment A1 taken before imaging and the atherosclerotic plaque lesions visualised by the MARS-CT3 imaging at different energy thresholds. (Middle row) The corresponding cross sections of the same specimen were stained with Von Kossa, Perls Prussian Blue and Oil-red-O for histological examination. The darker the color of staining solutions, the denser the plaque components. (Bottom row) The material decomposition images show the water-like, calcium-like and lipid-like images. The calcium-like image shows the iron and calcium deposits in the atherosclerotic plaque. The lipid is clearly distinguishable from soft tissue in atherosclerotic plaque. All of the CT images closely match the photographs taken before imaging and the histology examination performed afterwards.	173

Figure 11.11 (Top row) The photograph and the spectral CT images of atherosclerotic plaque segment (A2) at different energy thresholds. These images visualised by the MARS-CT3 imaging at 38 μm voxel size. (Middle row) The corresponding cross sections of the same specimen were stained with Von Kossa, Perls Prussian Blue and Oil-red-O for histological examination. (Bottom row) Three materials were decomposed in the image domain: the water-like, calcium-like and lipid-like images. The calcium deposits can easily be seen on the CT image. The low concentration of iron deposits appear as slightly dense tissues on the high resolution calcium-like image. The lipid is distinguished from soft tissue images. The MARS-CT3 images matched the photographs taken before imaging and the material decomposition images obtained from the MARS-CT3 imaging were confirmed by the histological examination. 174

Figure 11.12 (Top row) The photograph of A3 plaque segment and the corresponding spectral CT images obtained at different energy thresholds. (Middle row) The plaque staining photos show the plaque segment was stained with Von Kossa, Perls Prussian Blue and Oil-red-O to validate the calcium deposits, iron deposits and lipid respectively. The plaque staining photo shows that the small part of the plaque segment is slightly broken due to the handling process during staining. (Bottom row) The material decomposition images show the water-like, calcium-like and lipid-like images. The calcium-like image demonstrates the co-localisation of iron and calcium deposits in the plaque. The clusters of randomly distributed punctate iron deposits can also be seen on the CT image. The lipid and soft tissue images can be observed as separate components. The high resolution MARS-CT3 images closely match the photographs taken before imaging and the histological examination performed afterwards. 175

Figure 11.13 (Top row) The photograph of atherosclerotic plaque segment B1 and the corresponding multi-energy CT images. (Middle row) The plaque segment was stained with with Von Kossa, Perls Prussian Blue and Oil-red-O to validate the calcium deposits, iron deposits and lipid respectively. (Bottom row) The material decomposition technique can identify lipid from soft-tissue and calcium/iron deposits in atherosclerotic plaque. Plaque segment B1 has fewer iron deposits than A1, A2, and A3 plaque segments. The lipid is distinguishable from the soft tissue in the plaque images. The characterisation of atherosclerotic plaque determined by MARS-CT3 closely matches photographs taken before scanning and the histological examination performed afterwards. 176

Academic Contribution

This doctoral thesis was completed by preparing a series of academic papers, with the main aim to demonstrate the potential of spectral micro-CT imaging for the discrimination of lipid, iron deposits as a marker of hemorrhagic and calcium deposits of ex vivo atherosclerotic plaque compared with the use of histological examination as the gold standard. The candidate's contributions are summarised as follows:

i. Develop acquisition protocols, investigate capabilities of spectroscopic imaging and assess the imaging performance of the MARS-CT2 system. Identify the improvement and fed back into the design process for the MARS technical team members to develop the MARS-CT3 system.

ii. Evaluate the performance of the MARS-CT3 system to characterise atherosclerotic plaque components.

iii. Develop the ex vivo atherosclerotic plaque imaging protocol and analysis methods with phantom datasets.

iv. Evaluate the ex vivo atherosclerotic plaque imaging protocol with the MARS-CT3 system using surgical specimens. Characterise and validate the atherosclerotic plaque components.

The following publications were generated during this study. The candidate is also a contributing author for other papers in preparation during doctoral study.

1. Peer-Reviewed Journal Articles:

1.1 **Zainon, R**., Cook, N. J., Butler, A. P., Gieseg, S. P., Anderson, N. G., Buckenham, T. M., Shelkov, G., Tlustos, L., Roake, J. A., & Butler, P. H. (2010). High resolution multi-energy CT imaging of atherosclerotic plaque. *New Zealand Medical Journal*, *123*(1319), 97-98.

1.2 **Zainon, R**., Butler, A.P.H., Cook, N., Butzer, J., Schleich, N., de Ruiter, N., Tlustos, L., Clark, M. J., Heinz, R., & Butler, P.H. (2010). Construction and operation of the MARS-CT scanner. *Internetworking Indonesia Journal, 2*(1), 3-10.

1.3 Aamir, R., Lansley, S. P., **Zainon, R**., Fiederle, M., Faulerc, A., Greiffenberg, D., Butler, P. H., & Butler, A. P. H. (2011). Pixel sensitivity variations in a CdTe-Medipix2 detector using poly-energetic x-rays. *Journal of Instrumentation*, *6*(1), C01059.

1.4 Aamir, R., Walsh, M. F., Lansley, S. P., Doesburg, R. M., **Zainon, R**., de Ruiter N. J. A., Butler, P. H., Butler, & A. P. H. (2011). Characterisation of CdTe x-ray sensor layers on Medipix detector chips. *Materials Science Forum, 700,* 170-173.

1.5 Hurrell, M., Butler, A. P. H., Cook, N. J., Butler, P. H., Ronaldson, J. P., & **Zainon, R**. (2011). Spectral Hounsfield Units - A new radiological concept. *European Radiology*. doi:10.1007/s00330-011-2348-3.

1.6 **Zainon, R**., Ronaldson, J. P., Janmale, T., Scott, N. J., Buckenham, T. M., Butler, A. P., Butler, P. H., Doesburg, R. M., Gieseg, S. P., Roake, J. A. & Anderson, N. G. (2012). Spectral CT of carotid atherosclerotic plaque: comparison with histology. *European Radiology*. doi: 10.1007/s00330-012-2538-7.

1.7 Xu, Q., Yu, H., Bennett, J., He, P., **Zainon, R**., Doesburg, R., Opie, A., Walsh, M., Shen, H., Butler, A., Butler, P., Mou, X., & Wang, G. (2012). Image reconstruction for hybrid true-color micro-CT. *IEEE Transactions on Biomedical Engineering. 59*(6), 1711-1719.

2. Papers Published in Refereed Conference Proceedings:

2.1. Ronaldson, J. P., **Zainon, R**., Butler, A. P., & Butler, P. H. (2011). Performance of MARS-CT using Medipix3 for spectral imaging of soft-tissue. *Proceedings of the Nuclear Science Symposium*, Valencia, Spain, 23-26 October 2011.

2.2. **Zainon, R**., Ronaldson, J. P., Butler, A. P., & Butler, P. H. Establishing a linear basis for quantifying material composition using spectral computed tomography. P*roceedings of the World Congress on Technology and Engineering*, Shanghai, China, 28-30 October 2011.

3. Refereed Conference Abstracts:

3.1 **Zainon, R**., Dufreneix, S., de Ruiter, N., Cook, N. J., Butler, A. P. H., Gieseg, S. P., & Butler, P. H. (2009). Spectroscopic (multi-energy) x-ray CT of human atheroma. *Canterbury Health Research Poster Expo*, Christchurch, New Zealand, June 2009.

3.2 **Zainon, R**., Dufreneix, S., Nik, S. J., de Ruiter, N., Cook, N. J., Hurrell, M., Gieseg, S. P., Butler, A. P. H., Butler, P. H. (2009). Spectroscopic x-ray computed tomography imaging of plaque and arteries using the Medipix detector. *New Zealand Institute of Physics Conference,* Christchurch, New Zealand, July 2009.

3.3 **Zainon, R**., de Ruiter, N., Cook, N. J., Gieseg, S. P., Butler, A. P. H., & Butler, P. H. (2009). Multi-energy x-ray CT of excise plaques. *5th ECHO Singapore 2009 Conference,*Singapore, October 2009.

3.4 Gieseg, S. P, **Zainon, R**., Roake, J., Butler, A. P., & Butler, P. H. High resolution multi-energy CT imaging of atherosclerotic plaque: The future of x-ray CT imaging. *35th Annual Scientific Meeting of the Australian Atherosclerosis Society*, Melbourne, Australia, October 2009.

3.5 **Zainon, R**., de Ruiter, N., Cook, N. J., Gieseg, S.P., Butler, A.P.H, & Butler, P.H. (2009). Imaging human plaques with spectral CT. *ComBio Conference*. Christchurch, New Zealand, December 2009.

3.6 **Zainon, R**., Cook, N. J., Gieseg, S. P., Butler, A. P. H, & Butler, P. H. (2010). Spectroscopic imaging of excised plaques. *Canterbury Health Research Poster Expo*, Christchurch, New Zealand, May 2010.

3.7 Butler, A. P., Walsh, M. F., Butler, P. H., Doesburg, R., de Ruiter N. J. A., Ronaldson, J. P., **Zainon, R**., Woodfield, T., Siegert, A., Gieseg, S. P., Mohr, J. (2011). Development of a Medipix3 based spectral (multi-energy) CT for pre-clinical evaluation of biomakers. *The Royal Australian and New Zealand College of Radiologist Meeting*, Melbourne, Australia, October 2011.

3.8 Ronaldson, J. P., **Zainon, R**., Sedayo, A., Scott, N. J. A., Butler, A. P. B., Butler, P. H., Anderson, N. G. A. (2011). Towards quantifying the composition of soft-tissues by spectral CT imaging with Medipix3. *Radiological Society of North America Meeting*, Chicago, USA, Nov 2011.

4. Invited Talks:

These papers were presented by Dr Anthony Butler on behalf of MARS team at the CERN workshop at Geneva.

4.1 Butler, A. P. H., Ronaldson, J. P., Scott, N., **Zainon, R**., Geiseg, S. P., Janmale, T., Cook, N., Woodfield, T., Siegert, A. M., Mohr, J., Anderson, N. G., & Butler, P. H. (2011). Pre-clinical imaging with the MARS spectral micro-CT system. *Workshop on medical applications of spectroscopic x-ray detectors,* Geneva, April 2011

4.2 Butler, A. P. H., Walsh, M., Ronaldson, J. P., Opie, A., Amir, R., Doesburg, R., de Ruiter, N., **Zainon, R**., Mohr, J., Cook, N., Bones, P., & Butler, P. H. (2011). MARS: A pre-clinical spectral microCT system based on the Medipix family of energy selective photon-counting detectors. *Workshop on medical applications of spectroscopic x-ray detectors,* Geneva, April 2011.

4.3 Butler, A. P. H., Ronaldson, J. P., Scott, N., **Zainon, R**., Butler, P. H., Geiseg, S. P., Janmale, T., & Anderson, N. G. (2011). Soft tissue imaging with the MARS spectral CT scanner. *Queenstown Heart Meeting*, Queenstown, New Zealand, August 2011.

5. Paper in Preparation:

5.1 Ronaldson, J. P., **Zainon, R**., Scott, N. J., Gieseg, S. P., Butler, A. P., Butler, P. H., & Anderson, N. G. Towards quantifying the composition of soft-tissues by spectral CT imaging with Medipix3 . This paper was submitted to Medical Physics Journal.

6. Awards:

6.1 Universiti Sains Malaysia Academic Staff Training Scheme Fellowship (2009-2012).

This fellowship is awarded to the candidate by Ministry of Higher Education, Malaysia and Universiti Sains Malaysia to further Ph.D degree in University of Canterbury, New Zealand.

6.2 Best Student Poster Award (2010).

This prize is for the best poster presentation at the Canterbury Health Research Poster Expo, Christchurch, New Zealand.

Chapter 1

Introduction to the thesis

The MARS research group is developing spectral CT for wide use in preclinical and clinical healthcare including imaging of soft-tissues and novel contrast agents. This research supports the long term visionary goal to improve the clinical diagnosis of atherosclerosis by the application of spectral Computed Tomography (CT). The first section of this chapter describes the visionary and thesis goals. The clinical and technical backgrounds to this study are then provided. The following sections focus on the technical motivation for using spectral CT and the clinical significance of this research. Finally the thesis organisation is given followed by a summary of the main points.

1.1 Goals

1.1.1 The visionary goal

The long term visionary goal associated with this research is to develop spectral CT for diagnosing human disease and one of the potential applications is for spectral CT to be utilised in a clinical setting for diagnostic imaging of unstable (vulnerable) plaque components in vivo prior to pharmacological or surgical treatment. Identification of unstable (vulnerable) plaque is of utmost importance because of the high risk of it precipitating an acute thrombotic occlusion (vascular blockage caused by a blood clot).

1.1.2 The thesis goal

The particular goal of this study is to demonstrate the potential of the Medipix All Resolution System (MARS)-CT for discriminating the lipid core, iron deposits as a marker of intraplaque

hemorrhage and calcium deposits of ex vivo advanced human atherosclerotic plaques. Validation of the MARS-CT results will be by histological examination (the gold standard).

1.2 Clinical and technical background

Atherosclerosis or hardening of arteries is a systemic disease of the vessel wall that occurs in the aorta, carotid, coronary and peripheral arteries (Fuster et al., 1999). It is characterised by the deposition of plaques on the innermost layer of the arterial wall. Factors that may lead to plaque instability are lipid content and iron deposits. The iron deposits in the plaque can be seen as a marker of prior hemorrhagic, or bleeding events that put a person at risk for plaque eruption (Bornstein et al., 1990; Starry et al., 1995). The challenge is to diagnose a vulnerable plaque by the presence of these components and treat or remove it.

A review of the available literature on atherosclerosis shows that lumen size (the inner open space of a blood vessel) is not sufficient to predict the occurrence of clinical events. The information on plaque morphology and composition are more valuable in the vulnerability assessment than lumen size (Glagov et al., 1995; Pasterkamp et al., 2000; Libby, 2009). Many imaging modalities have been investigated in atherosclerotic plaque characterisation. The details about atherosclerosis imaging techniques with regard to their ability to identify unstable lesions at risk of rupture are covered more thoroughly in Chapter 6.

Many efforts have been made recently to extract meaningful information from CT scans, especially the identification of tissues or material being imaged, by using the characteristic energy-dependent attenuation of x-rays (Hounsfield et al., 1973). Furthermore, the use of CT in the hospitals has grown exponentially during the last 25 years, with similar trending of data from regions across the world (Thomas, 2011). The Organisation for Economic Co-operation

and Development (OECD) records the availability of medical equipment in all health care facilities, including the hospital and ambulatory sectors.

In New Zealand, the total CT scanners per million population have increased by more than 345% while the total MRI unit per million population has increased by 288% in the last two decades (OECD, 2011). This data shows that the availability of CT scans has significantly increased. It has also been reported that there is a remarkable growth in CT utilisation particularly in emergency departments (Gamble, 2010; RSNA, 2010; Guidera, 2010; Manos, 2011). It is worthwhile noting that the rates of CT imaging have risen because of various technological improvements that make them more useful in the diagnosis of many types of diseases and enable provide excellent care to be provided cost-effectively.

A large number of studies have been performed over the last few years to investigate the ability to characterise ex vivo atherosclerotic plaque composition by dual-energy CT imaging. Using synchrotron-based micro-CT (with voxel size of $(2\ \mu m)^3$ and beam energies of 16 keV and 20 keV), synchrotron based fluorescence microscopy and histology, Langheinrich et al. (2007) demonstrated the ability to detect and discriminate iron and calcium deposits in the wall of aorta by virtue of the size of the opacities (the area of individual iron deposits within a single CT slice being $<(100\ \mu m)^2$). The distribution of iron deposits within the plaques showed evidence of prior intraplaque hemorrhage in the mouse model of advanced atherosclerosis. Iron deposit is a marker of intraplaque hemorrhage that accumulates in the arterial wall.

A major challenge to using iron deposits as an imaging marker of plaque vulnerability is the concurrent presence of calcium, which is indistinguishable from iron in conventional imaging modalities. In 2009, Langheinrich et al. demonstrated the influence of voxel size on its ability

to discriminate iron and calcium deposits in ex vivo coronary arteries. At a voxel size of $(20\ \mu m)^3$ or smaller, iron deposits could be identified based on the CT grey scale value. Voxels of $(100\ \mu m)^3$ or larger cannot resolve nor distinguish iron deposits from calcifications by virtue of their CT grey scale values. The iron and calcium deposits cannot be differentiated at low resolution due to the partial volume effect. The partial volume effect is the loss of information in small objects or regions because of the limited resolution of the imaging system. The resulting CT value represents the average attenuation properties of the structure and the surroundings instead of the attenuation values to be determined.

On the other hand, a recent simulation study by Wang and his colleagues (Wang et al., 2010) demonstrated that iron and calcium deposits can be differentiated using their morphological features at voxel sizes up to $(200\ \mu m)^3$ using dual-energy CT. Wang et al. performed the simulation phantom of human arterial wall with iron and calcium deposits using voxel sizes from 4 to 600 microns at 80 kVp and 140 kVp. The dual-energy ratio map of iron and calcium was computed to distinguish material composition by taking the ratio of low and high energy images. The dual-energy ratio map of iron and calcium remain visually different at a voxel size of $(200\ \mu m)^3$. The ability to use larger voxels sizes makes clinical implementation easier, reduces image noise and decreases patient dose requirements. This study shows that the use of multiple energies might improve material separation.

Multi-energy CT, often known as spectral CT, yields valuable quantitative information about elemental and molecular composition of materials. It enables the identification of materials by decomposing the total attenuation of the material into the various physical contributions for each voxel (Schlomka et al., 2008). Feuerlein et al. (2008) used a preclinical spectral CT scanner with a single-line photon-counting cadmium telluride array detector (MEXC; Gamma

Medica Ideas, Northridge, Calif). It improved luminal depiction by differentiating among intravascular gadolinium-based contrast agent, calcified plaque and stent material in an artery phantom. Feuerlein et al. used the measurements of the six energy bins of the photon-counting detector to estimate the contributions to the total attenuation of the photoelectric effect, the Compton effect and the k-edge of gadolinium.

Cormode et al. (2010) performed a spectral CT study with contrast agents to characterise the macrophage burden, calcification and stenosis in atherosclerotic plaque. They used apolipoprotein E-knockout (Apo E-KO) mice as the model for atherosclerosis. The gold particles were absorbed by macrophages that cause inflammation in the arterial wall at the places of atherosclerotic plaques. Spectral CT enables differentiation of gold-based contrast agent (K-edge energy, 80 keV) from an iodinated contrast agent (K-edge energy, 33.2 keV) with the use K-edge of the materials. The advantages of the spectral CT method compared to other methods such as Magnetic Resonance Imaging (MRI) and Positron Emission Tomography (PET) include the lack of a need for pre-contrast scans, increased resolution and faster imaging.

1.3 Motivation for using spectral CT

This study was motivated by the application of various clinically relevant dual-energy CT imaging methods for material differentiation and elemental decomposition. Recent development of novel energy-resolved photon-counting detectors also motivates this work to explore the potential of these detectors in spectral CT imaging. These novel detectors have many advantages over energy-integrating x-ray detectors in x-ray CT, such as the ability to measure the spectrum of x-ray beams. It is known that the attenuation of x-ray photons is energy-dependent and each substance has a specific attenuation curve. Therefore, measurement of the specific attenuation responses can enable material

differentiation. Dual-energy datasets can be produced by using kV switching, dual source systems or sandwich detectors. In this case of kV switched or dual source CT, x-ray beams with different mean energies are used to measure the absorption characteristics of the material with standard non-spectroscopic detectors. Spectral CT is achieved in synchrotron CT by scanning over a range of narrow energies. In contrast, MARS spectral CT uses a fixed, but broad, energy x-ray beam and novel energy-resolved photon counting detectors to measure the energy dependent absorption information imprinted on the x-ray flux as it passes through the materials.

This study was designed to explore the potential of novel photon-counting x-ray detectors for assessing the unstable component (lipid core, iron deposits as a marker of intraplaque hemorrhage) and calcium deposits on surgical specimens of advanced human atherosclerotic plaque. Compared with standard detector technology, these detectors provide high spatial and energy resolution. Thus, spectral CT has the potential to provide high resolution images containing detailed information about plaque morphology and improved tissue differentiation. The ability to characterise the composition of atherosclerotic lesions, especially the unstable plaques that are more likely to undergo acute disruption and give rise to symptoms, may help to understand their natural histology and detect lesions with high risk for acute events. The detection of unstable plaques would help the surgeon to operate selectively on patients who are at most risk and improve treatment in treating atherosclerosis diseases (Pasterkamp et al., 2000).

As with all new modalities, the introduction and implementation of new technology and imaging methods into clinical applications will be a challenge. The medical application of such novel imaging systems demand precise conditions to be fulfilled and thus, work must be done to identify all the advantages and limitations before translating it for medical diagnosis.

Spectral CT imaging is currently available for research but not yet available for use in clinical practice. A necessary step in the development of the clinical application is to prove the concept of material differentiation by ex vivo spectral CT imaging of atherosclerotic plaques.

1.4 Clinical significance

The ability of the MARS-CT scanner using the Medipix photon-counting detector to obtain high resolution images together with spectral information allows, for the first time, accurate simultaneous assessment of lipid, iron deposits as a marker of intraplaque hemorrhage and calcium in advanced human atherosclerotic plaques. This research performed on surgical specimens with a spectral micro-CT scanner, represents a novel contribution to the science of medical imaging. With continuing technical developments, it should be possible to translate this technique onto a human scale CT system that will allow in vivo visualisation and analysis of atherosclerotic plaques prior to treatment. This would be a highly significant advance in clinical imaging. If unstable plaque composition could be predicted by imaging, stroke risk assessment might be refined, allowing better selection of patients for surgery. This would markedly improve the diagnosis and monitoring of atherosclerosis disease (myocardial infarction, stroke and peripheral vascular disease) (De Feyter et al., 2003; Matter et al., 2009; Halpern, 2011; Kiessling, 2011).

1.5 Thesis organisation

The research and development phases involved in the process of achieving the thesis goal are as follows:

i. Investigate the capabilities of spectroscopic imaging with the MARS-CT2 system. Evaluate the data acquisition and imaging performance of the MARS-CT2 system. Identify the improvement and feed back into the design process for MARS technical team members to develop the MARS-CT3 system.

ii. Develop the ex vivo atherosclerotic plaque imaging protocol, analysis methods and evaluate these using a phantom dataset.

iii. Evaluate and demonstrate the capabilities of the MARS-CT3 system to characterise atherosclerotic plaque components using surgical specimens.

iv. Validate the MARS-CT results against those of histological examination (the gold standard).

Based on the research and development phases above, the thesis is structured as follows:

Chapter 2 discusses the principles of x-ray interactions with matter. It also describes the usefulness of energy information obtained from CT imaging for obtaining functional information about tissues.

Chapter 3 focuses on conventional CT imaging. It presents the historical and basic physics of CT to non-physicists and other clinical specialists. This chapter provides a description of the properties of x-rays and how they are produced, the CT scanner features, tomographic image reconstruction and how different types of tissues display on the CT image. This chapter also discusses the evolution of spatial resolution in CT. Characteristics of CT image including contrast, spatial resolution, noise and artifacts are also described.

Chapter 4 presents recent advances in x-ray detector technology particularly the photon-counting (family of Medipix) detectors. It also presents the operating principles of photon-counting detectors and the advantages of this type of detector for CT imaging.

Chapter 5 discusses spectral CT. It describes the evolution of CT imaging from conventional (single energy) to dual-energy and spectral (multi-energy) CT. It also presents the development of the MARS-CT systems. The configuration details of the MARS-CT system,

MARS console and MARS workstation are also described. Some limitations in the MARS-CT2 were overcome by developments and enhancements that were implemented in the MARS-CT3 system. A description of the upgraded MARS-CT and its operation are also given in this chapter. The potential influencing factors on spectral CT imaging assessments are discussed.

As this study focuses on the use of spectral micro-CT imaging for the quantitative study of atherosclerosis, Chapter 6 provides the description of atherosclerosis and biological markers for vulnerable plaques. This chapter also includes a discussion on existing and emerging techniques with regard to their ability to identify unstable lesions at risk of rupture. It is followed by a discussion of the need for spectral CT to characterise atherosclerotic plaque and overcoming the barriers of standard non-invasive techniques. This chapter states a concise description of the issues and it discusses the particular focus of this thesis.

Chapter 7 demonstrates the preliminary studies of atherosclerotic plaque imaging with the MARS-CT2 system. It presents the development of acquisition protocols for imaging of ex vivo atherosclerotic plaque fixed in resin and unfixed specimens, investigates the capabilities of spectroscopic imaging and assesses the overall performance of the MARS-CT2 system. The spectral CT results are compared with images obtained from other imaging modalities. This chapter also discusses the limitations found in this system that were fed back into the design process to develop the MARS-CT3 system.

In order to obtain good quality spectral CT images, the MARS-CT3 system has to be calibrated before the system is used for CT imaging. Detailed discussion on the calibration of the photon-counting (Medipix) detector is presented in Chapter 8. This chapter also discusses the geometrical calibration, being the measurement of a set of parameters which sufficiently

describes the geometry of data acquisition. These parameters are needed for accurate tomographic reconstruction. The geometrical calibration of the MARS-CT3 scanner includes the protocol for motor controller calibration, determination of centre of rotation, x-ray projection magnification, vertical beam centre and detector translation skew.

Chapter 9 presents the performance evaluation of the MARS-CT3 system using phantoms fabricated for the evaluation of spatial resolution, image uniformity, pixel noise, linearity, spectroscopic performance. The results of dose measurements at the isocentre and demonstration images are also presented.

Chapter 10 describes a technique to analyse materials using spectral CT. This chapter discusses the theory of a linear algebra method used to quantify different materials. The linearity and spectroscopic response were evaluated before material decomposition was applied. Results from the linear algebra method for a number of material combinations are also presented.

Chapter 11 presents the assessment of the MARS-CT3 system for discrimination of unstable components (lipid core and iron deposits as a marker of intraplaque hemorrhage) and calcium deposits of ex vivo of advanced human atherosclerotic plaque. The results are compared with histological examination as this is usually taken to be the gold standard. The evaluation of imaging parameters for ex vivo atherosclerotic plaque with the MARS-CT3 scanner is presented. The protocol for preparing surgical specimens for imaging is also given in this chapter. It includes the excision of atherosclerotic plaque, preparation of specimens for imaging with the MARS-CT3, image processing, image analysis and histological examination. The results of the spectral analysis, quantification of spectral micro-CT images and the validation of this study are discussed.

The conclusion of this thesis is given in Chapter 12. Finally the list of references is presented.

1.6 Summary

1. The visionary goal of the MARS team is to develop spectral CT for diagnosing human disease and one of the potential applications is for spectral CT to be utilised in a clinical setting for diagnostic imaging of plaque components in vivo prior to pharmacological or surgical treatment.

2. If unstable plaque composition could be predicted by imaging, stroke risk assessment would be refined, allowing better selection of patients for surgery and early detection and prevention of acute cardiac events.

3. The main aim of this thesis is to demonstrate the advantages of spectral CT using micro-CT equipped with state of the art photon-counting detector technology. This study developed the necessary instrumentation and methods for demonstrating the discrimination of plaque components (lipid core, iron deposits as a marker of intraplaque hemorrhage and calcium deposits) in ex vivo advanced human atherosclerotic plaques. Results of spectral CT are compared with histological examination as this is usually taken to be the gold standard.

Chapter 2

Interactions of x-rays with matter

In this chapter an overview of x-ray interaction mechanisms is presented. The photoelectric, Compton and Rayleigh scattering mechanisms and their attenuation coefficients are discussed. A description of the dependence of the attenuation mechanisms on atomic number and photon energy is provided. The chapter concludes with a summary of the main points.

2.1 Introduction

Wilhelm Conrad Roentgen was the first person to discover the possibility of using electromagnetic radiation to create what we now know as the x-ray. Electromagnetic radiation can be described as a stream of photons, each carrying energy and moving at the speed of light (v = 3 x 10^8 ms^{-1}). Each photon contains a certain amount of energy and all electromagnetic radiation consists of these photons. The electromagnetic spectrum ranges from low energy radiation, such as radio waves and microwaves, to high energy radiation like x-rays and gamma rays. Figure 2.1 shows the electromagnetic spectrum.

The electromagnetic waves are typically described by any of the following three physical properties: the frequency, f, wavelength, λ, or photon energy, E. The relationship between energy and frequency of electromagnetic radiation is described in the Planck relation or the Planck-Einstein equation as shown in Equation 2.1.

$$E = hf \tag{2.1}$$

Photon energy is directly proportional to the frequency of the wave. The higher the frequency of the electromagnetic wave, the higher its energy. Planck's constant is denoted as *h*, and $h = 6.62 \times 10^{-34}$ J.s = 4.13×10^{-21} eV.s.

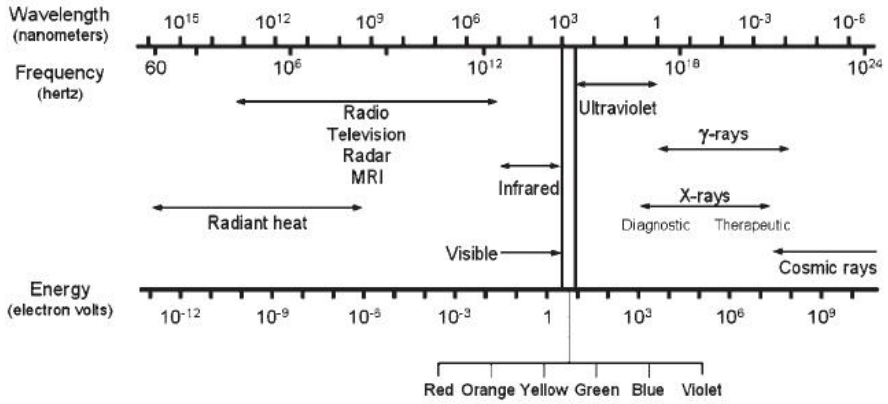

Figure 2.1 *The electromagnetic spectrum presented as a function of wavelength, frequency and energy. The x-rays are part of the high energy portion of the spectrum. Retrieved from Seibert (2004).*

X-ray radiography and CT imaging measure the relative transparency to x-rays as they pass through the body. Diagnostic x-ray imaging relies on the differential attenuation of x-rays when interacting with the object being imaged. As the x-ray beam passes through an object, it produces a variable transmitted x-ray flux that is dependent on the attenuation along the beam paths. Some of the x-rays will be absorbed, some scattered and some will penetrate without interacting. There are three major x-ray interactions involved in the diagnostic x-ray energy range (10-150 keV): photoelectric absorption, Rayleigh (coherent) scattering and Compton scattering. Pair production is also involved in x-ray interaction but it only occurs when the x-ray photon has energy greater than twice the rest mass of an electron (1.02 MeV). Therefore, only the first three processes will be discussed. The photoelectric absorption and Compton scattering interactions can result in energy deposition and secondary x-rays will be present after this initial interaction. Rayleigh scattering does not deposit energy but can scatter the photon to a new trajectory. See Figure 2.2.

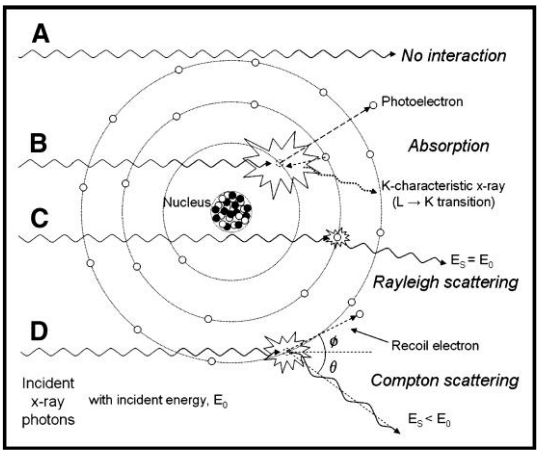

Figure 2.2 *The three major x-ray interactions involved in the diagnostic x-ray energy range (10-150 keV): photoelectric absorption, Rayleigh (coherent) scattering and Compton scattering. Retrieved from Siebert et al. (2005).*

2.2 Photoelectric absorption

Photoelectric absorption (Figure 2.2 (B)) is the process in which a photon interacts with an inner shell electron in the absorbing atom that has a binding energy similar to but less than the energy of the incident photon. If the incident photon energy is less than the binding energy of the electron, photoelectric interactions cannot occur but if the x-ray energy is equal to or greater than the binding energy, photoelectric absorption is feasible and a large attenuation occurs.

In this photoelectric interaction, the incident x-ray photon transfers its energy to the electron and the electron is ejected from its shell (e.g., K or L) with kinetic energy equal to the difference of the incident photon energy, E_0, and the electron shell binding energy, E_{BE}. The vacancy resulting from the electron ejection is filled by an electron from an outer shell (with lower binding energy), producing a characteristic x-ray equal in energy to the difference in electron binding energies of the inner electron shell and outer electron shell. The terms K-edge or L-edge absorption edge refers to the sudden jump in the probability of photoelectric absorption when the K- or L-shell interaction is energetically possible.

The probability of photoelectric absorption per unit mass of a material above the K-edge is approximately proportional to Z^3/E^3, where Z is the atomic number of the material and E is the energy of the incident photon. Therefore, photoelectric absorption increases with increasing atomic number and decreasing photon energy. These facts explain the large differences in attenuation between low-Z material like water and high-Z material like lead. The photoelectric interaction is the main reason for signal contrast in x-ray imaging. Larger x-ray transmission differences in matter occur at low energies, which enhance signal contrast

2.3 Rayleigh (coherent) scattering

Rayleigh scattering is also known as coherent scattering (Figure 2.2 (C)). It occurs when an incident x-ray photon interacts with many electrons at once and is scattered with negligible loss in the energy. Scattering is mainly in the forward direction and majority of the x-ray photons are scattered with a small angle. The probability of this event occurring is low and it is a minor contributor to the absorption coefficient.

2.4 Compton scattering

Compton scattering (Figure 2.2 (D)) occurs when the energy, E_0, of an incident photon is much greater than the binding energy of an atomic electron. The incident x-ray photon is deflected from its original path by this interaction and the electron gains energy. The electron is ejected from its orbital position at an angle, φ. The remainder of the energy, E_s, is transferred to a scattered x-ray photon with a trajectory at an angle, θ, relative to the trajectory of the incident photon. The scattered photon may travel in any direction (scattering through any angle θ from 0° to 180° while the recoil electron may only be directed forward relative to the angle of the incident photon (> 0° to ~90°).

The energy of the scattered photon is related to the scattering angle, θ, by considerations of energy and momentum conservation according to:

$$\frac{E_s}{E_0} = \frac{1}{1+\frac{E_0}{511\ keV}(1-\cos\theta)} \tag{2.2}$$

where E_s and E_0 are the scattered and incident photon energies. The largest effects occur when the photon energy is close to the rest mass of the electron is 511 keV. This equation shows that the scattered x-ray energy becomes smaller as the scattering angle increases. At higher incident energies, this effect is amplified. The energy of the recoiling electron E_{re}, is defined as:

$$E_{re} = E_0 - E_s \tag{2.3}$$

The energy transferred depends on a photon-electron interaction and it does not depend on the density, atomic number or any other property of the absorbing material.

2.5 The energy dependence of x-ray attenuation

The attenuation coefficient reflects the fractional reduction of x-ray intensity as it passes through matter. It is dependent on the thickness of a material, density of a material, atomic number and photon energy. The total attenuation is the sum of the attenuation due to different types of interactions. As discussed in the previous section, there are three major x-ray interactions in the diagnostic energy range of 10-150 keV: photoelectric absorption, Rayleigh (coherent) scattering and Compton scattering. Figure 2.3 (a) demonstrates the x-ray interactions and total mass attenuation coefficients for soft tissue (Z=7), as a function of energy.

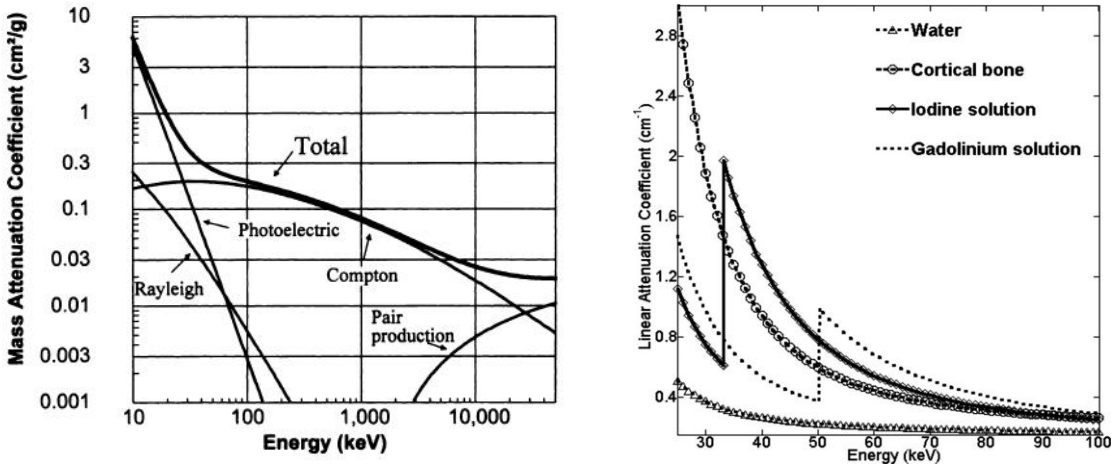

(a) (b)

Figure 2.3 *(a) Rayleigh, photoelectric, Compton, pair production and total mass attenuation coefficients for soft tissue (Z=7) as a function of energy. (b) The linear attenuation coefficients of water, bone, iodine (K-edge at 33.2 keV), gadolinium (K-edge at 50.2 keV). Retrieved from Bushberg, (1998) and Wang et al. (2011b).*

In the zone where the photoelectric effect is dominant, the attenuation varies approximately as E^{-3} whereas at higher energies, Compton scattering is the main mechanism of x-ray interaction with matter, the attenuation varies as E^{-1} (Alvarez & Macovski, 1976). At low energies the photoelectric absorption process aids the ability to detect subtle differences in tissue composition. On the other hand, Compton scattering interactions predominate over the majority of the diagnostic energy range in soft tissue and therefore subject contrast is chiefly derived from differences in tissue density. The pair production process is of no consequence in diagnostic radiography because of the extremely high energies required for pair production to occur. Therefore CT imaging is largely dependent on the different characteristics of the photoelectric and Compton effects.

In the presence of materials (e.g., contrast agents) with K-edges in the energy range of interest, the attenuation coefficients of these materials can be determined by measuring the x-ray absorption either side of the K-edge. The K-edge represents a sudden increase in

attenuation coefficient of the element above the electron binding energy as shown in Figure 2.3 (b). In this phenomenon, the photons with energies slightly greater than the binding energy of the electrons are more likely to be absorbed than photons with energy levels just below this binding energy and this produces a sudden increase in the attenuation coefficient at the K-shell energy.

Conventional CT imaging relies on measuring the total absorption of an object regardless of the particular energy of the incoming radiation. In fact, different combinations of materials can produce the same absorption. Thus, conventional CT is unable to distinguish these materials. Different types of material can be distinguished by taking advantage of the characteristic energy dependence of the photoelectric and Compton effects. The identification of K-edges within the diagnostic energy range allows multiple high-Z number elements to be distinguished simultaneously, if the attenuation coefficient is measured at multiple energies. The technique of acquiring spectral information and separating the contributions of the photoelectric and Compton effect is achievable with spectroscopic photon-counting detectors. The details of these novel detectors will be discussed in the next chapter.

2.6 Summary

1. CT imaging is largely dependent on the two major x-ray interactions: photoelectric and Compton effects. Rayleigh scattering is a minor contributor to the absorption coefficient. The probability of photoelectric absorption per unit mass of a material is approximately proportional to Z^3/E^3, thus photoelectric absorption increases with increasing atomic number and decreasing photon energy. These facts explain the large differences in attenuation between low and high-Z materials. Compton scattering

interactions predominate over the majority of the diagnostic energy range in soft tissue and therefore subject contrast is chiefly derived from differences in tissue density.

2. Conventional CT imaging only measures total absorption of the material regardless of the particular energy of incoming radiation, thus, differentiation of some materials is impossible.

3. The concept of gaining spectral information and separating the contributions of the Compton and photoelectric effects is a technique for material differentiation. Different types of material can be distinguished with spectroscopic photon-counting detectors that record energy information for each incident x-ray photon.

Chapter 3

Conventional CT imaging

This chapter begins with an historical review of x-ray imaging followed by an overview of the basic principles of CT suitable for non-physicists and other clinical specialists. It presents a description of x-ray production, the CT scanner features, tomographic image reconstruction and how different types of tissues display on the CT image. The evolution of spatial resolution in CT imaging is also discussed. This chapter describes the conventional measures of image quality in CT and factors affecting CT image quality. The chapter concludes with a summary of the main points.

3.1 Introduction

Diagnostic x-ray imaging has been used for over a century, after the published discovery of x-rays by Wilhelm Conrad Roentgen in 1896 (Roentgen, 1896; Swinton, 1896). The interiors of the human body can be seen from radiographic projections (Stanton, 1969). Figure 3.1 shows the first x-ray image Roentgen published. It is an image of his wife's hand which clearly revealed her wedding ring and bone. The image produced by x-rays is a projection (or shadow) of the objects in the path of the x-rays. The images formed are due to the different absorption rates of different tissues. In this image, the x-ray opaque regions such as bone appear darker than the x-ray transparent regions like fat and other soft tissues on a film recording of the x-ray image. This two-dimensional (2D) transmission image is called a radiograph.

Figure 3.1 *Bertha Roentgen's hand, the first x-ray image Roentgen ever published. Retrieved from Medcyclopaedia (2011).*

Planar x-ray radiography produces a simple 2D projection of the tissues lying between the x-ray source and the film. It is used for different purposes including abdominal radiography to study the liver, bladder, abdomen and pelvis; chest radiography for diseases of the lung and broken ribs and x-ray fluoroscopy (in which images are acquired continuously over a period of several minutes) for a number of different genitourinary and gastrointestinal diseases. However, the overlapping part of soft tissue or bone structures on the projected image can be difficult to interpret.

The introduction of CT in the 1970s was a major step toward reducing the superposition problem in diagnostic imaging. CT is used to overcome this problem by producing three-dimensional (3D) x-ray absorption images. CT differs from radiography in several aspects. A major difference is the way the systems work. CT measures the spatial distribution of a physical quantity from different angles with a detector and computes superposition-free images from the data. On the other hand, radiography records the radiation emitted from the x-ray tube and attenuated by the object from a single viewpoint with a detector, traditionally by film.

For CT imaging, a number of studies proved that the internal structure of an object can be reconstructed from multiple projections of the object. The mathematical principles behind the

reconstruction of the CT image were established by the mathematician Johann Radon. He introduced the concept of reconstructing an object on the basis of its line integrals (Radon, 1917). In 1963, a South African nuclear physicist Allan MacLeod Cormack developed a method of obtaining the distribution of x-ray attenuation coefficients for body tissue in the context of attempting to improve upon existing methods of radiation treatment planning (Cormack, 1963).

In addition, Richard Bates, an electrical engineer and his student Terence Peters, working at the University of Canterbury in Christchurch, New Zealand proposed a method for producing accurate cross-sections from x-ray shadowgrams by digital or optical filtering of traditional tomograms generated by out-of-plane blurring (Bates & Peters, 1971). They also resolved fundamental issues in CT and produced a seminal paper on the topic, just prior to CT's commercial development and use worldwide.

The most popular application of CT has been in the field of medical diagnostics where it was known as x-ray Computerised Axial Tomography (CAT) during the 1970s. The inventor of this imaging machine, Godfrey Hounsfield successfully conducted the first clinical trials on a prototype scanner in 1972 (Hounsfield, 1973). The first clinical image of a patient with a suspected brain lesion revealed the presence and location of a cystic tumour.

Following the successful introduction of the EMI head scanner by Hounsfield into the clinical arena, a period of intensive development and marketing of CT scanners by commercial manufacturers followed. A variety of CT scanner designs were developed directed primarily at improving scan speed and accuracy while maintaining patient comfort and safety (Ledley et al., 1974; Robb, 1982). In 1979, Godfrey Hounsfield was awarded the Nobel Prize for Medicine along with Allan M. Cormack who demonstrated that the mathematics

behind tomography is indeed applicable for real objects (Nobelprize, 1979). Improvements in tomographs by Smith et al. (1973), Peters (1974), Bates et al. (1983) together with other scientists have improved CT development and image reconstruction.

Historical details of the development of CT have been discussed in a number of review articles and books (Robb, 1982; Bates et al., 1983; Kalender, 2005). In particular, Robb, Bates, Peters and Kalender give a detailed discussion of the basic principles of CT within the context of the evolution of CT and the relatively short history of x-ray CT. In addition to the remarkable improvement in contrast resolution of CT over standard radiography, Robb mentions another fundamental reason for its remarkable success, namely that it derives from an ingenious engineering synthesis of several well-founded principles. Fleischmann & Boas reviewed some of the latest innovations in CT together with their historic roots (Fleischmann & Boas, 2011). This article explores earlier and simpler solutions to a given problem, or ideas which could not be implemented until today, but may shed some light on the current technology.

3.2 Basic principles of CT imaging

The basic components of CT imaging are the x-ray source, x-ray detector and object. The x-rays are produced by accelerating electrons with a high voltage and allowing them to collide with a high atomic number material such as the tungsten target (anode) in an x-ray tube. The energy gained by the electron is equal to the potential difference (voltage) between the anode and cathode usually expressed as the peak kilovoltage (kVp). When the electrons are suddenly decelerated (slowed or stopped) by a nucleus of an atom of the metal target, x-rays which are commonly known as bremsstrahlung or braking radiation are produced. The degree of interaction of the accelerated electron with the metal target nucleus can vary, so the energy

spectrum of the x-rays generated by this process is continuous. The energy of these x-rays given in kV ranges up to kVp.

On the other hand, characteristic radiation occurs when bombarding electrons have sufficient energy that when they strike the metal target, they eject an inner shell electron. Electrons from higher states drop down to fill the vacancy, emitting x-ray photons with specific (discrete) energies determined by the electron energy levels. These x-rays are called characteristic x-rays. Figure 3.2 shows the x-ray spectrum with a combination of bremsstrahlung and characteristic radiation (the sharp peaks are characteristic radiation associated with the atoms in the target).

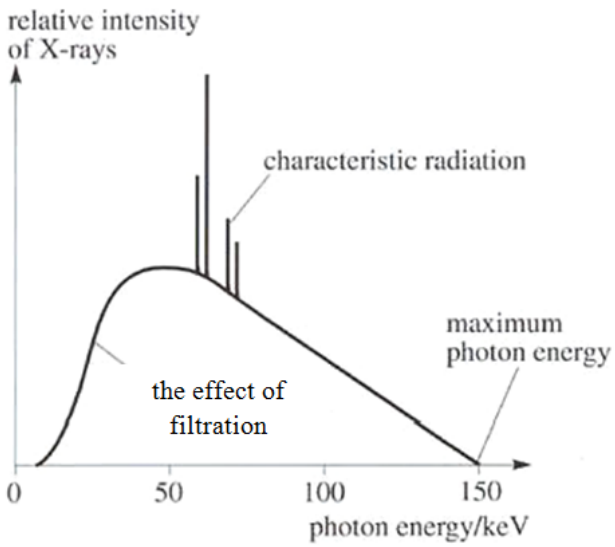

Figure 3.2 *The emission spectrum for a tungsten target x-ray tube operated at 150 kVp. Characteristic K x-ray emission occurs for tungsten whenever the tube voltage exceeds 60 kVp, corresponding to the K-shell binding energy for tungsten. The rising edge is due to the effect of the filtration. The purpose of the filtration is to enrich the beam with high energy photons by absorbing the lower energy component of the spectrum. The characteristic x-rays are seen as sharp peaks on top of the broad continuum from the bremsstrahlung. The area under the spectrum represents the total number of x-rays. Retrieved from OpenLearn LabSpace (2005).*

The lowest energy x-rays are absorbed by the x-ray tube and x-ray filters. These lower energy x-rays are less penetrating and do not contribute to image formation but add to patient dose. Most x-ray manufacturers add filtration to filter out the low energy x-rays. The composition of an x-ray spectrum with respect to bremsstrahlung and characteristic radiation depends on three factors; the anode material, kilovoltage and filtration.

The basic setup of CT imaging is shown in Figure 3.3. The x-ray source and detectors rotate together around the patient, producing a series of projections at a number of different angles. The image is then reconstructed from the resulting projection data producing cross-sectional images of areas of the body.

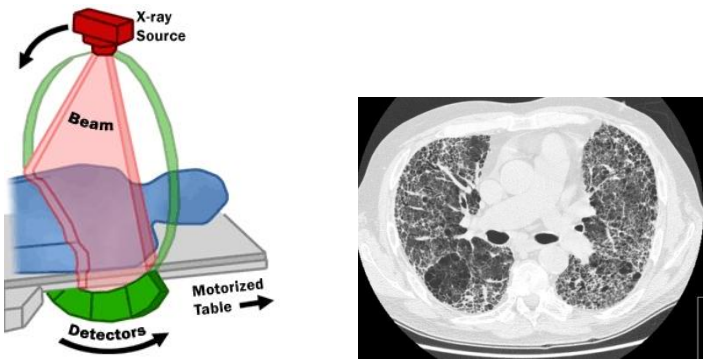

Figure 3.3 *(Left) The basic setup of CT imaging. The x-ray source and detector unit rotate synchronously around the patient. Data is essentially acquired continuously during rotation. (Right) An example of a single-slice CT image of the lung. Retrieved from U.S. Department of Health and Human Services (2010).*

Conventional CT systems use integrating detectors. These are composed of detecting elements such as scintillating crystals and photodiodes. These detectors measure the energy deposited by the interactions of x-ray photons as they pass through the object and convert the locally absorbed x-ray energy into a visible light. This type of detector provides integrated information about the total energy of the transmitted beam. Information about the energy distribution of the detected x-ray flux is not recorded. Therefore, certain types and densities of material cannot be differentiated with this type of detector.

3.2.1 Image reconstruction in CT

The first CT machines used iterative reconstruction methods, the algebraic reconstruction technique (ART), to provide a cross-sectional image based on the attenuation measurements of x-rays transmitted through a patient's body. For larger data volumes, finer image matrices and the higher demand on image quality, approaches based on ART led to unacceptably high computation times (Kalender, 2005).

CT image reconstruction is a process to retrieve x-ray attenuation coefficients from their integrals along the beam path (Herman, 1980). The basic principles of CT image reconstruction have been reviewed in books by Avinash C. Kak (Kak et al., 1988), Jerrold T. Bushberg (Bushberg et al., 2001) and Jiang Hsieh (Hsieh, 2003). For mono-energetic sources the attenuation occurs exponentially in matter as shown in Equation (3.1).

$$I = I_0 \exp\left(-\int_L \mu\,(x,y)d\xi\right) \tag{3.1}$$

where $\mu(x, y)$ represents the attenuation coefficient at a point (x, y), L is the path of the ray and ξ is the distance along L. In CT, dividing the measured photon counts by the incident photon counts and taking the negative logarithm yields samples of the Radon transform of the linear attenuation map. Thus, the total attenuation of p of a ray position ξ on the projection angle, φ, is given by the line integral:

$$p(\xi,\varphi) = \ln\left(\frac{I}{I_0}\right) = -\int_L \mu\,(x,y)\,d\xi \tag{3.2}$$

In polar coordinates, the value of ξ onto which the point (x, y) will be projected at angle, φ, can be written as:

$$\xi = x\,\cos\varphi + y\,\sin\varphi \tag{3.3}$$

Equation (3.2) can also be written as:

$$p\,(\xi,\varphi) = \int f(x,y)\delta\,(x\,\cos\varphi + y\,\sin\varphi - \xi)\,dx\,dy \tag{3.4}$$

where $f(x, y)$ represents $\mu(x, y)$, δ is the Dirac delta function and the coordinates x, y, ξ and δ are defined in Figure 3.4.

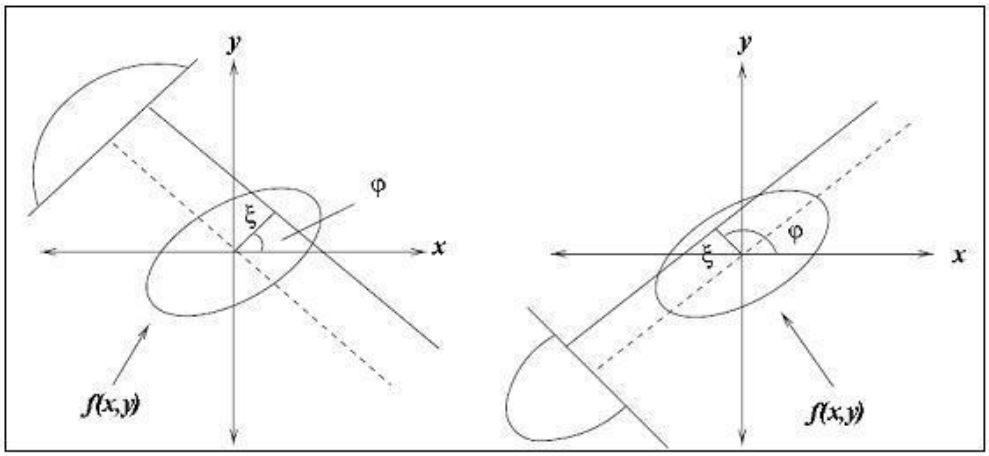

Figure 3.4 *The coordinate systems for Radon transform.*

The function $p(\xi, \varphi)$ is often referred to as a sinogram because a single point in the object $f(x,y)$ is mapped to a sinusoid in this projection space. A sinogram is a way to display the projections, where projection data at one view are put in one row of the sinogram and the vertical direction represents the view angle. A point in the object volume corresponds to a sine wave in the sinogram.

To reconstruct a cross section requires us to find $f(x,y)$ for given knowledge of $p(\xi, \varphi)$. In today's CT scanners the so-called convolution-backprojection procedure is usually utilised (Kalender, 2005). The most popular form of image reconstruction is based on a method first described by mathematicians Ramachandran and Lakshminarayanan known as filtered

backprojection (Ramachandran & Lakshminarayan, 1971). The back projection process can be formulated as:

$$f\ (x,y) = \int_0^{\pi} d\varphi\ p\ (\varphi,\xi)^*\ k(\xi)|_{\xi = x\cos\ \varphi\ +\ y\sin\ \varphi} \tag{3.5}$$

where $p(\varphi, \xi)$ represents the centre of rotation and $k(\xi)$ is the reconstruction kernel. This method is based on equations that describe an exact solution for the reconstruction in which the projection data are first filtered using a convolution filter or kernel and then back projected. The kernel is adjusted so that the final image is an exact representation of the scanned object. Using the Fast Fourier Transform, the number of computations required for the convolution step can be reduced by performing the convolution in Fourier space. Figure 3.5 shows a computer simulation of filtered back projection.

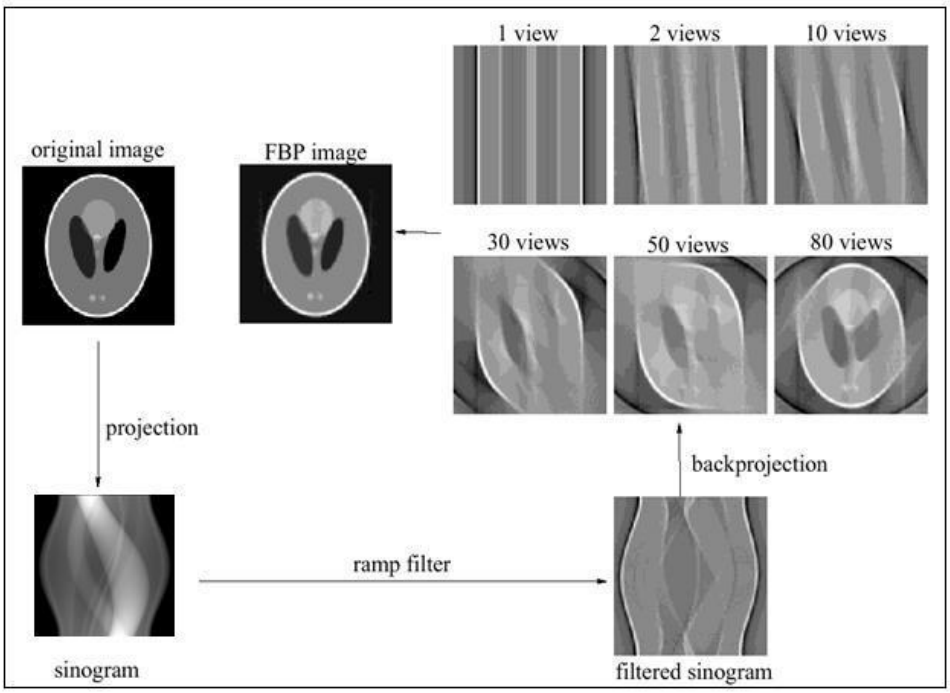

Figure 3.5 *A computer simulation of filtered back projection. Retrieved from AAPM (2010).*

The aforementioned section presents the 2D algorithms used to reconstruct the slice of the measured object. To reconstruct a volume segment, the complete procedure must be performed slice-by-slice with a small movement of the object or of the source-detector system between each slice. For 3D reconstruction from circular cone beam projections, the Feldkamp-Davis-Kress (FDK) algorithm is a well known algorithm for the planar detector configuration. It was the first practical algorithm for cone beam CT acquired from a circular source trajectory (Feldkamp, Davis & Kress, 1984). FDK has been the most widely implemented method for 3D cone beam reconstruction from transmitted x-ray projections because of its modest computational requirements and relative ease of implementation. Figure 3.6 shows the geometry and gives the parameters for the FDK algorithm with a planar detector. The projection angle β, the fan angle γ, the cone angle k, and the source trajectory radius R, are also shown in the figure.

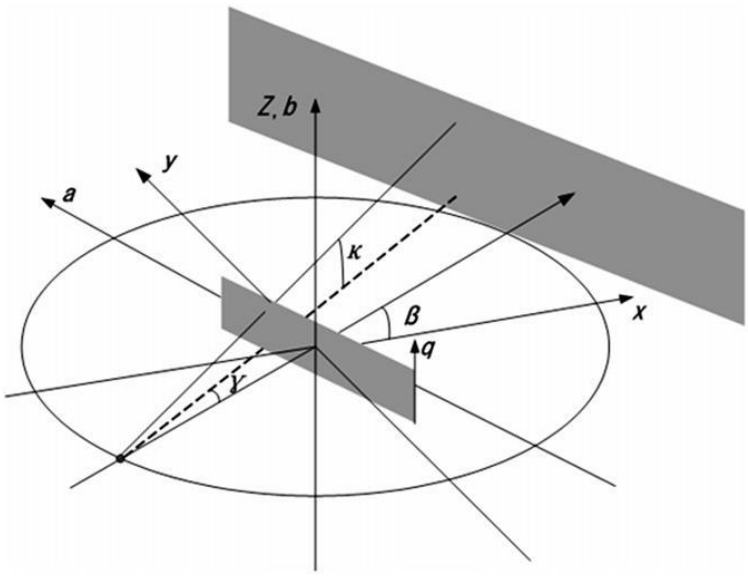

Figure 3.6 *The geometry description and parameters for the FDK algorithm. Retrieved from Li et al. (2008).*

The detector plane (a, b) is placed on the rotation axis where b-axis coincides with the z-axis. The projection data, p^F, from planar detector is defined as $p^F(\beta, a, b)$. In the FDK method, the projection data are processed row by row, pre-weighted, and then convolution with the rampfilter $g^P(a)$ is applied on the pre-weighted data:

$$\tilde{p}^F(\beta, a, b) = \left(\frac{R}{\sqrt{R^2 + a^2 + b^2}} p^F(\beta, a, b) * g^p(a)\right) \tag{3.6}$$

The pre-weighting factor is geometrically described as the product of two cosine factors of the fan angle and cone angle. It is defined as:

$$\frac{R}{\sqrt{R^2 + a^2 + b^2}} = \frac{R}{\sqrt{R^2 + a^2}} \frac{\sqrt{R^2 + a^2}}{\sqrt{R^2 + a^2 + b^2}} = \cos\gamma \cos k \tag{3.7}$$

The pre-weighted and filtered projection data are backprojected into the reconstructed voxels as:

$$f_{FDK}(x, y, z) = \int_0^{2\pi} \frac{R^2}{U(x, y, \beta)^2} \tilde{p}^F\big(\beta, a(x, y, \beta), b(x, y, z, \beta)\big) d\beta \tag{3.8}$$

where $a(x, y, \beta)$ and $b(x, y, z, \beta)$ are:

$$a(x, y, \beta) = R \frac{-x \sin\beta + y \cos\beta}{R + x \cos\beta + y \sin\beta} \tag{3.9}$$

$$b(x, y, z, \beta) = z \frac{R}{R + x \cos\beta + y \sin\beta} \tag{3.10}$$

The weighting in (3.8) is a function of the distance $U(x, y, \beta)$ between the source and the line parallel with the detector that intersects the image point (x, y) as shown in Figure 3.6. This distance can be expressed as:

$$U(x, y, \beta) = R + x\cos\beta + y\sin\beta \tag{3.11}$$

The integral is replaced by a sum over the projection angles for the discrete case. A 2D interpolation of the filtered projection data is then required for each term of the back projection sum.

3.2.2 CT image display

The reconstructed CT images are usually displayed as grey scale images. The pixel on the CT image displays the average x-ray attenuation properties of the tissue in the corresponding voxel. These attenuation values are often referred to as CT numbers and specified in Hounsfield Units (HU) (Hounsfield, 1973). As introduced by Brooks (1977), the CT value of an arbitrary tissue, x, with attenuation coefficient μ_x is normalised to water. The CT value is obtained as shown in Equation (3.12):

$$\text{CT value} = \frac{\mu_{x} - \mu_{water}}{\mu_{water} - \mu_{air}} 1000 \text{ HU} \tag{3.12}$$

The CT values of water and air are independent of the energy of the x-rays and therefore constitute the fixed points for the CT value scale. The air has a CT value -1000 HU and water, the most common calibration material, has a value of 0 HU. Figure 3.7 shows the scale of CT value of the most important human organs. The lower attenuating tissues exhibit negative CT values due to their lower attenuation compared to water. The positive CT values corresponding to other tissue types such as muscle, connective tissue and most soft tissue

organs are due to the physical density of these tissues. Basically, the CT system will be calibrated against some typical object before any quantitative assessment of CT values is justified.

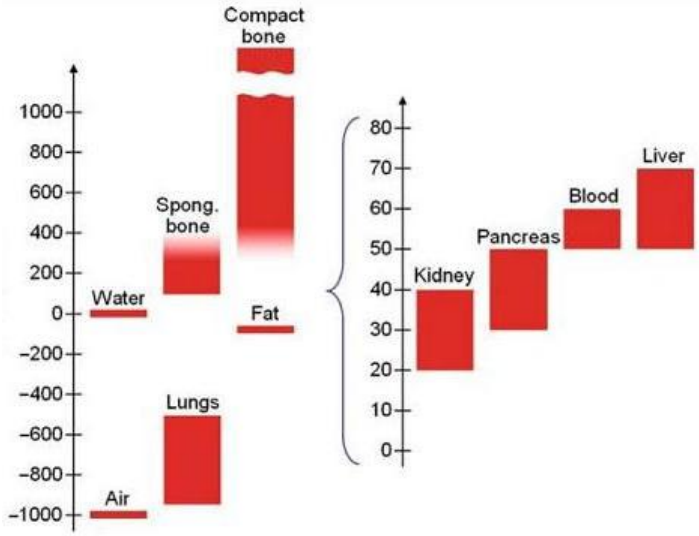

Figure 3.7 *The CT Hounsfield scale for various human organs at an effective energy of about 70 keV. The CT values show the attenuation coefficient of the tissues relative to the density of water. The typical HU range of compact bone is 300 HU to 1300 HU. Retrieved from Kachelrieß (2008).*

3.3 Evolution of spatial resolution in CT imaging

Dramatic advances in imaging technology have been made in the molecular and genomic imaging fields. Some objects of interest are far smaller than the human body and it has been important to scale down clinical imaging modalities for specialised measurements of small objects with a high resolution. Recent developments both in microfocus x-ray sources and pixel detectors have resulted in the development of cone-beam CT systems with resolving power in the order of tens of micrometers, creating a field known as microtomography (Ritman, 2004; Landis & Keane, 2010). Typical x-ray tube parameters used in micro-CT systems are focal spot sizes in the range of 10-100 μm and tube currents of at most a few mA and anode voltage of 25-75 kV (Cherry, 2004).

Micro-CT has been widely used in preclinical examinations such as scans of tissue samples, organs or small animals (ex vivo or in vivo) that are used as models to evaluate human diseases and therapies (Paulus et al., 1999; Holdsworth & Thorton, 2002; Lee et al., 2003). It has also been used as a tool for indirect approaches to molecular imaging (Ritman, 2004). The widespread availability of micro-CT has driven the imaging technology forward and easy to use imaging systems are available that can provide high sensitivity, high resolution, quantitative images of specific biological targets in vivo and at low cost. Figure 3.8 shows the scales involved in hierarchical fashion ranging from whole bodies to the sub-cellular level.

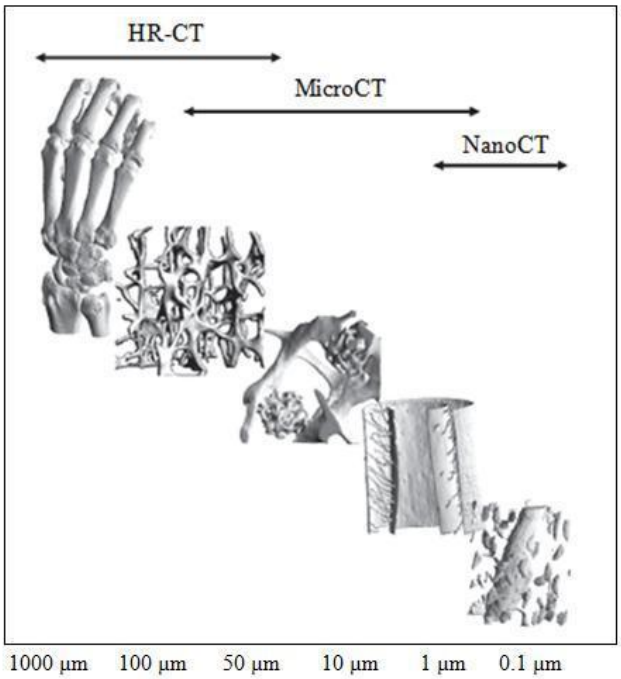

Figure 3.8 *The hierarchy of scales associated with different forms of CT. The CT technique can be used over the range of different resolutions, whilst using the same physical principles. In high resolution CT, normal x-ray tubes can be used as a source, whereas for micro-CT special microfocus x-ray tubes are required. The lower range of micro-CT as well as the nano-CT domain is currently best assessed using synchrotron radiation. The images show from left to right, human hand, trabecular bone structure, microcallus, murine cortical bone surface of a femur with internal vasculature and capillary in bone surrounded by osteocyte lacunae. Retrieved from Stauber et al. (2008).*

Many articles on micro-CT have been discussed and published. Articles written by Ritman (2007), Landis & Keane (2010) and Wang et al. (2011a) provide description of the physics and the mathematical analysis behind the technique. They include example applications to specific material characterisation problems, with a particular focus on the utilisation of 3D image processing that can be used to extract a wide range of useful information.

One of the major challenges for in vivo micro-CT imaging is the radiation dose received by the subject. The radiation dose of a standard micro-CT scan is relatively high mainly due to the larger photon fluence needed to maintain an adequate signal-to-noise ratio (SNR) at the higher spatial resolution. The cumulative radiation dose could influence the experimental outcome by affecting animal survival rates and tumour growth (Willekens et al., 2010). The smaller voxel size in micro-CT requires higher radiation doses to produce images comparable to clinical CT. Therefore, its sensitivity is ultimately limited by its potential to induce radiation damage. Improvements in the detector technology, the optimisation of the x-ray spectrum and imaging geometry are needed to improve SNR and allow a reduction in the radiation dose for micro-CT to be capable of safely acquiring high quality micro-CT images.

3.4 CT image quality

The basis for judging CT image quality is the ability to extract relevant information present in the image for the diagnostic task. It is a concept of central importance for the evaluation of the imaging system. The choice of x-ray tube voltage and output will affect the quality of the CT image as well as the radiation dose received by the patient. CT image quality is dependent upon four important factors to produce the best possible image for the anatomical region being imaged. The four factors are: image contrast, spatial resolution, image noise and

artifacts. The aim in CT imaging is to optimise image quality within suitable radiation dose constraints. Therefore compromises have to be made depending on the diagnostic task.

3.4.1 Image contrast

Image contrast is the difference in the measured intensity of one area relative to another. The measurement of the contrast is derived from the attenuation differences between an object and the background material. The image contrast is related to photon energy but is independent of x-ray beam intensity (e.g., milliampere second (mAs)). The photoelectric effect dominates in low-energy x-rays and varies with material properties approximately as ρZ^3 and with x-ray energy as E^{-3}. At higher energies, Compton scattering is the dominant interaction and it is essentially independent of the effective atomic number of the tissue, is proportional to the tissue electron density, and is weakly dependent on the energy of the incident x-ray. Thus the radiographic contrast initially reduces quickly with energy for most materials.

The ability to distinguish between materials depends upon their contrast and also upon the measurement noise of the system. Poor counting statistics can render two materials indistinguishable regardless of the differences in their attenuation values. The contrast-to-noise ratio (CNR) quantifies contrast relative to random pixel noise. Other factors affecting the image CNR is the x-ray filtration, object size and the type of the lesion being investigated (Huda, 2002). The SNR is a measure of the average value of a signal relative to its background noise. A thicker tissue will decrease the SNR because the x-rays have to travel through a greater thickness and give a greater attenuation. These factors reduce the CNR of the image. The value of CNR has been used to interpret the quality of CT image.

The CNR is defined as:

$$\mathrm{CNR} = \frac{\mu_{\mathrm{detail}} - \mu_{\mathrm{background}}}{\sqrt{\sigma^2\mathrm{detail} + \sigma^2\mathrm{background}}} \tag{3.13}$$

where μ_{detail} and $\mu_{\mathrm{background}}$ are the attenuation coefficients for the detail (material) and the background and σ_{detail} and $\sigma_{\mathrm{background}}$ are the corresponding standard deviation for the detail and the background. CNR is also known as the difference in SNR between two different materials.

3.4.2 Spatial resolution

Another important descriptor of image quality is spatial resolution. The spatial resolution describes the capability of an imaging system to display fine details separately. It is generally determined for high-contrast structures in order to eliminate the influence of noise on this measurement. The decisive geometrical factors influencing the resolution in the scan plane are the focus size, the scan geometry, the detector element spacing, the aperture and the movement of the focus during the measurement (Goldman, 2007). The evaluation of spatial resolution is performed by direct or indirect measurements.

The standard direct measurement of spatial resolution is measurement with a series of hole patterns or bar tests. The spatial resolution of an image using this technique is defined to be the size of the smallest hole or bar patterns that is separately visible on the image. It is typically given in line pairs per millimeter. The spatial resolution can be determined indirectly by calculation of the point spread function (PSF) from a thin wire phantom or edge phantom. The PSF is subjected to a Fourier transform to obtain the modulation transfer function (MTF). The spatial resolution is taken from the full width at half maximum of the PSF or the 10% value of the MTF.

3.4.3 Image noise

Image noise is defined as the random fluctuation of pixel values in a region that receives uniform radiation exposure. It is important for the detection of low-contrast lesions which may be obscured by higher levels of image noise. The image noise can be quantified as the standard deviation of the voxel values in a homogeneous phantom (typically a water phantom) and it is determined by the number of x-rays contributing to each detector measurement. The fewer the x-rays, the greater the graininess or mottle of the image. There are several parameters that affect the number of detected x-rays.

The first parameter is the x-ray tube current. The number of x-rays produced by the x-ray beam is proportional to the x-ray tube amperage. Doubling the x-ray tube current will double the x-ray beam intensity. The x-ray tube current is usually considered together with the scan time, thus, the product of the x-ray tube current in mA and scan time or exposure time in s is known as mAs. The x-ray beam exposure is always proportional to the mAs. At a fixed x-ray tube voltage, halving the mAs will increase the image noise by a factor $\sqrt{2}$

The slice thickness also affects the number of x-rays detected and hence the noise of the image. The slice thickness is related to the beam width and therefore changing the thickness will change the number of detected x-rays proportionally.

The x-ray tube voltage also affects the image noise as it is related to the x-ray tube output intensity and energy spectrum. Changing the x-ray tube voltage changes the shape of the x-ray spectrum. Increasing the tube voltage increases the x-ray tube output intensity. The image noise and image contrast decrease with increasing tube voltage. The reconstruction filters also affect the appearance of noise in the image. Sharp filters enhance the noise but the smooth filter blurs the noise and reduces the visual impact.

To summarise, the image noise can be reduced by increasing mAs, kV and slice thickness. However increasing kV will reduce contrast and increasing slice thickness will reduce resolution in the z-axis. The CT image noise can be minimised by the use of various reconstruction filters.

3.4.4 Artifacts

Artifacts are defined as any structure that is seen on an image but is not representative of the actual anatomy. The common types of CT artifacts are shading artifacts, ring artifacts and streak artifacts (Hsieh, 2003). The beam-hardening effect is the most common type of shading artifact. The beam hardening effect derives its name from its underlying cause: the increase in mean x-ray energy (hardening) of the x-ray beam as it passes through the object. This occurs because the lower energy photons are generally absorbed more easily than higher energy photons. There are two types of artifact that can result from this effect: so-called cupping artifacts and the appearance of dark bands or streaks between dense objects in the image.

Ring artifacts arise from errors, imbalances, calibration drifts or other inaccuracies in an element of a detector array relative to its neighbors. This circular artifact visible on a clinical image would rarely be confused with disease. Another artifact is the streak artifacts which occur in very heterogeneous cross sections because the portion of the beam that passes through one of the objects at certain tube positions is hardened less than when it passes through multiple objects at other tube positions. Thus, dark bands or streaks can appear between dense objects in an image. This type of artifact occurs both in bony regions of the body and in scans where a contrast medium has been used. This artifact might be mistaken for disease in nearby anatomy (Barrett & Nicholas, 2004). All of these types of artifacts degrade the CT image quality and thereby make an accurate interpretation more difficult.

3.5 Summary

1. Since the discovery of x-rays by Wilhelm Conrad Roentgen, x-ray techniques have been developed for clinical practice. The introduction of CT in 1972 was a major step towards reducing the superposition problem in diagnostic imaging. CT measures the spatial distribution of a physical quantity to be imaged by acquiring x-ray projections from different angles with a detector and computing superposition-free images from the data. On the other hand, the radiography records radiation emitted from the x-ray tube and attenuated by the object viewed from a single viewpoint. Radiographic images comprise the superposition of attenuation from multiple details and can be difficult to interpret. Radiographic images are nowadays normally acquired by flat panel digital detectors but were traditionally acquired by film.

2. The computed attenuation coefficients are displayed as CT values in HU relative to the attenuation of water. Recent developments in high resolution micro-CT and the widespread availability of this technology provide researchers with access to high sensitivity, high resolution, quantitative images of specific biological targets in vivo and low cost.

3. CT image quality is described in terms of image contrast, spatial resolution, image noise and artifacts. In standard CT with energy-integrating detectors, acceptable image quality must be traded against acceptable radiation dose. In spectral CT, image quality may be enhanced without dose penalties through the use of spectroscopic photoncounting detectors that record more information per x-ray event.

Chapter 4

The Medipix photon-counting detector

This chapter gives an overview of recent advances in x-ray detector technology and particularly the development of the Medipix photon-counting detector. It describes the operating principles of the Medipix detectors. The advantages of these energy-resolving photon-counting detectors are compared to conventional energy-integrating detectors used in clinical CT systems. This chapter concludes with a summary of the main points.

4.1 Introduction

The x-ray detector is one of the most important components in a CT system. It plays a special role in recording the flux distribution of the incident ionising radiation. Progress in CT performance depends upon the concurrent development of x-ray detector technology. Conventional x-ray detectors used in CT systems are classified as energy-integrating in contrast to detectors such as Medipix that are classified as photon-counting.

Energy-integrating detectors are commonly used in current clinical CT systems as discussed in Chapter 3. The signals from multiple x-ray interactions accumulate over a certain sampling period and the detector produces a signal that is proportional to the overall energy deposited by all of the photons in the x-ray spectrum. Thus, information about the energy of individual photons is lost and the ability to distinguish some materials is reduced using this type of detector.

Photon-counting detectors operate using a different principle. The signal from each photon interaction in the detector material is processed individually and the spatial distribution of

incident events is recorded as a distribution of counts rather than total energy. Furthermore because each signal pulse is processed individually, detectors like Medipix are able to discriminate each event on the basis of their pulse-height and thereby record the energy spectra of the incident flux.

The development of energy-resolving photon-counting detectors such as Medipix is enabling a new evolution in CT imaging. These detectors were developed by the Medipix collaboration at the European Organisation for Nuclear Research (CERN) (Medipix, 2011). The development and use of photon-counting detectors has been studied extensively over the last decade (Chmeissani & Mikulec, 2001; Llopart, 2002; Llopart & Campbell, 2003; Fornaini et al., 2004; Ballabriga et al., 2007; Ballabriga, 2011). These studies describe the many design improvements that have taken place in photon-counting detector technology. Several technical challenges have been identified and addressed, including the need for improved count rate capabilities of the detectors and readout electronics for x-ray CT imaging applications.

Spectroscopic photon-counting detectors offer a number of advantages for medical applications. These include the potential for improved contrast detail, spectroscopic material discrimination and reduced electronic noise (e.g. dark current) leading to an increase in SNR (Beuville et al., 1998; Bert et al., 2003; Shikhaliev et al., 2005; Fralliccіardi, 2009a; Fralliccіardi, 2009b).

Spectroscopic photon-counting detectors may also provide significant dose reduction by improving image quality in terms of SNR for a given flux (Watt et al., 2003). The demanding requirements for medical imaging applications such as uniformity of response, detector size, counting rate and contrast sensitivity are driving the optimisation and improvement of the design of these novel pixel detectors (Mikulec et al., 2003).

4.2 Medipix detectors

The Medipix detectors are hybrid pixel detectors. They consist of a semiconductor sensor layer bump-bonded to a readout Application Specific Integrated Circuit (ASIC) (Figure 4.1a). Bump bonding is the process that connects each ASIC pixel to the semiconductor layer with a bump of solder. Each pixel of the ASIC contains its own comparator and an individual counter for processing events that occur within the corresponding pixel region of the sensor layer.

The hybrid concept is particularly suitable for medical applications. It is fast due to thousands of counting circuits working in parallel, it provides individually adjustable pixel electronics and the capability to select the sensor material and the electronic layer independently.

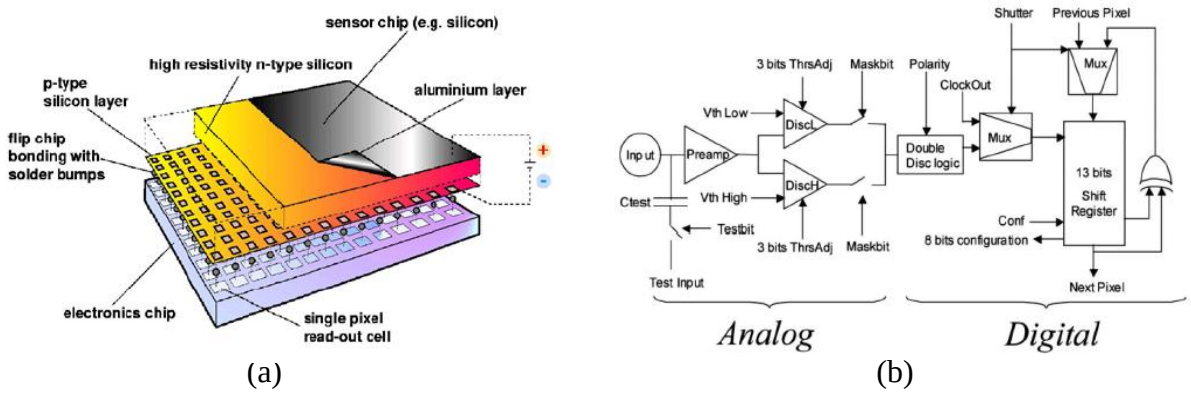

Figure 4.1 *Medipix detector assemblies. (a) The Medipix detection system and (b) the electronic circuitry of a Medipix2 pixel cell. The analog side contains a charge preamplifier with direct current leakage current compensation, a test capacitance and two branches of identical discriminators. The digital side contains the double discriminator logic and 13-bit shift register.*

Schematic diagrams of the Medipix detector are shown in Figure 4.1. The Medipix detector enables direct conversion of individual x-ray photons into an ionisation cloud of electrons and holes within the semiconductor sensor. A depletion layer free from charge carriers is created in the detection layer by the reverse bias voltage applied to the semiconductor. Most incoming x-ray photons interact with the sensor layer by the photoelectric effect and deposit their energy with a photoelectron. This electron sheds its large kinetic energy through the creation of many electron-hole pairs along its path. These electron and hole charge carriers drift towards the anode and cathode respectively where their charge is measured by the underlying ASIC layer. These ASICs have an electronics chain for each pixel in the detector. The electric signal is amplified and increments a counter if the signal is above a pre-set threshold.

The hybrid detector design allows for a choice of sensor layer to be bonded on the CMOS ASIC depending on the imaging problem. There are three semiconductor materials available for bump bonding onto the Medipix ASIC: Silicon (Si), Gallium Arsenide (GaAs) and Cadmium Telluride (CdTe). These three semiconductor materials have different detection characteristics. The energy dependent x-ray absorption coefficient of the material determines its intrinsic photon detection efficiency. This in turn influences the choice of x-ray source parameters and the relevant energy range that can be imaged.

Figure 4.2 shows the absorption probability of different sensor materials in the energy range relevant to medical imaging. Si is chosen for its uniformity and availability but it has modest quantum efficiency up to around 35 keV. This makes Si suitable only for preclinical imaging of soft tissues. GaAs at the same thickness has a higher absorption probability which makes it a reasonable choice for applications using x-ray energies up to around 50 keV. On the other hand, high-Z materials like CdTe are needed for applications that require a high efficiency up to 100 keV. At this time, it is difficult to grow crystals of GaAs or CdTe of suitable quality for use with Medipix ASICs.

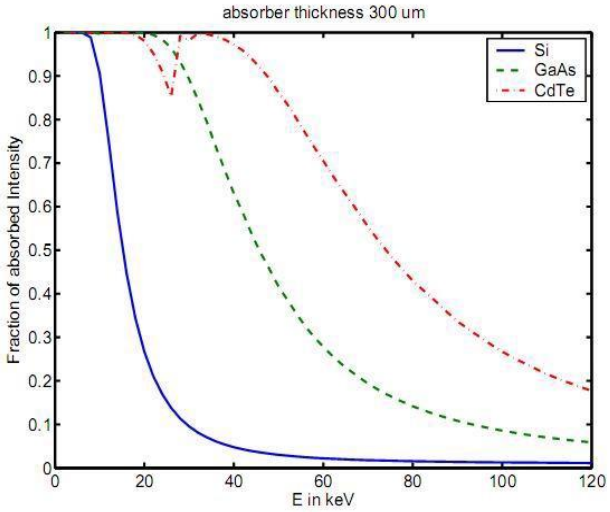

Figure 4.2 *Absorption probabilities of different semiconductor materials with 300 µm thickness. The choice of sensor layer depends on the availability of the sensor layer for application. For most energies Si has a lower absorption probability compared to GaAs and CdTe. The higher-Z materials like GaAs or CdTe, have better conversion efficiencies than Si for x-rays in the energy-range used for medical imaging (20-100 keV). Retrieved from Mitschke (2006).*

The Medipix collaboration has developed a number of different versions of the Medipix detector: Medipix1 (Campbell et al., 1998), Medipix2 MXR and Timepix (Llopart & Campbell, 2003; Medipix, 2011) and recently the Medipix3 detectors (Ballabriga et al., 2007). The Medipix1 was designed with an array of 64 × 64 pixels. The individual pixel size was (170 × 170) μm^2 giving a total active area of 1.18 cm^2. Each pixel contained a preamplifier, an adjustable threshold and a counter. The Medipix1 detector was extensively studied over the years by the Medipix collaboration and this led to the design of the improved Medipix2 detector.

The Medipix2 detector represents an improvement on Medipix1 in circuit design. A single Medipix2 detector was designed with an array of 256 × 256 pixels each of size (55 × 55) μm^2 giving a total area of 1.96 cm^2. Each pixel has two adjustable energy thresholds and a 14-bit counter. Both of these Medipix detectors operate in single photon-counting mode, in which

the signal from a photon is detected only if it exceeds a predetermined threshold (Medipix1) or falls within a predetermined range (Medipix2). The reduction in pixel dimension from Medipix1 to Medipix2 is possible because of the tiny dimensions of individual transistors and high number of metal interconnects layers.

Differences between the Medipix1 and Medipix2 detectors include the higher intrinsic spatial resolution (55 μm pixel pitch) of Medipix2. Each Medipix2 pixel also has two thresholds meaning that the Medipix2 detector can selectively count only those photons that fall within a certain energy range (energy window). Furthermore, Medipix2 also has double-polarity charge sensitivity. This allows it to collect either electron or hole charge carriers from the radiation induced ionisation. This feature is important for room temperature compound semiconductors, such as CdTe, where transport and collection of electrons is preferred to holes.

However, pixellated photon-counting detectors have an intrinsic limitation called the charge sharing effect (Campbell et al., 2008). The charge sharing effect occurs due to the diffusion of charge when it drifts toward the pixel electrodes under the influence of the bias field. The charge spreads laterally, and by the time it reaches the electrode the charge cloud extends over multiple pixels instead of a single pixel. In this case, each pixel records only a fraction of the event energy. It is a well-known feature of finely pixellated devices and has been evaluated as a function of energy within the Medipix2 collaboration (Tlustos, 2005; Pennicard et al., 2010; Gimenez et al., 2011). The charge sharing effect has a strong impact on the performance of fine-pitch pixellated detectors as multiple counts can be induced in adjacent pixels from a single x-ray photon of high energy in the detector bulk. As a consequence charge sharing will also degrade the energy resolution (Pellegrini et al., 2007).

The single Medipix2 ASIC is made in 0.25 μm CMOS (Llopart et al., 2002). The Medipix3 detectors increase the number of counts per pixel by using 0.13 μm CMOS (Ballabriga et al., 2007). The Medipix3 consists of 256 × 256 pixels with a pitch of 55 μm and total detection area of 1.96 cm^2. Medpix3 provides better spectroscopic functionality through multiple thresholds per pixel. The Medipix3 detectors are also designed with two additional operational modes: single pixel mode and a charge summing mode. Single pixel mode is the traditional mode of operation where each pixel operates independently processing pulses from individual interaction events.

It has been shown that the charge-sharing events are successfully eliminated when Medipix3 is operated in charge summing mode (Ballabriga, 2011). In this new operating mode, the full charge generated by a photon is reconstructed by neighboring pixels and summing the charge collected in each neighborhood. The event is then assigned as a single hit to the summing circuit with the largest charge deposited.

The imaging performance of the Medipix detectors and their potential for medical applications have been discussed in many publications (Bert et al., 2003; Roessl & Proksa, 2007; Roessl et al., 2009; Butzer et al., 2008; Butler et al., 2008; Feuerlein et al., 2008; Firsching et al., 2009; Boll et al., 2009; Frallicciardi et al., 2009a; Frallicciardi et al., 2009b; Anderson et al., 2010). However an issue with the Medipix detector is its small detecting area -it is challenging to scan a large object. Members of the Medipix collaboration have addressed this problem by developing multi-detector boards that is capable of carrying a 2 × N chip array (e.g., a 2 × 2 quad Medipix array is 28 mm × 28 mm). The Medipix read out chips are placed next to each other with a gap of less than 200 μm between them.

Figure 4.3 shows a single Medipix3 and a MARS camera with a Medipix3 detector array. Mounting a number of detectors within a multi-detector board increases the heat produced. This can cause temperature instabilities during operation that may degrade the performance of Medipix detectors (Ronaldson et al., 2011a). The MARS research group have overcome this issue by installing a Peltier cooler (thermoelectric heat pump) onto the detector board to maintain the detector at constant temperature during operation.

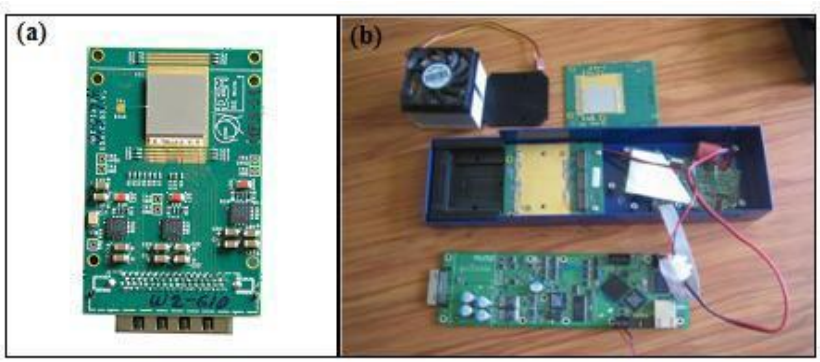

Figure 4.3 *(a) A single Medipix3 detector with 300 µm Si sensor layer has 256 x 256 pixels in a detection area of 14 mm × 14 mm. (b) A multi-detector board capable of carrying up to 2 × 3 Medipix3 detectors. A Peltier cooler (thermoelectric heat pump) was mounted onto the multi-chip board to maintain the Medipix detector at a constant temperature during scanning.*

4.3 Summary

1. The development of innovative energy-resolving photon-counting detectors that are capable of measuring single photon events provides better performance compared to conventional energy-integrating detectors. Photon-counting detectors process each event individually and can provide an essentially noise free measure of the spatial flux distribution. Energy-resolving detectors also provide spectroscopic data that may allow different materials to be distinguished based on the energy dependence of their linear attenuation coefficients.

2. A number of technical developments have evolved with the family of Medipix detectors. These include increased spatial resolution, flexible signal processing for handling both electron and hole charge carriers and the development of charge summing mode designed to correct the charge-sharing effect that degrades the performance of fine-pitch pixel detectors.

3. Improvements in CT performance that may result from the adoption of high resolution spectroscopic photon-counting detectors include improved detectability of fine details, the ability to discriminate between materials and tissue types by the spectroscopic characteristics of their absorption coefficients and the reduction of electronic noise leading to improved SNR.

4. A further potential advantage that may result from the use of spectroscopic photon-counting detectors is a reduction in dose for a given contrast resolution. In conventional CT, acceptable image quality must be traded against acceptable radiation dose. In spectral CT, image quality may be enhanced without dose penalties through the use of spectroscopic photon-counting detectors that record more information per x-ray event.

Chapter 5

Spectral CT

This chapter focuses on the evolution of CT imaging. It discusses the technological basis for conventional, dual-energy and spectral (multi-energy) CT. It also covers the development of the MARS-CT spectral micro-CT scanners that have been developed and built by our research group in Christchurch, New Zealand. The Medipix photon-counting x-ray detectors developed at CERN are a key component of the MARS-CT systems that are being developed for preclinical research. MARS-CT is being developed as a joint project between the Universities of Canterbury and Otago, New Zealand, and the CERN Medipix collaboration, Geneva. The operational details of the MARS-CT systems used for pre-clinical applications are reviewed. This chapter also discusses the configuration details of the MARS-CT systems, MARS console and MARS workstation. Potential influencing factors for spectral CT imaging assessment are also discussed. The chapter concludes with a summary of the main points.

5.1 Introduction

As discussed in Chapter 2, to differentiate different types of tissues, some physical property that differs between them needs to be measured. Chapter 3 discussed the principle of conventional CT imaging and showed that this type of system is sub-optimal with regard to its ability to differentiate and classify tissues. Conventional CT based on a single photon energy range has limited value in this respect. With knowledge of how x-rays interact with materials, the new development of energy resolving photon-counting detectors allow material information to be extracted from spectral CT data, thus enabling material differentiation.

The development of spectral CT promises to enable exciting new research and ultimately provide improved clinical diagnostic capability based on quantitative tissue characterisation. The basic principle of spectral CT was introduced by Hounsfield in 1973 (Hounsfield, 1973). He demonstrated that the atomic numbers of two materials can be determined by imaging these materials at two different kilovoltages with CT. Three years later, Alvarez and Macovski proposed a technique for performing separate reconstructions of the two basic x-ray interactions; photoelectric absorption which occurs at low energies and depends on atomic number, and Compton scatter which occurs at higher energies and depends on electron density (Alvarez & Macovski, 1976).

A number of authors have presented methods by which additional information (such as effective atomic number and electron density) can be extracted from CT scans carried out at different energies (Rutherford et al., 1976a; Rutherford et al., 1976b; Millner et al., 1979; Harding & Tischler, 1986; Roessl & Proksa, 2007). Spectral CT images are a useful measure because the energy dependence of the x-ray attenuation coefficient of an object is a function of elemental composition and density.

The following section focuses on the evolution of CT imaging for improving the capability of CT for quantitative tissue characterisation. It is followed by a description of the spectral micro-CT systems developed by our research group in Christchurch, New Zealand. These systems are being provided for researchers to take advantage of recent advances in x-ray detector technology in their work to develop exciting pre-clinical research applications.

5.2 Evolution of CT imaging

Conventional CT technology is of proven clinical value for both diagnostic and interventional purposes. It has generated steady enthusiasm because of the rapid development and emerging

capabilities of the technology. The continuing technical development of CT such as improvements in spatial and temporal resolution, multislice capabilities, speed, innovative and improving structural design of the scanner (e.g., dual source CT) provide radiologists and physicians with more detailed anatomical information allowing better discrimination of tissues and thus more accurate diagnosis (Kalender, 2005).

Another evolving aspect is the data handling, storing, printing and transmission of information in medical imaging (Peters et al., 1986). In the 1980s, Peters reported that CT planning systems were being introduced to establish frame related coordinate systems based on fiducial markers that were recognised on a slice-by-slice basis in CT images. These programs ran on the CT computers which typically were 16 bit minicomputers. As computer hardware became cheaper and more widely available, independent systems evolved that could read images from different modalities and from scanners supplied by different manufacturers (Hardy & Koch, 1982; Hardy et al., 1983; Peters et al., 1986). The evolution of the Digital Imaging and Communications in Medicine (DICOM) standard (Clunie 2006) in the mid 1980s has largely eliminated the problems of data incompatibility between manufacturers (Peters, 2006). These technical advances improve the workflow and data management.

The following paragraphs describe the evolution of CT imaging techniques and the technological basis for dual-energy and spectral CT. The concept behind all forms of CT imaging is to measure the x-ray attenuation properties to characterise the tissues accurately. Figure 5.1 illustrates the evolution of the CT imaging technique from conventional (single energy) CT scanning to dual-energy and spectral CT.

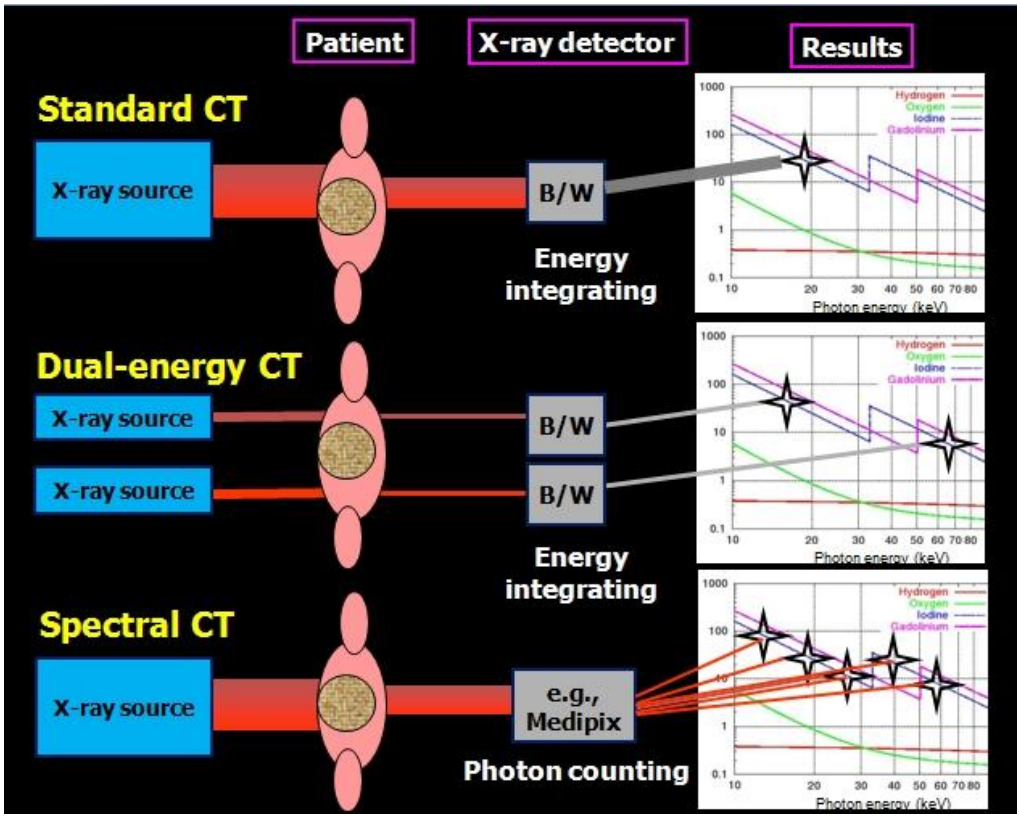

Figure 5.1 *Differences between conventional CT, dual-energy CT and spectral CT. The conventional CT system measures the x-ray flux averaged over the entire spectrum, dual-energy CT measures the flux over two separate spectra and spectral CT detects the flux within multiple energy bands of a single spectrum. The multiple energies are measured by a photon-counting detector, (Medipix) allows a more complete attenuation curve to be reconstructed. Spectral CT can identify multiple materials simultaneously whereas conventional and dual-energy CT have insufficient information to differentiate these materials. This diagram has been used by other MARS team members in several published papers (Anderson et al., 2010; Zainon et al., 2010a) and talks. The diagram has been modified here to suit the thesis context.*

In conventional CT, an image is created by passing x-ray beams through an object from multiple directions and measuring the resultant decrease in their intensity. Each material's x-ray attenuation depends on its atomic number and electron density. The grey levels in a CT slice correspond to x-ray attenuation, which reflects the proportion of x-rays scattered or absorbed as they pass through each voxel. So conventional CT characterises tissues with a

single scalar value in HU, giving total attenuation in a voxel but it cannot reliably differentiate many types of tissue. This is because it measures the cumulative attenuation over the entire energy range for all tissues within the voxel and information about energy dependence of the attenuation coefficient is not retained.

On the other hand, the dual-energy CT technique for improving material separation uses two incident x-ray energy spectra, from a single source repeated at a different tube kilovoltage or by using different source filtrations or both (Marshall et al., 1981; Marshall et al., 1984; Kalender et al., 1986). It can be performed using dual-source synchronous acquisition (Flohr et al., 2006), single-source sequential acquisition and single-source fast-kVp-switching acquisition (Pavlicek et al., 2010). In dual-energy CT, an additional attenuation measurement is obtained at a second energy, allowing the differentiation of the two materials. It exploits the differential relative attenuation of x-ray photons exhibited by materials at different x-ray energies to generate a pair of images that separate structures.

The first attempts to assess the feasibility and usefulness of dual-energy CT for medical indications date back several decades (Millner et al., 1979; Chiro et al., 1979; Kalender et al., 1986; Vetter et al., 1986). These early experimental prototypes ordinarily required the acquisition of two separate CT data sets at different kilovoltage levels. The clinical applications of the aforementioned dual-energy CT are bone removal (Sommer et al., 2009; Yamamoto et al., 2009; Uotani et al., 2009), iodine content computation (Johnson et al., 2007; Graser et al., 2009), differentiation between calcium and iodine (Tran et al., 2009) or between blood, blood mixed with pus, bile and urine (Mahnken et al., 2009) as well as classification of kidney stones (Primak et al., 2007; Stolzmann et al, 2008). Subsequent image co-registration

was required which limited their clinical utility and naturally precluded imaging the beating heart.

State of the art of micro-CT imaging is now capable of providing improved material characterisation using spectral CT. This concept involves the use of a single standard x-ray beam and an energy resolving photon-counting detector. The detector uses a semiconductor sensor layer to directly convert x-ray photons into electron-hole pairs and records the properties of an x-ray beam on a photon by photon basis. Thus, multiple energy measurements necessary for enhanced material discrimination can be obtained from a conventional CT scan. Spectral CT utilises this useful detector technology by dividing a single, broad x-ray spectrum into definable and separate energy bands. Subsequent processing of the spectral data can be used to increase tissue contrast or enable material differentiation.

Spectral CT provides images acquired at multiple energies and these images are known as spectroscopic or spectral CT images. The energy dependence of the x-ray linear attenuation coefficients are functions of the energy dependent probabilities of the Compton and photoelectric interactions as determined by elemental composition and density of the material. Spectral CT data thus enables enhanced differentiation of tissue types such as bone, muscle, fat and contrast agents either through analysis of the relative contributions of the Compton and photoelectric effects or of the elemental composition. Spectral CT is also promoted as colour CT. The component images from the analysis of the Spectral CT data can be combined into a single composite image with colour coding for each contribution.

5.3 Development of the MARS-CT systems

Recent developments in novel spectroscopic photon-counting detector technology have enabled the design of CT systems with high spatial resolution and spectral capability. This

technology has extended the capability of micro-CT beyond what was previously achievable. Spectral micro-CT scanners have a number of advantages over traditional clinical CT scanners.

Firstly they provide images with high spatial resolution. As discussed in Chapter 3, the spatial resolution is determined by the x-ray source focal spot size, magnification factor and the detector pixel size. Conventional CT systems typically have a spatial resolution of $(0.5\ mm)^3$ (Geleijns & Dewey, 2010). Micro-CT systems utilise micro-focus x-ray tubes and high resolution imaging detectors and in principle are able to produce images with a spatial resolution of the order of a few tens of microns. This resolution is sufficient for the evaluation of the 3D micro-structure of specimens.

Secondly, spectroscopic photon-counting detectors measure the energy distribution of photons with no additional weight and noise (Wang et al., 2011a). Thus, spectral micro-CT systems equipped with these novel detectors provide the potential for implementing advanced imaging techniques. The spectral information can be used to provide enhanced contrast resolution or to classify and quantify relevant materials within specific biological targets (Alvarez & Makowski, 1976). In principle, improvements in resolution, sensitivity and quantitative accuracy for specimen imaging are possible with spectral micro-CT. These scanners have been specifically designed to obtain anatomical, functional and molecular information. Therefore, spectral micro-CT imaging is now considered as an alternative functional imaging technique (De Kamp et al., 2010).

Our research group in Christchurch, New Zealand has developed a number of novel spectral micro-CT scanners (Butzer et al., 2008; Butler et al., 2008; Anderson et al., 2009; Zainon et al., 2010a; Walsh et al., 2011; Butler et al., 2011b; Butler et al., 2011c). These systems are

based on semiconductor photon-counting detectors developed by the Medipix European collaboration. These detectors are popular for various kinds of imaging applications due to their advantages over charge-integrating systems. Our research group focuses on the application of these novel photon-counting detectors for pre-clinical research.

The spectral micro-CT scanner equipped with the Medipix detector simultaneously provides well resolved spatial and energy x-ray data and so is referred to as the Medipix All Resolution System (MARS). The MARS-CT1 was a proof-of-concept device produced in 2008. A year later the MARS-CT2 scanner was designed and manufactured. Limitations in both versions were identified and design improvements were incorporated in the MARS-CT3. The development and design of the MARS-CT scanners has been led by the Department of Physics and Astronomy, University of Canterbury with assistance from University of Otago, Christchurch and local industry. Performance testing of the scanners and development of research application protocols is taking place at the Bioengineering Laboratory in the Department of Radiology at Christchurch Hospital, New Zealand.

To date, these scanners have been used for pre-clinical applications such as imaging of multiple contrast agents (Butzer et al., 2008; Firsching et al., 2009; Anderson et al., 2010; Butler et al., 2011c), atherosclerotic plaque imaging (Zainon et al., 2009; Zainon et al., 2010b) and soft tissue imaging (Melzer et al., 2008; Butler et al. 2008; Berg et al., 2009; Butler et al., 2011b; Ronaldson et al., 2011b). Compared with other CT technology, the MARS-CT systems are able to provide more information to the researchers, enabling tissue differentiation without the drawbacks of the dual-source approach. Development of the technology and application protocol is an ongoing process and the MARS research group is continuing to advance the field of spectral micro-CT technology.

5.3.1 The MARS-CT systems

The MARS-CT system comprises several sub-systems. Figure 5.2 shows the workflow of a MARS-CT system. The sub-systems include the MARS Scanning Unit, the MARS Console and the MARS Workstation. The MARS Scanning Unit consists of the scanner gantry, Medipix detector, micro-focus x-ray tube and Medipix readout system. The MARS Console provides the man-machine interface and is the control unit for all scanning/examination procedures. The MARS Workstation is the data processor for image processing, image reconstruction and evaluation of scanning/examination results.

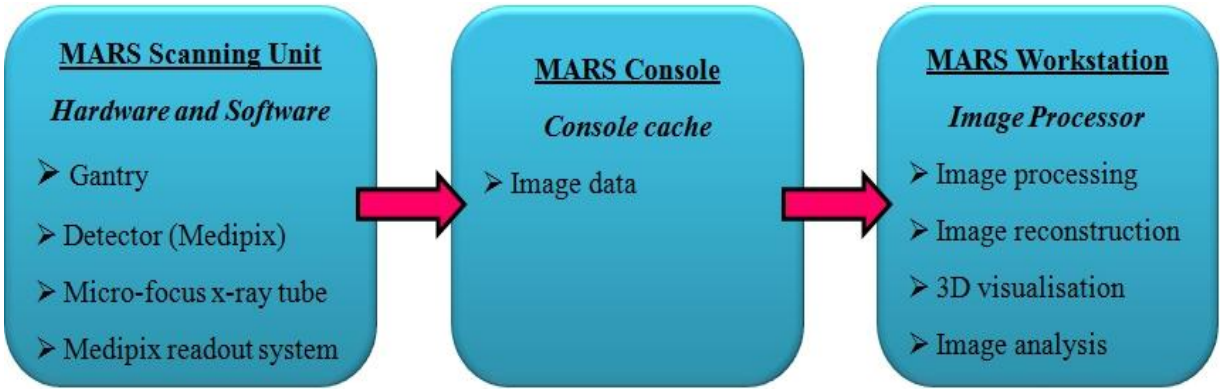

Figure 5.2 *The MARS-CT workflow. There are three different sub-systems involved in this process. The MARS scanning unit consists of the scanner gantry, the micro-focus x-ray tube and the Medipix readout system. The physical scanning processes are performed in this unit. The man-machine interface is implemented in the MARS Console that also temporarily caches the scan data. The image pre-processing, image reconstruction, 3D visualisation and analysis of images are performed in the MARS Workstation.*

5.3.1.1 MARS scanning unit

The MARS-CT scanning unit system consists of a rotating gantry that holds the x-ray source and detector. It also has control systems that control the gantry motors and various power supplies. The Medipix detector and x-ray tube are housed in a ring shaped unit called the gantry. The rotating gantry is driven by a computer-controlled stepper motor system. The

gantry rotates around the fixed object during scanning (Figure 5.3). The scanner was designed with adjustable source-to-object distance (SOD) and source-to-detector distance (SDD) so that users can mechanically change the magnification. The Medipix readout system is an interface board for the Medipix detector. It supports serial communication with the Medipix detector.

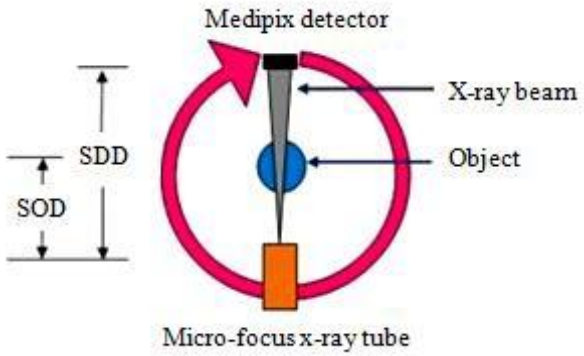

Figure 5.3 *The object is placed in the centre of the rotating gantry carrying the Medipix detector and micro-focus x-ray source. The SOD and SDD are adjustable so that users can mechanically change the magnification.*

5.3.1.2 MARS console

The MARS Console allows the operator to communicate with the computer and scanner. The operating console is connected to the MARS scanning apparatus and supplies instructions to the apparatus to perform the scanning data acquisition operations. It also includes a menu for selecting imaging parameters such as the scan region of a subject, energy range and exposure times. The MARS Console also temporarily stores the scanning data prior to processing in the MARS Workstation.

5.3.1.3 MARS Workstation

Images stored in MARS console are transferred to the MARS Workstation for image pre-processing, image reconstruction and 3D visualisation. This workstation employs a

variety of features to streamline the reporting of spectral CT data. These aspects enable the researcher to analyse the spectral CT data and produce spectral images using methods such as Principle Components Analysis (PCA) (Butler et al., 2011a).

5.3.2 The MARS-CT2 system

The MARS-CT2 scanner is housed in a lead shielded box consisting of 1.8 mm lead sandwiched between 0.5 mm aluminium and 0.5 mm stainless steel. The scanner gantry is constructed from two solid steel endplates attached to each other by four steel rods to form a strong and rigid rotating unit. For safety reasons, the scanner sample doors are interlocked and a warning light on the scanner box illuminates automatically when x-rays are being produced. The cables going to the rotating gantry are arranged to accommodate a half twist as they leave the scanner through a port in line with the centre of rotation. The endplates rotate on large diameter bearings, leaving a 106 mm hole for sample tubes to pass through. The MARS-CT2 scanner can accommodate a sample up to 100 mm diameter and 200 mm length.

Figure 5.4 shows the MARS-CT2 system. The micro focus x-ray tube and high voltage generator are located on one side of the gantry. The x-ray tube can be moved in or out to give various amounts of imaging magnification. A fan has been mounted to cool the x-ray tube and allow continuous operation at full current. On the opposite side, a Medipix2 detector is positioned. It is mounted on a plate that allows fine angular adjustment to ensure the detector pixels are aligned with the vertical axis. Since the detectors are small (either a single detector at 14 mm × 14 mm, or a quad detector assembly at 28 mm × 28 mm) they can be translated vertically to create a complete projection radiograph. The scanner was designed to take full advantage of the high spatial and energy resolution that Medipix2 offers (55 μm × 55 μm pixels). The mounting plate is connected to a screw-drive which accurately translates the

detector to each imaging position. The screw-drive is supported by the steel base plate and can be translated perpendicular to the axis of rotation to accommodate different sample sizes (Zainon et al., 2010a).

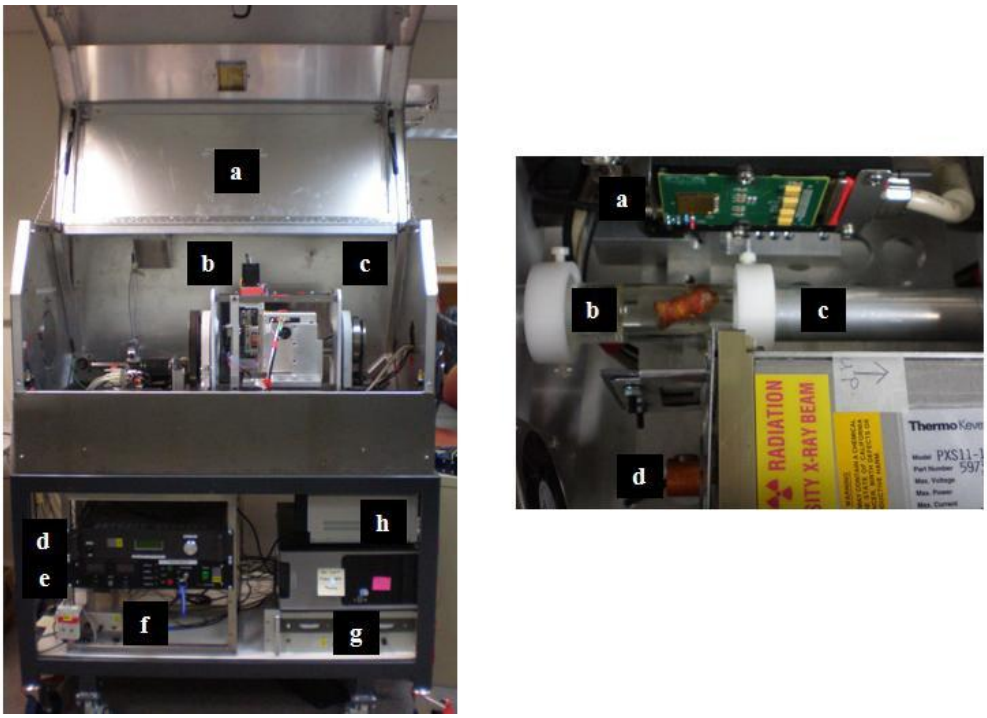

Figure 5.4 *(Left) The MARS-CT2 scanner with its main components labelled: (a) lead shielded box, (b) stepper motor, (c) gantry, (d) motor controller, (e) x-ray controller, (f) fan switch, (g) power supply and (h) MUROS power. (Right) The scanner gantry with its main components labelled: (a) Medipix detector, (b) sample (in this case a human atherosclerotic plaque fixed in resin), (c) sample holder and (d) micro focus x-ray tube.*

During the scanning process, at each position of the gantry and detector, an image frame of the object is acquired and saved onto the computer. Multiple frames from each position can be combined into a single, larger image known as the projection image. Projection data is gathered from specified angles in both gantry rotation directions and the sub-images are then reordered and spliced together.

A Thermo Scientific Kevex PXS11-150-75 micro-focus x-ray source (Scotts Valley, United States) is installed in the MARS-CT2 scanner. It has a tungsten anode with a focal spot size of

45 µm and a 0.13 mm beryllium exit window. An additional 0.5 mm aluminium filtration was installed to remove the soft x-ray component from the spectrum. The maximum tube current and accelerating voltage are 0.15 mA and 75 kVp.

5.3.3 The MARS-CT3 system

The design of the MARS-CT3 scanner incorporates various mechanical and electromechanical improvements. Sub-projects have been set up to develop the designs of the MARS camera and software (Doesburg et al., 2009). It demonstrates that the design improvements will make this scanner suitable for longer term research projects. Compared with the previous version, the MARS-CT3 scanner has a shorter scan time, computer controlled adjustable geometrical magnification and improved software interfaces and protocols. The MARS-CT3 scanner interfaces via ethernet to a separate MARS camera unit that can accommodate single or multiple Medipix detectors according to the imaging application. The MARS camera unit is being developed separately from the main gantry unit and is capable of greater data transfer speeds than the old MUROS based system.

Figure 5.5 shows the MARS-CT3 scanner. The MARS-CT3 scanner is designed for use with x-ray tubes such as the Source Ray SB 80 1K (Ronkonkoma, New York). This device has a tungsten anode with a focal spot size of 33 µm. The maximum tube current and accelerating voltage are 1 mA and 80 kVp respectively. The Source Ray SB 80 1K includes 1.8 mm of aluminium (equivalent) intrinsic filtration. This removes the low energy portion of the spectrum to minimise surface dose and reduce the beam hardening effect. Compared with the Kevex x-ray unit used in the MARS-CT2 scanner, the reduced focal spot size and increased power of the Source-Ray SB-80-1K results in better spatial resolution and reduced acquisition times.

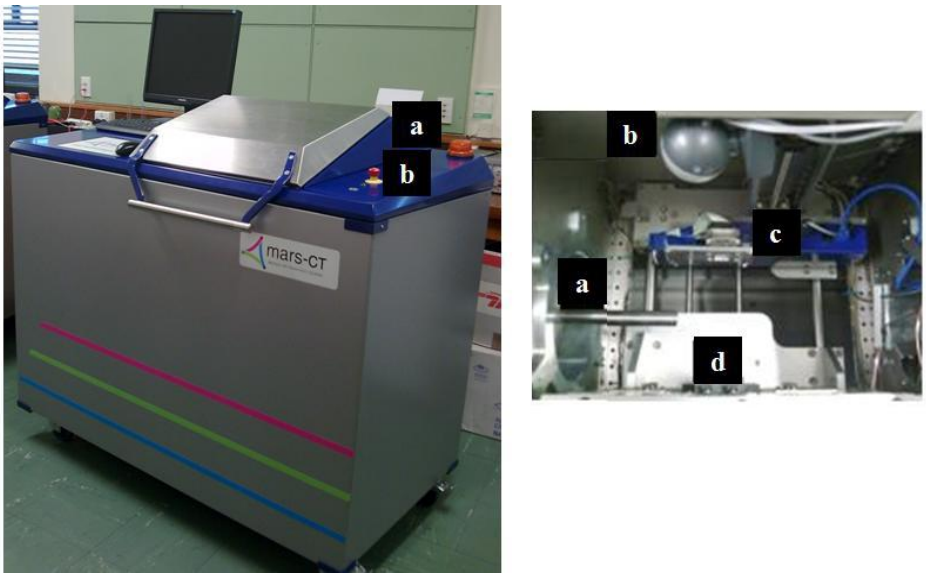

Figure 5.5 *(Left) The MARS-CT3 system. (a) A warning light (it illuminates when x-rays are on) and (b) the emergency stop button. (Right) The top view of the gantry. (a) The sample holder, (b) webcam, (c) Medipix3 detector box and (d) x-ray tube.*

The MARS-CT3 scanner machine-human interface is more advanced than that of the previous system and provides a graphical user interface (GUI) for all operations. The control and interface software is also being developed as a separate sub-project and aims to make the scanner operation more intuitive and easier for new users. In addition to the GUI interface, the new software also utilises a webcam installed inside the scanner to view the position of the sample in the gantry.

5.4 Potential influencing factors on spectral CT imaging assessment

There are variety of factors that affect the spectral CT imaging assessment. These factors include CT image acquisition parameters, CT image reconstruction settings and evaluation method of spectral CT images. These factors are summarised in three parts in Figure 5.6. A good combination of spectral CT imaging parameters will give good image quality for pre-clinical assessments. The first part covers the CT image acquisition parameters. It includes the

x-ray tube settings such as x-ray tube current, x-ray tube voltage, focal spot size, pre-filtering at the x-ray tube, object magnification, exposure time, number of projections and x-ray detector properties. The second part presents the CT image reconstruction factors that affect the image features. These factors include the resulting voxel size, image reconstruction type and settings, grey scale range and artifact reduction methods. The last part is the evaluation of spectral CT image. It includes the evaluation method used to analyse the spectral CT images and reference grey scale range.

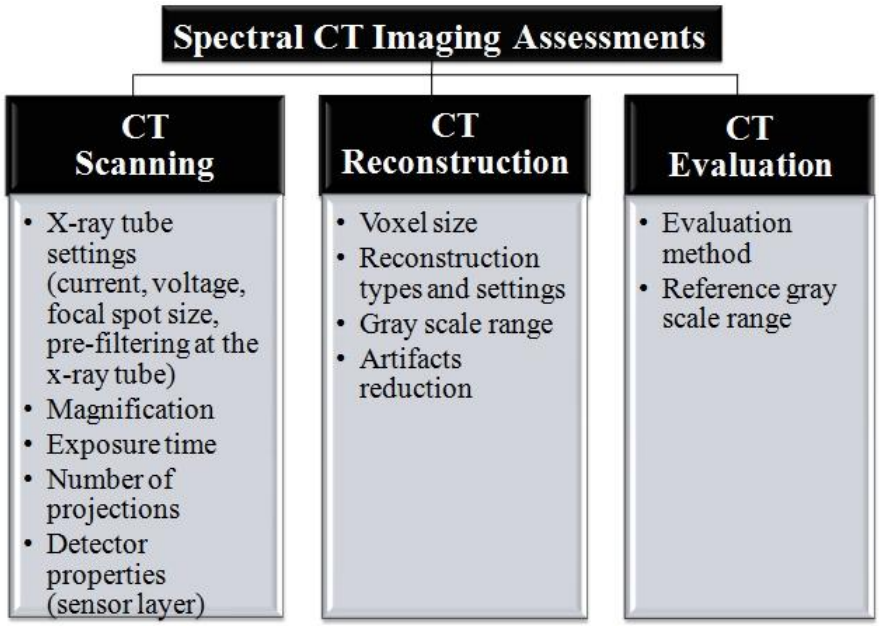

Figure 5.6 *Factors potentially influencing spectral CT assessment.*

For spectral CT scanning parameters, the x-ray tube settings such as the x-ray tube current, x-ray voltage potential and the exposure time are adjustable and these parameters control the energy and intensity of the x-ray flux. The image noise and image contrast rely on these parameters and therefore, the most suitable combination of x-ray tube voltage and current have to be chosen to suit the imaging purpose. As discussed in Chapter 3, the image noise is determined primarily by the number of detected photons interacting with the detector. The

image noise can be reduced by increasing the x-ray tube current or exposure time and voltage but at the cost of increased radiation dose. On the other hand, the image contrast only depends on the x-ray tube voltage. CT image contrast increases as the tube voltage decreases and better tissue contrast is achieved with relatively low voltages.

The focal spot size is the area of electron interaction and emanation of x-rays from the target surface. Ideally, the use of a small focal spot is preferred to minimise geometric blurring of object structure. The pre-filtering at the x-ray tube will reduce the number of x-rays with low energies that are emitted from the tube. These lower energy photons are not useful for CT imaging as such x-rays do not have sufficient energy to pass through the object and reach the detector. Therefore, the lower energy photons just add to the subject dose without providing any benefit to image quality. In CT imaging, the object magnification is obtained as a consequence of the system geometry. The SDD and SOD can be adjusted to get appropriate object magnification for different assessments. The number of projections affects the image quality in terms of image noise and image contrast. In addition, the properties of the selected sensor layer have to suit the imaging purpose. As discussed in Chapter 4, there are 3 different types of sensor layer used with Medipix detectors: Si, GaAs and CdTe.

In CT reconstruction, the diagnostic imaging assessments rely on the CT reconstruction settings and resulting voxel size to determine the visibility of the object structure. Larger voxel sizes generally produce images with less noise but fine details may be lost. When viewing the reconstructed images, the grey scale range or, as it is more usually known, the window setting determines the visibility of low contrast features and noise in a CT image. A narrow grey scale range or window enhances image contrast and thus also the visibility of noise. Well chosen window settings used to view the image will give reasonable image

quality and aid the visualisation of features of interest. Reduction of artifacts is performed using filtering algorithms in the image reconstruction process. Selection of image filtration requires a compromise between the desired level of noise reduction and unwanted blurring of image details.

These considerations apply equally to spectral CT as to conventional CT. However, in addition, to maintain exact registration between the different energy images, one may choose to use the same reconstruction parameters when reconstructing each spectral CT energy dataset. After analysis of the elemental or interaction components, selection of appropriate reconstructed image grey scale or window settings will assist the differentiation of different types of material.

5.5 Summary

1. Our research team in Christchurch, New Zealand has designed and built a number of spectral micro-CT systems based on the Medipix family of energy resolving photon-counting detectors. The design path of these spectral micro-CT systems has taken account of various pre-clinical research requirements as well as the need for system reliability and longevity. To date, these scanners have been used for pre-clinical applications such as imaging studies of atherosclerotic plaque, fatty liver and multiple contrast agents.

2. Improvements in resolution, sensitivity and quantitative accuracy for pre-clinical specimen imaging are possible with spectral micro-CT systems. Compared with current clinical CT, state of the art spectral micro-CT provides a number of advantages. Firstly it has higher spatial resolution. Secondly, it offers excellent contrast resolution which is adequate to allow quantitative analysis of certain

biological targets. Thirdly, it enables spectroscopic imaging for improved contrast resolution and materials discrimination. Lastly, compared with conventional CT, spectral CT can be used to reduce the radiation dose for a given CNR.

3. There are a variety of factors that may influence the quality of assessments based on spectral CT imaging. These factors include the CT image acquisition parameters, CT image reconstruction settings and CT evaluation method. Careful selection of imaging parameters is required to produce the best spectral CT imaging results.

Chapter 6

Atherosclerosis Imaging

This chapter provides background material on imaging for atherosclerosis including a description of atherosclerosis and the biological markers for vulnerable plaques. It also discusses existing and emerging imaging techniques with regard to their ability to identify unstable lesions at risk of rupture. This chapter states the need for characterising atherosclerosis and how spectral CT can be used to overcome the barriers associated with standard non-invasive techniques. A concise description of the issues and the particular focus of this thesis are then stated. The chapter concludes with a summary of the main points.

6.1 Atherosclerosis

Recent studies have revealed that there are mainly two different kinds of atherosclerotic lesion: stable and unstable plaques. The rupture of so-called vulnerable or unstable atherosclerotic lesions is responsible for a significant proportion of myocardial infarcts and strokes (Kullo et al., 1998). Atherosclerosis can cause a heart attack if it completely blocks the blood flow in the heart (coronary) arteries. It can also cause a stroke if it completely blocks the brain (carotid) arteries. It is often debilitating or fatal (American Heart Association, 2011).

The well-known risk factors of this disease are cigarette smoking and hypercholesterolemia (Allen et al., 1988) but there are also other contributing factors such as high blood pressure, physical inactivity and obesity (American Heart Association, 2011). Detection of patients at

risk using advanced imaging with spectral CT would represent a significant advance in diagnostic capability.

Figures 6.1 and 6.2 illustrate the progress of atherosclerosis and the structure of atherosclerotic plaque. The stable plaque typically has a thick fibrous cap with an abundance of vascular smooth muscle cells and a lipid core that represents less than half the plaque volume. On the other hand, the unstable plaque consists of large lipid deposition that accounts for more than half the volume of the plaque. It has many infiltrating macrophages and a thin collagen and smooth muscle cell layer (fibrous cap) that covers the lipid pool core (Gutstein & Fuster, 1999).

The unstable plaque is prone to inflammatory changes near the thin fibrous cap, activated proteases weaken the fibrous cap and a sudden rupture of the unstable plaque may occur. The lipid core contains many thrombogenic (tending to produce a thrombus or clot) factors. Thus, the rupture of an unstable plaque may subsequently obstruct arterial blood flow, resulting in acute myocardial infarction, heart attack or sudden death.

Clinical evidence shows that the fine structure and composition of atherosclerotic plaque rather than the degree of arterial stenosis appears to be a critical determinant of plaque stability and thrombogenicity (Pasterkamp et al., 2000; Schaar et al., 2004; Rudd et al., 2005). Therefore, it has become an important clinical goal to rapidly identify those persons with potentially unstable plaques who are at high risk of clinical syndromes. Early treatment can minimise the potential complications. The identification of persons at high risk for cardiovascular events is the major focus of primary prevention efforts because lifestyle changes and pharmacological interventions have been shown to increase the life expectancy of high-risk persons.

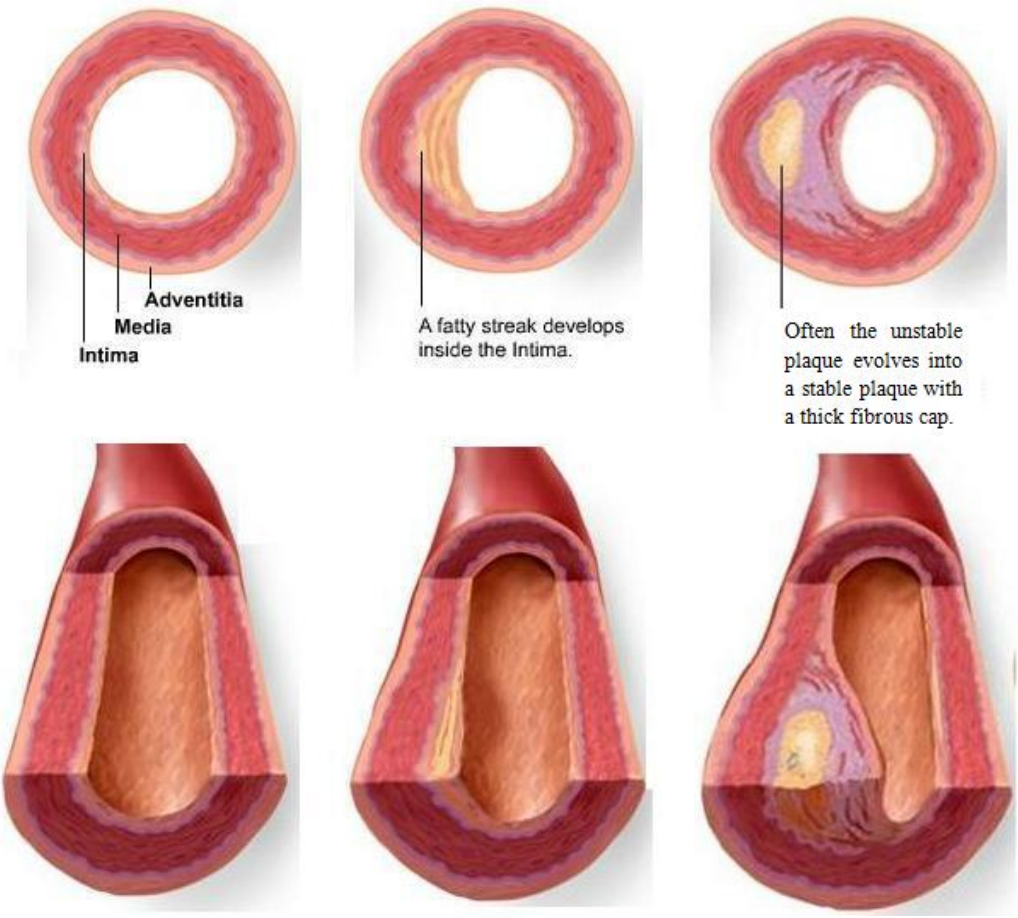

Figure 6.1 *The formation of a stable atherosclerotic plaque. (a) The human artery has three different layers: the intima (the innermost layer and site of plaque formation), the media (consisting of mostly smooth muscle cells) and the adventitia (the outer layer of the artery). Plaque builds up on the innermost layer of the arteries and is formed from cholesterol, fat, calcium and other substances in the blood. (b) The fatty streak develops inside the intima. (c) It can evolve into a stable plaque with a thick fibrous cap and a small fatty core. Retrieved from American Heart Association (2011).*

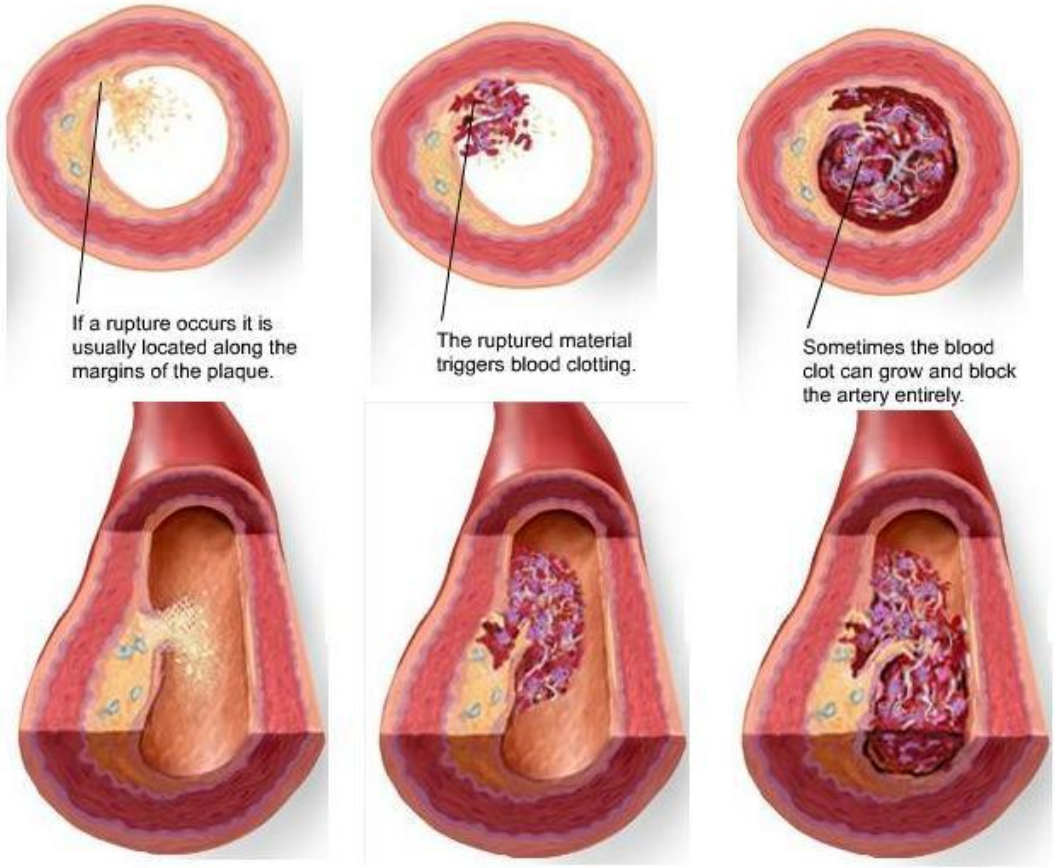

(a) (b) (c)

Figure 6.2 *The formation of an unstable atherosclerotic plaque. (a) Once the fatty streak develops inside the intima, it can develop into an unstable plaque with a thin fibrous cap and large fatty core. It is vulnerable to rupture. (b) The ruptured material from an unstable plaque protrudes into the artery, causing a partial or complete obstruction to blood flow. (c) The blood clot can grow, leading to a sudden occlusion of the artery. This condition is called arterial thrombosis. Retrieved from American Heart Association (2011).*

6.2 Characterisation of atherosclerotic lesions by various imaging modalities

Characterisation of atherosclerotic plaques is clinically highly relevant. The role of atherosclerosis imaging is to aid risk stratification. The aim of clinical risk stratification is to depict as closely as possible the histology and then precisely target treatment to specific problem lesions (Stary et al., 1995). Over the last decade, there has been much interest in the use of imaging to identify patients at risk of atherosclerotic disease. Modalities capable of characterising the tissue of the atherosclerotic lesion may help to understand its natural history and detect lesions with high risk for acute events. It is therefore, important that in addition to being able to identify the presence of disease, the imaging modality must be able to detect the presence of vulnerable plaque.

There has been increased recognition that atherosclerosis imaging adds greatly to the ability to identify patients at high risk for cardiac events. Several techniques are being used nowadays to define atherosclerotic plaque composition. It is noted that the perfect imaging technique would provide the maximum amount of diagnostic information whilst being non-invasive, cheap and safe (Pasterkamp et al., 2000).

For the clinician, the modality that aims to characterise the vulnerable plaque should have diagnostic or predictive value. Thus, validation of imaged features like lipid or fibrous cap, plaque type and inflammation must not only be based on a priori knowledge of the expected localisation of that feature within the image but also on histology. Secondly, the modality should be safely applicable for in-vivo studies and thirdly the predictive value of the vulnerable plaque determinants for a plaque to rupture needs to be investigated.

To the best of our knowledge, current diagnostic modalities are insufficient to detect vulnerable carotid lesions. Until now, no studies have been performed on the predictive value of each of the three vulnerable plaque markers (the iron deposits, lipid core and thin fibrous cap) (Pasterkamp et al., 2000; Rudd et al., 2005). This section reviews current invasive and non-invasive imaging modalities that have been used in imaging atherosclerosis in the context of the aforementioned imaging requirements.

6.2.1 Invasive techniques

There are several multiple invasive modalities that have been used to assess atherosclerotic plaque composition. However, the disadvantages of these procedures are their high cost, and the associated substantial procedural morbidity and mortality. Consequently, these procedures are only justified in intermediate to high-risk symptomatic patients (Hoffman et al., 2005). Angiography and intravascular ultrasound are invasive imaging modalities that have been utilised in clinical practice for imaging patients suffering from atherosclerosis.

Angiography has been the gold-standard modality for diagnosing occlusive coronary artery disease for the past 60 years. The presence or absence of atherosclerosis is judged according to whether or not there is stenosis (luminal narrowing). Ambrose et al. (1988), Little et al. (1988) and Gaemperli et al. (2010) have shown that the flow limiting stenoses are present only in 30% - 40% of cases of myocardial infarction. Thus, this technology is limited in its ability to detect non-stenotic plaque providing insufficient data regarding vessel wall and plaque composition and underestimating the severity of the plaque burden (Rudd et al., 2005; Hoffman et al., 2005; van Gils et al., 2012). Furthermore, angiography is not suitable for serial monitoring of symptomatic patients because it is invasive and uses ionising radiation. Therefore, angiography falls well short of fulfilling the criteria for the perfect

imaging method to diagnose and monitor atherosclerosis. However, it will continue to be used to guide intervention (angioplasty or bypass surgery) for symptomatic lesions for the foreseeable future (Rudd et al., 2005).

Intravascular ultrasound (IVUS) requires an intravascular catheter-based ultrasound to provide cross-sectional images of the coronary artery lumen and vessel wall with an in-plane resolution of 80-150 μm. IVUS can differentiate atherosclerotic plaque composition such as lipid core, fibrous cap, surface thrombus, intraplaque hemorrhage and calcification because of their differences in acoustic impedance (Nissen et al., 2001). Mintz et al. (2001) and Nair et al. (2002) reported that, based on plaque echogeneity, the plaque composition can be divided into three groups: highly echo-reflective (calcified), hyperechoic (fibrosis or microcalcification) and hypoechoic (thrombotic or lipid). Therefore, IVUS has clear advantages over angiography for the detection of unstable lesions.

However, IVUS provides only limited characterisation of calcified plaque. The acoustic impedance of the calcification is so high that characterisation is frequently impossible. Since IVUS is costly and invasive, it can only be used clinically in patients that undergo angiography (Rudd et al., 2005; Hoffman et al., 2005) or during an intervention in which it can aid in the selection of the most appropriate transcatheter therapy (Fayad et al., 2000). Nissen et al. (2004) reported that it has also been used to monitor the effects of plaque stabilising drugs, such as statins, on atherosclerotic progression.

A further three invasive imaging modalities are thermography, spectroscopy and Optical Coherence Tomography (OCT). These modalities are currently used in investigations of atherosclerosis and Rudd et al. (2005) reported that they are likely to remain as research tools for the foreseeable future. Thermography uses a temperature sensitive thermistor mounted on an intravascular

catheter inserted into the lumen of an artery to detect the small changes in artery wall temperature that are associated with atherosclerotic plaques (Stefanadis et al., 1999; Rudd et al., 2005). It has the potential to identify the plaque inflammation but it provides no information on plaque size, site or ultrastructure of atherosclerotic plaque.

Raman spectroscopy or near infrared spectroscopy (NIRS) is an intravascular, catheter based method. Under illumination by a laser or broadband infrared light source, various plaque components emit unique spectra that can be used to characterise the chemical composition of the plaque. This technology can distinguish calcified from lipid-rich plaque (Brennan et al., 1997) but provides neither functional nor structural information about the plaque (Romer et al., 2000). On the other hand, OCT uses a similar technique to IVUS based on light interferometry to visualise subsurface structure in tissues (Yabushita et al., 2002, Giattina et al., 2006). In particular, it enables the differentiation of plaque into fibrous, lipid and calcified components.

6.2.2 Non-invasive techniques

The non-invasive techniques have lower complication rates than do their invasive counterparts and therefore, have greater potential for both screening of high-risk patients and for long term follow-up studies (Hoffman et al., 2005). There are four non-invasive methods that will be discussed in this section.

The first method is transvascular (surface) ultrasound. The ultrasound probe is placed directly over the site of interest and it is mainly used to image large accessible arteries such as carotid, aorta and lower limb arteries. This B-mode ultrasound is capable of imaging and measuring the thickness of the vessel wall and intima media based on the echogenicity of the plaque. It is also capable of estimating the degree of luminal stenosis by measuring the blood flow velocity. However, it is impossible to characterise the plaque morphology and delineate the

features of the lesion with this technology due to its low SNR. The principal advantages of this imaging modality are its widespread availability, low cost, lack of side effects and short examination time.

The second non-invasive imaging modality used for atherosclerosis studies is MRI. Compared with x-ray based methods, a particular advantage of MRI for the characterisation of atherosclerotic plaque composition is that it does not involve ionising radiation and studies can therefore be repeated to monitor the progression and regression of the disease (Hoffman et al, 2005; Choe, 2005). Hatsukami et al. (2000) and Yuan et al. (2001) demonstrated that MRI allows the characterisation of the fibrous cap and lipid core of the atherosclerotic plaque. The lipid core appears hyper intense on T1 and proton density but has a low-intermediate signal on T2. Calcification and fibrous lesions have low and low-intermediate signals respectively on all the sequences. Lima et al. (2004) used MRI to assess the response of the plaque to treatment and found that the size of aortic plaque is reduced with the use of statin to lower cholesterol levels. Currently, research is being directed toward the use of magnetic resonance contrast agents such as ultra small particles of iron oxide that are engulfed by macrophages within the plaque thus enabling macrophage imaging (Kooi et al., 2003). To date, whole body MRI at 1.5 T has insufficient resolution (400 μm) for accurate measurements of cap thickness and characterisation of the atherosclerotic lesion within the coronary circulation.

The third non-invasive imaging modality is CT. There has been a growing interest in assessment of plaque burden with the use of CT. Multi-slice spiral CT (MSCT) is increasingly important for the imaging of coronary heart disease (Tan et al., 2008). It has been developed from traditional single slice helical CT and relies on the use of a rotating gantry with up to

256 rows of detectors and the injection of contrast agent to differentiate vessel lumen from wall (Rudd et al., 2005). MSCT has the ability to identify stenotic and non-stenotic plaque and distinguish non-calcified plaque (lipid and fibrous tissue) from calcified and mixed plaque that contains both calcified and non-calcified tissue (Cademartiri et al., 2006). MSCT can also assess luminal stenosis at the expense of a high radiation dose (Rudd et al., 2005; Tan et al., 2008). However a sub-classification between lipid and fibrous plaques appears difficult. The visualisation of non-calcified lesions is hampered by plaque and vessel sizes compared with the limited spatial resolution of presently available CT technology (Cademartiri et al., 2006).

The dual-energy CT and micro-CT scans show that these imaging modalities can detect excess iron deposits in plaque (Langheinrich et al., 2007;). However, non-invasive imaging of iron deposits is challenging because it often coexists with calcium deposits in atherosclerotic plaques, yet it is indistinguishable from calcium on standard MRI and CT. The scans usually show narrowing of arteries from plaque build-up but that does not identify if the plaque inside those vessel walls is imminently dangerous. Current non-invasive imaging for plaque does not yet have the necessary resolution to detect iron as a natural marker in high risk plaque patients.

6.3 The need for spectral CT imaging in characterisation of atherosclerotic plaque

The overall problem relates to the diagnostic capability of clinical equipment. Diagnosis and monitoring of patients and the effectiveness of their treatment is currently hampered by the inability of existing technology to image the features of unstable plaques. Currently available clinical equipment does not have the spatial resolution to distinguish material components by

morphology nor the spectroscopic capability to derive the composition from spectral characteristics.

The unstable or vulnerable plaques constitute a high-risk because of their propensity to rupture, thus predisposing the patient to an acute event. Previous studies have shown that current CT technology can detect calcification within atherosclerotic plaques but cannot identify lipid or iron deposits as a marker of intraplaque hemorrhage (Knollman et al., 2008). These limitations are due to lack of spatial resolution, image noise and the fundamental limitations of energy integrating detector technology.

At the spatial resolution of interest, clinical CT scanners suffer from partial volume effects due to the relatively large detector pixel size compared with the small hemorrhage deposits ($(10\ \mu m)^3$ to $(100\ \mu m)^3$) in human atherosclerotic plaque (Langheinrich et al., 2007). Thus identifying patients with vulnerable plaques is unreliable with currently available techniques, and accurate screening of patients for possible treatment is not feasible (Cademartiri et al., 2006).

Until a suitable clinical method becomes available, the use of various imaging modalities described above will be restricted to research aimed at identifying features of atherosclerotic plaques that render them potentially unstable. It is the contention of our research group that spectral CT has the potential to make in vivo measurement of the material components of atherosclerotic human plaque and thereby provide the solution to this overall problem. The effectiveness of material differentiation and quantification methods depends upon many factors (Firsching et al., 2004, Clavijo and Pelc, 2009, Liu et al., 2009; Mikulec et. al., 2003). CT system performance, x-ray tube and detector characteristics, the selection of detector

energy thresholds and the suppression of artefacts will each affect the ability to distinguish and quantify plaque components.

The next chapters of this thesis investigate these factors and, with the use of MARS-CT, demonstrates the capability of spectral CT to characterise ex vivo human advanced atherosclerotic plaques and compares the performance of spectral CT with other modalities. The next chapters include the investigation and implementation of material decomposition of the plaques using MARS-CT. The result of spectral CT imaging is compared with histological examinations (the gold standard).

6.4 Summary

1. Current imaging modalities have limited ability to detect the three markers for a plaque to rupture: lipid core, iron deposits as marker of intraplaque hemorrhage and a thin fibrous cap.

2. High resolution spectral CT equipped with photon counting detectors provide high spatial and energy resolution. This capability may potentially be used to determine the composition of atherosclerotic plaques and identify the presence of markers for plaque instability.

3. The next chapters of this thesis will demonstrate the feasibility of differentiating plaque components in ex vivo advanced human atherosclerotic plaques. Comparisons will be made with other modalities. The final evaluation will be by comparison of spectral CT results with those of histological examination (the gold standard).

Chapter 7

Preliminary studies on atherosclerotic plaque with the MARS-CT2 system

This chapter describes a preliminary study on atherosclerotic plaque using spectral micro-CT. The aim was to explore the potential of the MARS-CT2 system equipped with a Medipix2-MXR ASIC bump-bonded to GaAs and CdTe sensor layers to image and detect the atherosclerotic plaque lesions. The data acquisition protocols for ex vivo atherosclerotic plaque imaging are described and the selection of appropriate CT imaging parameters is discussed. The reconstructed CT images and the results of applying the PCA method to the spectral CT data to differentiate material types by their spectroscopic absorption characteristics are presented. The spectral CT results are compared with images obtained from other modalities. Structural features and material components of the atherosclerotic plaques are identified and the ability of the different imaging methods to visualise the plaques is examined. The limitations of this study are identified and improvements in technique and equipment for assessing atherosclerotic plaque components with the next version of the scanner (MARS-CT3) are recommended. The chapter concludes with a summary of the main findings from this study. This work has been presented at two conferences and published in the New Zealand Medical Journal (Zainon et al., 2009; Zainon et al., 2010b; Zainon et al., 2010c).

7.1 Introduction

Atherosclerosis is the 'silent killer' responsible for coronary heart disease, cerebrovascular disease (stroke) and heart attack. This disease is the world's largest killer, claiming 17.3 million lives a year (World Heart Organisation, 2011). In the Western world, atherosclerosis is a leading cause of morbidity and mortality. In New Zealand, it is the leading single cause of death accounting for almost over 40% of deaths annually (Hay, 2004; National Heart Foundation of New Zealand, 2007). Thus, it becomes increasingly important to be able to predict the risk factors of these diseases based on the plaque composition. Atherosclerotic plaque composition is the primary determinant of whether or not a plaque is likely to rupture (Ross, 1999). Characterisation of plaque and identification of vulnerable plaque is a clinically relevant goal.

Identification and differentiation of unstable features such as lipid and hemorrhage in atherosclerotic plaques may improve risk stratification for incident cardiovascular events (American Heart Association, 2011). As discussed in Chapter 6, these plaques are referred to as unstable, vulnerable and of high-risk because of their propensity to rupture, thus predisposing the patient to an acute event. This type of plaque is an important determinant of acute clinical events regardless of the amount of calcium or the degree of initial luminal narrowing (Cai et al., 2002).

Current invasive and non-invasive imaging modalities are unable to adequately characterise the vulnerable plaque components. The ideal clinical imaging modality would be non-invasive, cheap, safe and effective for assessing plaque vulnerability. New developments in x-ray CT imaging offer the potential for differentiating tissues and materials based on differences in x-ray attenuation coefficients. Micro-CT scanning was first developed in the

1980s (Elliot & Dover, 1982; Flannery et al., 1987). It has been used primarily to provide 3D images of anatomic structures of human specimens and/or small animals, to detect and monitor disease. A major difference between micro-CT and clinical CT is the ability of micro-CT to represent objects within small voxels thereby reducing the effect of partial volume artifacts. Partial volume artifacts are the representation of complex anatomical structures by voxel grey scale values that are the average over the different features of interest. The amount of structural information lost in this way depends on the length scales and relative x-ray attenuation coefficients of the anatomical features within the voxel volume. In the context of plaque characterisation, the partial volume effect is the main limitation of clinical CT.

Recent advances in x-ray detector technology include the development of high resolution spectroscopic photon-counting detectors. Micro-CT systems equipped with photon-counting detectors can perform high spatial resolution spectroscopic imaging for visualisation of complex morphology and improved soft tissue contrast. Spectral CT is a new approach that might allow superior tissue discrimination for studies on atherosclerotic plaques.

This study was designed to explore the capacity of the MARS-CT2 scanner to image and characterise excised atherosclerotic plaque. Spectral CT measurements at different and relatively independent energies are obtained through the use of energy resolving detectors that provide simultaneous measurements of the x-ray attenuation at multiple energies using standard polychromatic x-ray sources. These detectors typically use solid-state radiation sensors combined with fast readout ASICs that process the signals from individual photon interactions. The application of this recently developed technology to distinguish different

types of plaque tissues using high resolution spectral CT imaging is a novel approach with the potential to greatly enhance future health studies.

7.2 Materials and Methods

7.2.1 Study design

Three human advanced atherosclerotic plaques were scanned with the MARS-CT2 system. As soon as the plaques were removed from surgery, the specimens were placed in specimen containers packed with ice. The plaques were transported on ice to the imaging lab in a biohazard marked container. Two of the plaques (femoral and carotid artery plaques) were fixed in resin (CraftSmart liquid gloss, CraftSmart Australia, Glayton North, Australia) in a 25 mm internal diameter polymethyl methacrylate (PMMA) tube prior to imaging. The other surgical specimen was unfixed and stored in a -80 °C freezer.

The frozen unfixed specimen was sliced into segments of length 2 to 3 mm using a hand held microtome blade prior to imaging. This work was performed in a 4 °C cold-room to maintain the freshness of the specimen. Each cut surface was photographed at high resolution by the biology photography technician. The ex vivo spectral micro-CT study of the unfixed specimens were obtained after photographing the plaques. The unfixed specimens were then returned to the -80 °C freezer while the images were processed. A femoral plaque fixed in resin was imaged with MRI at 1.5 T using fast imaging with steady-state acquisition (FIESTA). The high resolution CT images of femoral plaque in resin were compared with the pre-operative CT and MRI images. The ex vivo spectral micro-CT images of excised specimen were compared to high resolution photographs of the plaque.

7.2.2 Ex vivo MARS-CT2 scanning protocol

The advanced femoral and carotid artery plaques in resin were imaged with the MARS-CT2 scanner equipped with a single Medipix2-MXR ASIC bump-bonded to a GaAs sensor layer. The unfixed ex vivo advanced carotid artery plaque was scanned with the same scanner but equipped with a single Medipix2-MXR ASIC bump-bonded to a CdTe sensor layer. The imaging was performed using these different approaches to assess the capability of MARS-CT2 system for assessing the advanced atherosclerotic plaque components under different conditions. The study assessed the different sensor layers with a view to obtaining good image quality over a range of detection energies. The effects of scanning conditions and choice of sensor layer on the ability to analyse atherosclerotic plaque components with spectral CT were qualitatively assessed by comparison of the CT images with the high resolution plaque photographs.

The MARS-CT2 scanner used a Thermo Scientific Kevex PXS11-150-75 micro-focus x-ray source (Scotts Valley, United States) with beryllium exit window. The focal spot size of the x-ray tube was 45 μm. An additional 0.5 mm of aluminium filtration was used to remove the soft x-ray component from the spectrum. The magnification factor was 1.41 and an isotropic voxel of $(43\ \mu m)^3$ was used for the reconstructed images.

The advanced femoral and carotid artery plaques fixed in resin were imaged using x-ray settings of 75 kVp, 0.15 mA and four threshold energies: 14.5, 21.5, 28.6 and 39.2 keV. The same tube voltage and tube current was used for imaging the unfixed advanced atherosclerotic plaque. The frozen specimen was scanned with four energies: 14.0, 20.0, 25.0 and 34.5 keV. In both cases the scanning was performed with 303 projection angles over 360° and an exposure time selected to acquire 2000 counts per pixel with the open beam. The

frozen unfixed plaque was transferred to a 15 ml falcon tube packed with dry ice at both ends of the tube to keep the specimens frozen during the scan. Flat-field measurements were taken after specimen scanning to correct for variations in pixel response.

7.2.3 Ex vivo MRI scanning protocol

The femoral plaque embedded in resin was imaged with a HRW array coil in a 1.5 T GE Sigma Excite MR scanner (GE Medical Systems, Milwaukee, Wisconsin, USA). Parameters for the 3D FIESTA were as follows: TR/TE 7.15/2.17 ms, field of view (FOV) 10 cm, thickness 1.8 mm, 320 × 256 matrix, number of excitations (NEX) 2, flip angle 55°.

7.2.4 MARS-CT image processing

The frames were stitched to form large area projections. The projection images were corrected and normalised using the flat-field images. The normalised images were reconstructed using the Octopus commercial CT reconstruction software version 8.2 (Dierick et al., 2004). The reconstructed CT slices for the specimen images were calibrated in HU using air and resin references. For the fixed plaques, the resin was assumed to be water equivalent ($\mu_{\text{resin}} = \mu_{\text{water}}$). For the frozen plaque, the images were processed and normalised to water and air (Brooks, 1977) as expressed in Equation 7.1:

$$\text{CT} = \frac{\mu - \mu_{water}}{\mu_{water} - \mu_{air}} 1000 \text{ HU} \tag{7.1}$$

where the μ is the attenuation coefficient of the reconstructed object and μ_{air} and μ_{water} are the attenuation coefficients of air and water respectively.

The spectral micro-CT images were analysed with PCA (Butler et al., 2011a) to determine the different spectral characteristics. The results were evaluated by comparing the CT image of

the femoral plaque in resin with the MRI image and comparing the unfixed plaque images with the high resolution plaque photographs taken prior to scanning.

7.3 Results

Figure 7.1 shows a reconstructed slice of femoral plaque fixed in resin. The high spatial resolution of the MARS-CT2 scanner was able to visualise the structure of the plaque. Two types of opacities were observed within the atherosclerotic lesion. One type of opacity appears as clusters of randomly distributed punctate deposits and the other as a confluent accumulation located in the arch of the atherosclerotic plaque. As can be seen in the image, some ring artifacts were visible due to pixel-to-pixel variations of the threshold positions that were inadequately corrected during flat field normalisation.

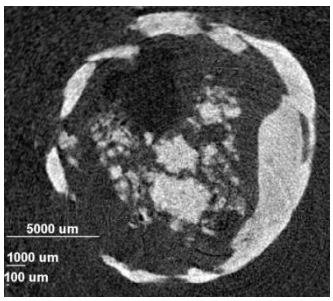

Figure 7.1 *A single slice of femoral artery plaque fixed in resin. The complexity of the plaque structure is apparent. Large confluent dense areas (with a linear size >1000 µm) are seen peripherally, whereas the central densities tend to be punctate and much smaller (with a linear size from 100 µm to 1000 µm). Some ring artifacts are also visible. The plaque was imaged at 75 kVp with the detector threshold set at 14.5 keV.*

The ex vivo femoral plaque fixed in resin was also imaged with other modalities. Figure 7.2 compares a high resolution ex vivo femoral plaque image obtained from the MARS-CT2 scanner with a CT image acquired from a clinical Multi-Detector Computed Tomography

(MDCT) and MRI images. The pre-operative CT image was obtained during routine patient care for diagnosis and surgical planning. The spatial resolution of the MDCT and MRI images is poor compared with that of the MARS-CT2 image.

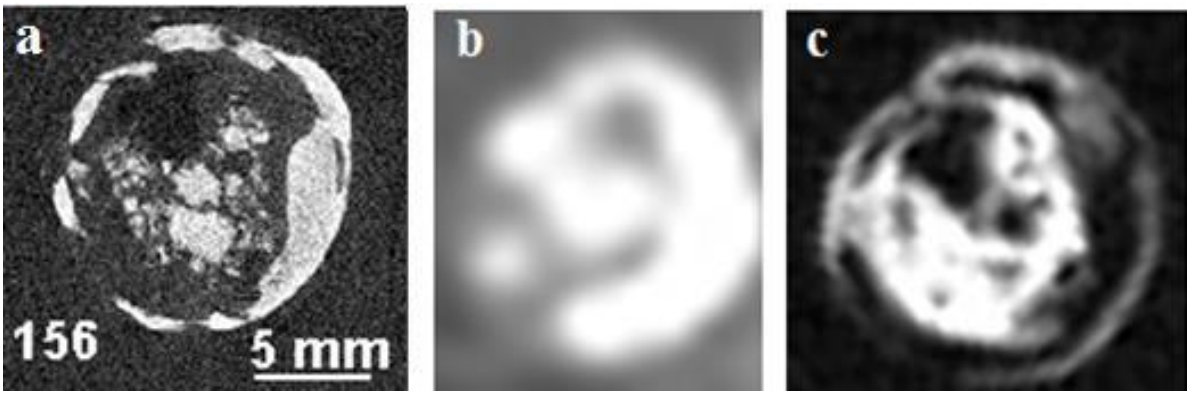

Figure 7.2 *Matching of multi-modality images. The femoral plaque images acquired from (a) high resolution of MARS-CT2 scanner, (b) clinical MDCT scanner, (c) MRI scanner with 1.5 T 3D FIESTA. The high resolution MARS-CT2 image shows the femoral plaque lesions and the structure within the plaque whereas the spatial resolution of the images from the other modalities is too poor to visualise these features.*

Figure 7.3 shows a high resolution image from the MARS-CT2 system and a MDCT image of a selected slice of carotid artery plaque. The relatively poor resolution of the MDCT image does not allow much of the plaque structure to be identified. Two peripheral calcifications are evident but many of the other features are indistinct. The higher resolution of the MARS-CT2 system clearly reveals the detailed structure of the plaque.

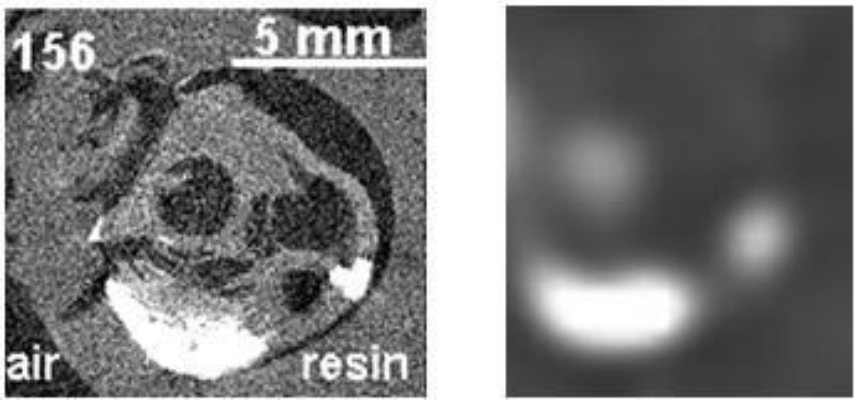

Figure 7.3 *A high resolution MARS-CT2 image (left) and a MDCT image (right) of slice 156 of the carotid artery plaque.*

Figure 7.4 shows the excised femoral and carotid artery plaques fixed in resin. These plaques were imaged with the MARS-CT2 scanner using multiple threshold energies. The image is annotated with the slice location number of each image used in Figures 7.5 and 7.6.

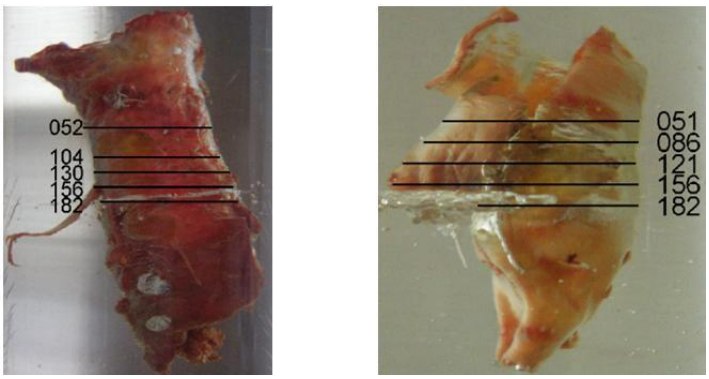

Figure 7.4 *Excised femoral plaque (left) and carotid plaque (right). Both plaques were fixed in resin within a 25 mm internal diameter PMMA tube. The annotations give the slice location number of each image used in Figures 7.4 and 7.5.*

The spectral images of femoral artery and carotid artery plaques (fixed in resin) obtained at several energies with the MARS-CT2 scanner are shown in Figures 7.5 and 7.6. Excellent detail is seen in both plaque lesions. The calcification in both plaques show decreasing

attenuation with increasing energies. This characteristic is typical for medium-*Z* materials where attenuation is dominated by photoelectric absorption at low energies and Compton scattering contributions increase and become more significant with increasing energy. Imaging of these spectral differences allows intrinsic tissue contrast to be enhanced by additional data processing such as principal components analysis (PCA). The ring artifacts on the images are due to imperfect flat-field correction. Additional sources of noise in the images are random errors in the flat-field correction data and in the object projection images. The images acquired with high threshold energies appear noisier and exhibit more ring artifacts than those obtained with low threshold energies because of the reduction in available signal at higher threshold energies. The noise in the difference image is further increased due to the accumulation of two sets of random errors and the reduction in net signal.

These high resolution images demonstrate the complexity of calcification morphology and the internal architecture of the plaque, although this has been distorted by surgery and fixation. The bright opacities in plaque are clearly distinguishable from the less opaque regions by their spectroscopic characteristics as well as the grey scale appearance. At lower energies, the highly detailed morphology of both the highly absorbing (bright) and less absorbing (dark) regions is apparent. As the energy threshold is increased the contrast due to the difference in absorption is reduced, especially in the less absorbing non-calcified regions. The images of slice 156 in Figure 7.5 show the air trapped in the resin. This carotid plaque has large confluent calcified areas peripherally but lacks the small central densities of the femoral plaque.

The colour CT images of all advanced atherosclerotic plaque images were obtained by PCA analysis. PCA was applied to enhance the images by identifying and extracting the components of greatest variance within the spectral data set. In the femoral artery image of

Figure 7.5, the bright pink colour correlates with the calcification whereas the blue region correlates with the air. In the carotid artery image of Figure 7.6, the calcified region is coded bright yellow and the air region is coded blue. On both images, the spectroscopic contrast for distinguishing soft tissues and lipid is apparently much less than that for distinguishing calcium.

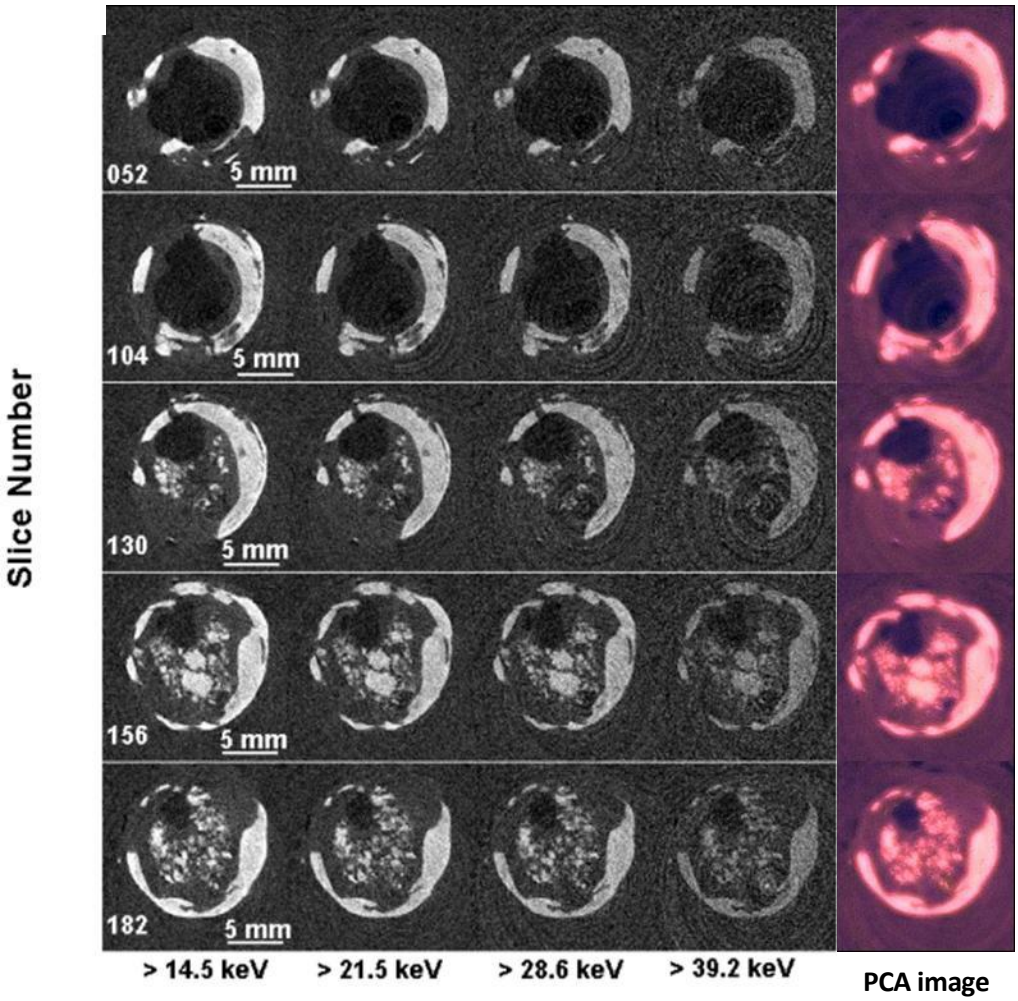

Figure 7.5 *Spectral images of femoral artery plaque (fixed in resin) obtained at several energies. These images were scaled to HU normalised using regions of air (the black region on the CT greyscale image) and resin. The colour coded images were obtained from PCA.*

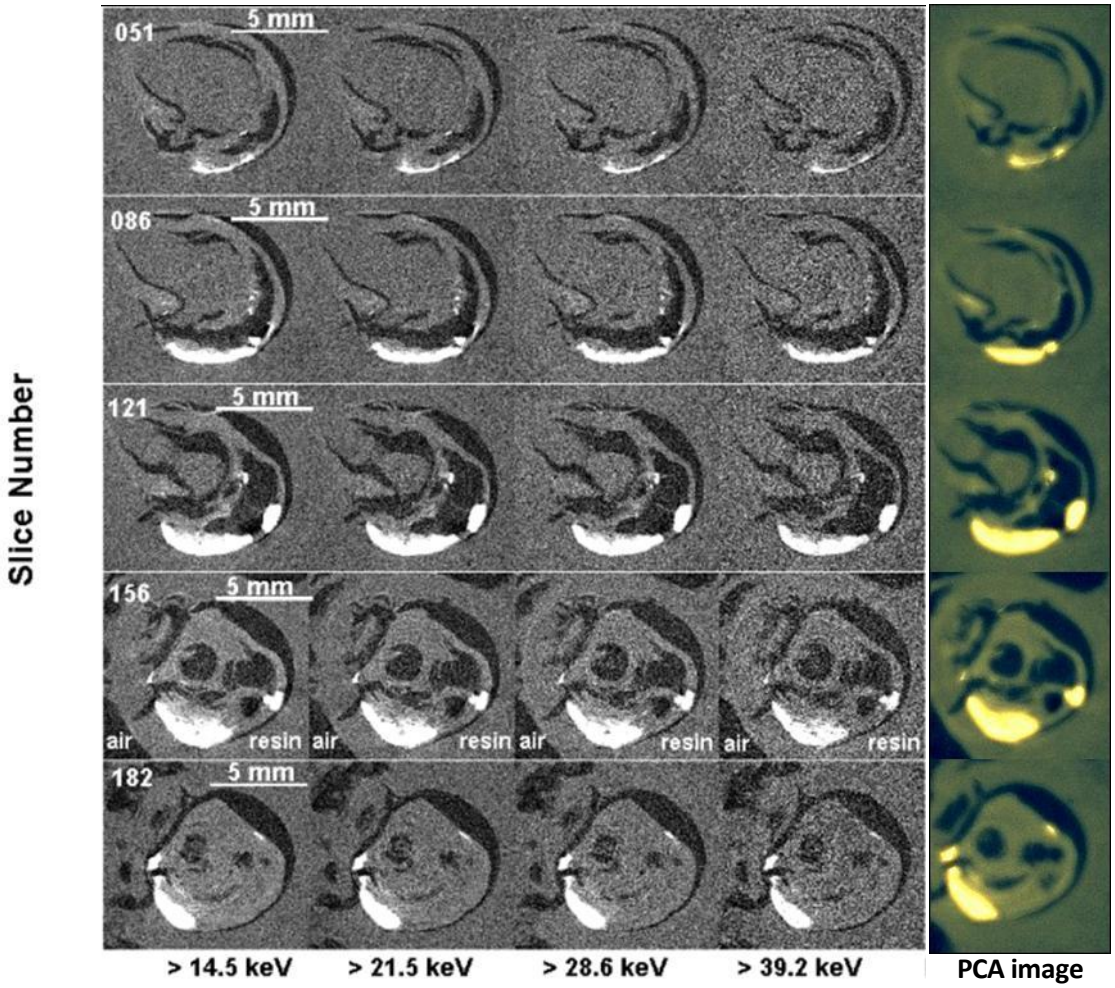

Figure 7.6 *Spectral images of cross sections through carotid artery plaque (fixed in resin). Several images were selected at different energies to display the progression of calcification in plaque and the response of absorption characteristics of dense and non-dense regions over the entire energy range. The colour coded images were obtained from PCA.*

The dual-energy subtraction imaging technique is an alternative approach to PCA for imaging and visualising energy-dependent attenuation differences. With this technique, the spectral CT images are calibrated in HU the usual way so that air corresponds to -1000 HU and water to 0 HU, then the difference between the high and low energy images is calculated to cancel out the background soft-tissue structures. Figure 7.7 shows the results of applying dual-energy subtraction to the femoral artery dataset. The subtraction images indicate that the

atherosclerotic plaque tissues are spectroscopically distinct from resin. If there were no energy related contrast differences then the subtraction images would be blank.

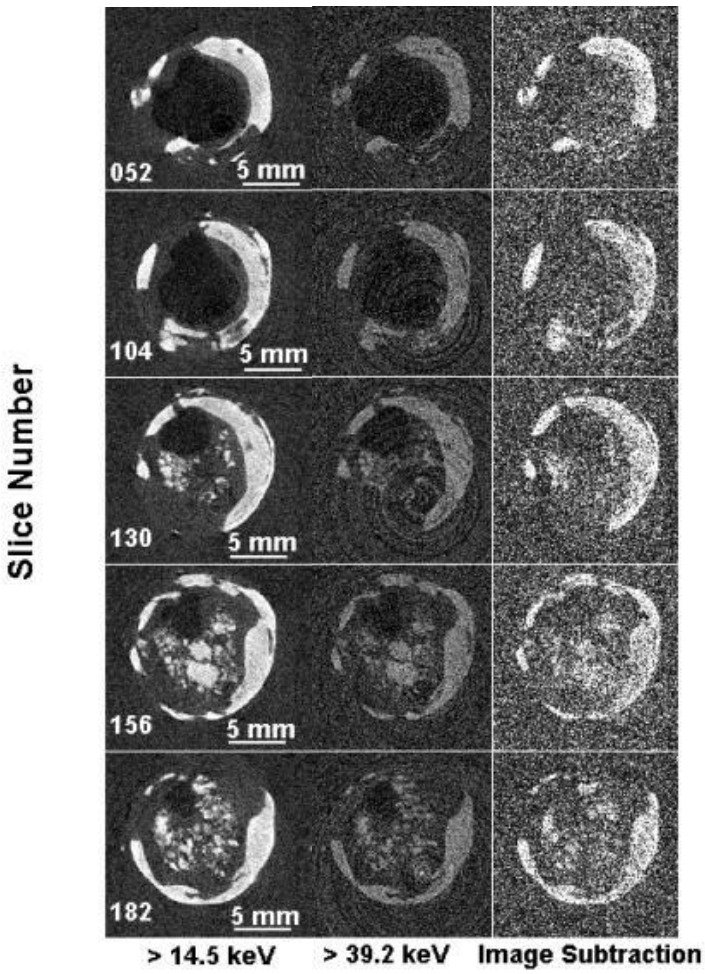

Figure 7.7 *The low and high energy images of femoral artery plaque (fixed in resin). These images were scaled to HU normalised using regions of air and resin. The images in the final column are subtraction images showing the difference in HU between images obtained using the lowest and highest threshold energies.*

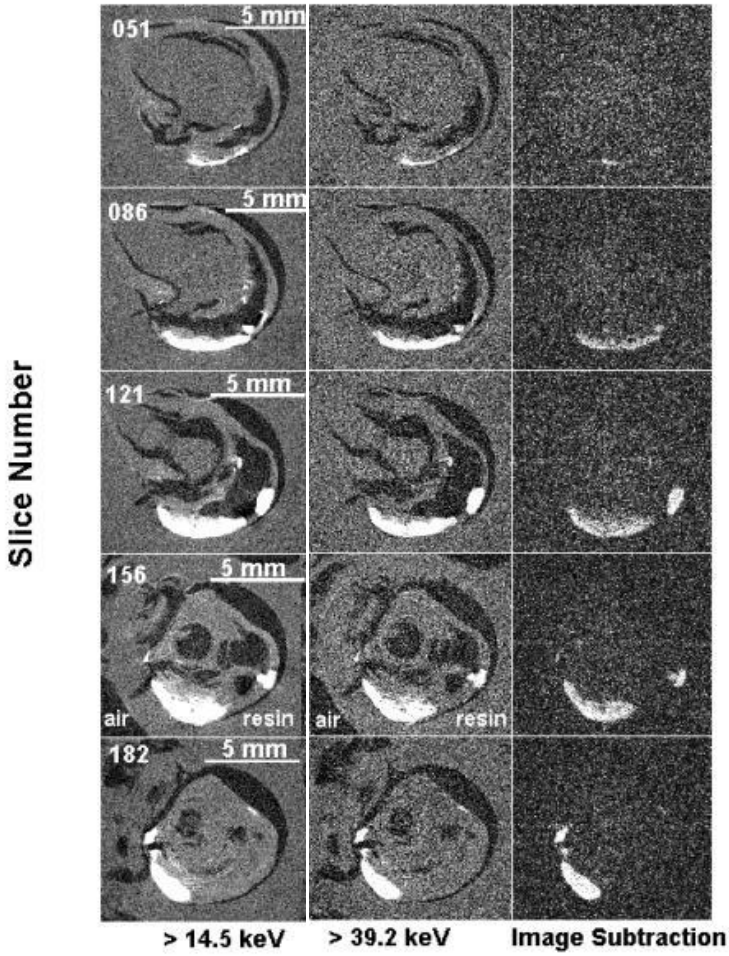

Figure 7.8 *The low and high energy images of cross sections through carotid artery plaque (fixed in resin). The images in the final column are subtraction images showing the difference in HU between images obtained using the lowest and highest threshold energies.*

Figure 7.9 demonstrates the spectral CT images, PCA image and photograph of each section of the unfixed plaque. The spectral CT images are scaled to CT numbers measured in HU. The energy dependence of CT number varies with material according to atomic number. The differences in energy dependence are identified using PCA and used to classify the components of the plaque.

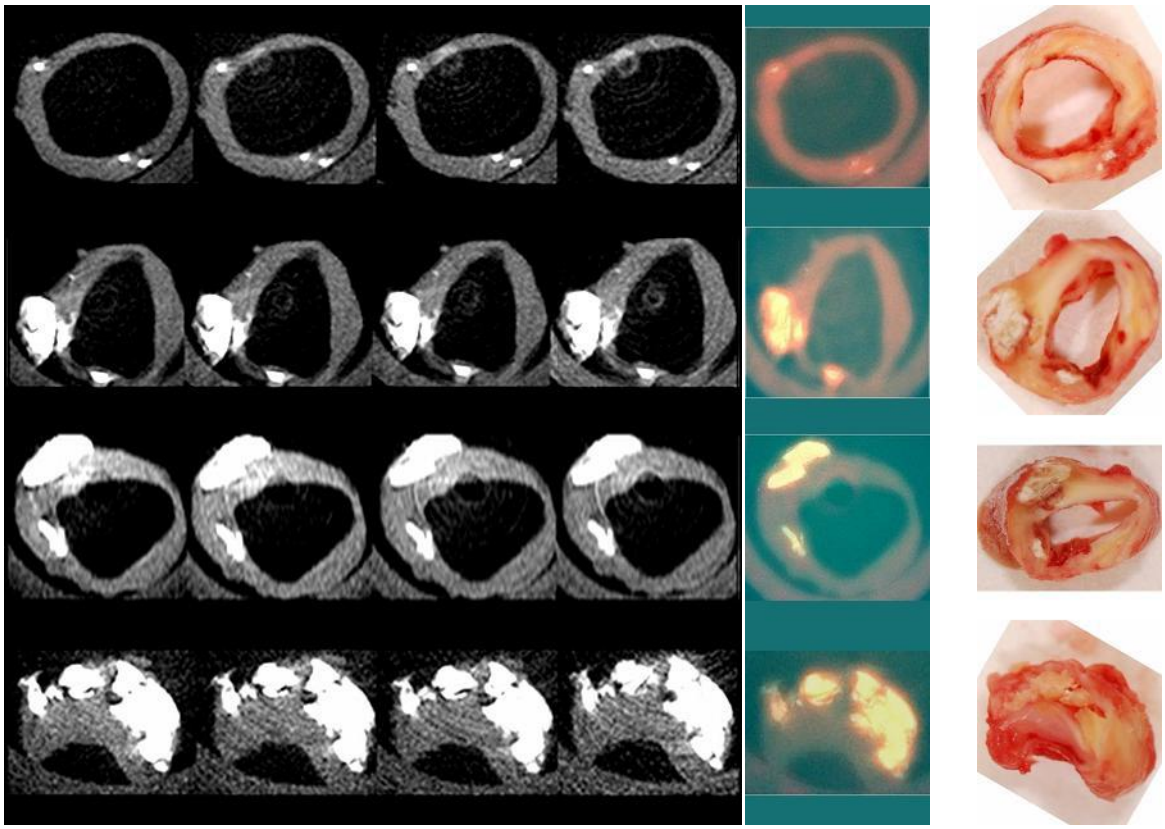

>14.0 keV >20.0 keV >25.0 keV >34.5 keV PCA image Photograph

Figure 7.9 *Spectral images, PCA images and photographs of 3 mm slices of a carotid artery plaque, snap frozen. The plaque was imaged using four energy thresholds: 14.0 keV, 20.0 keV, 25.0 keV and 34.5 keV.*

7.4 Discussion

In the present study, there are two key findings. Firstly, the high resolution of the MARS-CT2 scanner enables the visualisation of the complex structure of advanced atherosclerotic plaque. Secondly, different components of atherosclerotic plaques have different energy responses to x-rays that can be measured and visualised using spectral CT. These results were achieved using the novel Medipix photon-counting detector to measure the intrinsic properties of the tissue without the presence of contrast agent.

Plaque morphology is an important predictor of postoperative outcomes and identification of patients at risk will lead to better and earlier diagnosis of cardiovascular disease (Pasterkamp et al., 2000). Conventional CT does not provide enough resolution to distinguish the necessary tissue structures. The results of this study show that the MARS-CT2 scanner can be used to assess the complex morphology of the atherosclerotic plaque lesions.

The MARS-CT2 images show dense deposits in advanced atherosclerotic plaques forming complex structures. There are two types of opacities within the plaques: the confluent peripherally and punctate centrally. These appearances are similar to synchrotron images of human coronary atheroma reported by Langheinrich et al (2007). They showed that the peripheral, highly attenuating areas of plaque were due to calcifications with a linear size greater than 1000 μm while the tiny random dots of increased attenuation (usually <100 μm) were iron from intraplaque haemorrhage. Based on this, it is possible that the confluent and punctate densities in our plaques are also calcium and iron respectively. However, this study was not designed to distinguish iron and calcium deposits in the plaque. To distinguish and determine the distribution of iron and calcium at high resolution within atherosclerotic plaque it will be necessary to include histology and staining specifically for these materials. The resin preservation technique used in this study limits our ability to apply these methods and future work should focus on fresh, unfixed specimens. A study specifically aimed at separating these two elements with histological correlation is the next logical step.

Images obtained from high resolution scanning with MARS-CT2 were compared with conventional CT and MRI images. MARS-CT2 allowed reconstructions to be made using a voxel size of $(43\ \mu m)^3$. Compared with this, images acquired from conventional MDCT and

MRI had poor spatial resolution and identification of fine structure within the plaque was impossible.

The spectral CT images display the attenuation characteristics of the various plaque materials over the entire energy range. At lower energies, the detailed morphology of the bright opacities as well as the less opaque regions is apparent. As the energy increases, the image contrast decreases. The bright opacities are clearly distinguishable from the less opaque regions by their spectroscopic characteristics as well as their grey scale values. Generating CT images at different photon energies and then generating a difference image by subtraction can highlight material specific variations in energy dependent x-ray attenuation (due to photo-electric and Compton effects). This shows that spectral information from multi-energy imaging can be used to differentiate different types of tissue. If there were no material specific variations in contrast with energy then the difference images would be blank. However the spectroscopic contrast was poor and many materials were indistinguishable. This may have been partly due to the choices of sensor layer and imaging parameters.

The surgical specimens were imaged with an x-ray tube accelerating voltage of 75 kVp with a range of detector threshold energies up to 40 keV. The detector sensor layers used were GaAs and CdTe. These sensor layers have good detection efficiency up to 80 and 100 keV respectively (Zwerger et al., 2007), but currently, the uniformity of these sensor layers is not as good as that of the Si sensor layer. The maximum variation in attenuation coefficient for soft tissue samples occurs at low x-ray energies. Thus, the uniformity of the sensor is more important than its detection efficiency at higher energies.

The tube voltage setting of 75 kVp produces a relatively hard x-ray spectrum and so is also not ideal for obtaining high contrast in soft tissues. Use of a lower accelerating voltage will

produce a greater proportion of x-rays that will be completely absorbed (photoelectric effect) rather than scattered (Compton interactions) and thus, will enhance the tissue contrast. In summary, the choice of sensor layer and imaging parameters used in this study could be improved upon. For future studies, the experimental design should consider use of a more uniform sensor layer (such as Si) and a lower tube voltage, together with an increased current or exposure time. Careful selection of these imaging parameters will improve the image contrast and enhance the assessments of atherosclerotic plaque components.

The capabilities of the MARS-CT2 scanner for imaging the unfixed ex vivo atherosclerotic plaque were also investigated. In comparison with the results for the fixed specimens, the images of the unfixed specimens show greater contrast and this approach allows the CT images to be validated against other methods such as photography and histology. Since the MARS-CT2 scanner was not designed for fresh specimen imaging, the scan time and imaging parameters have to be taken into account to preserve the freshness of the scan specimens. Thus, to keep the specimen frozen, dry ice was placed at both ends of the sample tube. Unfortunately, this technique works only for relatively short scans (~1 hour). The total scan time of the plaques with the MARS-CT2 scanner is 2.5 hours for 2 detector positions, four energies and 303 projection angles. Thus, to image unfixed and fresh surgical specimens, improved acquisition speeds and an appropriate cooling system will be needed for the next generation of MARS-CT scanner. At the time of the final submission of this thesis, various improvements have been performed on the mechanical system and software. As a result the scan time has been reduced by a factor of 3.75.

The spectral CT images of both the fixed and unfixed specimens were analysed with PCA to enhance the spectral images in the energy domain from a statistical analysis of the number of independent patterns of spectral variation. The method requires no a priori knowledge of the

materials being imaged and it can be applied to large data sets. The method is able to identify and extract the important features of a dataset into only a few basis images that can be easily interpreted. The application of PCA was performed on reconstructed CT slices to separate different materials and display the relevant information in only a single coloured image.

However, the PCA method was only successful in highlighting materials in the plaque with a relatively large difference in atomic number. The CT images analysed with PCA may have insufficient contrast for differentiating lipid and soft tissues in the plaque. Furthermore, PCA does not use a priori knowledge of the materials present, so it cannot be used to decompose the spectral data into a previously selected set of basis materials. Thus, an alternative analysis technique will be required for specific analysis of materials such as soft tissues, calcium, iron and lipid.

A common problem with CT is the appearance of imaging artifacts. The most prominent artifacts observed in this study are ring artifacts. Ideally these types of artifact are avoided by optimising the imaging conditions and correcting for pixel variations using flat-field images during image processing. The ring artifacts from the Medipix detector are due to a combination of fixed-pattern noise and detector inhomogeneities that vary over the course of the scan. The energy dependence of the flat-field correction has been reported previously (Mikulec et al., 2003). It was noted that simple flat-field corrections are generally inadequate. In addition, the pixel inhomogeneity pattern on the CdTe sensor layer is affected by the high flux irradiation and also cannot be fully corrected using a simple flat-field correction (Aamir et al., 2011). The simple flat-field correction technique used in this study corrects for the fixed-pattern noise component but the variable component remains to cause ring artifacts in the reconstructed images. Therefore, improved flat-field correction and ring artifact suppression may be needed for future work.

In summary, this study has shown the potential for using high resolution multi-energy spectral CT for depicting the internal structure of excised atherosclerotic plaque and discriminating the material components. The use of the MARS-CT2 and the PCA method was successful in depicting and discriminating some of the plaque structures and materials. It suggests that spectral CT may have the potential to independently differentiate vulnerable plaque markers such as iron deposits and lipid. However, it should be possible to obtain improved measurement results by studying the material composition of fresh (unfixed) specimens of excised atherosclerotic plaque with a better selection of spectral CT scanning parameters, sensor layer, improved specimen cooling and reduced imaging time. The results would be correlated using cross-sectional photography and histological examination.

7.5 Conclusion

In conclusion, this preliminary study on multi-energy imaging of atherosclerotic plaques performed with the MARS-CT2 and Medipix2-MXR photon-counting detector shows that high resolution spectral CT is able to visualise the plaque morphology and determine the differences in absorption spectra of different materials in the plaques. The potential for the MARS-CT2 scanner to be used as a research tool for characterising fresh (unfixed) specimens of excised atherosclerotic plaques has been demonstrated. The use of cross-sectional photographic images for validating the morphology and structure has also been demonstrated. Sectioning the unfixed plaques will also allow correlation with histological examination.

A better combination of imaging parameters such as reduced tube voltage, increased tube current, and the use of a more uniform and more stable Si sensor layer will improve the image

contrast. This will also enhance the spectroscopic assessments of atherosclerotic plaque components.

For future studies on fresh (unfixed) plaques a cooling system will be needed as well as improvements in the speed of data acquisition. However, technological challenges remain to be solved with the design of the MARS camera readout to improve the speed of data transfer and to allow the use of $2 \times N$ chip arrays. Improvements in flat-field correction and ring artifact suppression techniques should be implemented to compensate for the effects of pixel response variations on the reconstructed images. Many of these issues are addressed in the following chapters.

In this study, PCA has been used to determine the presence of plaque materials with distinct x-ray absorption properties. This technique does not require nor allow the use of an a priori set of basis materials. For future imaging studies of specific materials (e.g. calcium, iron and lipid) within the plaques the use of an alternative material decomposition technique should be investigated.

7.6 Summary

1. This study demonstrates that the MARS-CT2 scanner is able to image and characterise fresh and fixed specimens of excised atherosclerotic plaque. The energy information obtained from multi-energy imaging allows the characterisation of plaque components with cross-sectional photography and histological examination as a gold standard.

2. Further consideration of imaging parameters such as tube voltage, tube current, energy range and the choice of sensor layer is required to improve the image contrast and enhance the assessments of ex vivo atherosclerotic plaque components.

3. A cooling system is needed for future imaging of fresh surgical specimens. Increasing the MARS readout speed and size of the detector by creating a $2 \times N$ chip array will enable shorter scan times and reduce the cooling requirements.

4. Improvements in flat-field correction and ring artifacts suppression techniques are needed to reduce the effect of pixel response variations on the reconstructed images.

5. PCA has been used to successfully determine the presence of different materials within the plaques. However, this technique does not allow the use of an a priori set of basis materials. For future imaging studies of specific materials (e.g. calcium, iron and lipid) an alternative material decomposition technique will be required.

Chapter 8

Calibration of the MARS-CT3 system with Medipix3

The limitations of the MARS-CT2 system identified in the preceding chapters were addressed in the design of the revised MARS-CT3 system. This system incorporates the MARS camera: a new design of readout capable of supporting both Medipix2 and the latest Medipix3 detector chips. A version of MARS-CT3 incorporating a MARS camera with a Medipix3 with Si sensor was provided for further studies of atherosclerotic plaques. It is anticipated that the performance of the upgraded MARS-CT3 with Medipix3 will be sufficient to characterise the composition and morphology of atherosclerotic plaques and thereby determine the presence of markers for vulnerable plaques.

To achieve this goal, it is first necessary to calibrate the x-ray detector and scanning gantry sub-systems. This chapter presents the methods and results for both calibrations. The section on the Medipix3 configuration and calibration discusses threshold equalization and energy calibration. The subsequent sections on the geometrical calibration and alignment of the scanning gantry include the protocols for determining the motor controller calibration, centre of rotation, x-ray projection magnification, vertical beam centre and detector skew. Finally, a summary of the main points of this chapter is presented.

The candidate has performed this work with the MARS commissioning team members (Dr Nicholas Cook, J Paul Ronaldson, Dr Judy Mohr, Raja Aamir and Maggie Anderson), as part of commissioning the system for biomedical research applications.

Portions of this work have been documented in the MARS quality system documentation (MARS, 2011).

8.1 Introduction

The MARS-CT3 system supplied for this work is a completely new scanner design with a number of significant improvements over the MARS-CT2 including computer-controlled source and camera axes and a new MARS camera readout and Medipix3 detector sub-system. To achieve the optimum measurement performance, several calibrations need to be done. These calibrations include equalisation and energy calibration of the Medipix3 detector and geometrical calibration of the spectral micro-CT system.

The first and second generation of Medipix detectors successfully demonstrated the potential for hybrid spectroscopic photon-counting detectors to provide new and useful information for x-ray CT imaging (Campbell et al., 1998; Llopart & Campbell, 2003). The Medipix3 detector is the latest generation of the Medipix family. The main motivation of its design was to eliminate the charge sharing effect that occurs when charge from a single event is shared between adjacent pixels. This has been achieved with the implementation of a new operating mode referred to as charge summing mode. However, because of temperature instabilities and pixel allocation biases associated with the Medipix3 when operated in charge summing mode (Ronaldson et al., 2011a), the Medipix3 detector was operated in single pixel mode for this work. Nevertheless the detector is an advanced design and the use of a Si sensor layer is expected to provide improved image quality and soft-tissue contrast compared with the previous system.

The geometry of the MARS-CT scanning gantry sub-system has five moveable axes driven by computer-controlled stepper motors that require calibration and characterisation. These

moveable axes include the vertical movement of the x-ray detector, the lateral movement of the x-ray detector and x-ray source platforms to adjust the magnification, and the rotation of the scanner gantry. Accurate characterisation of each axis is essential to ensure that the system will produce images free of misalignment artifacts. Parameters obtained from the geometric calibration are needed for the tomographic image reconstruction.

The reconstructed image quality crucially depends on the precise knowledge of the scan geometry of the acquisition system. Therefore, calibration methods are needed to account for a potential misalignment of the acquisition system (Noo et al., 2000; Lee et al., 2003; Kim et al., 2005; Cho et al., 2005; Ohta et al., 2006; Perilli et al., 2007; Gui et al., 2009). In the past few years, several methods have been proposed to calibrate micro-CT systems (Rougee et al., 1993; Von Smekal et al., 2004; Kalender, 2005; Cho et al., 2005; Yang et al., 2006; Sun et al., 2006; Hu et al., 2010). The usual approach is to use the projection data of a known calibration object (a phantom) to determine the calibration parameters. This approach was adopted for this work and a number of simple geometric calibration phantoms were built to calibrate the MARS-CT system.

8.2 Materials and Methods

8.2.1 Medipix3 configuration and calibration

The MARS-CT3 system was equipped with a single Medipix3 detector bump bonded to a 300 μm Si sensor layer. It has 256 × 256 pixels and a pitch of 55 μm. The scanner was equipped with a Source-Ray SB-80-1K x-ray tube (Source-Ray Inc, Ronkonkoma, New York) with tungsten anode and 1.8 mm of aluminium (equivalent) intrinsic filtration.

The Medipix3 detector needs to be configured and calibrated before it is used in the experimental work. Configuration consists of setting the 25 global Digital-to-Analog-

Converters (DACs) and then equalising the pixel thresholds by adjusting the 5-bit pixel DACs. The procedure used was that described by the chip designer (Ballabriga, 2011) and previously implemented in a characterisation study of the Medipix3 (Ronaldson et al., 2011a).

The energy calibration is performed to relate the arbitrary units of the threshold DAC to physical units of photon energy. The energy calibration of the Medipix3 detector was performed by passing x-rays through different metal foils with known fluorescence lines such as molybdenum or indium. The fluorescence spectra were recorded by performing a threshold scan and numerically differentiating the response curve.

The 17.5 keV K_α x-ray line from Molybdenum and the 24.2 keV K_α x-ray line from indium generated from foils with sub-millimetre thickness were used for energy calibration. The differentiated response curve was plotted against the threshold DAC values. The DAC values corresponding to the locations of the fluorescence peaks were noted and the energy calibration was determined by a linear regression fit of threshold DAC index against the corresponding fluorescence peak energies.

8.2.2 Geometrical calibration of the MARS-CT scanner

A precise knowledge of the imaging system geometry is required for accurate image reconstruction. The geometrical calibration of the MARS-CT system consists of measuring values for the centre of rotation (COR), vertical beam centre (VBC), detector translation skew and x-ray projection magnification. The x-ray projection magnification is determined by the source to object and source to detector distances (SOD and SDD).

The geometry of the MARS-CT system described using Cartesian coordinates (x, y, z) is shown in Figure 8.1. The axis directions are given by the right hand rule. Ideally the x-axis is coincident with the axis of rotation of the gantry, the y axis is perpendicular to the x-axis and

parallel with the plane of the detector, and *z*-axis is the normal to the detector. The projection of the principal axis of rotation (i.e., the axis the gantry rotates about) onto the imaging device is known as the centre of rotation (COR). The beam axis is perpendicular to this axis and also called the optical axis. The vertical beam centre (VBC) is the beam axis detector column where the optical axis and the x-ray detector intersect.

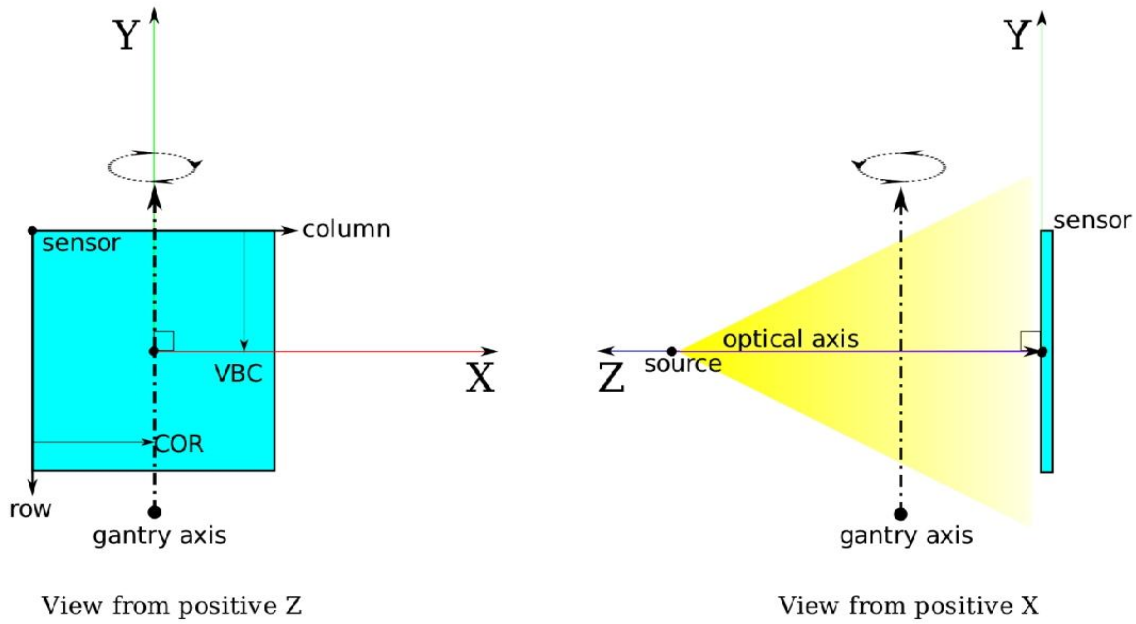

Figure 8.1 *The geometry of MARS-CT system. The view from positive Z shows the COR and VBC sensor column and row locations. The view from positive X shows the relative locations of the source, gantry axis and optical axis.*

In the MARS-CT system, the gantry axis is horizontal but the images obtained from the MARS camera are rotated 90° anticlockwise (from the observer's viewpoint). In the CT reconstruction software package (Octopus), the assumed orientation of the stage rotating axis is vertical and the image frames are referred to as though they are projections onto a single unrotated vertical screen. After the frames from a number of detector positions have been

stitched, the result is a single frame with an image oriented as though it had been collected using equipment in the standard arrangement described in the Octopus manual (Dierick et al., 2004).

In this standard geometry, the image column numbers correspond to a horizontal location in physical space and the image row numbers correspond to a vertical location in space. The projection of the rotation axis onto the imaging device is known as the centre of rotation. The optical axis is perpendicular to the gantry axis. The vertical beam centre is given by the detector column where the optical axis and the x-ray detector intersect.

Before the orientations and locations of the various scanning axes are determined it is necessary to confirm the nominal values for the motor drive index coefficients.

8.2.2.1 Motor controller calibration

The accuracy of the motor drive movements was checked by measuring displacements of the motor drive for a series of known stepper motor index values. The scanner gantry was rotated to expose the motor drives to the access port (Figure 8.2). Both the x-ray detector and x-ray source were moved to their initial positions (with index value = 0 which is furthermost from the sample axis position). The x-ray detector was moved by increments of 4000 index values from its initial position. The movement of the exposed detector motor drive was measured for each increment. Then, the same method was repeated to check the accuracy of the x-ray motor drive movement with index value.

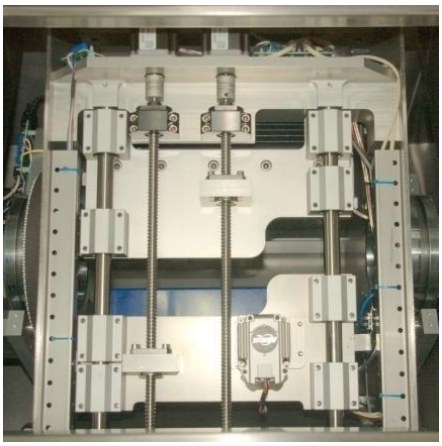

Figure 8.2 *X-ray detector and source motor drives of MARS-CT scanner. The view is of the bottom of the gantry and the blue box of the MARS camera is just visible between the movable x-ray and camera platforms.*

8.2.2.2 Centre of rotation

The centre of rotation refers to the projection from the x-ray source through the axis of rotation onto the detector surface. The image column number corresponds to the centre of rotation value used within the CT reconstruction software. A wire phantom (Figure 8.3) was used in this study to evaluate the centre of rotation. The phantom was placed in the scanner and projection images acquired at gantry angles 180˚ apart. The images were superimposed and the column where the images of the diagonal wire intersect was identified.

Figure 8.3 *The wire phantom used to find the centre of rotation.*

8.2.2.3 X-ray projection magnification

The object magnification was evaluated as a function of detector position for each of four gantry rotation positions 0°, 90°, 180° and 270°. A phantom containing a steel ball with a diameter of 3.88 mm was used for this purpose (Figure 8.4). This experiment was also performed to find the SOD and SDD of the scanner. The object magnification, $M(i)$, for each detector position was calculated from the ratio of the diameter, S_i, of a steel ball phantom on the x-ray image to its known diameter, S_0:

$$M(i) = \frac{S_i}{S_0} \tag{8.1}$$

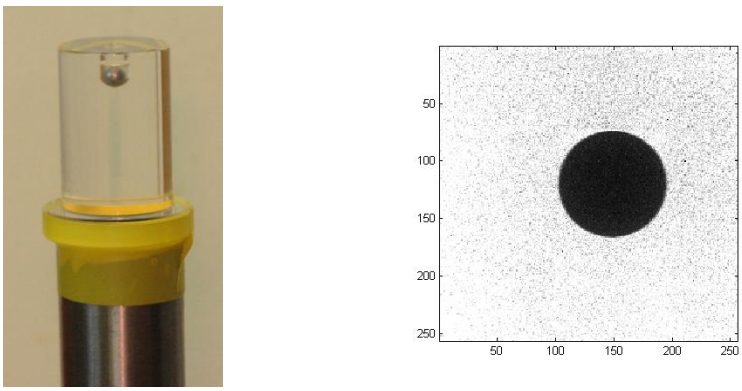

(a) (b)

Figure 8.4 *(a) The magnification phantom and (b) a projection image of the phantom.*

8.2.2.4 Vertical beam centre and gantry tilt

The vertical beam centre corresponds to the row number where the optical axis meets perpendicularly with the detector surface. Figure 8.5 shows the vertical beam centre measurement phantom. For a truly circular gantry rotation the image path is the perspective projection of an ellipse. If the SOD is sufficiently large with respect to the orbit of the target object then an ellipse is an adequate approximation. The ratio of the minor and major axes of

the ellipse determines the offset to the VBC. In addition the angle of the ellipse with respect to the axes of the imaging plane is equal in magnitude to the gantry tilt (and opposite in sign). Thus this measurement can be used to determine both the VBC and gantry tilt.

The phantom was placed in the scanner with the high contrast object close to the optical axis. Then the gantry was rotated and the phantom was scanned. The projection path of the high contrast object was plotted and an ellipse fitted to the data. The VBC and gantry tilt were determined from the results of the fit.

8.2.2.5 Detector translation skew

The detector translation skew was measured using the same small ball bearing phantom as used for measurement of the vertical beam centre (Figure 8.5(a)). The detector translation skew measurement was evaluated using a single detector at multiple positions. The effective skew of the detector depends on the direction of detector travel with respect to the image axes. The phantom was placed in the scanner with the projection of the high contrast object at one edge of the frame as shown in Figure 8.5(b). The detector was moved along its vertical translation axis with 100 index value increments. A projection measurement was acquired at each position.

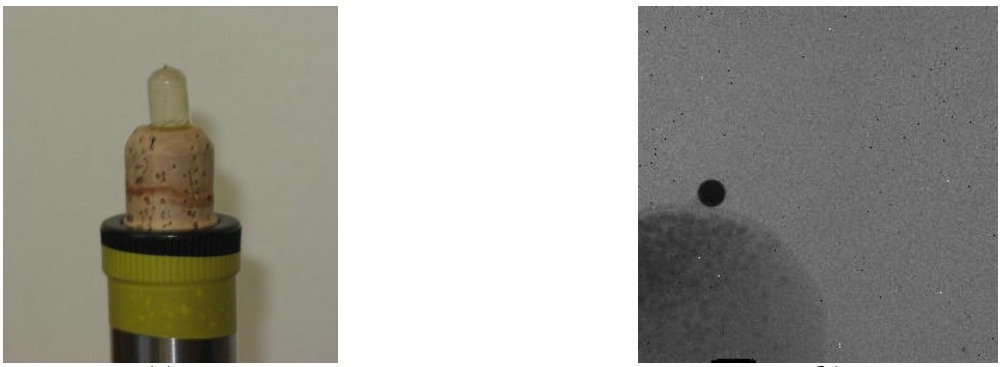

(a) (b)

Figure 8.5 *(a) The phantom used for measurement of the vertical beam centre and detector translation skew. A high contrast steel ball is mounted on the tip of the phantom. (b) A projection image of the phantom.*

8.3 Results and Discussion

8.3.1 Energy calibration of Medipix detector

Figure 8.6 shows the spectra obtained with molybdenum and indium foils within the open beam. The peaks correspond to the molybdenum and indium K fluorescence lines at 17.5 and 22.5 keV. A third point was determined from the location of the centre of the noise floor (threshold DAC = 16, not shown). The locations of the fluorescence peaks and the noise floor were used to determine the relationship between the arbitrary units of threshold and the physical units of photon energy (keV). Figure 8.7 shows the linear relationship between these two variables.

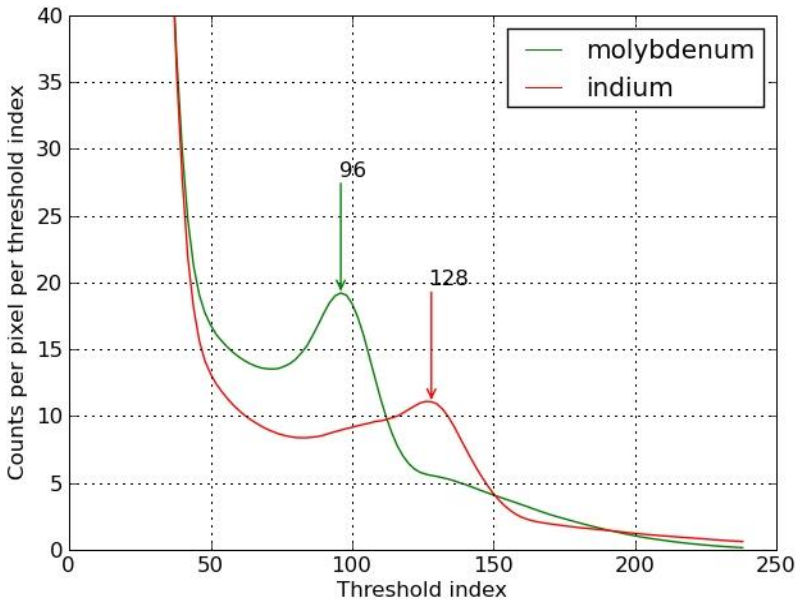

Figure 8.6 *The spectra obtained with molybdenum and indium foils within the open beam. The peaks correspond to the molybdenum and indium K fluorescence lines at 17.5 keV and 22.5 keV respectively.*

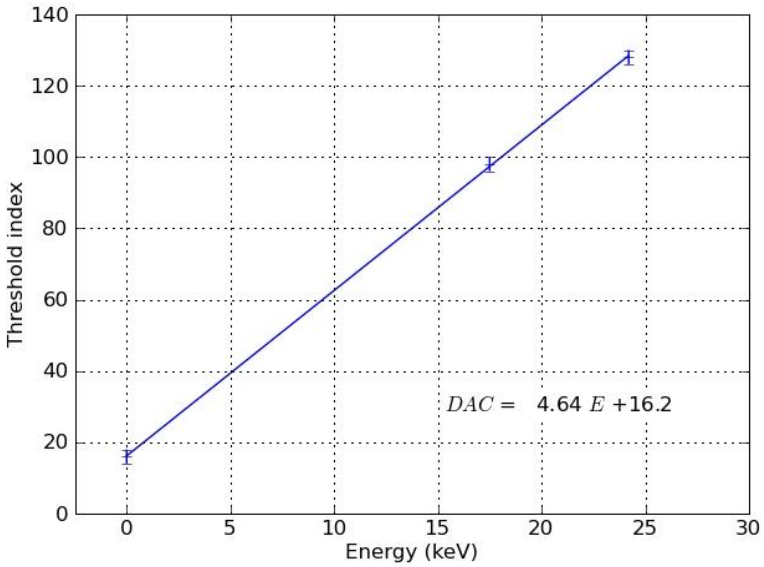

Figure 8.7 *A linear regression fit of the threshold DAC values for the two fluorescence peaks and the noise floor against the corresponding energies is shown. The straight line relationship gives the threshold DAC value in terms of detector threshold energy E.*

8.3.2 Calibration of motor controller

The movements of the x-ray detector and x-ray source were evaluated by plotting the measured displacement against index values. Figure 8.8 demonstrates the results from movements of both the x-ray detector and x-ray source as a function of index value. Both graphs show straight lines with gradients consistent with the nominal index motor coefficients. The displacement rates for both the x-ray detector and x-ray source motors are 2×10^{-4} cm/index.

Thus, for movement of the x-ray detector, $m = (2.00 \pm 0.04) \times 10^{-4}$ cm/index while for movement of the x-ray source, $m = (2.00 \pm 0.11) \times 10^{-4}$ cm/index.

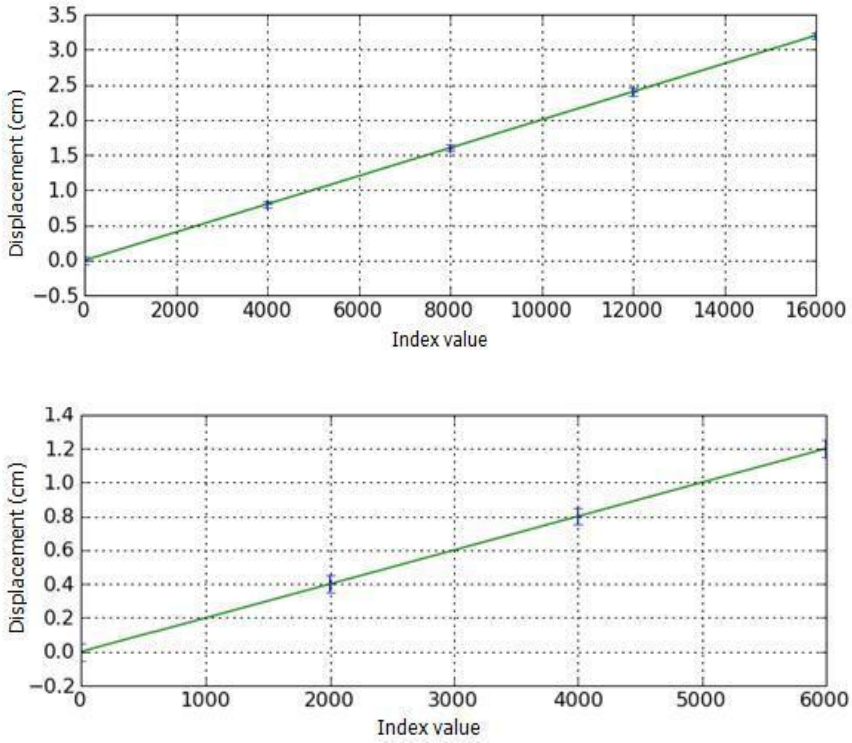

Figure 8.8 *The x-ray detector (top) and x-ray source (bottom) displacements plotted as a function of index value.*

8.3.3 Scanner geometry measurement

8.3.3.1 Centre of rotation

The centre of rotation of the scanner is obtained from the point of intersection of the projected images of the diagonal wire. Figure 8.9 shows the superimposed images of the wire phantom and the corresponding column number. In this case the centre of rotation is at column 137.

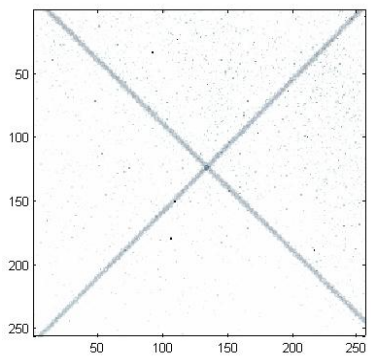

Figure 8.9 *The superimposed images of a wire phantom taken with the gantry rotated by 180°. The intersection of the images of the diagonal wire indicates the centre of rotation of the scanner. In this case the centre of rotation is at column 137.*

8.3.3.2 X-ray projection magnification

The magnification of the steel ball phantom was plotted against detector index and a linear fit for object magnification obtained. Figure 8.10 shows the magnification as a function of detector position index *i* for four gantry angles 90° apart.

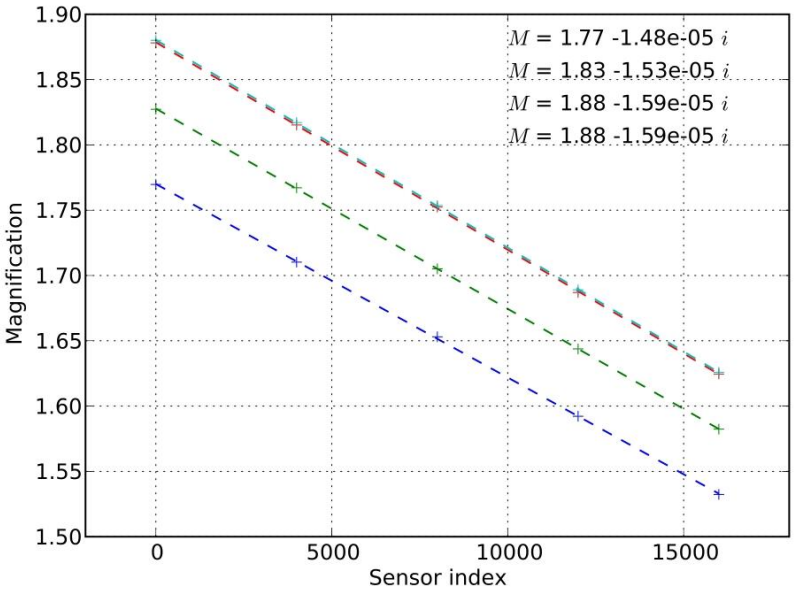

Figure 8.10 *The object magnification with detector position for four gantry angles 90° apart. In each case the SOD is obtained from the reciprocal of the gradient and the SDD by substitution into the equation for magnification.*

The SOD was determined from the gradients of the fitted lines (see Figure 8.10):

$$SOD = \frac{-\Delta\, SDD\ (i)}{\Delta M\ (i)} \tag{8.2}$$

The results were averaged over the four gantry rotation angles to reduce errors caused by misalignment of the ball with the rotation axis. The SOD and intercept $M(0)$ were substituted into the following equation for magnification to give the SDD at zero detector position index:

$$M = \frac{SDD}{SOD} \tag{8.3}$$

The average SOD obtained from the gradient is *SOD* = 64581 index units and the average SDD for zero detector position index is *SDD* = 118777 index units. The detector and x-ray platforms move closer together with the motor index at a rate of 2 x 10^{-3} mm/index. Therefore the SDD and SOD as functions of detector and x-ray indices *i* and *j* are:

$$SDD\ (i,j) = (237.6 - (i + j)\text{x}\ 2\ \cdot 10^{-3})\text{mm} \tag{8.4}$$

$$SOD\ (j) = (129.2 - j\ \text{x}\ 2\ \cdot 10^{-3})\text{mm} \tag{8.5}$$

The magnification *M(i,j)* as a function of the motor index values can now be calculated by substitution of equations (8.4) and (8.5) into (8.3).

8.3.3.3 Vertical beam centre and gantry tilt

Figure 8.11 shows the path of the phantom ball as the gantry rotated. The path that the phantom ball projects onto the imaging plane is approximated by an ellipse with major axis *a* and minor axis *b*. The minor axis of the ellipse vanishes when the ball is positioned at the vertical beam centre.

The projections of the phantom were plotted and an ellipse was fitted to the data. The row location C_y of the ellipse and the sizes of the major and minor axes a and b were used to determine the row displacement to the vertical beam centre. The orientation of the ellipse was assumed to be perpendicular to the row number axis and the orbit size is much less than the SDD, therefore:

$$\Delta y = SDD\ \frac{b}{a} \tag{8.6}$$

$$VBC = C_y \pm \Delta y \tag{8.7}$$

In this case, based on Figure 8.11 the position of the centre of the ellipse is (230.3; 232.5) pixels. The track of the ball was measured with the camera at sensor index position 16000 corresponding to SDD = 205.6 mm, hence the row number of the vertical beam centre is 303 pixels. The rotation angle of 0.2° corresponds to the tilt of the gantry axis (-0.2°).

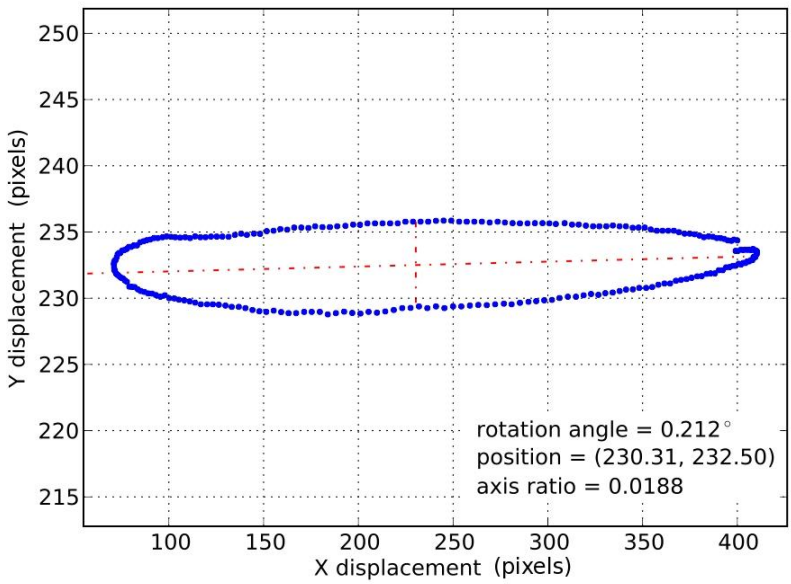

Figure 8.11 *The projections of the phantom were plotted and an ellipse was fitted to the data.*

8.3.3.4 Detector translation skew

The displacement location of the high contrast ball was plotted for different detector translation index values. The gradient was recorded for use in the frame stitching algorithm. The effective detector translation skew for multiple detector positions is $\theta = 89.05°$ with respect to the image row axis as shown in Figure 8.12.

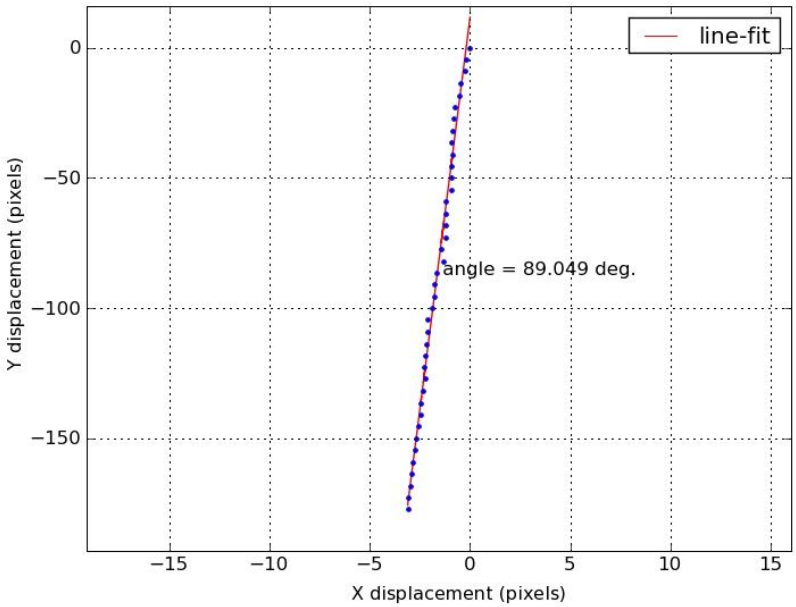

Figure 8.12 *The ball position displacement is plotted for a series of detector translations. The image stitching vector is determined from the motor index coefficient and the sine of the angle $\theta = 89.05°$ of the fitted line with respect to the y-displacement axis.*

8.4 Conclusion

The proposed calibration methods have been used to successfully calibrate the Medipix3 detector within the MARS camera and the electromechanical gantry sub-system of the MARS-CT system. The equalisation and energy calibration of the Medipix3 detector was successfully performed. The energy calibration was completed using x-ray fluorescence spectra generated by the open beam x-ray interactions with thin metal foils of molybdenum and indium.

The geometric calibration technique is easy to implement and uses a number of simple calibration phantoms. These phantoms provide an easily analysable set of projection data. This geometric calibration involves the estimation of a set of parameters that describe the geometry of the spectral micro-CT system and are essential for accurate image reconstruction.

8.5 Summary

1. The equalisation and energy calibration of the Medipix3 detector must be performed prior to imaging. The performance of the MARS-CT system depends on the uniformity of pixel response and the ability to accurately select thresholds of known energy.

2. The energy calibration of the Medipix3 detector was successfully performed. The energy calibration was completed using x-ray fluorescence peaks. The methods used are simple to implement and may be repeated regularly to optimise the performance of the Medipix3 detector.

3. The proposed geometric calibration technique uses simple calibration phantoms. The geometrical calibration of the tomographic system is important as the reconstructed

image quality of a CT system crucially depends on the precise knowledge of the scanning geometry. The proposed methods have been used to determine the COR, VBC, gantry tilt and detector translation skew angle.

4. The methods for calibration of the Medipix3 detector and the MARS-CT system are part of the overall commissioning protocol and may be used to prepare the system for pre-clinical applications.

Chapter 9

Performance evaluation of the MARS-CT3 system

This chapter describes the performance assessment of the MARS-CT3 system prior to being used for pre-clinical studies. The performance evaluation of the MARS-CT3 system was investigated in terms of spatial resolution, image uniformity, pixel noise, linearity, spectroscopic calibration and dose measurement with calibration phantoms. The methods and results are described and discussed. This chapter also presents demonstration images obtained from the MARS-CT3 system. The data acquisition and image processing methods are also described. The chapter concludes with a summary of the main points. Most of this work has been presented at the Nuclear Science Symposium and Medical Imaging Conference in Valencia, Spain (Ronaldson et al., 2011b). The candidate is one of the co-authors of this paper.

9.1 Introduction

The MARS-CT scanners are designed for use in various pre-clinical applications such as soft tissue imaging (Melzer et al., 2008; Butler et al. 2008; Berg et al., 2009; Zainon et al., 2010b; Butler et al., 2011b; Ronaldson et al., 2011c) and multiple contrast agents imaging (Butzer et al., 2008; Anderson et al., 2010; Butler et al., 2011c). The requirements in terms of sample size, spatial resolution, quantitative accuracy and precision differ by application. Thus, the performance of this scanner has to be evaluated against the requirements of the intended pre-clinical applications. Furthermore, as technical developments are implemented within new

versions of the scanner, re-evaluation of the performance is necessary to confirm the continuing accuracy of the system and the absence of technical problems such as electronic drift or electromechanical inaccuracies that may be introduced by system upgrades.

The criteria for evaluating the performance of the MARS-CT systems have been inspired by the quality control recommendations for clinical CT scanners in Report No.39 of the American Association of Physicists in Medicine (AAPM, 1993). The report states there is a need for scanner performance evaluation, scan parameter optimisation and a quality assurance system to monitor scanner stability. The calibration phantoms used in this work were designed and fabricated specifically for this purpose. The performance evaluation of the MARS-CT3 system was evaluated in terms of spatial resolution, uniformity, pixel noise, linearity, spectroscopic performance and dose measurement.

9.2 Materials and methods

9.2.1 MARS-CT system

The MARS-CT3 system was equipped with a single Medipix3 detector that was bump bonded to a 300 μm Si sensor layer. It has a format of 256 × 256 pixels with a pitch of 55 μm. This detector was operated in single-pixel mode. It was mounted within a fan-cooled MARS camera readout box (Mars Bioimaging, Christchurch, New Zealand). The Source-Ray SB-80-1K x-ray tube (Source-Ray Inc, Ronkonkoma, New York) had a tungsten anode and included 1.8 mm of aluminium (equivalent) intrinsic filtration. The focal spot size was 33 μm and the maximum accelerating voltage and tube current were 80 kVp and 1 mA respectively. The magnification of the MARS-CT3 is adjustable via moveable x-ray detector and x-ray source

platforms. The x-ray detector and x-ray source positions were held constant in this work to provide a magnification factor of 1.44 and an isotropic voxel size of $(38\ \mu m)^3$.

9.2.2 Scanning protocol and data processing

A scanning protocol with 250 projection angles was used to scan the phantoms for performance assessment of the MARS-CT3 system. The measurements were performed with the micro-focus x-ray source operating at 50 kVp and 0.5 mA with detector exposure times that were chosen to give approximately 2000 counts per pixel in open beam. Flat-field measurements for each detector position were taken before and after the sample scan to compensate for variations in detector performance that occur over the duration of the scan.

The raw projection data obtained were then corrected and normalised using a combination of the initial and final flat-field projection images. Frames were stitched to form large area projections and sinograms formed from the normalised data. The sinograms were filtered (Munch et al., 2009) to reduce ring artifacts before the CT images were reconstructed using the Octopus commercial CT reconstruction software (Dierick et al., 2004). The reconstructed images from the phantom data obtained from the MARS-CT3 system were stacked and averaged to represent a slice thickness of 1 mm. A single reconstructed slice for each biological specimen together with the 1 mm slice averages for the phantom data were calibrated in HU using air and water references. The uncertainties on the CT numbers were obtained by standard error propagation of the observed pixel noise.

9.2.3 Performance evaluation

Results from the preliminary study of atherosclerotic plaque imaging with the MARS-CT2 system (Chapter 7) showed that improvements in system performance were needed for a quantitative study. Performance evaluation of the MARS-CT3 system was by measurement of

the spatial resolution, image uniformity, pixel noise, linearity, spectroscopic calibration and dose measurement. The calibration phantoms were fabricated to evaluate these aspects of performance of the MARS-CT3 system.

9.2.3.1 Spatial resolution

The spatial resolution was determined from the MTF measured at the edge of a cylindrical perspex phantom of diameter 10 mm with polished surfaces (Figure 9.1). The phantom was scanned at 50 kVp with a threshold energy of 10 keV and reconstructions performed without beam hardening correction. The reconstructed slices corresponding to a thickness of 1 mm were stacked and averaged. The edge profile of the perspex-air boundary was numerically differentiated and the MTF computed from the Fourier transform of the result. The resolution corresponding to the spatial frequency at 10% MTF was determined.

Figure 9.1 *The MTF phantom used in the measurement of spatial resolution of the system. The diameters of the three sections from top to bottom were 5, 10 and 15 mm respectively.*

9.2.3.2 Image uniformity

Image uniformity was evaluated by measuring the CT numbers at the centre and periphery of a water phantom of diameter 15 mm with perspex walls of thickness 1.5 mm respectively. The water phantom was scanned at 50 kVp with a threshold energy of 10 keV with the MARS-CT3 system. CT reconstructions performed with simple polynomial beam hardening

correction (Herman, 1979) for phantom data obtained. The reconstructed slices corresponding to a thickness of 1 mm were stacked and averaged. The mean CT number and standard deviation per pixel in regions of interest at the centre and near the periphery of the reconstruction were determined and compared. The CT number profile through the centre of the phantom was also evaluated and examined graphically.

9.2.3.3 Pixel noise

The pixel noise characteristics were analysed by measuring the relationship between pixel noise and exposure from scans of a water phantom of diameter 15 mm with perspex walls of thickness 1.5 mm. This phantom was scanned with a fixed tube voltage of 50 kVp and threshold energy of 10 keV for a number of exposure (Q = current x time) settings. The standard deviation, σ, of CT number for regions of interest (ROI) taken from CT reconstructions corresponding to a slice thickness of 1 mm were used to evaluate the relationship between noise and exposure. The graph of σ^2 against Q^{-1} was examined to determine the relative contributions of random (quantum) and systematic effects.

9.2.3.4 Linearity

A 10 mm diameter perspex phantom with 2 mm diameter inserts containing aqueous solutions of calcium chloride at concentrations of 74.9, 147.0, 294.0 and 735.0 $mg.ml^{-1}$ were used to evaluate the linearity of the system. The calcium chloride phantom was scanned at 50 kVp with threshold energy of 12.3 keV. The CT number response and standard uncertainty for ROIs over the centre of each solution insert were calculated from the reconstructed images. The relationship between signal intensity and calcium chloride concentration was determined by linear regression.

9.2.3.5 Spectroscopic calibration

The spectroscopic calibration was performed by scanning a 10 mm diameter perspex phantom with 2 mm diameter inserts containing: sunflower oil (fat surrogate), 3 $mg.ml^{-1}$ of iodine Ultravist 300 (Bayer Schering Pharma, Berlin), 50 $mg.ml^{-1}$ of ferric nitrate, 200 $mg.ml^{-1}$ of calcium chloride, air and water. For brevity, the ferric nitrate, calcium chloride, sunflower oil and iodine are represented as 'Ca', 'Fe', 'Oil' and 'I' in the following sections. The multicontrast phantom was scanned at 50 kVp with threshold energies of 9.8, 15.1, 20.4, 25.6, 30.9 and 36.2 keV. The CT number response and uncertainty for ROIs over the centre of each material insert were calculated from the reconstructed images. The CT number was plotted against threshold energies for each material. The ability to distinguish material types was confirmed by comparing the spectroscopic CT responses.

9.2.3.6 Dose measurement

A pencil shaped ionisation chamber (Unfors Xi CT) was used to measure the dose rate in air at the isocentre of the MARS-CT3 system. The micro-focus x-ray source and x-ray detector were set at the same positions as for phantom and specimen imaging. The pencil chamber dosimeter was placed at the isocentre of the scanner. Tube voltages of 35 kVp, 50 kVp, 80 kVp and tube currents of 100 µA, 500 µA, 1000 µA were used to acquire integrated doses over 10 s from which the dose rates were obtained. The dose rates at different kVp were measured to quantify the x-ray exposure to be expected under different scanning conditions.

9.2.4 Demonstration with biological specimens

Two biological specimens were scanned to demonstrate the performance of the MARS-CT3 system. A human femoral plaque set in resin (Craftsmart liquid gloss, CraftSmart Australia, Glayton North, Australia) was scanned at 50 kVp with threshold energy of 9.8 keV.

An Apo-E deficient mouse was injected with iodine contrast agent into the tail vein and euthanised a few minutes later. A CT scan of the abdominal region was taken at 50 kVp and threshold energy of 9.8 keV.

9.3 Results

9.3.1 Spatial resolution

Figure 9.2 shows the MTF phantom image and the graph of line spread function (LSF) and MTF. The MTF falls to 10% of its maximum at a spatial frequency of 8.8 mm^{-1} equivalent to a resolution of 110 µm. The spatial resolution of the system (110 µm) is sufficient to allow imaging of most objects within small animal models and human specimens.

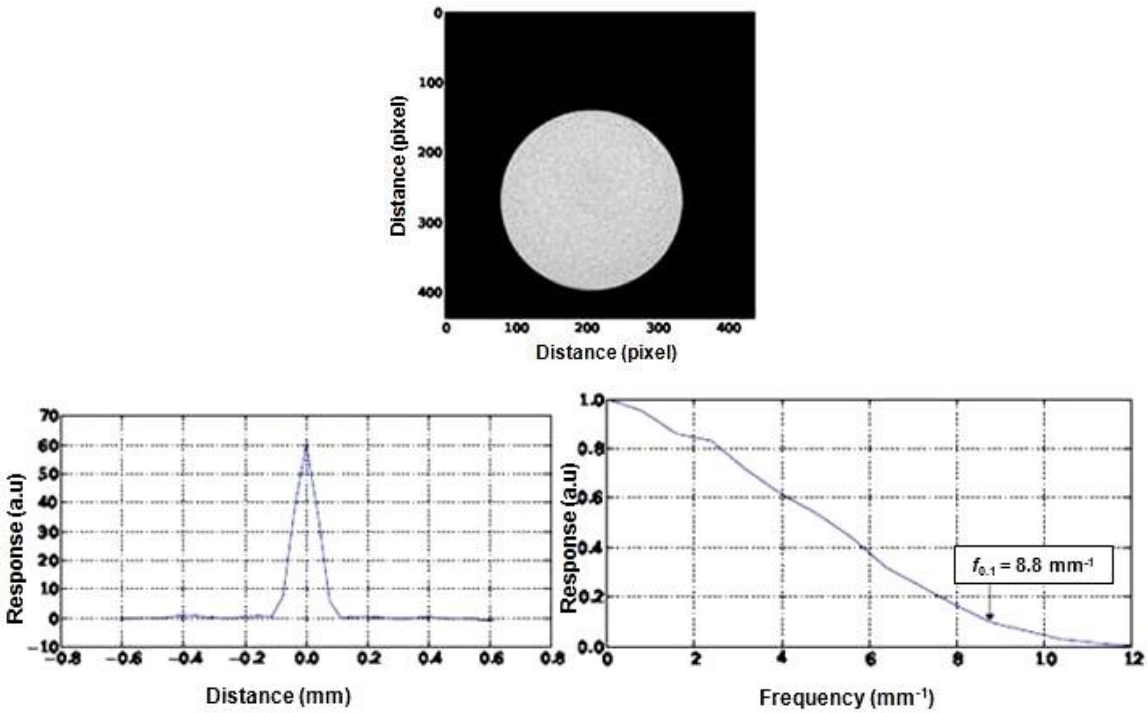

Figure 9.2 *(Top) A reconstructed image of perspex phantom used for evaluation of spatial resolution. (Bottom left) The LSF and (bottom right) MTF measured at the edge of the perspex phantom. The MTF falls to 10% of its maximum value at a spatial frequency of 8.8 mm^{-1}. The phantom was scanned at 50 kVp with threshold energy of 9.8 keV.*

9.3.2 Image uniformity

Figure 9.3 shows the reconstructed slices from the uniformity phantoms with mean CT numbers for ROIs located at the centre and near the periphery. The signal intensity profile taken through the centre of water phantom is presented. The mean CT number and standard deviation values range from -11.8 to +11.4 HU and from 23.5 to 35.8 HU respectively. The CT number profile through the water phantom is essentially uniform and located near 0 HU for the region containing water.

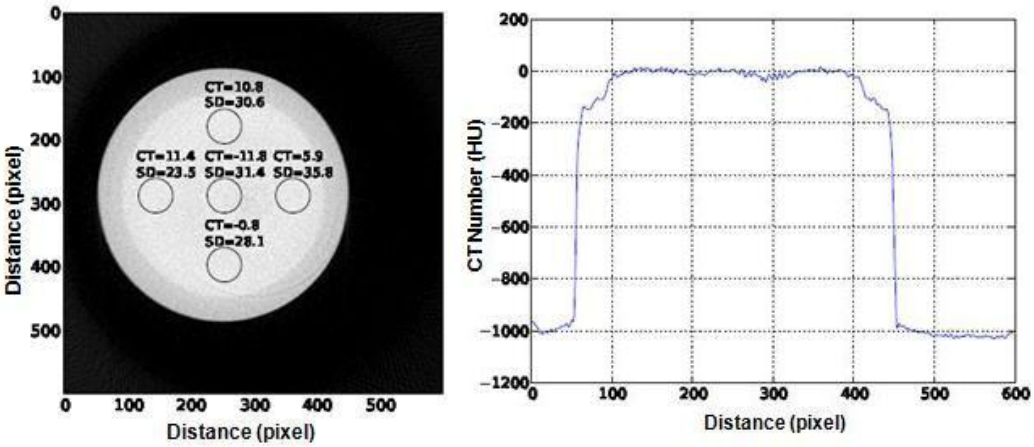

(a) (b)

Figure 9.3 *(a) A reconstructed slice of a 15 mm diameter water-filled phantom with CT response uniformity (after beam hardening correction) measured at the centre and near the periphery. (b) The CT number profile through the centre of the phantom. The phantom was scanned at 50 kVp with a threshold energy of 9.8 keV.*

The standard uncertainty (JCGM, 2008) due to residual non-uniformity after beam hardening correction is 6.7 HU. It is computed as shown in Equation (9.1).

$$\sigma_u = \frac{11.4+11.8}{2 \cdot \sqrt{3}} \text{ HU} = 6.7 \text{ HU} \tag{9.1}$$

9.3.3 Pixel noise

Pixel noise describes the extent of the variation in CT number in an image of a uniform medium. It is a critical limiting factor in CT since much soft tissue detail is low contrast in nature (AAPM, 1993). Figure 9.4 shows the water phantom images scanned with different exposures at 50 kVp.

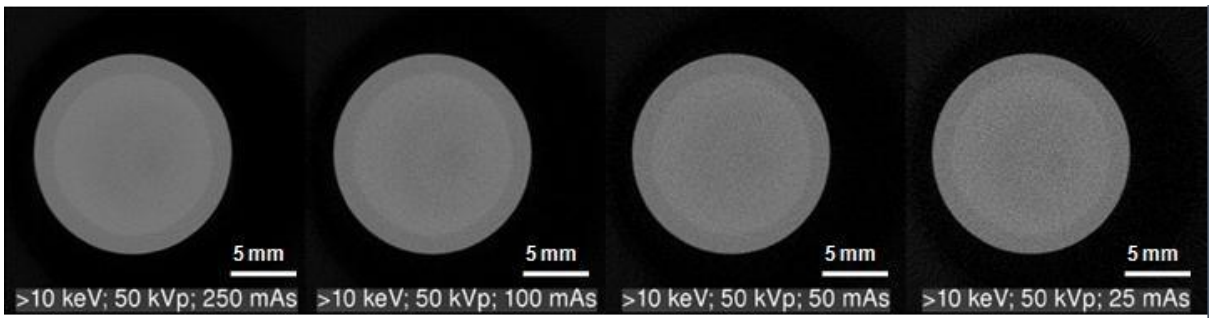

Figure 9.4 *CT slices of the water phantom obtained at different exposure times: 250 mAs, 100 mAs, 50 mAs and 25 mAs. The CT image noise depends on the number of x-ray photons contributing to the image.*

Figure 9.5 shows quantitative measurement of the pixel noise variance (σ^2) in the reconstructed images as a function of reciprocal exposure (Q^{-1}). Noise variance is approximately linear (R^2 = 0.994) with reciprocal exposure:

$$\sigma^2 = 157.6 \text{ HU} + 165.4 \text{ HU}^2\text{mAs x } Q^{-1} \tag{9.2}$$

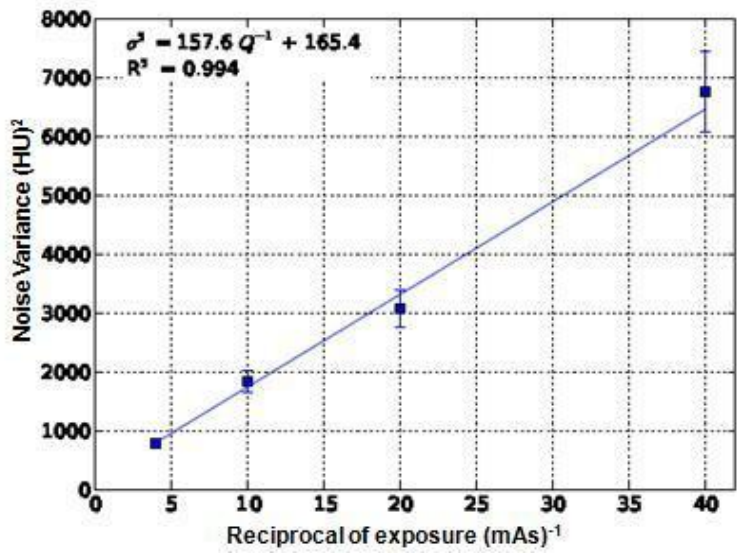

Figure 9.5 *Graph of noise variance, σ^2, against reciprocal exposure Q^{-1} from scans of a 15 mm diameter water phantom. The noise variance is approximately linear (R^2 = 0.994) with reciprocal exposure.*

9.3.4 Linearity

The CT reconstruction of the linearity phantom and the CT number response to the calcium chloride solutions of various concentrations are shown in Figure 9.6. Regression analysis indicates that the system is linear over the range of concentrations up to 294.0 mg.ml^{-1} (R^2 = 0.997). Beyond this concentration, corresponding to a CT number of approximately 2000 HU, the CT number response is underestimated.

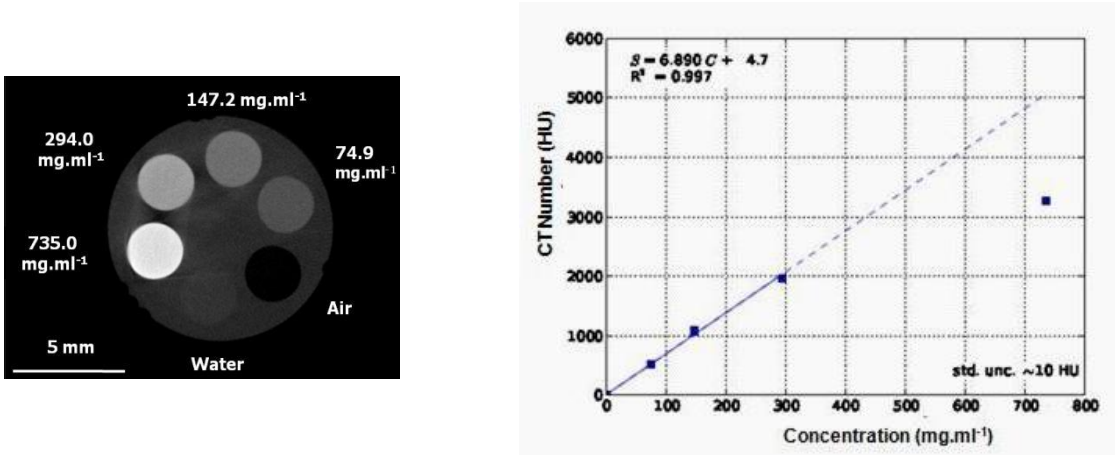

(a) (b)

Figure 9.6 *(a) The reconstructed CT image of the phantom with air, water and calcium chloride at concentrations of 74.9, 147.0, 294.0 and 735.0 mg.ml^{-1} and (b) the measured CT numbers, S, as a function of calcium chloride concentration, C. The phantom was scanned at 50 kVp with a threshold energy of 12.3 keV.*

9.3.5 Spectroscopic calibration

The CT reconstructions of a multi-contrast phantom and the measured CT numbers versus threshold energies for each material are shown in Figures 9.7 and 9.8.

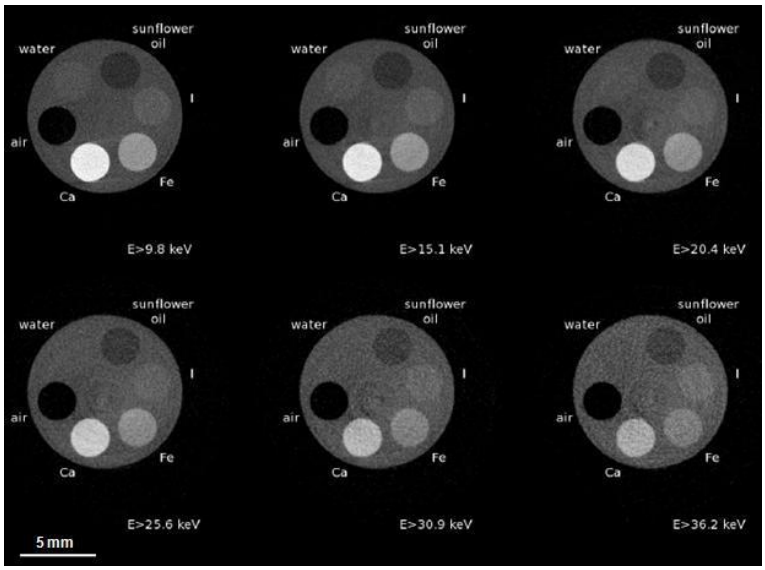

Figure 9.7 *(a)-(f) Spectral CT reconstructions of a perspex phantom containing Ca, Fe, I, oil, water and air at six different energies. The photoelectric and Compton effects that contribute to spectral response in attenuation are energy and material dependent.*

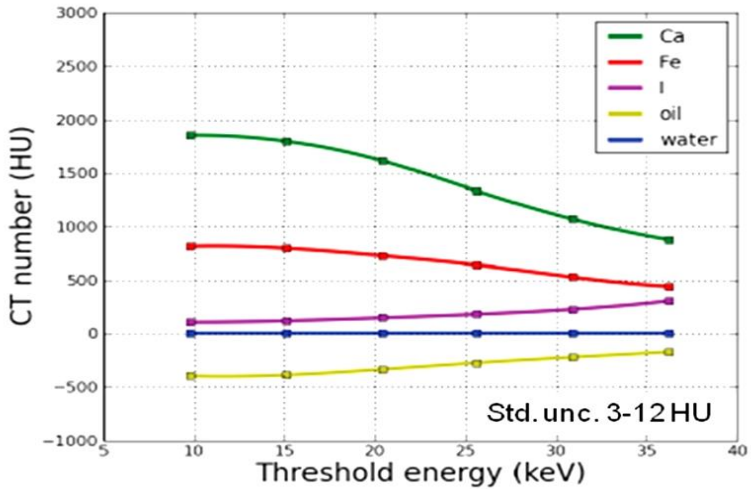

Figure 9.8 *The spectral dependence of the CT values of Ca, Fe, I, oil and water. Additional attenuation measurement obtained at different energies allowing the differentiation of materials.*

9.3.6 Dose measurement

Figure 9.9 shows the relationship between dose rate measured in $mGy.s^{-1}$ and tube current in mA. Phantom and specimen imaging in this study were performed with 50 kVp and 0.5 mA corresponding to a received dose rate of 1 $mGy.s^{-1}$. Increasing the current increases the radiation dose rate proportionally.

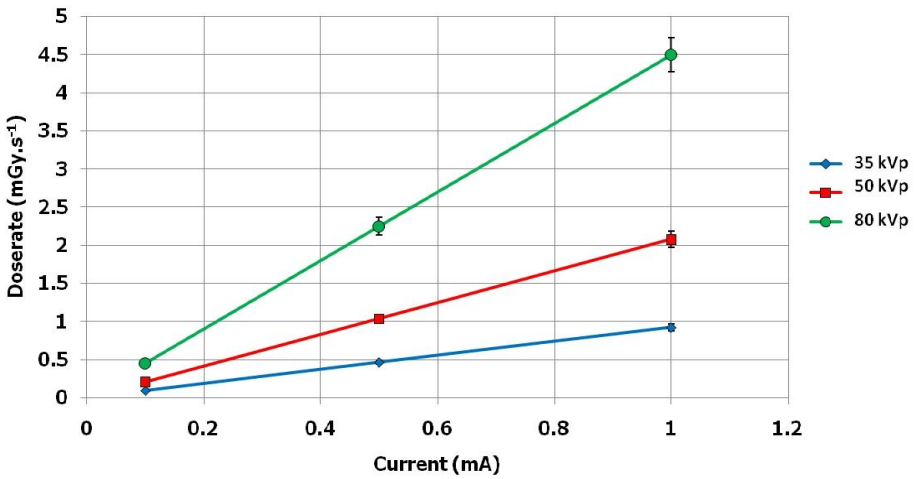

Figure 9.9 *The dose rate measured at the isocentre for different tube voltages as a function of current.*

9.3.7 Demonstration with biological specimens

Two biological specimens were scanned to demonstrate the performance of the MARS-CT3 system. Figure 9.10 shows single slice CT images of a human femoral plaque in resin (Craftsmart liquid gloss, CraftSmart Australia, Glayton North, Australia) and the abdominal region of a euthanised mouse with kidneys enhanced using iodine contrast agent. The mouse was injected with iodine contrast agent into the tail vein and euthanised a few minutes later. These specimens were scanned at 50 kVp with threshold energy of 10 keV. These images show acceptable image quality for soft tissue imaging. The scanning of animal and human tissue was approved by regional ethics committees - Human Ethics (URB/07/02/001) and Animal Ethics (University of Otago Animal Ethics Approval C8/07).

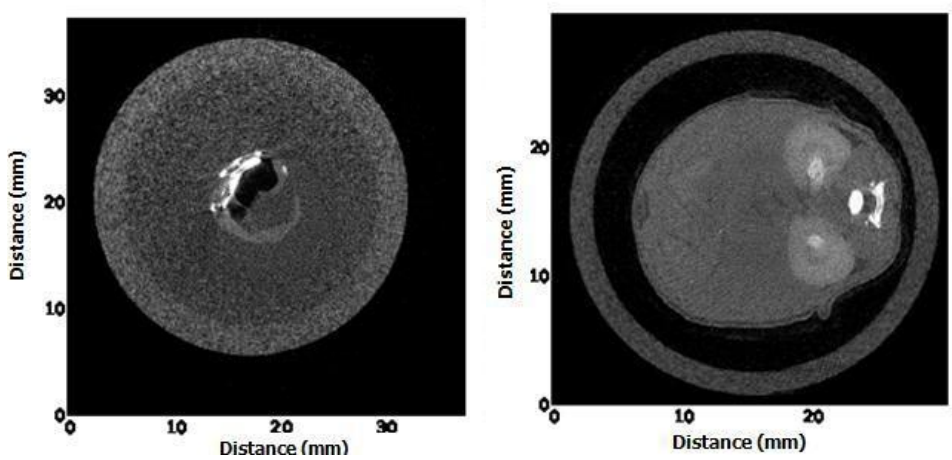

Figure 9.10 *A single slice of femoral plaque in resin and the abdominal region of a euthanized mouse with kidneys enhanced using iodine contrast agent.*

9.4 Discussion

9.4.1 Spatial resolution

Spatial resolution is defined as the size of the smallest possible feature that can be detected by an imaging system. The spatial resolution properties of an imaging system may be described by its MTF. MTF describes the variation of apparent contrast that is recorded by the imaging

system as a function of spatial frequency. As for clinical CT, the spatial resolution of the micro-CT system is affected by various physical parameters such as the focal spot size, the detector element size, the magnification ratio, the reconstruction algorithm and detector resolving power (Holdsworth et al., 1993).

The spatial resolution of the MARS-CT3 system is 110 μm at the magnification ratio of 1.44 is sufficient for pre-clinical examinations such as scans of tissue samples, organs or small animals that are used as models to evaluate human diseases. In atherosclerotic plaque study, this configuration system may not be able to resolve the iron deposits or fine micro-calcification with a single energy measurement (Langheinrich et al., 2009). The detection of iron deposits in the plaque can be differentiated from their morphological features at voxel sizes up to $(200\ \mu m)^3$ with multi-energy measurements (Wang et al., 2010). In this case, the detection of iron deposits in the plaque is not limited to the spatial resolution of the system. However, better spatial resolution might be obtained from the MARS-CT3 system by using a higher magnification ratio or an x-ray tube with a smaller focal spot size.

9.4.2 Image uniformity

The CT number profile through the water phantom is essentially uniform. Ideally, the same attenuation coefficient should be recorded for a homogenous material regardless of the measurement position within a reconstructed slice. However, some systematic effects such as beam hardening that occurs with polychromatic sources cause cupping artefacts in the reconstructed slices and require specific corrections to the data prior to reconstruction (Herman, 1979). The polynomial beam-hardening correction reduces the cupping artifacts and improves the uniformity of CT image.

9.4.3 Pixel noise

Image noise is the random fluctuations of pixel counts in a region that receives the same radiation exposure as another. The statistical fluctuation of CT numbers within a homogenous region of interest contributes to the measurement uncertainties of derived quantities such as linear attenuation and material composition. Statistical noise particularly affects the ability to detect low contrast materials (Lin et al., 1993). The amount of random quantum noise present in the reconstructed image depends on scan parameters such as mAs and ideally other sources of system error should be relatively insignificant (Kalender, 2001).

As expected image pixel noise increases with decreasing tube current. The tube kilovoltage and current affect both image contrast and dose delivered to the object. Therefore, these technical parameters must be selected carefully to provide adequate CNR at minimal dose. A tube voltage of 50 kVp was chosen for this study because the focus is on soft tissue imaging and other studies also used the same tube voltage for this application (Zhu et al., 2009; Zhang et al., 2010). The use of a higher tube voltage would reduce contrast resolution for soft tissues whereas the x-ray flux obtained with lower voltages would be insufficiently penetrating and beam hardening effects would become significant.

The general form of the relation between pixel noise and exposure obtained from our results (Figure 9.5) concur with the established result that image noise is inversely related to the square root of exposure Q (Judy et al., 1977; Lin et al., 1993; McNitt-Gray, 2006). Total measured pixel noise can be written as the quadrature summation of random quantum noise and system noise (Du et al., 2007; Zhu et al., 2009). The systematic component of the noise is given by the intercept (12.6 HU) of Figure 9.5. For low exposure measurements, the contribution from random quantum effects will dominate the total noise of the system whereas

the systematic contribution will limit the performance of the MARS-CT3 system for higher exposures.

9.4.4 Linearity

Linearity is important for quantitative applications such as the analysis of blood clots and calcium deposits in atherosclerotic plaque (Langheinrich et al., 2007; Hyafil et al., 2007), fat or iron in the metabolic syndrome (Luu et al., 2009) and improved detection of microcalcification in breast cancer (Lemacks et al., 2002). These specific tasks require accurate CT numbers to be able to distinguish different types of tissues. The linear range of the MARS-CT3 system operated at 50 kVp extends to approximately 2000 HU which is adequate for most soft-tissue materials. However, the CT numbers of more highly attenuating materials may not be accurately measured by the system in its current configuration.

Optimisation of scanning parameters such as peak voltage and selection of energy bins will be required for acceptable performance in some applications. As well as the beam hardening mentioned above, it can cause an artificial reduction in the measured attenuation values that appear as dark bands or streaks between dense objects. The magnitude of the effect depends on the thickness, density and atomic number of tissues in the ray path (Judy et al., 1977). The Source-Ray x-ray tube used for this work includes filtering equivalent to 1.8 mm aluminium that is designed to remove the low energy portion of the spectrum and thereby reduce beam hardening effects. Nevertheless, beam hardening streaks are evident in the measurements of the calcium chloride linearity phantom (Figure 9.6).

9.4.5 Spectroscopic calibration

Spectral CT imaging is becoming an important pre-clinical technique for determining material types (Schlomka et al., 2008; Anderson et al., 2010). Spectral CT is able to discriminate and

quantify materials according to differences in the energy dependence of their attenuation coefficients. The x-ray attenuation properties are energy and material dependent. The spectroscopic characteristics of CT number measured with the MARS-CT3 system are consistent with the energy dependent attenuation coefficients of the test materials (Ca, Fe, I, oil and water).

At low energies the CT number response for the higher-*Z* materials is much greater than that of water due to the strong influence of the photoelectric effect at these energies. With increasing energy the CT numbers for these materials decrease as the relative contribution of the photoelectric effect reduces and Compton scattering becomes more significant. The CT numbers of the lower-*Z* materials increase with energy. The CT number for iodine increases with energy due to the influence of the K-edge at 33.2 keV. The reference materials within the phantom are relevant to pre-clinical spectral CT research. It is therefore expected that a basis for quantification can be established for the analysis of tissue specimens and small animal models (Zainon et al., 2011).

9.4.6 Dose measurement

The issue of radiation exposure is generally not a problem for in vitro measurements of samples such as surgical specimens or dead specimens. The dose rate measurement at the isocentre of the scanner for specimen and phantom imaging in this study is 1 $mGy.s^{-1}$. This dose rate is acceptable for in vitro imaging of specimens but must be taken into account when imaging live biological systems such as intact specimens and live animals.

The radiation dose depends in tube current (amperage), scan time and tube peak kilovoltage. Findings of our measurements are in good agreement with the expectation that a 50% reduction in mA produces a 50% reduction in dose and it also shows that image noise increases by 40% with this condition. Another aspect that affects radiation dose is the tube

voltage. Increasing the tube voltage increases the intensity and mean energy of the x-ray output thereby increasing the radiation dose rate at the sample. Furthermore, higher energy x-rays are more penetrating and there will be a consequent increase in the intensity of the x-ray flux that passes through the object to reach the detector.

9.5 Conclusions

The performance of the MARS-CT3 scanner has been evaluated. Phantoms were fabricated for evaluation of image quality such as spatial resolution, uniformity, pixel noise, linearity, spectroscopic performance and dose measurement in MARS-CT3 system. The performance of the MARS-CT3 system was found to be acceptable for our soft tissue imaging research applications. System spatial resolution is investigated in terms of MTF and it falls to 10% of its maximum value at a spatial frequency of 8.8 mm^{-1}. This corresponds to a spatial resolution of 110 μm.

The uniformity result from the MARS-CT3 system shows that the CT number profile through the phantom is essentially uniform. The noise variance is inversely related to the reciprocal of exposure. The linear range of the MARS-CT3 system extends to approximately 2000 HU due to the beam hardening effect. It is adequate for most soft-tissue materials but the CT numbers of more highly attenuating materials may not be accurately measured by the system in its current configuration. Corrections for beam hardening and ring artefacts are required for accurate results. Further optimisation of system parameters will be required for specific applications.

The spectroscopic response of CT number is characteristic of the relevant test materials. The received dose rate at the isocentre is 1 $mGy.s^{-1}$ with 50 kVp and 0.5 mA settings. The overall

performance of the MARS-CT3 system is demonstrated in cross-sectional images of human femoral plaque and mice. The image quality is acceptable for soft tissue imaging.

At present, several MARS-CT systems have been developed each with particular improvements in software and hardware. The calibration phantoms used in this study allow these measurements to be repeated for these spectral micro-CT systems on a regular basis as part of a routine quality assurance program.

9.6 Summary

1. The physical performance characteristics of the MARS-CT3 system have been evaluated and found to be acceptable for our soft tissue imaging research applications.

2. Calibration phantoms were used to evaluate various image-quality parameters including spatial resolution, image uniformity, pixel noise, linearity, spectral response and dose rate at the isocentre.

3. The calibration phantoms used in this study allow these measurements to be repeated on a regular basis, as part of a routine quality assurance.

Chapter 10

Material decomposition with spectral CT imaging

This chapter describes the application of a technique for determining material composition using spectral CT imaging. The technique uses linear algebra to model the effective attenuation measured by spectral CT in terms of a number of basis materials. The effectiveness of the method for quantifying components to be found in atherosclerotic plaques with and without additional linear constraints is described. This work involves the evaluation of the system linearity and spectroscopic response. Examples of material decomposition applied to spectral CT images are also given in this chapter. This work has been presented at the World Congress on Technology and Engineering: Bioinformatics and Biomedical Engineering Conference in Shanghai, China (Zainon et al., 2011).

10.1 Introduction

Spectral CT is a new trend in x-ray CT that expands the single energy measurement of CT to multiple energies. The potential to use spectral information from x-ray beams was first reported in the mid 1970s. The early work focused on material decomposition of the linear attenuation coefficient into contributions from the photoelectric process and the Compton effect with two spectrally distinct measurements (Alvarez & Macovski, 1976).

In recent years, the development of spectroscopic photon-counting detectors have opened up new possibilities for improving material-specific imaging with spectral (multi-energy) CT. The signal output in integrating detector is dependent on the energy flux integrated over the entire x-ray spectrum. Therefore, no element-specific attenuation profiles with characteristic

photon energy distributions can be obtained. In contrast, spectral CT with the use of energyresolving photon-counting detectors is capable of extracting quantitative information about the elemental, molecular information of tissues and contrast materials on the basis of their attenuation properties (Schlomka et al., 2008; Anderson et al., 2010; Aslund et al., 2010; Shikhaliev & Fritz, 2011; Wang et al., 2011b).

Quantitative approaches for pre-clinical material decomposition using spectral CT imaging have been published and most of the studies focus on rigorous basis decomposition methods (Firsching et al., 2004; Roessl & Proksa, 2007; Schlomka et al., 2008; Shikhaliev, 2008; Liu et al., 2009; Butler et al., 2011a). Firsching et al. (2004) developed a technique to reconstruct the stoichiometric composition of the material examined with a maximum likelihood estimation approach. This method uses vector space transformations to calculate the effective areal density for each considered material inside the object.

On the other hand, Roessl and Proksa (2007) presented the theory of projection-based material decomposition from energy-binned photon-counting data in imaging K-edge material. The image processing described in this study is based on an extension of the dual-energy method first introduced by Alvarez and Macovski (1976) to a higher number of basis components. They demonstrated this technique using simulated images of an atherosclerotic coronary vessel filled with gadolinium-based contrast agent. The images resulting from the energy-selective measurements and maximum likelihood-based pre-processing showed the differentiation between various basis components including images showing only the contrast agent. In this work, gadolinium was used as contrast agent but other high-Z materials are feasible. A year later, Schlomka et al. (2008) proved the feasibility of spectral CT imaging

to differentiate multi-contrast agents simultaneously with the use of energy discriminating detectors with more than two energy bins.

Three-material decomposition developed by Liu et al. (2009) can measure elemental concentrations and mass fractions under low noise imaging conditions using dual-energy CT. The algorithm is based on mass-conservation and they demonstrate that the proposed method is heavily dependent on the dual-energy ratios of the two elements in the mixture. Factors that affect CT number accuracy such as beam hardening, scatter and the partial volume effect might produce an error in material analysis. In the same case, Kelcz et al. (1979) also reported that errors in material analysis due to errors in CT number measurements may be amplified especially if the dual-energy ratios of the two elements are close. Therefore, they highlighted that the most critical factor in material mass-fraction decomposition is the difference in dual energy ratios of the two elements in the tissue.

Butler et al. (2011a) demonstrated that spectral CT imaging can differentiate multiple contrast agents and background tissues in the intact non-living mouse using PCA. The goal of PCA is to identify linearly independent patterns of variance within a data set. The analysis is performed on acquisitions taken of the same object in different spectral bands. The PCA method leads to a representation of the data in several components that span a majority of the variance. Results show that it allows the separation of spectral data into different channels: background tissues and different contrast agents. This implies that multiple radiographic contrast materials could be given at different time points of an examination but imaged at a single phase.

In this work, a linear algebra technique is proposed to decompose spectral CT images into basis material images and thereby differentiate atherosclerotic plaque components.

The MARS-CT3 scanner has been calibrated experimentally with phantoms containing known solutions of clinically relevant materials and the resulting spectroscopic CT data analysed to determine the feasibility of the proposed analysis method.

10.2 Theory

CT numbers are effective linear attenuation values measured in reconstructed voxels and scaled (Brooks, 1977) so that by definition CT_{air} = -1000 HU and CT_{water} = 0 HU.

$$CT = \frac{\mu - \mu_{water}}{\mu_{water} - \mu_{air}} 1000 \tag{10.1}$$

The CT number measurements can be transformed into values that are directly proportional to the attenuation coefficients of the unknown materials. For $\mu_{\text{air}} << \mu_{\text{water}}$ we obtain:

$$z = 1 + \frac{CT}{1000} \approx \frac{\mu}{\mu_{water}} \tag{10.2}$$

In cases where beam-hardening and scattering are negligible Beer's Law applies and the effective linear attenuation coefficient of a mixture of material components x_i, $i = 1 \ldots M$ is the sum of the attenuation coefficients for the individual components.

$$z = \frac{\Sigma_i \mu_i x_i}{\mu_{water}} \tag{10.3}$$

Measuring the CT numbers of a set of material components at multiple energy thresholds $j = 1 \ldots N$ allows us to write a linear matrix equation for the transformed variables $[z_j]$ in terms of the (unknown) composition $[x_i]$ and a spectroscopic calibration matrix **A** with errors which ϵ we will assume follow a Gaussian distribution:

$$\boldsymbol{z} = \mathbf{A} \cdot \mathbf{x} + \epsilon \tag{10.4}$$

Constraints can be built into the expression above by augmenting it with additional linear equations. From an initial estimate of the composition $\mathbf{x_0}$ and its covariance $\mathbf{P_0}$, the optimal solution (Rodgers, 1996) for the updated composition $\mathbf{x_1}$ and covariance $\mathbf{P_1}$ given a measurement $\mathbf{z}$ with covariance $\mathbf{C_z}$ is:

$$\mathbf{P_1} = \left(\mathbf{A}^\top {\mathbf{C_z}}^{-1}\mathbf{A} + {\mathbf{P_0}}^{-1}\right)^{-1} \tag{10.5}$$

$$\mathbf{x_1} = \mathbf{x_0} + \mathbf{P_1} \cdot \mathbf{A}^\top {\mathbf{C_z}}^{-1}(\mathbf{z} - \mathbf{A} \cdot \mathbf{x_0}) \tag{10.6}$$

The effectiveness of the measurement may be measured by the reduction in information entropy, δH, of the covariance matrix $\mathbf{P_1}$ and by the increase in the effective number of degrees of freedom of the system. The information entropy is a logarithmic measure of the volume of the uncertainty covariance with change after measurement given by:

$$\delta H = \frac{1}{2}\left(\log(\det(\mathbf{P_1})) \ - \log(\det(\mathbf{P_0}))\right) \tag{10.7}$$

The effective number of degrees of freedom for the fitted composition measures the number of components recovered by the measurement and is given by the trace of the *hat* matrix:

$$\nu = \mathrm{tr}\left(\mathbf{A}^\top \mathbf{P_1} \mathbf{A}^\top \ {\mathbf{C}_z}^{-1}\right) \tag{10.8}$$

10.3 Materials and Methods

10.3.1 Spectral CT system

The MARS-CT scanner comprises a Source-Ray SB-80-1K micro-focus x-ray tube (Source-Ray Inc., Ronkonkoma, New York) and a Medipix3 detector within a rotating gantry driven by computer-controlled stepper motors. The Medipix3 photon-counting detector is bump bonded onto a 300 µm thick silicon sensor layer and configured in 55 µm fine-pitch mode.

The CT gantry has the facility for providing variable magnification via movable camera and source platforms. For this work the source-to-detector and source-to-object distances were held constant to provide a magnification factor of 1.44 and a CT reconstruction voxel size of $(38\ \mu m)^3$.

The measurements were performed at 50 kVp and 0.5 mA with detector exposure times that were chosen to give approximately 2000 counts per pixel in open beam. Large area projection images at each angle were obtained by moving the detector and tiling the individual images in software. Flat-field measurements for each detector position were taken before and after the sample scan to compensate the variations in detector performance over the duration of the scan. The raw projection data obtained were then corrected and normalised using a combination of the initial and final flat-field projection images. Frames were stitched to form large area projections and sinograms formed from the normalised data before reconstructing the CT slices using the Octopus commercial CT reconstruction software (Dierick et al., 2004).

10.3.2 Linearity

A perspex phantom of 10 mm diameter containing aqueous calcium chloride solutions of various concentration 74.9, 147.2, 294.0 ad 735.0 mg ml^{-1} was used to evaluate the linearity of the system response with calcium concentration. It was scanned at 50 kVp with threshold energy of 12.3 keV. The CT number and standard deviation for each concentration were measured in Hounsfield units for an ROI placed manually over each solution insert. The relationship between CT number and calcium chloride concentration was determined by linear regression analysis.

10.3.3 Spectroscopy

A perspex phantom of 10 mm diameter containing ferric nitrate, calcium chloride, sunflower oil, iodine, air and water was used to evaluate the spectroscopic CT number response for different materials. The phantom was scanned at 50 kVp with threshold energies of 9.8, 15.1, 20.4, 25.6, 30.9 and 36.2 keV. The CT number and standard deviation for each material were measured in HU for an ROI placed manually over each solution insert. The relationship between CT number and detector threshold energy was evaluated graphically.

10.3.4 Materials Analysis

The spectroscopic CT number response for each material was transformed as described above to be proportional to the material attenuation coefficient. For sunflower oil and water the response was expressed in terms of a unit volume of the liquid at room temperature. For the dissolved species (Ca, Fe, I) we expressed the response in terms of the attenuation of the species alone.

$$A_{ij} = \frac{CT_{ij}}{1000} + 1 \text{ for water and oil} \tag{10.9}$$

$$A_{ij} = \frac{1}{C}\frac{CT_{ij}}{1000} \text{ for dissolved species} \tag{10.10}$$

where C is the molar concentration of the dissolved species.

Response matrices were assembled for measurement scenarios with different sets of unknowns: (i) {Ca, Fe, Oil, Water}; (ii) {I, Oil, Water}; (iii) {Oil, Water}. An optional volume conservation constraint was also included: $V_{oil} + V_{water} = constant$. The change in information entropy and the number of degrees of freedom obtained were calculated for measurements using up to six energies for both the constrained and unconstrained systems of

equations. The initial state of uncertainty (covariance matrix) before measurement was defined to be $\mathbf{P_0} = \mathbf{I}$. For each scenario the expected covariance matrix after measurement $\mathbf{P_1}$ was calculated using the appropriate response matrix **A** and an input data covariance matrix $\mathbf{C_z}$ computed assuming standard measurement uncertainties of 10 HU on the CT number data.

The change in information entropy after a set of measurements was computed from the determinant of the updated covariance matrix $\mathbf{P_1}$:

$$\delta H = \frac{1}{2}\log(\det(\mathbf{P_1})) \tag{10.11}$$

The number of degrees of freedom of the system after a set of measurements was computed from the trace of the *hat* matrix as described previously.

10.4 Results

10.4.1 Linearity

Figure 10.1 shows a CT reconstruction of the linearity phantom and the graph of CT number as a function of increasing calcium chloride concentration. The result of the linear regression shows that the system is linear over the range of concentrations to at least 294.0 mg.ml^{-1} with R^2 of 0.997. It is not linear up to the highest concentration of calcium chloride (735.0 mg.ml^{-1}).

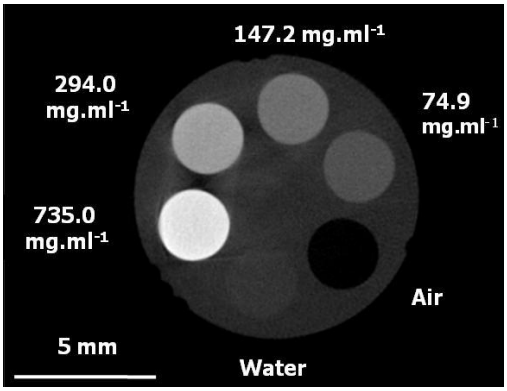

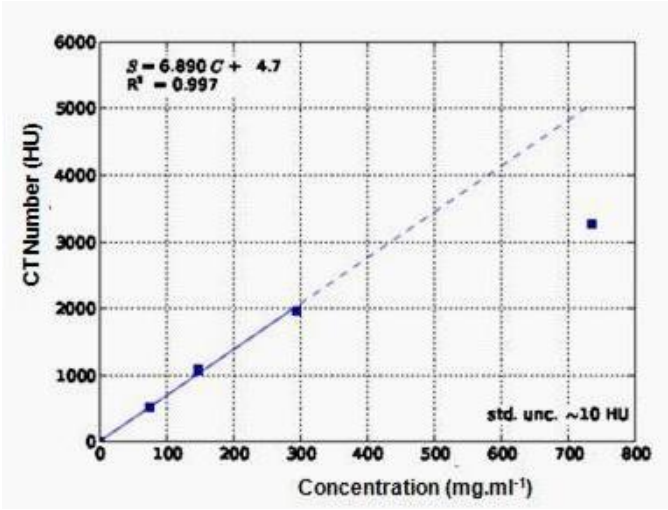

(a) (b)

Figure 10.1 *(a) A reconstructed CT image of the perspex phantom with solutions of different concentrations of calcium chloride acquired with a threshold energy of 12.3 keV and a tube voltage of 50 kVp. (b) The measured CT numbers as a function of concentration. There is a linear increase in attenuation with increasing calcium chloride concentration to ~300 mg.ml^{-1} corresponding to a CT number of ~2000 HU (R^2 = 0.997). The standard uncertainties for the measured data are in the range 10 HU.*

10.4.2 Spectroscopy

The CT reconstructions for all six energy thresholds are shown in Figure 10.2. The higher-*Z* materials such as Ca and Fe show stronger decreases in attenuation than that of water, with increasing energies due to strong influence of the photoelectric effect at lower energies. As the energy increases the relative contribution of the photoelectric effect reduces and Compton scattering becomes more significant.

The iodine solution exhibits strong attenuation at 33.2 keV due to the influence of the K-edge of iodine and this can be seen on the CT images and on the spectral graph (Figures 10.2 and 10.3). The light materials (lower density) such as oil, water and perspex have larger hydrogen content and the attenuation of these materials is dominated by Compton scatter.

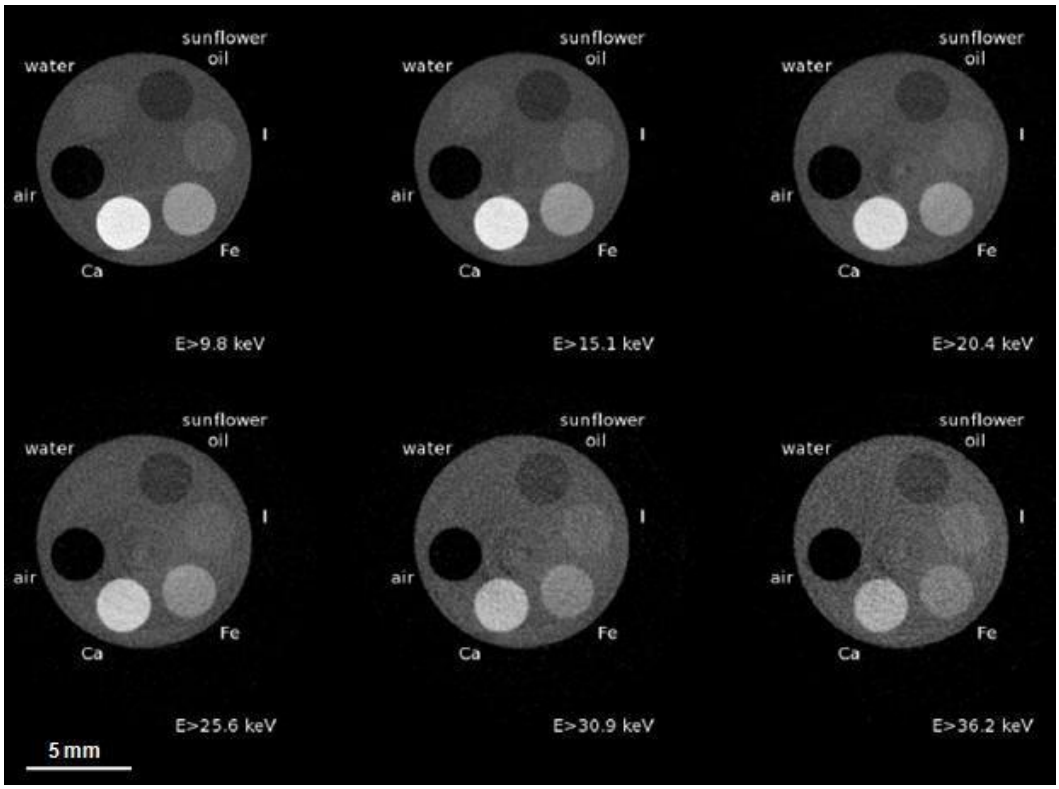

Figure 10.2 *Spectral CT reconstructions of a perspex phantom containing Ca, Fe, oil, water and air. Data were acquired with a tube voltage of 50 kVp and six threshold energies.*

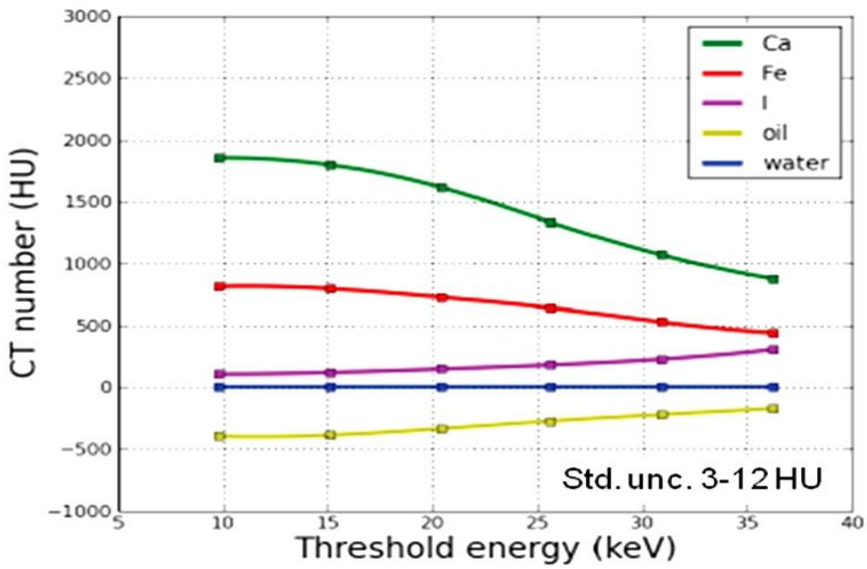

Figure 10.3 *The material-specific CT numbers of materials tested (Ca, Fe, I, oil and water) plotted versus photon energy. The spectroscopic response to the materials tested is consistent with the energy dependent attenuation coefficients for those materials. The standard uncertainties for each data point are 10 HU.*

10.4.3 Material analysis

Results from linearity and spectral analysis demonstrate that the response of the CT system is approximately linear up to ~2000 HU for our sample size and it can measure the spectroscopic response for different materials of interest effectively. Therefore, quantification of materials of interest within atherosclerotic plaques can be performed with this system. The cumulative information entropy and the number of degrees of freedom after a sequence of up to six measurements at different threshold energies for both the unconstrained and constrained systems of equations are given in Figure 10.4.

The unconstrained measurements of {Oil, Water} recover two degrees of freedom after the first three spectroscopic measurements have been made. The full number of degrees of freedom for the {I, Oil, Water} case are recovered only after six spectroscopic measurements. For the constrained system, the full number of degrees of freedom for these two scenarios is quickly recovered after only the first and third spectroscopic measurements respectively. The full number of degrees of freedom for {Ca, Fe, Oil, Water} are never recovered with either system of equations. In all cases the information entropy is significantly improved by the use of volume constraints.

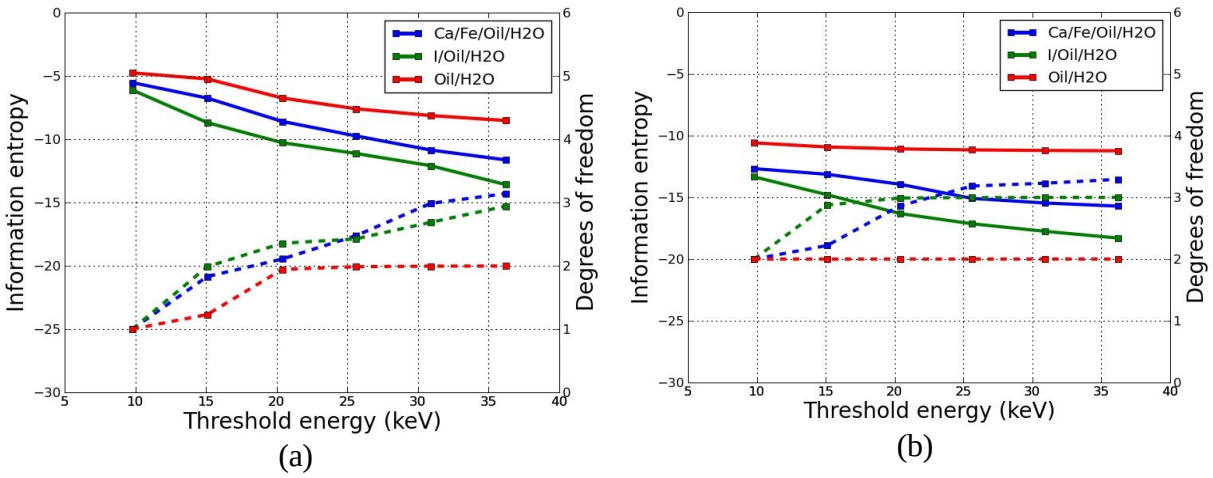

Figure 10.4 *(a) The cumulative information entropy (solid lines) and number of degrees of freedom (dashed lines) retrieved by a sequence of spectral CT measurements for an unconstrained system. (b) The cumulative information entropy and number of degrees of freedom for a system including volume constraints on oil and water.*

Figure 10.5 shows the CT images of basis materials obtained from the proposed technique. The materials were decomposed into four basis functions: high-*Z*, K-edge (iodine), low-*Z* and water. The high-*Z* image is dominated by the photoelectric effect and Fe and Ca are the most prominent in the high-*Z* image. Iodine is distinguished from the other high-*Z* materials by its K-edge and it is shown separately in the K-edge image. The Compton effect is more dominant in the low-*Z* image and this distinguishes oil and the perspex. The water image is characterised by the contributions of both Compton and photoelectric effects and water is most visible in this image. The basis material decomposition can distinguish high-*Z* material, low-*Z* material and K-edge material in the reconstructed images from spectral information. However, the method is unable to distinguish Fe and Ca independently in the energy range of interest.

As can be seen in the images, there are some ring and beam hardening artifacts. The ring artifacts are due to pixel-to-pixel variations of the threshold positions while the beam hardening effects appear on the reconstructed image as streaks and shadows.

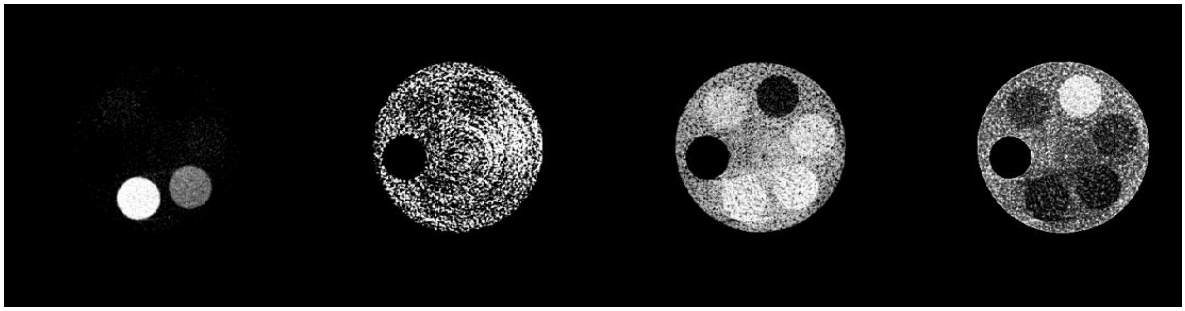

(a) (b) (c) (d)

Figure 10.5 *Material-selective images obtained from the proposed technique. (a) Fe and Ca, (b) K-edge material (iodine), (c) water and (d) oil images.*

10.5 Discussion

In this study, we demonstrated that multi-material decomposition is experimentally feasible with our Medipix3 energy-resolving photon-counting detector. Recently there has been a noticeable trend towards quantitative micro-CT imaging (Schladitz, 2011). Our spectral micro-CT scanner with energy-resolving photon-counting detector takes advantage of the detector capability to produce basis material images with spectral CT measurements. This evaluation was performed with phantoms containing surrogates for materials found in atherosclerotic plaque. The system linearity and spectral analysis were evaluated before performing basis material decomposition. The linearity measurements indicate that the system response is linear up to ~300 $mg.ml^{-1}$ of calcium chloride corresponding to a CT number of ~2000 HU. The beam hardening effects limits the linearity of the system at higher concentrations.

The spectroscopic response to the materials tested (Ca, Fe, I, oil and water) is consistent with the energy dependent attenuation coefficients for those materials. At low energies the CT number response for the higher-*Z* materials is much greater than that of water due to the strong influence of the photoelectric effect at these energies. With increasing energy the CT numbers for these materials decrease as the relative contribution of the photoelectric effect reduces and Compton scattering becomes more significant. The CT number for iodine increases with threshold energy due to the influence of the K-edge at 33.2 keV.

The spectral measurements contain information about the spectral dependence of the x-ray absorption in the object and can be used to extract information about elemental composition of the object. Using the volume constraint based algorithm described in this study, we demonstrate that the linear method for materials analysis performs well for up to three materials {Ca/Fe, Oil, Water}. In the absence of a K-edge, the effective atomic numbers and densities are the keys to distinguishing these materials. The effective atomic number and density determine the relative contributions of the photoelectric and Compton effects. The energy dependence of the resulting attenuation curves forms the basis for separating these materials.

Alternatively, with the presence of K-edge material, the linear method for material analysis can categorised materials into four categories: K-edge material (e.g., iodine), high-*Z* materials (e.g., Ca, Fe), low-*Z* materials (e.g., oil) and others (e.g., close to water). In this case, the material with K-edge features readily identifiable K-edge effects in the energy range of interest and demonstrates different energy dependence from those without K-edges. Thus, this phenomenon facilitates the material separation in the energy range investigated.

The most significant limitation found in this study is the inability to simultaneously distinguish the four material unknowns: Ca, Fe, oil, and water. The material analysis is unable to return the full number of degrees of freedom even with the use of six energy thresholds. The differentiation of Fe from Ca is more challenging because neither material has a K-edge within the energy range investigated and exhibit then similar Compton and photoelectric contributions to their attenuation coefficients over the energy range investigated. The proposed algebra technique can be used to distinguish the atherosclerotic plaque components such as differentiation of lipid from the soft tissues. However, to distinguish both Fe and Ca may require further work to investigate the impact of additional energy thresholds and/or alternative constraints such as mass conservation (Liu et al., 2009).

A lesser problem is the appearance of some ring and beam hardening artifacts on the reconstructed images. These artifacts in the reconstructed spectral CT images propagate through to the differentiated material images. Image quality must be improved to reduce this problem.

10.6 Conclusions

The linearity of the MARS-CT system and the calibration of spectroscopic response for different materials of interest have been evaluated prior to material quantification analysis. Results from these measurements indicate that spectral CT can be applied to a range of materials found in atherosclerotic plaques up to approximately 2000 HU. Material analysis is viable using the proposed linear algebra method for a number of material combinations and the efficacy of the method is improved with the use of appropriate volume constraints. However the method may not be able to simultaneously distinguish Fe, Ca, oil and water without additional data or constraints.

10.7 Summary

1. Over the range of clinically relevant energies, x-ray attenuation is caused by the combination of the photoelectric and Compton effects. These two mechanisms are both energy and material-dependent. Material differentiation and elemental decomposition is therefore possible with spectral CT.

2. The linearity and spectroscopic response of the MARS-CT system was found to be acceptable for atherosclerotic plaque material decomposition. The linear algebra technique proposed in this study is able to quantify materials such as {Oil, Water}, {I, Oil, Water}, {Ca, Oil, Water} and {Fe, Oil, Water}. The efficacy of the method is improved with the use of appropriate volume constraints.

3. For the case of four material unknowns {Ca, Fe, Oil and Water}, this study shows that the analysis needs additional information or constraints to independently distinguish these materials.

Chapter 11

Characterising ex vivo human carotid arteries with the MARS-CT3

This chapter presents a study of the potential of the MARS-CT3 scanner for characterising ex vivo atherosclerotic plaques. The results of the spectral CT examinations are compared to histology. The first section of this chapter presents a phantoms study designed for evaluating the parameters for ex vivo atherosclerotic plaque imaging. It is followed by a description of the methods for preparing specimens, specimen imaging, image processing, image analysis and histological examination. The analysis and results of the experimental work are then presented in the following section. This chapter also describes the limitations of this study. The findings of this study are given in the conclusion. The final section summarises the main points of this chapter.

11.1 Introduction

The morphological features and composition of atherosclerotic plaque have been suggested as a complement to luminal narrowing for assessment of plaque vulnerability (Ross, 1999). The presence of lipid or haemorrhage in carotid plaques has been shown to be a risk factor for producing carotid occlusion (Bornstein et al., 1990). Carotid artery plaques with a large lipid core are also considered to represent an increased risk for stroke. The vulnerable plaque is considered to be a plaque with less calcification but with substantial fibrous and lipid components. The non-invasive identification of high-risk or vulnerable atherosclerotic plaques is one of the ultimate goals of imaging. It would dramatically improve risk

stratification of both symptomatic and asymptomatic patients. Primary prevention includes changes in lifestyle or drug therapy especially in patients at high risk of a cardiovascular event (Pasterkamp et al., 2000).

Previous studies have shown that non-invasive in vivo imaging of atherosclerotic plaques holds promise for clinical decision-making and treatment. Multiple non-invasive imaging modalities such as CT (De Weert et al., 2006) and MRI (Larose et al., 2005; Yuan et al., 2006) have been used to detect and classify plaque either in vivo or experimentally. Current clinical CT systems cannot identify iron deposits as a marker of intraplaque hemorrhage (Knollman, 2008). These limitations are due to lack of spatial resolution. At the required resolution, most clinical CT systems suffer from the partial volume effect due to the large detector pixel size compared with the small hemorrhage deposits ($(10\ \mu m)^3$ to $(100\ \mu m)^3$) in human atherosclerotic plaque (Langheinrich et al., 2007). Calcified plaque characterisation is also impaired by beam-hardening artefacts.

A major challenge in using iron as an imaging marker of vulnerable plaque is the co-localisation of iron and calcium deposits. It is difficult to detect and distinguish these two components using low resolution conventional CT systems equipped with standard integrating detectors. However, differentiation of iron deposits from co-localised calcium as a marker for hemorrhage inside individual plaques might be possible using spectral CT. The multiple energy datasets measured by spectral CT allow material differentiation according to their spectroscopic attenuation properties.

Secondly, the iron deposits in vulnerable plaque are very small. Therefore, the detection of iron deposits requires high spatial resolution. Although haemorrhage has been detected in mouse atherosclerotic plaques using dual-energy micro-CT (Langheinrich et al, 2007) and

MRI (Chu et al., 2004), in general, vulnerable plaques in humans are unable to be detected using current imaging techniques. Moreover, the use of MRI is expensive and time consuming, and not sufficiently available for population-wide use.

Recently, the development of new targeted nanoparticle contrast agents has led to molecular imaging of specific plaque components (Cherry, 2004). The nanoparticle contrast agents are usually used to detect the plaque inflammation. However, there are several challenges in this field including the lack of standardised evaluation of new CT contrast agents, the cost of the agents and the need to prove the biocompatibility (Cormode & Fayad, 2011). It has been suggested that studies must be performed to evaluate the toxicity and excretion rates of these agents.

This study focuses on the ex vivo evaluation of atherosclerotic plaque components, particularly lipid and hemorrhage, by spectral micro-CT imaging (using the MARS-CT3 without a contrast agent) in comparison with histology. The aim of this work was to demonstrate that images acquired from energy resolved photon-counting detectors contain the requisite information to allow separation of specific materials of interest. Limitations in preliminary studies of atherosclerotic plaque imaging with the MARS-CT2 were overcome by improving the imaging parameters with the MARS-CT3.

This study was designed as follows. Firstly, the imaging parameters and performance of the MARS-CT3 scanner were evaluated using a phantom dataset designed for assessment of ex vivo atherosclerotic plaque. Secondly, the determination of the sensitivity for separating iron and calcium was performed by evaluating the dual-energy ratio difference between iron and calcium. Thirdly, the imaging protocol of ex vivo atherosclerotic plaques with the MARS-CT3 was developed based on results obtained from phantom studies. Finally, material

specific images were reconstructed from spectral CT images using the linear basis technique and validation was performed by histology.

11.2 Materials and Methods

11.2.1 Evaluation of imaging parameters

The evaluation of suitable imaging parameters for unfixed (fresh) ex vivo carotid atherosclerotic plaque with the MARS-CT3 scanner equipped with a Source-Ray SB-80-1K micro-focus x-ray tube (Source-Ray Inc., Ronkonkoma, New York) and quad Si Medipix3 detector was performed by phantom studies. Several assessments were performed with calibration phantoms including evaluation of the effects of the number of projections, tube voltage and detector energy thresholds on image quality, and the sensitivity for separating iron and calcium. A 5 mm diameter perspex phantom was imaged with different numbers of projection angles to determine a suitable number of projection angles to be used for ex vivo atherosclerotic plaque imaging. This calibration phantom was scanned at 50 kVp with 125, 250, 500 and 1000 projections. It was imaged with a threshold energy of 10 keV.

The evaluation of the best tube voltage for specimen imaging was performed with a multi-contrast phantom. A 10 mm diameter perspex phantom was prepared containing sunflower oil, 3 $mg.ml^{-1}$ of iodine Ultravist 300 (Bayer Schering Pharma, Berlin), 50 $mg.ml^{-1}$ of ferric nitrate, 200 $mg.ml^{-1}$ of calcium chloride, air and water. The diameter of each insert was 2 mm. This calibration phantom was scanned with four threshold energies, 10, 16, 22 and 28 keV, at three tube voltages: 35, 50 and 80 kVp.

The same phantom was used to determine the sensitivity for separating iron and calcium with the MARS-CT3 scanner. The phantom can be considered clinically relevant for ex vivo studies because the diameter matches the average diameter of the human artery. The

sensitivity was evaluated by measuring the difference in dual-energy ratios between iron and calcium in the 10 mm multi-contrast phantom for different tube voltages.

The spectral CT analysis of materials that mimic atherosclerotic plaque components were evaluated using the spectral CT images of the multi-contrast phantom. An ROI was drawn on the CT images for each material insert and for each ROI, the mean CT number and standard uncertainties were measured. The mean CT numbers of each material were plotted against threshold energy for each selected tube voltage.

11.2.2 Preparation of atherosclerotic plaque imaging

The excised carotid atherosclerotic plaques obtained from surgery were placed in specimen containers on dry ice. For primary plaque imaging, the plaques were placed in a 15 mm diameter polypropylene tube and imaged using the MARS-CT3 scanner. The primary plaque imaging was performed to choose the optimal slice locations that have low levels of calcification and no major calcification deposits. This was important as the calcification might cause difficulty during plaque sectioning.

For plaque sectioning, the plaques were sliced into 3 mm segments using a hand held microtome blade in a 4 °C fridge. Cut points were determined by CT imaging. Each cut surface was photographed at high resolution by the biology photography technician. Each segment was placed in a 15 mm diameter of polypropylene tube and imaged using the MARS-CT3 scanner. The plaques were returned to the -80 °C freezer while the CT data were processed. Then, the sectioned plaques were stained for histological examination.

11.2.2.1 Ex vivo MARS-CT3 imaging protocol of the excise carotid atherosclerotic plaque

The calibration phantoms and unfixed (fresh) plaques were scanned with the MARS-CT3 equipped with a quad Medipix3 detector bump-bonded to a 300 μm Si sensor layer. It has 512 × 512 pixels with 55 μm pitch. This scanner used a Source-Ray SB-80-1K micro-focus x-ray tube (Source-Ray inc, Ronkonkoma, NY) with a 33 μm focal spot, a tungsten anode and 1.8 mm of aluminium (equivalent) intrinsic filtration. The tube voltage and x-ray beam current were set to 50 kVp and 0.5 mA respectively. Exposure times were chosen to give approximately 2000 counts per pixel in open beam.

The best imaging parameters were chosen from the calibration phantom imaging results. For primary imaging, two excised carotid atherosclerotic plaques were scanned with 250 projection angles at 50 kVp and energy of 10 keV. For spectroscopic measurements, the plaque segments were scanned at 50 kVp with four threshold energies: 10, 16, 22 and 28 keV. The magnification factor was set to 1.58 and the isotropic voxel size was $(38\ \mu m)^3$. Frequent flat-field measurements were taken to compensate the variations in detector performance over the duration of the scan.

Two designs of cooling chamber were evaluated for keeping the specimens cool during the scan. The first cooling chamber was made of polystyrene (Figure 11.1(top)). This chamber can be filled with 500 ml of liquid nitrogen. The cool gas evaporating from the chamber was delivered to the specimen via a tube. After several trial scans, it was determined that this chamber did not provide adequate cooling over the full duration of the scan. The liquid nitrogen remained in the chamber for approximately 45 min. A second cooling chamber was created as shown in Figure 11.1 (bottom). A steel thermos was used to keep liquid nitrogen. A bolt was attached through the cap of the cooling chamber for thermal conduction and a vent-

hole added to prevent pressurisation. The specimen sample bottle was attached to the bolt to act as a cold-chamber for the sample. The second cooling chamber was able to keep the specimens cool for approximately 90 min.

Figure 11.1 *Cooling chambers used for keeping the specimens cool during imaging. (Top) The first cooling chamber could be filled with 500 ml of liquid nitrogen and remained cold for approximately 45 min. (Bottom) The second design of cooling chamber also contained 500 ml of liquid nitrogen but remained cool for approximately 90 min.*

11.2.2.2 MARS-CT3 image processing

The raw projection images of calibration phantoms were corrected and normalised using flat-field images. The raw projection images of the excised carotid atherosclerotic plaques were corrected and normalised using a combination of consecutive flat-field images. The gaps between the individual Medipix3 detectors were interpolated by nearest-neighbour interpolation. The physical gap between adjacent ASICs was about 4 pixels and the pixels on the edges of the ASIC were unusable due to their high sensitivity resulting in a total gap to be interpolated of approximately 6 pixels. The sinograms were filtered to reduce ring artifacts. After pre-processing, the CT slices were reconstructed using the Octopus commercial CT reconstruction software (Dierick et al., 2004). The reconstructed calibration phantom images were stacked and averaged to represent a slice thickness of 1 mm.

The plaque segments have an irregular shape at the cutting edge. This makes the correlation between CT image, plaque photograph and histology difficult as a single CT reconstructed slice does not match the shape of the cutting edge of the plaque. The top row of Figure 11.2 shows the irregular cutting edge of the carotid atherosclerotic plaque. Slice A shows the first slice, slice B presents the next few slices of the plaque and slice C shows the surface of the plaque. The bottom row shows the corresponding CT images. The images at slice A and slice B do not match the cutting edge of plaque at C that is required for image correlation between the MARS-CT3 images, plaque photograph and histology. Therefore an irregular surface 'slice' image was reconstructed from the data set to visualise the tissue voxels on the plaque surface. The voxel size for the surface 'slice' images was the same as that of the axial CT slices.

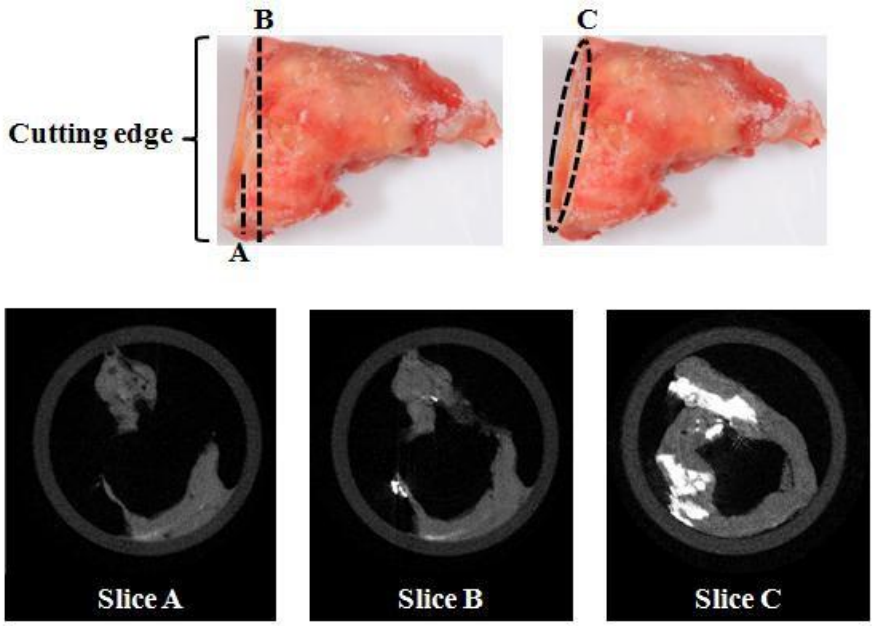

Figure 11.2 *The cutting edge of the plaque segment and the corresponding CT reconstructed slices. The surface 'slice' image (Slice C) shows the surface of the plaque exposed by the histological cutting C.*

11.2.2.3 Image analysis

Both calibration phantoms and specimen images were calibrated in HU using air and water references. The water reference was obtained from the calibration phantom scanned prior to specimen imaging. The evaluation of the effect of the number of projection images on image noise were performed by evaluating the image noise in the images reconstructed from 125, 250, 500 and 1000 projections.

The determination of the best tube voltage for specimen imaging were performed by comparing the image contrast of different materials in calibration phantoms at 35, 50 and 80 kVp. The CNR is defined as:

$$CNR = \frac{\mu_{detail} - \mu_{background}}{\sqrt{\sigma^2_{detail} + \sigma^2_{background}}} \tag{11.1}$$

The dual-energy ratio determines the contrast between two materials at different energies. The dual-energy ratio of iron and calcium solutions in a multi-contrast phantom is computed by dividing the mean CT numbers of the low-energy dataset by the mean high energy CT value:

$$\text{Dual energy ratio} = \frac{\text{CT Number}_{\text{Low keV}}}{\text{CT Number}_{\text{High keV}}} \tag{11.2}$$

The ability to discriminate between different materials in spectral CT imaging depends primarily on the relative difference in dual-energy ratios (Wang et al., 2010). In this case we define the relative difference as the difference in the dual-energy ratio between calcium and iron divided by the average of the dual-energy ratio for these two materials. The evaluation of the relative difference in dual-energy ratio can be used to improve the performance of

material-specific spectral CT imaging by selection of suitable energy ranges. The percentage dual-energy ratio difference for any specific pair of energies is expressed as:

$$\text{Dual energy ratio difference} = \frac{\text{Dual energy ratio}_{Ca} - \text{Dual energy ratio}_{Fe}}{\text{Dual energy ratio}_{Ca} + \text{Dual energy ratio}_{Fe}} \text{ x 2 x 100} \qquad (11.3)$$

The dual-energy ratio difference of iron and calcium were plotted and evaluated for each possible combination of energy used in this study. This was repeated for each different tube voltage.

The excised carotid atherosclerotic plaque components were decomposed using the material decomposition technique as described in Chapter 10. Validation of the specimen images was by histological analysis.

11.2.3 Ex vivo histological processing of carotid endarterectomy specimens

The gold standard for validation of the MARS-CT3 images is histological examination after processing the plaque sections with common staining techniques. The plaque sections were stained with modified Von Kossa, Perls Prussian Blue and Oil-red-O to identify calcium, iron deposits and lipid respectively. The modified Von Kossa, Perls Prussian Blue and Oil-red-O staining protocols used were taken from the protocol database (Protocol database, 2011). This work was performed by biochemists under the supervision of Dr Nicola Scott.

The plaque segments were re-photographed prior to plaque staining. For Von Kossa calcium staining, the plaque segments were immersion fixed for 3 min in 10% neutral buffered formalin then rinsed in several changes of distilled water. The plaque segments were then incubated in 1% silver nitrate solution under ultraviolet light for 20 min. The plaque segments were rinsed in several changes of distilled water followed by 5 min in 5% sodium thiosulfate

solution to remove any unreacted silver nitrate. After further rinsing in distilled water, the plaque segments were photographed.

The plaque segments were stained for iron using a Perls Prussian blue mixed method. After rinsing with distilled water, the plaque segments were immersed in a solution containing equal parts ferrocyanide (2% solution) and hydrochloric acid (2% solution) for 10 min. The plaque segments were then rinsed in several changes of distilled water and photographed for the co-localisation of calcium and iron deposits.

Finally the plaques were stained for the presence of lipid with Oil-red-O. The plaque segments were immersed for 10 min in freshly filtered Oil-red-O working solution. The Oil-red-O working solution was made by combining three parts saturated stock solution with two parts distilled water and filtering through a syringe-driven filter unit. The syringe had a 0.22 µm pore. The plaque segments were then rinsed in several changes of distilled water and finally photographed for the combined co-localisation of calcium, iron and lipid.

11.2.3.1 Postprocessing of ex vivo spectral micro-CT images and histological sections

After sectioning the plaque, the ex vivo MARS-CT3 images were registered to the histological sections by scaling, translation and rotation transformation with ImageJ 1.44p software (National Institutes of Health, USA). The translation and rotation were adjusted to match the orientations of the CT slice and corresponding histological sections. The surface slice images obtained from the MARS-CT3 scanner were matched with the plaque photographs and histology by observing the overall morphological features of the plaques.

11.3 Results

11.3.1 Phantom study

11.3.1.1 Determination of number of projections

A 5 mm perspex phantom was used to evaluate the image noise at different numbers of projection angles. The image noise is defined as the measured standard deviation of pixel grey-scale values in the homogenous perspex phantom. This image noise can be influenced by a large number of technical parameters used in the scan including the tube current and exposure time (tube current-time product or mAs setting), peak tube voltage, reconstruction filter, detector efficiency and focal spot size.

This study was conducted to evaluate the image noise at different numbers of projection angles with other technical factors held constant. This image noise evaluation is important particularly for viewing low-contrast soft-tissue structures. The trade-off between scanning time and image noise required for this particular task was then considered.

Figure 11.3 shows the results from imaging the perspex with 125, 250, 500 and 1000 projections. The CT reconstructed image noise increases with decreasing numbers of projections. The standard deviation obtained from reconstructing with each number of projections was recorded and plotted against number of projections as shown in Figure 11.4.

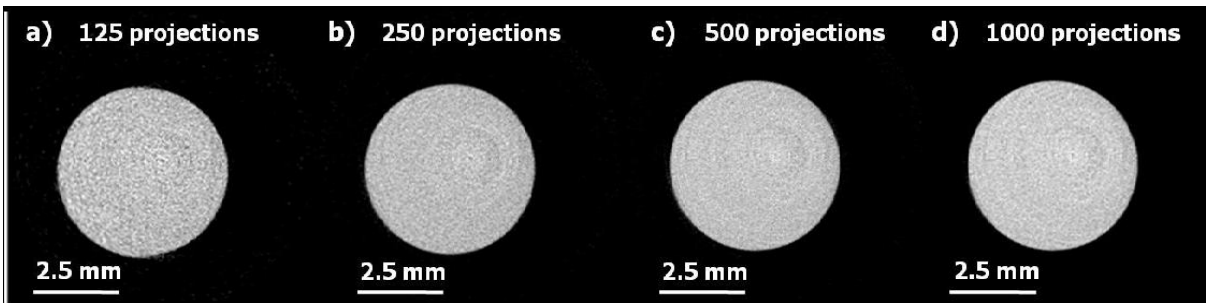

Figure 11.3 *The perspex phantom images acquired on the same scanner with all the technical factors the same except the number of projection angles. The perspex phantom was scanned with 125, 250, 500 and 1000 projection angles to evaluate the image noise.*

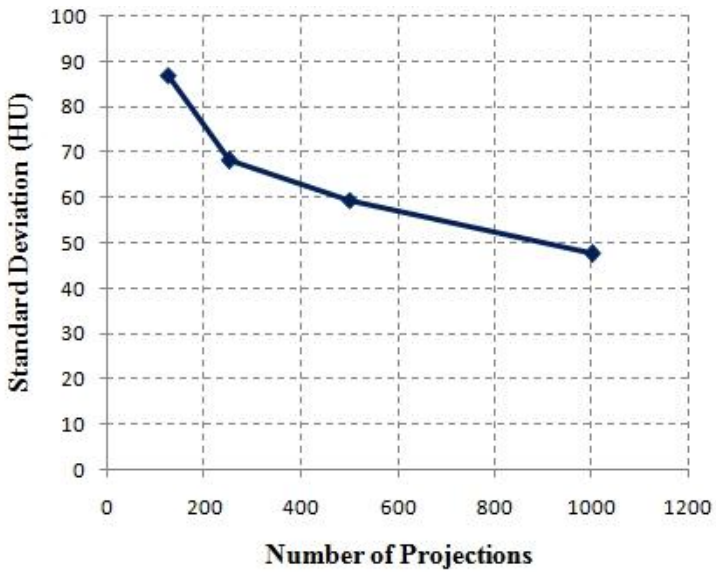

Figure 11.4 *Standard deviation of pixel grey-scale value for the perspex phantom imaged with different numbers of projection angles.*

11.3.1.2 Evaluation of tube voltage

The CNR of different materials was analysed with the multi-contrast phantom at 35, 50 and 80 kVp. The CNR measurements quantify the image contrast compared to the noise. Better CNR will provide good contrast and less noise but several other parameters must also be considered before choosing the best tube voltage for specimen imaging. The results are shown in Figure 11.5. This figure shows that tube voltage affects both image contrast and

noise. The CNR is greatest at the lowest tube voltage (35 kVp), but the noise is also highest at this setting.

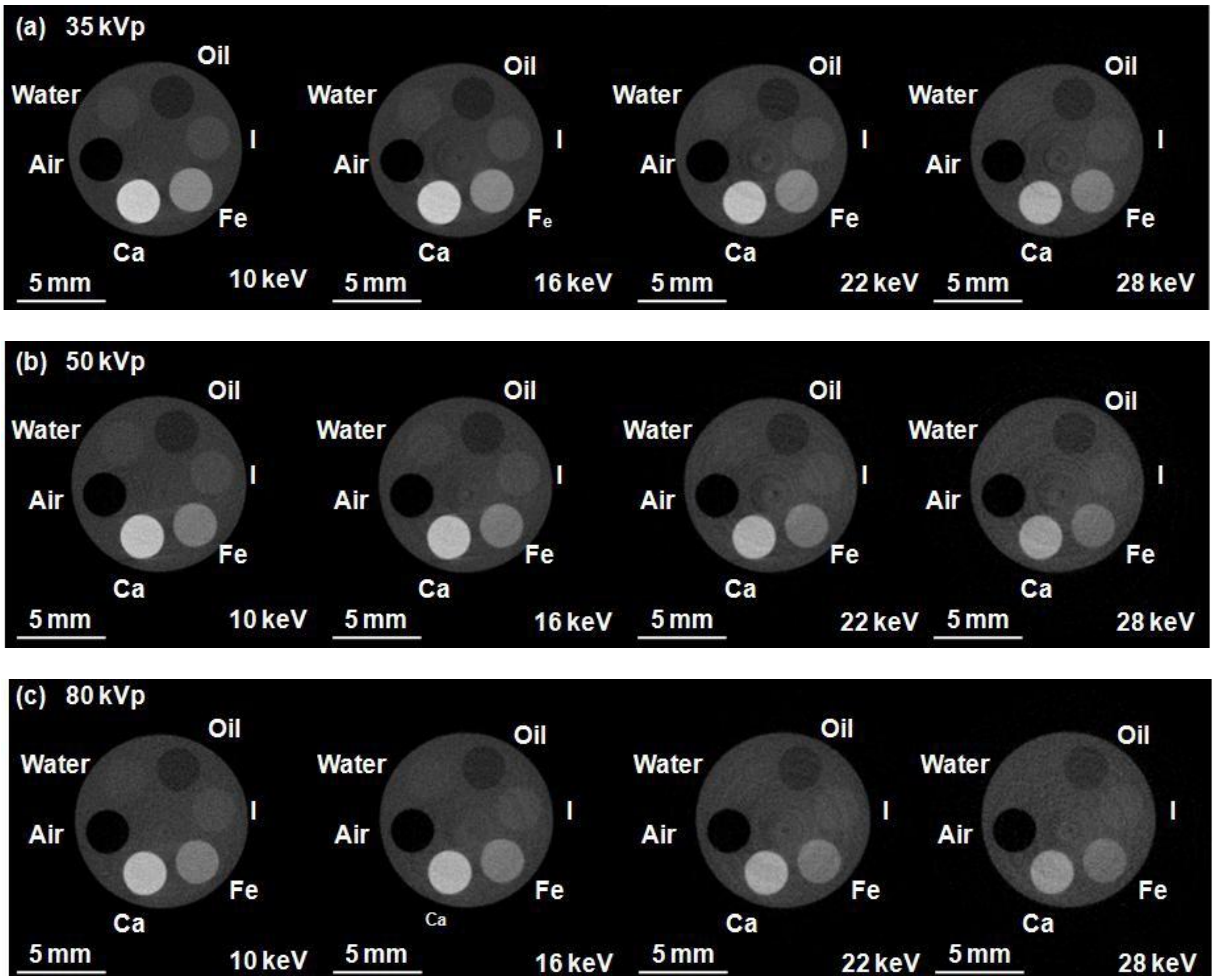

Figure 11.5 *The MARS-CT3 images of various solutions of contrast material within the calibration phantom, showing the effect of increasing tube voltage. (a) 35 kVp, (b) 50 kVp and (c) 80 kVp. This phantom was scanned at four threshold energies: 10, 16, 22 and 28 keV.*

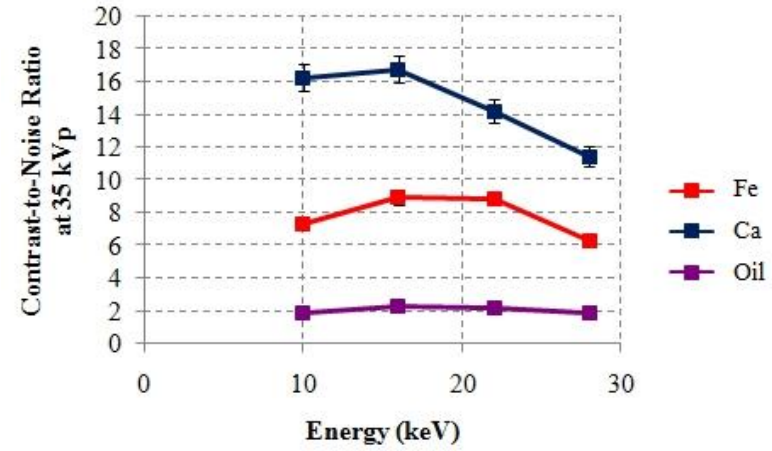

(a)

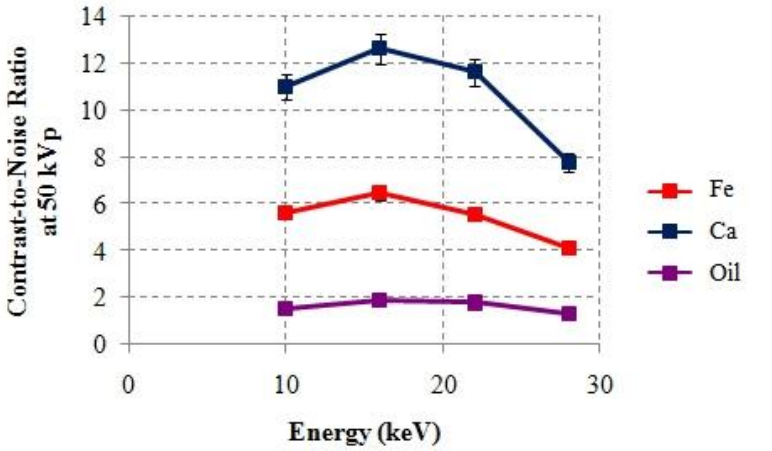

(b)

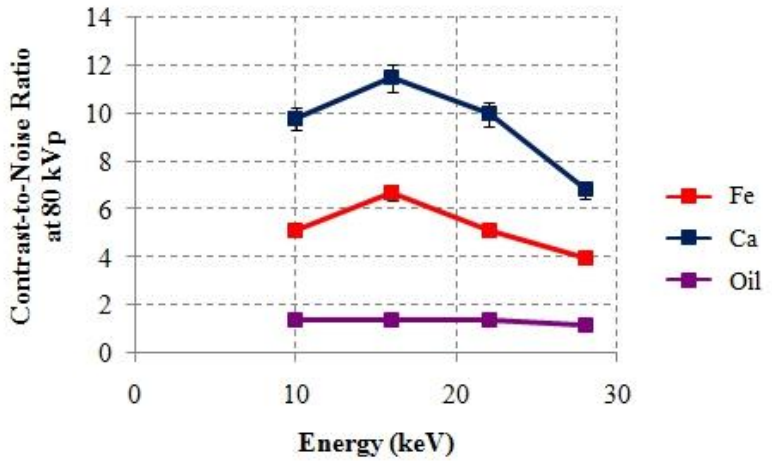

(c)

Figure 11.6 *CNR in oil and aqueous solutions of iron and calcium in a multi-contrast phantom as a function of tube voltages (35, 50 and 80 kVp). These materials mimic iron, calcium deposits and lipid in atherosclerotic plaque.*

The CNR for image regions of materials that mimic atherosclerotic plaque components such as iron, calcium and lipid was investigated using this phantom. The CNR of each solution was plotted against the energies for each tube voltage as shown in Figure 11.6. The CNR of calcium and iron reduced by approximately 25-30% with an increase in tube voltage from 35 kVp to 50 kVp, and by approximately 8-17% with an increase in the tube voltage from 50 kVp to 80 kVp. The CNR of oil which mimics lipid reduced by approximately 10% with an increase in tube voltage from 35 kVp to 50 kVp and by a similar amount with a further increase in tube voltage from 50 kVp to 80 kVp.

11.3.1.3 Evaluation of sensitivity for differentiating iron and calcium

The sensitivity for distinguishing iron and calcium was assessed using the phantom dataset at different tube voltages with multiple energies. The ability to discriminate between these two materials in spectral CT imaging depends primarily on the differences in dual-energy ratios for any specific pair of energies. Selecting an appropriate pair of energies will increase the sensitivity for discrimination. This phantom was scanned with four threshold energies at 10, 16, 22 and 28 keV. This energy range was selected as Si has a high absorption efficiency at energies below 30 keV.

The dual-energy ratio difference between iron and calcium as a function of all possible combinations of high and low energies used in spectral CT are presented in Figure 11.7. The maximum separation between iron and calcium occurs when the energies are most different. In this case, the maximum relative dual energy ratio differences are: 5.6%, 7.6 % and 12% for tube voltages of 35, 50 and 80 kVp respectively.

As expected the energy pair of 10 keV and 28 keV provides the maximum separation for iron and calcium. In general two materials may be distinguished by the energy dependent

differences in the attenuation coefficients at two well chosen energies. The greater the spectral separation, the easier it is to differentiate between the two materials. The effective energy of a spectral measurement depends upon both the energy threshold and the x-ray spectrum. Increasing the x-ray tube voltage increases the average photon energy and the attenuation coefficients are thus measured at a slightly higher effective energy. The greatest material separation in this case was obtained with 80 kVp. Compared with lower tube voltages, this has resulted in a measurable increase in the dual energy ratio difference for the calcium and iron pair. These results show that the selection of an appropriate accelerating voltage and semiconductor material can help to maximise the sensitivity of spectral CT performance. High *Z* semiconductor material allows greatest selection of pair of detector threshold energies that gives maximum separation between iron and calcium. This is relevant for distinguishing two materials with close atomic numbers like calcium ($Z = 20$) and iron ($Z = 26$).

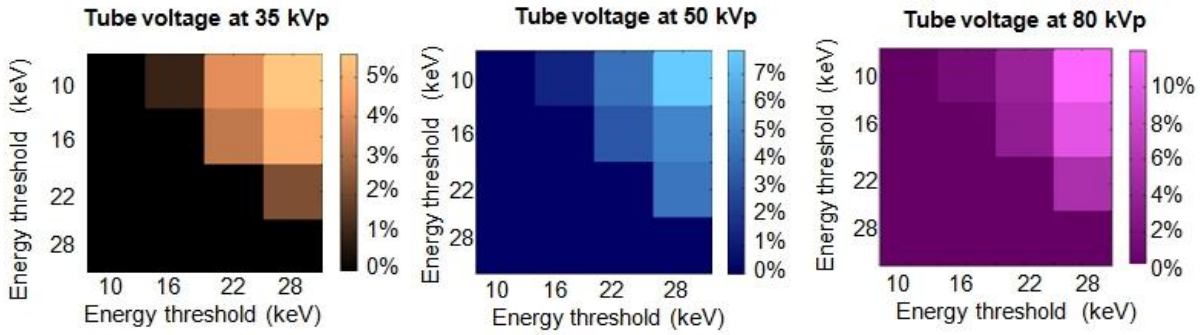

(a) (b) (c)

Figure 11.7 *The differences in dual-energy ratios for the combination of threshold energy pairs to discriminate iron and calcium at different tube voltages (a) 35 kVp, (b) 50 kVp and (c) 80 kVp.*

11.3.1.4 Demonstration of spectral CT analysis with a multi-contrast phantom

The spectral CT response was investigated using a multi-contrast phantom. This phantom contains different types of solution mimicking different types of atherosclerotic plaque

components. A reconstructed slice of the multi-contrast phantom is as shown in Figure 11.5 (B). A plot of CT number against threshold energies at 50 kVp is presented in Figure 11.8.

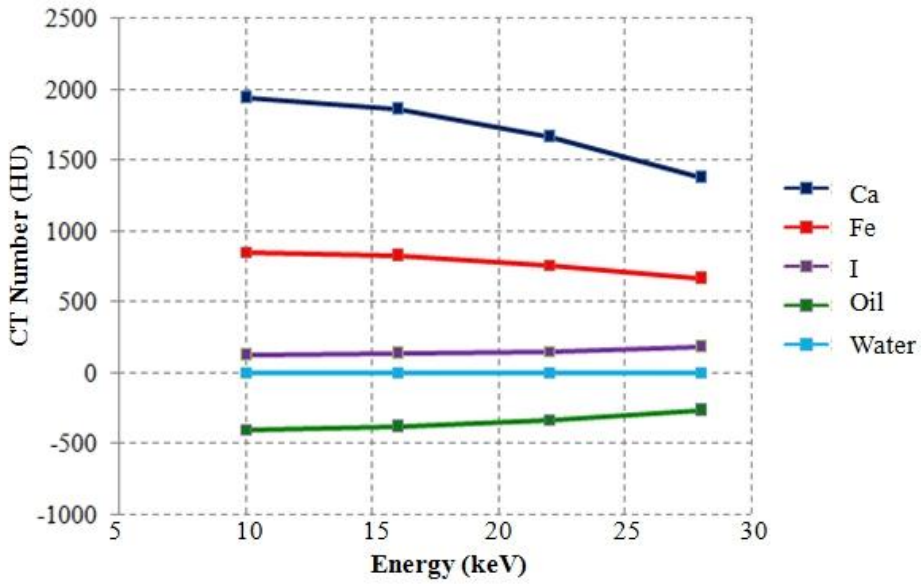

Figure 11.8 *A plot of CT number for different materials in the multi-contrast phantom evaluated against threshold energies at 50 kVp. The standard uncertainties are in the range 4-15 HU. The CT number response is characteristic of the material.*

11.3.2 Ex vivo atherosclerotic plaque images

The MARS-CT3 images of the atherosclerotic plaque segments and the respective photomicrographs are shown in Figures 11.10 to 11.13. The MARS-CT3 images closely match the histology. The specimens were scanned with four threshold energies: 10, 16, 22 and 28 keV at a tube voltage of 50 kVp. The soft tissue has highest contrast at lowest energy. The attenuation of calcium/iron deposits in atherosclerotic plaque decreases as the energy increases because of the relative contributions of the photoelectric effect and Compton scattering.

The photoelectric effect reduces as the energy increases and Compton scattering becomes more significant. The atherosclerotic plaque segment images show significant beam hardening artifacts around the calcified regions particularly in the low energy dataset. The beam hardening artifacts reduce with increasing energy threshold.

The calcium/iron deposits, lipid and soft tissue images were obtained using the linear basis technique in Chapter 10. The iron deposits are indistinguishable from calcium deposits with this material analysis technique. However, the morphology of iron deposits can be seen on the MARS-CT3 images. The local accumulations of randomly distributed punctate deposits or small clusters of iron deposits have good correlation with histology. The useful spectral CT information enhances material decomposition to differentiate the lipid from the soft tissue in atherosclerotic plaque (an important marker for vulnerable plaque). The material-specific images obtained from this technique were validated with histological analysis.

The corresponding plaque segments were subsequently stained with Von Kossa, Perls Prussian Blue and Oil-red-O to validate the calcium deposits, iron deposits and lipid respectively. The darker the color of staining solutions, the denser the plaque components. The Von Kossa calcium staining shows dark brown on the histological examination confirming the presence of calcium deposits. Using Perls's staining, iron deposits are shown with a blue color. Large lipid deposits are stained red by Oil-red-O.

Figure 11.9 *Plaque A has been cut into small segments. A1-A3 and B1 corresponds to the cutting edges of the plaques which have been scanned with the MARS-CT3 scanner.*

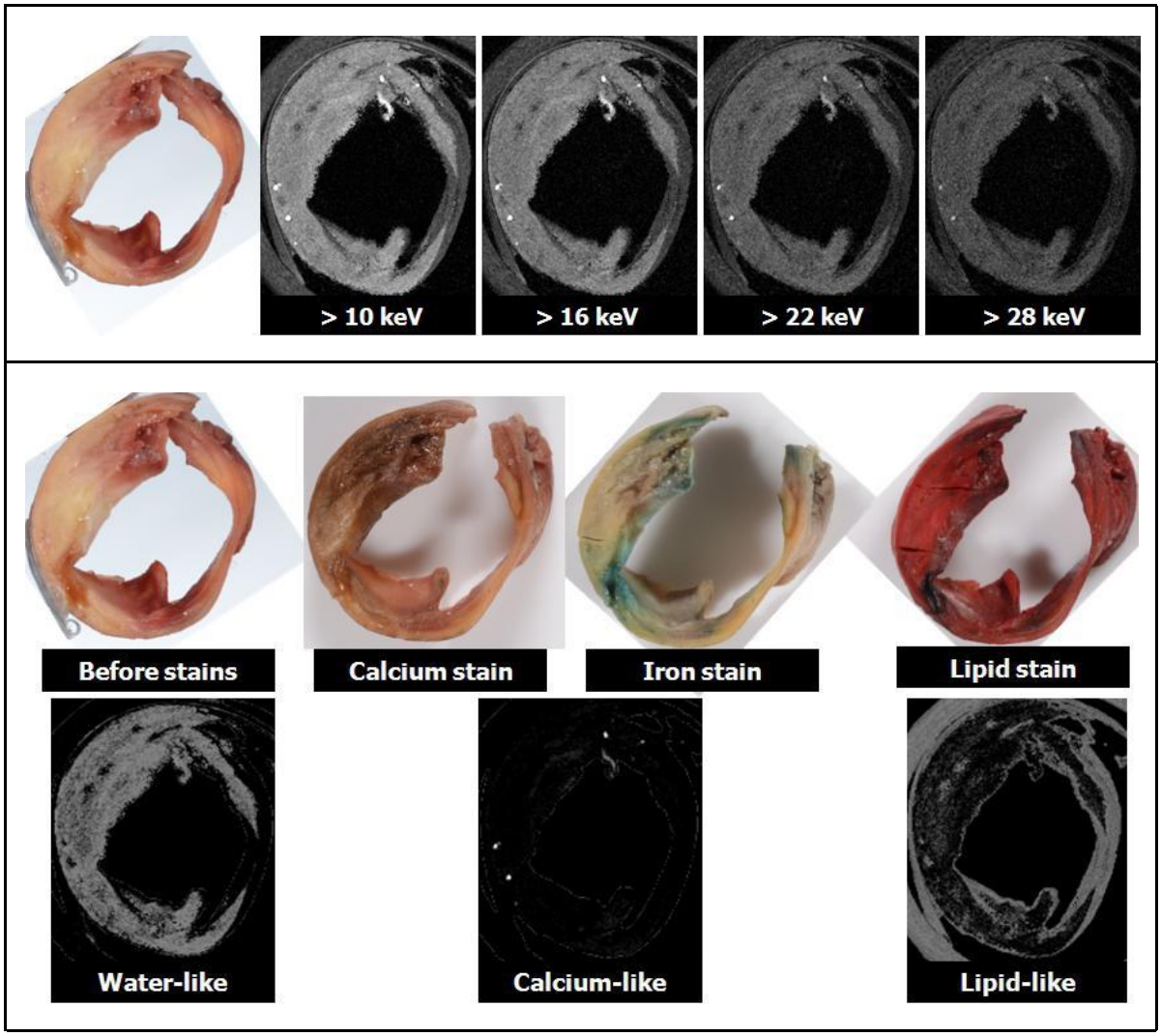

Figure 11.10 *(Top row) The photograph of atherosclerotic plaque segment A1 taken before imaging and the atherosclerotic plaque lesions visualised by the MARS-CT3 imaging at different energy thresholds. (Middle row) The corresponding cross sections of the same specimen were stained with Von Kossa, Perls Prussian Blue and Oil-red-O for histological examination. The darker the color of staining solutions, the denser the plaque components. (Bottom row) The material decomposition images show the water-like, calcium-like and lipid-like images. The calcium-like image shows the iron and calcium deposits in the atherosclerotic plaque. The lipid is clearly distinguishable from soft tissue in atherosclerotic plaque. All of the CT images closely match the photographs taken before imaging and the histology examination performed afterwards.*

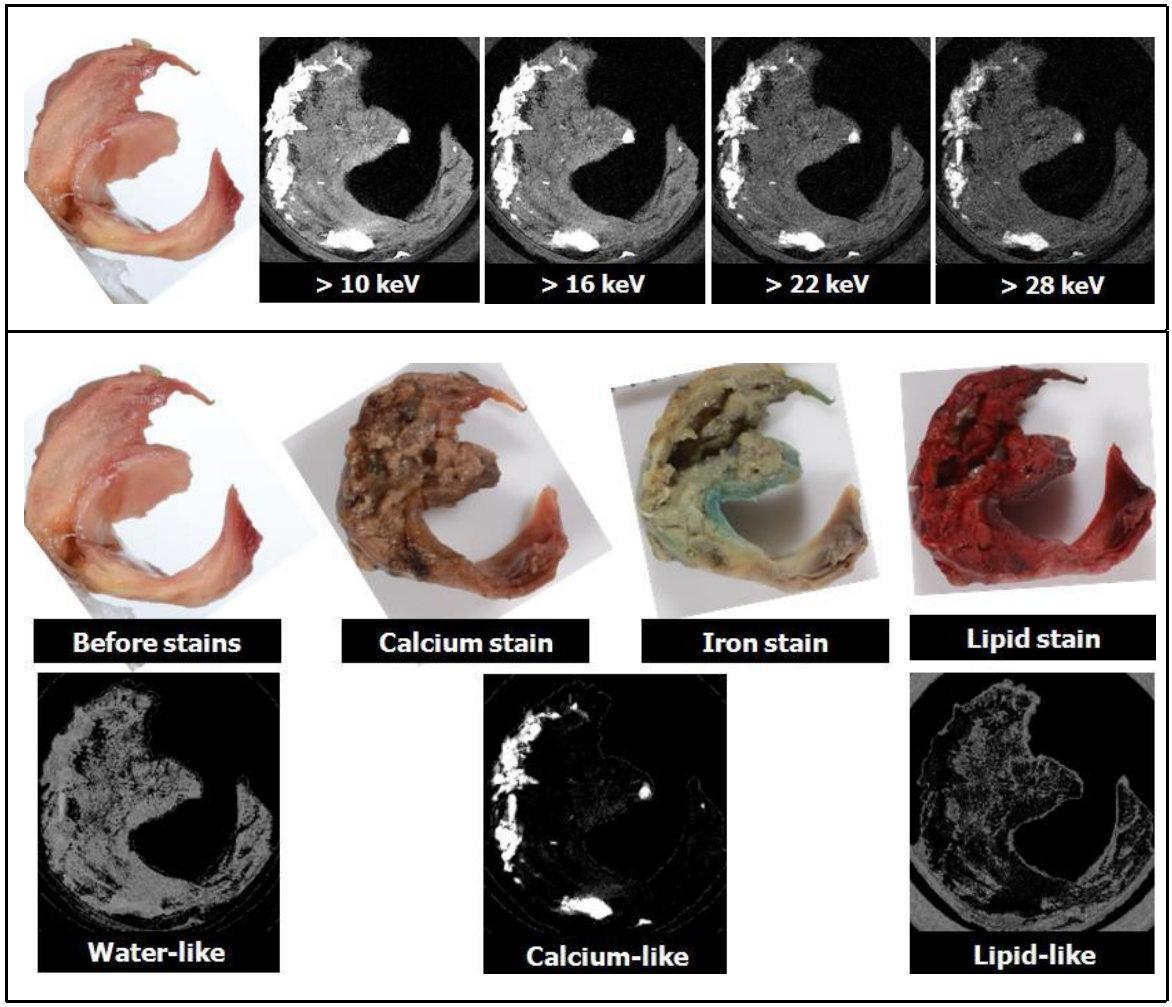

Figure 11.11 *(Top row) The photograph and the spectral CT images of atherosclerotic plaque segment (A2) at different energy thresholds. These images visualised by the MARS-CT3 imaging at 38 µm voxel size. (Middle row) The corresponding cross sections of the same specimen were stained with Von Kossa, Perls Prussian Blue and Oil-red-O for histological examination. (Bottom row) Three materials were decomposed in the image domain: the water-like,calcium-like and lipid-like images. The calcium deposits can easily be seen on the CT image. The low concentration of iron deposits appear as slightly dense tissues on the high resolution calcium-like image. The lipid is distinguished from soft tissue images. The MARS-CT3 images matched the photographs taken before imaging and the material decomposition images obtained from the MARS-CT3 imaging were confirmed by the histological examination.*

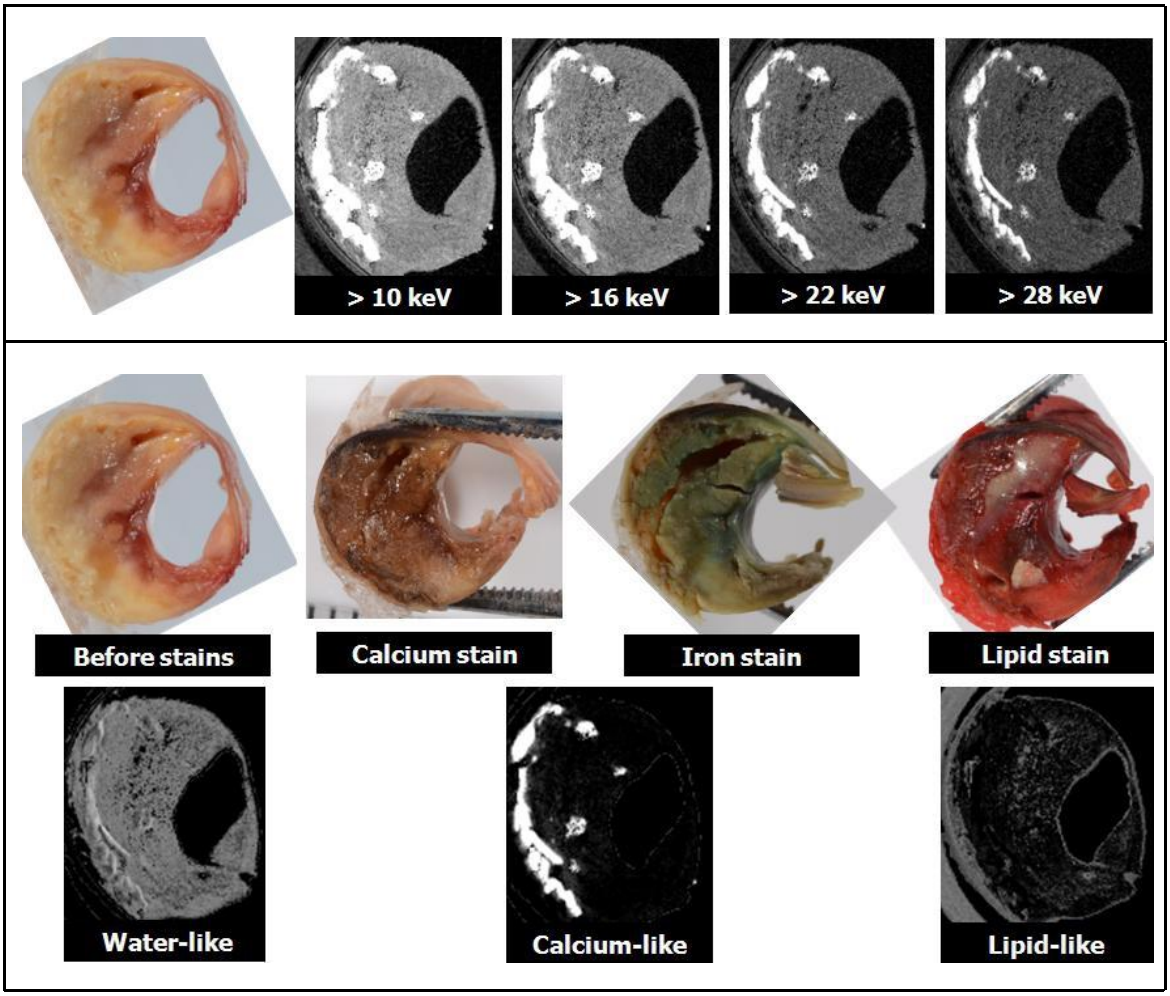

Figure 11.12 *(Top row) The photograph of A3 plaque segment and the corresponding spectral CT images obtained at different energy thresholds. (Middle row) The plaque staining photos show the plaque segment was stained with Von Kossa, Perls Prussian Blue and Oil-red-O to validate the calcium deposits, iron deposits and lipid respectively. The plaque staining photo shows that the small part of the plaque segment is slightly broken due to the handling process during staining. (Bottom row) The material decomposition images show the water-like, calcium-like and lipid-like images. The calcium-like image demonstrates the co-localisation of iron and calcium deposits in the plaque. The clusters of randomly distributed punctate iron deposits can also be seen on the CT image. The lipid and soft tissue images can be observed as separate components. The high resolution MARS-CT3 images closely match the photographs taken before imaging and the histological examination performed afterwards.*

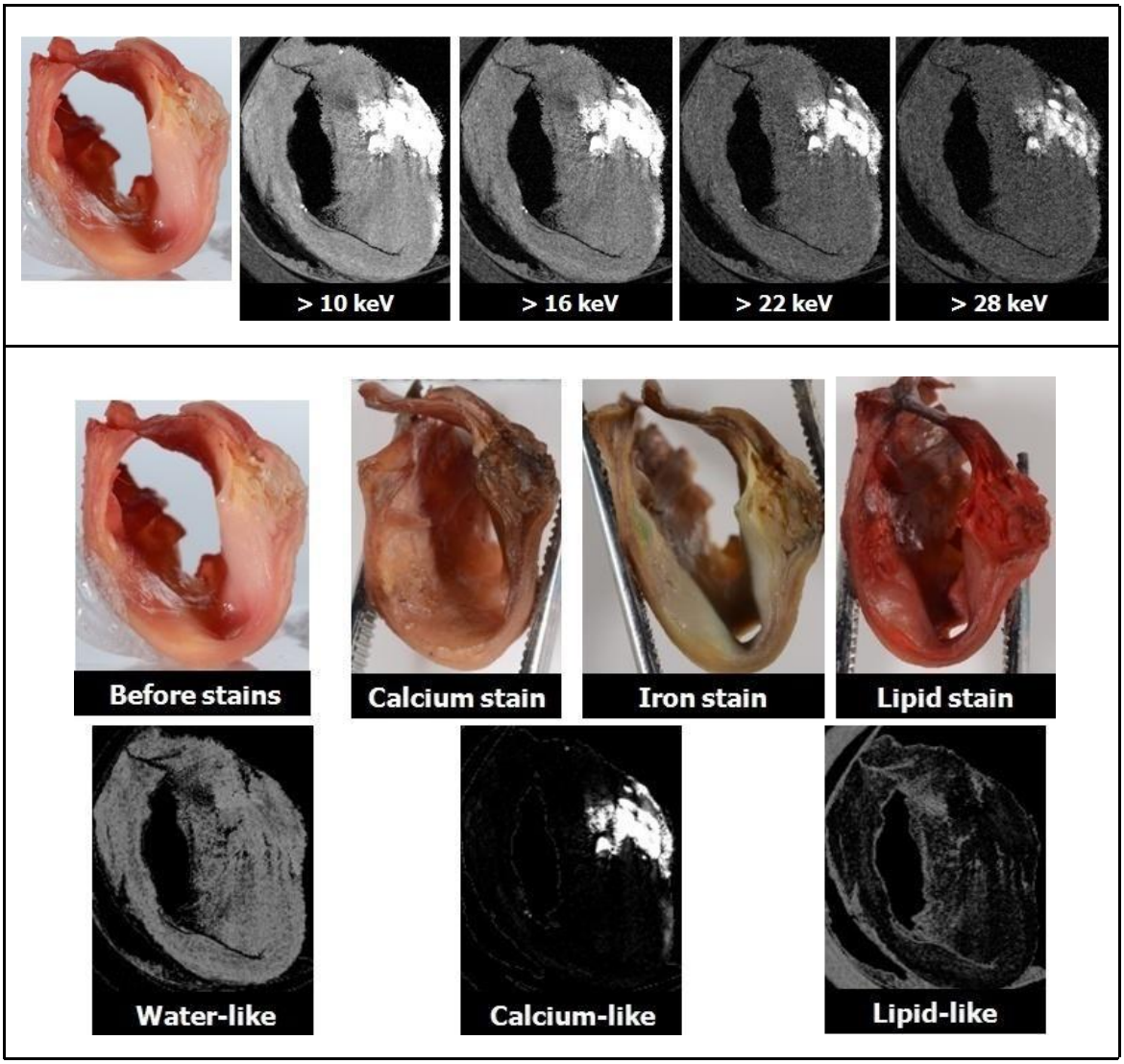

Figure 11.13 *(Top row) The photograph of atherosclerotic plaque segment B1 and the corresponding multi-energy CT images. (Middle row) The plaque segment was stained with with Von Kossa, Perls Prussian Blue and Oil-red-O to validate the calcium deposits, iron deposits and lipid respectively. (Bottom row) The material decomposition technique can identify lipid from soft-tissue and calcium/iron deposits in atherosclerotic plaque. Plaque segment B1 has fewer iron deposits than A1, A2, and A3 plaque segments. The lipid is distinguishable from the soft tissue in the plaque images. The characterisation of atherosclerotic plaque determined by MARS-CT3 closely matches photographs taken before scanning and the histological examination performed afterwards.*

11.4 Discussion

This study demonstrates the proof of principle that the MARS-CT3 scanner equipped with Medipix3 detector can characterise the atherosclerotic plaque components. The phantom studies designed to assess the effects of various scanning parameters on the image quality of ex vivo atherosclerotic plaque imaging have been used to enhance the performance of the MARS-CT3 scanner. The high contrast and spatial resolution provided by the MARS-CT3 scanner allowed characterisation of calcium/iron deposits and lipid which accurately reflects the composition of the lesion as validated by histological examination as a gold standard. The lipid is distinguishable from soft tissue in the plaque images. This study also shows that at the high resolution of ex vivo scanning, the iron deposits can be identified based on CT grey scale value and morphology. The spectral CT information allows decomposition of atherosclerotic plaque components.

In phantom studies, the effect of the numbers of projections on reconstructed image noise was investigated with the MARS-CT3 scanner. The image noise increases as the number of projection angles of CT imaging decreases. The image noise influences the visibility of high resolution details. One thousand projections gave less noise than reconstructions with fewer projections but was not justified when the time taken to scan the specimens was considered. Considering the overall scan time, electronic stability over time, pixel noise and the requirement to keep the specimens cool, 250 projection angles were selected for specimen imaging.

The tube voltage for ex vivo atherosclerotic plaque imaging was selected after considering the results of the phantom study. Soft tissue contrast was evaluated for the multi-contrast phantom as a function of tube voltage. The 80 kVp setting (the highest tube voltage) has the

highest x-ray output in terms of both flux and energy and thus the CT images acquired at 80 kVp have less image noise but also less image contrast. For ex vivo atherosclerotic plaque studies, the effect of using a tube voltage of 80 kVp on the visibility of plaque lesions such as lipid and soft tissue should be considered. The CNR of oil that mimics lipid in atherosclerotic plaque is relatively poor at 80 kVp. The lowest tube voltage (35 kVp) provides high image contrast but with an increased level of noise in the images caused by the reduced photon flux. Therefore, 50 kVp was selected for ex vivo atherosclerotic plaque imaging as this tube voltage gives good CNR for oil, iron and calcium solutions which are lipid, soft-tissue, iron and calcium surrogates respectively. Other studies have also used 50 kVp for small animal and human specimen imaging (Paulus et al., 2009).

After determining the optimum number of projection angles and tube voltage, the evaluation of sensitivity for iron and calcium separation was performed. To evaluate the potential for discrimination with spectral CT, the dual-energy ratios for iron and calcium on the combination of energy pairs were assessed using spectral CT images of the multi-contrast phantom acquired at different tube voltages. The dual-energy ratio difference analysis determines the difference in image contrast between iron and calcium for the combination of threshold energy pairs used in this study. The results of this study demonstrate that the use of appropriate tube voltage and energy range can increase the dual-energy contrast between two materials. The higher the dual-energy ratio difference on the combination of energy pairs, the easier to differentiate iron and calcium. A large increase in dual-energy ratio difference can significantly enhance the ability of spectral CT to discriminate between calcium and iron deposits. This technique may be of clinical value for the non-invasive detection of intraplaque hemorrhage as a marker for vulnerable plaques before rupture.

The results of this study indicate that the dual-energy ratio difference for calcium and iron increased from 5.6% to 7.6% with a tube voltage increase from 35 kVp to 50 kVp and to 12% with a further increase to 80 kVp. The relative separation between iron and calcium is greatest when the threshold energy pairs are most different: 10 and 28 keV. By increasing the tube voltage, the x-ray beam spectrum is shifted to the higher, more penetrating, energies. Thus, the contrast of objects under examination will reduce. However, these spectroscopic effects depend upon the atomic number of the material. At higher tube voltages such as 80 kVp the relative contribution of the photoelectric effect is reduced compared to that of the Compton effect and this difference is more pronounced for materials with higher atomic number such as iron. A tube voltage of 50 kVp was chosen for this study to enhance the image contrast for soft tissue imaging however higher tube voltages and increased threshold energies may be more suitable for the discrimination of iron and calcium.

The Medipix3 photon counting detector allows a flexible choice of multiple energies for scanning. A well chosen energy pair will improve the detection of atherosclerotic plaque components. This study was performed with quad Si Medipix3 detector because it is homogenous and has good absorption efficiency for low energy imaging. Accordingly this detector has given excellent results for soft tissue imaging. However, the restricted energy range limits the ability to discriminate between materials such as calcium and iron.

The spectral CT analysis of the multi-contrast phantom using the selected number of projections and tube voltage was performed to confirm the ability of the MARS-CT3 to image the plaque material components. The spectral CT analysis shows that the attenuation of x-ray photons is energy dependent and that each material has a specific attenuation curve. This spectral CT data confirms that differentiation and classification of materials is possible

with multi-energy imaging. On the other hand, ring artifacts were observed in many images. The ring artifacts are due to pixel variations that are not compensated by the flat-field correction. The flat-field scan was performed only after a phantom scan. The pixels response varies over the time due temperature instabilities during operation and it degrades the performance of Medipix detectors (Ronaldson et al., 2011a). As the pixels vary over the time, these flat-field measurements do not compensate the pixel variations. An improved flat-field measurement technique using multiple flat-field measurements taken before, during and after specimen scanning was used to overcome this problem. The Medipix3.1 detectors will be available in the near future for imaging and the initial tests at CERN suggest the pixel response will be more stable. Therefore, this problem may be reduced with the new version of Medipix detectors.

Based on phantom studies, the imaging protocol of ex vivo atherosclerotic plaque was developed. The image quality obtained from the MARS-CT3 system is better than those obtained from the MARS-CT2 scanner (Chapter 6). By taking multiple flat-field measurements, the pixel variations are well corrected and improvements can be seen on the atherosclerotic plaque images. The new cooling chamber works well and keeps the specimen frozen during the scan.

The characterisation of atherosclerotic plaque determined by the MARS-CT3 images closely matched the histological examination and photographs taken before scanning. The high spatial resolution of the MARS-CT3 scanner revealed the spatial distribution of clusters of randomly distributed punctate iron deposits. The low concentration of iron deposits can also be detected on the MARS-CT3 scanner. It appears as dense tissues on the MARS-CT3 images. The high contrast spectral CT images obtained from Si Medipix3 detector highlights

the contrast difference from the soft tissue. The material-specific images obtained from the linear basis technique provide separate calcium/iron deposits, lipid and soft tissue images. The material decomposition technique can identify lipid from soft-tissue and calcium/iron deposits in atherosclerotic plaque. The detection of lipid in atherosclerotic plaque has been the main goal of non-invasive characterisation of plaque morphology in recent times. The presence of a large lipid core is a key feature of plaque instability as it has been shown to be causative of plaque rupture with subsequent acute coronary thrombosis (Oliver et al., 1999).

Previous studies have demonstrated that high resolution micro-CT imaging allows detection and discrimination of iron and calcium deposits in atherosclerotic plaque by virtue of the different sizes of the individual iron and calcium deposits and by their individual CT grey scale values (Langheinrich et al., 2009). Further investigation by Wang et al. (2011) demonstrated that the iron and calcium remain visually different for voxel sizes up to 200 μm.

Results from this study show that the MARS-CT3 scanner can detect vulnerable plaque based on the presence of a substantial lipid core and iron deposits in atherosclerotic plaques. The iron deposits can be observed by their morphology on the high resolution MARS-CT3 images. The MARS-CT3 images show a high correlation with the histological analysis. The phantom studies suggest that the difference in dual-energy ratio on the combination energy pairs may allow differentiation of iron and calcium deposits. Therefore, the iron and calcium deposits are distinct on spectral CT.

The beam hardening effects are observed on the atherosclerotic plaque images particularly at low energy. However, there is substantial reduction in the beam-hardening effect in the higher energy dataset.

11.5 Limitations

Our study has two significant limitations. Firstly this study was performed with a limited detector energy range. Thus, the separation of iron and calcium deposits in atherosclerotic plaques based on energy information is limited. Other sensor layer materials such as CdTe and GaAs will extend the energy range for spectral CT imaging.

Secondly the presence of artifacts such as ring artifacts in the higher energy datasets and beam hardening in the lower energy images limited the ability to distinguish materials both by morphology and spectroscopy. Some artifacts are the result of technological limitations in current detector design whilst others such as beam hardening are physical effects that may be eliminated by improvements in measurement and analysis techniques. The availability of Medipix3.1 detectors in the near future will improve the image quality as this detector has been designed with a more stable pixel response.

11.6 Conclusion

This study demonstrates that the composition of atherosclerotic plaques can be determined by the MARS-CT3 equipped with Si Medipix3 detector and the results accurately reflect the composition of plaque as validated by histological examination. The material-specific images obtained from the linear basis technique differentiate lipid and iron/calcium deposits in atherosclerotic plaque.

The results of a phantom study assessment of the imaging parameters for ex vivo atherosclerotic plaque were used to enhance the performance of the MARS-CT3 scanner for the characterisation of plaque lesions. The difference in the dual-energy ratio between calcium

and iron in a phantom on the combination of energy pairs shows that spectral CT can enhance the separation of these two materials.

A good combination of tube voltage, tube current and the use of a quad Si Medipix3 detector provided high contrast resolution for imaging atherosclerotic plaque lesions. An improved flat-field measurement technique was used to overcome limitations in detector performance. Two designs of cooling chamber were evaluated. The selected design was able to maintain the specimen at a cool temperature for the full duration of the scan and thereby preserve the condition of the atherosclerotic plaque lesions.

11.7 Summary

1. The MARS-CT3 scanner equipped with a Si Medipix3 detector can accurately determine the composition of atherosclerotic plaque lesions. This has been validated using histological examination as a gold standard. The MARS-CT3 scanner can be used to detect vulnerable plaque based on the presence of a substantial lipid core and iron deposits. The high resolution MARS-CT3 scanner reveals the spatial distribution and local accumulation of iron and calcium deposits in the plaque.

2. The spectral information from multi-energy MARS-CT3 allows characterisation of lipid and iron/calcium deposits in atherosclerotic plaque using the linear basis technique. The material specific images closely match the histology.

3. The results of the dual-energy ratio differences of iron and calcium deposits in a phantom on the combination of energy pairs, demonstrate the ability of spectral CT to differentiate these two materials.

4. The evaluation of scan parameters on phantom studies provides useful information for choosing the best imaging parameters and has been used to improve image quality for ex vivo imaging of atherosclerotic plaques with the MARS-CT3 scanner. An improved multi-flat-field measurement technique has been used to minimise the effect of the pixel sensitivity variations that are observed with the Medipix3 detector. The condition of the ex vivo specimen was preserved with an improved cooling chamber.

Chapter 12

Conclusion and further work

12.1 Summary of conclusions

In *Chapter 1* the aim of this thesis was described in terms of the immediate pre-clinical applications for ex vivo studies of human atherosclerotic plaques. The chapter was also discussed the significance of this thesis as a staging post towards achieving the vision of using spectral CT for full scale human applications. The clinical significance of both of these objectives was related to burden of cardiovascular disease and the potential for improved diagnosis through the detection of so called vulnerable plaques. It was noted that current imaging modalities have only limited ability to detect the three markers (lipid core, iron deposits as marker of intraplaque hemorrhage and a thin fibrous cap) for this condition. Spectral CT was proposed as a possible technique for distinguishing vulnerable plaques by their material components and morphology. The aim of this thesis was to develop techniques for ex vivo analysis of human atherosclerotic plaques by spectral CT using spectroscopic photon-counting detectors and to demonstrate the potential advantages of this technology. The clinical significance of this study for improved assessment of cardiovascular risk and the novelty of the technical approach were thus explained.

Chapters 2 and 3 provided the technical background necessary to understand the remainder of this work. In *Chapter 2* the basic mechanisms by which x-rays interact with matter were described. The relative significance of each of these modes of interaction was seen to vary with energy and material type, and the significance of this to spectral CT was explained.

In *Chapter 3* a description of the basic principles of CT was given. The particular measures by which clinical CT performance is evaluated were defined. Some of the imaging problems and artifacts that may be common to both clinical and spectral CT were described.

In *Chapter 4* the principles and capabilities of the Medipix family of photon counting detectors were presented. The improved spatial resolution and energy resolving capabilities of this technology were seen to enable more information to be recorded from the incident x-ray flux than standard integrating detectors. It was agreed that the use of this novel photon counting detector technology in spectral CT has the potential to provide significantly more information about the components of biological materials than conventional CT.

Chapter 5 described the technological basis for conventional, dual energy and spectral CT. The concept of retrieving spectral information and using it to separate the photoelectric and Compton scattering contributions was explained. Improvements in spatial resolution and the potential uses of the additional energy resolving ability compared with CT systems using standard detector technology were noted. Our research group in Christchurch, New Zealand, has been developing spectral micro-CT (MARS-CT) systems equipped with Medipix detectors. It is a joint project between the Universities of Canterbury and Otago, New Zealand, CERN Medipix collaboration and Geneva. The characteristics of the electromechanical gantry, x-ray tube, Medipix readout system and detector were presented. The selection of x-ray tube and detector type were made on the basis of a wide range of potential research applications. The imaging parameters for spectral CT imaging were also discussed. The overall conclusion from this part of the thesis was that, in principle, spectral micro-CT using high resolution photon counting detectors such as Medipix detectors has the

potential to characterise the material composition and thereby enable the detection of vulnerable atherosclerotic plaques.

Chapter 6 introduced the atherosclerotic condition and described the abilities and limitations of different imaging modalities currently available for its diagnosis. The characteristics of an ideal modality were proposed. The ability to non-invasively detect lipid core and iron deposits as markers for vulnerable plaques is an important goal in the quest for improved diagnosis of atherosclerotic disease. It was argued that there are currently no suitable modalities available for this task and that spectral CT has the potential to meet these requirements more closely than competing technologies.

In *Chapter 7* the performance of different modalities for the characterisation of ex vivo atherosclerotic plaques was experimentally investigated. The results of plaque examinations using clinical CT, MRI and MARS-CT2 with a Medipix2 CdTe detector were compared. The ability to image fixed (in resin) and unfixed (fresh) plaque specimens were also considered. It was concluded that the performance of the MARS-CT2 scanner was significantly better than the other modalities in terms of spatial resolution. It was also found that the additional spectral data provided by MARS-CT2 yielded important information about the tissue types not available with standard CT. It was found that imaging the unfixed (fresh) specimens yielded better results than fixed specimen imaging. Some limitations in the cooling method used to maintain the condition of the unfixed (fresh) plaque specimens were identified. The overall conclusion was that spectral CT using the Medipix detector was a promising technique but further developments and modifications to the scanner configuration, including detector type and scanning parameters were required to obtain the best results.

The improvements in system design, configuration and atherosclerotic plaque measurement protocol identified in the preceding chapters were implemented by the MARS technical team members in the revised MARS-CT3 system incorporating the Medipix3 detector. *Chapter 8* described the initial calibration and setting to work of the MARS-CT3 system. The calibration protocols were developed and the major geometrical parameters were determined by the candidate and MARS commissioning team members including J Paul Ronaldson, Judy Mohr, Maggie Anderson, Dr Nicholas Cook.

The imaging performance of the MARS-CT3 was evaluated in *Chapter 9*. Scanning protocols and preprocessing methods were developed specifically for this scanner. The performance of the scanner in terms of spatial resolution, image uniformity, pixel noise, CT number linearity, dose rate at the isocentre and spectroscopic response was determined. The protocols for some of these performance measurements were incorporated into the routine QA requirements for operating the scanner. The overall system performance was found to be suitable for preclinical studies of atherosclerotic plaques.

A linear method for material decomposition was proposed in *Chapter 10*. The linearity of the system over the range of interest was proven by experimental measurement. The linear decomposition method was demonstrated using phantoms containing iron, calcium, water (soft-tissue surrogate) and oil (lipid surrogate). The efficacy of the method was improved with the addition of appropriate volume constraints. It was concluded that three of the four materials could be determined simultaneously but that it was not possible using the current MARS-CT3 to distinguish iron from calcium in the presence of water and oil using spectral information alone. Additional constraints or measurement information would be required to simultaneously distinguish all of these materials.

The MARS-CT3 spectral micro CT system incorporating a Medipix3 Si detector was used in *Chapter 11* for the final study of this thesis. The study design incorporated the improvements in scanner configuration and measurement protocol identified in earlier chapters. The analysis of the spectral CT data used the linear basis method proposed in the previous chapter. Imaging was performed on unfixed (fresh) specimens contained within an improved design of cooling chamber. Validation of the spectral CT results was by comparison with histology and staining. It was found that the materials analysis results were in good agreement with the results of the histology and staining and that lipid and calcium in various concentrations were easily distinguishable from the surrounding tissue. Furthermore the presence of iron could be inferred from the morphology visible on the high resolution MARS-CT3 images and therefore that this system was capable of detecting vulnerable plaques. A preliminary analysis of the scanning parameters used in this work was made and showed how the ability to differentiate certain materials such as calcium and iron could be improved by selection of appropriate x-ray parameters and detector threshold energies. Some problems with imaging artifacts were noted that were due to a combination of physical and electronic effects.

The overall conclusion from this final phase of the thesis was that MARS-CT3 provides sufficient spectral and morphological information to allow the assessment of unstable plaque components (lipid and iron components). In the short term this will enable ex vivo assessment and analysis of plaques using spectral micro-CT. Improvements in performance can be expected with further developments in detector design and optimisation of scanning parameters. Ultimately this work may lead to improvements in the diagnosis and monitoring of atherosclerotic disease in full scale human applications.

12.2 Future work

Three areas for additional work that will improve the analysis of ex vivo atherosclerotic plaques are identified. These relate to (i) improving the results obtained from the existing technique by continuing development and implementation of the underlying data processing and calibration methods; (ii) the acquisition of additional spectral data through further optimisation of the scanning parameters and instrument configuration; and (iii) the acquisition and use of additional data not currently considered within the scope of this thesis.

i. ***Further developments of the existing technique.*** The presence of artifacts from both technological and physical effects may in some cases confound the analysis of material components and work to minimise these problems will enhance the performance of future studies. Artifacts resulting from technological effects include ring and shadow artifacts from unstable electronic components. The impact of some of these effects will reduce with external developments such as improvements in the design of detector technology. It is reported that the pixel response of the new Medipix3.1 detector is more stable and these detectors will be available in the near future. The design and implementation of measurement protocols, and filtering techniques aimed at minimising the presence of artifacts would be beneficial. Fundamental physical effects such as beam hardening and streak artifacts caused by the presence of highly absorbing calcifications within softer tissues may be reduced using appropriate correction techniques. A number of methods have been implemented for conventional CT including polynomial beam hardening correction (Herman, 1979) and metal artifact reduction (Kalender et al., 1987). These should be investigated and compared with spectral methods such as energy binning and dual energy corrections (Alvarez & Macovski, 1976).

ii. ***The acquisition of additional or more optimal spectral information.*** The range and number of detector threshold energies has not been optimised. Further consideration of the sensitivity for discriminating particular materials of interest may yield a better set of detector threshold energies. More fundamentally, the selection of sensor layer material and thickness should also be considered for each application. The effective energy range of each sensor material varies with type, thickness and for specimens containing higher-Z materials such as iron and calcium. However the assessment of detector types would need to consider other factors including spectral response, resolution and sensor homogeneity. The imminent availability of the Medipix3 charge summing and spectroscopic modes may retrieve additional spectroscopic information from existing sensor types. This may impact on the choice of sensor layer. Similarly the characteristics of the x-ray source including filtration and voltage should be investigated. An objective method for determining the optimum scanner configuration for retrieving spectral information appropriate to a given application would be beneficial.

iii. ***The utilisation of further material specific information.*** The linear basis technique as used in this work considered the spectral vector and its magnitude as independently defining the material type and concentration respectively. However each material may be defined by other criteria such as expected range of attenuation values and morphology. It has already been noted that the morphology of calcium and iron deposits within vulnerable plaques may be used to distinguish these materials in many cases. Further evaluation of the spectral data may provide additional useful information not considered within this thesis. For example, the mass absorption coefficient is approximately related to ρZ^3 and thus for similar ranges in density the

distribution of attenuation values expected from calcium deposits (Z=20) may be distinct from those expected from punctate iron deposits (Z=26). Additional investigations to more comprehensively evaluate these characteristics may yield additional criteria for material discrimination.

References

Aamir, R., Lansley, S. P., Zainon, R., Fiederle, M., Faulerc, A., Greiffenberg, D., Butler, P. H., & Butler, A. P. H. (2011). Pixel sensitivity variations in a CdTe-Medipix2 detector using poly-energetic x-rays. Journal of Instrumentation, 6(1), C01059.

AAPM. (1993). *Specification and acceptance testing of computed tomography scanners*. (Report No. 39). New York.

Allen, D. R., Browse, N. L., Rutt, D. L., Butler, L., & Fletcher, C. (1988). The effect of cigarette smoke, nicotine, and carbon monoxide on the permeability of the arterial wall. *Journal of Vascular Surgery, 7*(1), 139-152.

Alvarez, R. E., & Macovski, A. (1976). Energy-selective reconstructions in x-ray computerised tomography. *Physics in Medicine and Biology*, *21*(5), 733-744.

Ambrose J. (1973). Computerised transverse axial scanning (tomography). Part 2: Clinical application. *British Journal of Radiology*, *46*, 1023-1047.

Ambrose, J. A., Tannembaum, M. A., Alexopoulos, D., Hjemdahl-Monsen, C. E., Leavy, J., Weiss, M., Borrico, S., Gorlin, R., & Fuster, V. (1988). Angiographic progression of coronary artery disease and the development of myocardial infarction. *Journal of the American College of Cardiology, 12*(1), 56-62.

American Heart Association. (2011). *Atherosclerosis.* Retrieved from http://www.heart.org/HEARTORG/Conditions/Cholesterol/WhyCholesterolMatters/Atherosclerosis_UCM_305564_Article.jsp

Anderson, N. G., Butler, A. P., Scott, N., Cook, N. J., Butzer, J., Schleich, N., Firsching, M., & Butler, P. H. (2009). Colour CT x-ray spectroscopic images of mice using Medipix-2 detector. *European Radiology, 393*(1), pS228.

Anderson, N. G., Butler, A. P., Scott, N.J., Cook, N.J., Butzer, J.S., Schleich, N., Firsching, M., Grasset, R.., de Ruiter, N., Campbell, M., & Butler, P. H. (2010). Spectroscopic (multi-energy) CT distinguishes iodine and barium contrast material in MICE. *European Radiology, 20*(9), 2126-2134.

Aslund, M., Fredenberg, E., Telman, M., & Danielsson, M. (2010). Detectors for the future x-ray imaging. *Radiation Protection Dosimetry, 139* (1-3), 327-333.

Ballabriga, R., Campbell, M., Heijne, E. H. M., Llopart, X., & Tlustos, L. (2007). The Medipix3 prototype, a pixel readout chip working in single photon counting mode

with improved spectrometric performance. *IEEE Transactions on Nuclear Science, 54*(1), 1824-1829.

Ballabriga, R., Campbell, M., Heijne, E., Llopart, X., Tlustos, L., & Wong, W. (2011). Medipix3: A 64 k pixel detector readout chip working in single photon counting mode with improved spectrometric performance. *Nuclear Instruments and Methods in Physics Research A*, *633*(1), S15-S18.

Barrett, J. F., & Keat, N. (2004). Artifacts in CT: Recognition and Avoidance[1]. *Radiographics, 24*(6)*,* 1679-1691.

Bates, R. H. T., & Peters, T. M. (1971). Towards Improvements in Tomography. *New Zealand Journal of Science, 14*, 883.

Bates, R. H. T., Garden, K., & Peters, T. M. (1983). Overview of Computerized Tomography with Emphasis on Future Developments. *Proceedings of the IEEE*, *71*(3), 356-372.

Berg, K. B., Carr, J. M., Clark, M. J., Cook, N. J., Anderson, N. G., Scott, N. J., Butler, A. P., Butler, P. H., & Butler, A. P. H. (February, 2009). *Pilot Study to confirm that Fat and liver can be distinguished by spectroscopic tissue response on a Medipix-All-Resolution System-CT (MARS-CT).* Paper presented at the Advanced Material and Nanotechnology 4 Conference, Dunedin, New Zealand.

Bert, C., Niederlöhner, D., Giersch, J., Pfeiffer, K. F. & Anton, G. (2003). Computed tomography using the Medipix1 chip. *Nuclear Instrumentation Methods in Physics Research A*, *509*, 240-250.

Beuville, E., Cederström, B., Danielsson, M., Luo, L., Nygren, D., Oltman, E., & Vestlund, J. (1998). In application specific integrated circuit and data acquisition system for digital x-ray imaging. *Nuclear Instrumentation Methods in Physics Research A*, *406*, 337-342.

Boll, D. T., Hoffmann, M. H., Huber, N., Bossert, A. S., Aschoff, A. J., & Fleiter, T. R. (2006). Spectral coronary multidetector computed tomography angiography: dual benefit by facilitating plaque characterisation and enhancing lumen depiction. *Journal of Computer Assisted Tomography, 30*(5), 804-811.

Boll, D. T., Patil, N. A., Paulson, E. K., Merkle, E. M., Nelson, R. C., Schindera, S. T., Roessl, E., Martens, G., Proksa, R., Fleiter, T. R., & Schlomka, J. P. (2009). Focal cystic high-attenuation lesions: characterisation in renal phantom by using photon-counting spectral CT-improved differentiation of lesion composition. *Radiology, 254*(1)*,* 270-276.

Bornstein, N. M., Krajewski, A., Lewis, A. J., & Norris, J. W. (1990). Clinical significance of carotid plaque hemorrhage. *Archives of Neurology, 47*, 958-959.

Brennan, J. F., Romer, T. J., Lees, R. S., Tercyak, A. M., Kramer, J. R., & Feld, M. S. (1997). Determination of human coronary artery composition by Raman spectroscopy. *Circulation, 96*(1), 99-105.

Brooks, R. A. (1977). A quantitative theory of the Hounsfield unit and its application to dual-energy scanning. *Journal of Computed Assisted Tomography, 1*(4), 487-493.

Bushberg, J. T. (1998). The AAPM/RSNA physics tutorial for residents. *RadioGraphics, 18*(2), 457-468.

Bushberg, J. T., Seibert, J. A., Jr., E. M. L., & Boone, J. M. (2001). The essential physics of medical imaging (2nd ed.). Baltimore: Lippincott Williams & Wilkins.

Butler, A. P. H., Anderson, N. G., Tipples, R., Cook, N., Watts, R., Meyer, J. Bell, A. J., Melzer, T. R., & Butler, P. H. (2008). Biomedical x-ray imaging with spectroscopic pixel detectors. *Nuclear Instrumentation Methods in Physics Research A, 591,* 141-146.

Butler, A. P. H., Butzer, J., Schleich, N., Cook, N. J., Anderson, N. G., Scott, N., de Ruiter, N., Grasset, R., Tlustos, L., & Butler, P. H. (2011a). Processing of spectral X-ray data with principal components analysis. *Nuclear Instruments and Methods in Physics Research A, 633*(1), S140-S142. doi: 10.1016/j.nima.2010.06.149.

Butler, A. P., Ronaldson, P., Scott, N., Zainon, R., Butler, P., Gieseg, S., Janmale, T., & Anderson, N. (2011b, August). *Soft tissue imaging with the MARS spectral CT scanner.* Paper presented at the Queenstown Heart Meeting.

Butler, A. P., Ronaldson, P., Walsh, M. Aamir, R., Doesburg, R., de Ruiter, N., Scott, N., Zainon, R., Geiseg, S., Woodfield, T., Siegert, A., Mohr, J., Anderson, N., & Butler, P. H. (2011c, October). *Development of a Medipix3 based spectral (multi-energy) CT for pre-clinical evaluation of biomarkers*. Paper presented for the Royal Australia and New Zealand College of Radiologists Annual Scientific Meeting.

Butzer, J. S., Butler, A. P. H., Cook, N. J., Butler, P. H., Ross, F., Schleich, N., Selkrik, J., Watts, R., Meyerm J., Scott, N.J., van Leeuwen, D., Hemmingson, S., Melzer, T.R., & Anderson, N. G. (2008). MARS: A 3D spectroscopic x-ray imaging device based on Medipix. Paper presented at the IEEE Nuclear Science Symposium and Medical Imaging Conference, Dresden, Germany.

Cademartiri, F., La Grutta, L., Palumbo, A. A., Maffei, E., Runza, G., Bartolotta, T. V., Pugliese, F., Mollet, N. R. A., Midiri, M., & Krestin, G. P. (2006). Coronary plaque

imaging with multi-slice computed tomography: technique and clinical applications. *European Radiology Supplement, 16*(7), M44-M53.

Cai, J. M., Hatsukami, T. S., Ferguson, M. S., Small, R., Polissar, N. L., & Yuan, C. (2002). Classification of human carotid atherosclerotic lesions with in vivo multicontrast magnetic resonance imaging. *Circulation*, *106*(11),1368-1373.

Campbell, M., Heijne, E. H. M., Meddeler, G., Perniogotti, E., & Snoeys, W. (1998). X-ray imaging using a hybrid photon counting GaAs pixel detector. *IEEE Transactions on Nuclear Science, 45*(3), 751-753.

Campbell, M., Heijne, E., Holy, T., Jakubek, J., Idarraga, Jakubek, J., Lebel. C., Leroy, C., Llopart, X., Pospisil, S., & Vykydal, Z. (2008). Study of the charge sharing in a silicon pixel detector by means of alpha-particles interacting with a Medipix2 device, *Nuclear Instruments Methods in Physics Resrach Section A, 591*,38-41.

Cherry, S. R. (2004). In vivo genomic and molecular imaging: new challenges for imaging physics. *Physics in Medicine and Biology*, *49*, R13-48.

Chiro, G. D., Brooks, R. A., Kessler, R. M., Johnston, G. S., Jones, A. E., Herdt, J. R., & Sheridan, W. T. (1979). Tissue signatures with dual-energy computed tomography. *Radiology, 131,* 521-523.

Chmeissani, M. & Mikulec, B. (2001). Performance limits of a single photon counting pixel system. *Nuclear Instruments and Methods in Physics Research A*, *460*(1), 81-90.

Cho, Y., Moseley, D. J., Siewerdsen, J. H., & Jaffray, D. A. (2005). Accurate technique for complete geometric calibration of cone-beam computed tomography systems. *Medical Physics, 32*(4), 968-983. doi: 10.1118/1.1869652.

Choe, Y. H. (2005). Non-invasive imaging of atherosclerotic plaques using MRI and CT. *Korean Circulation Journal, 35,* 1-14.

Chu, B., Kampschulte, A., & Ferguson, M. S. (2004). Hemorrhage in the atherosclerotic carotid plaque: a high resolution MRI study. *Stroke, 35*(5)*,* 1079-1084.

Clavijo, A. A., & Pelc, N. J. (2009). Image quality optimisation for dual-energy computed tomography (DECT) three-material decomposition. *Revista Ingenieria Biomedica, 3*(5), 33-42.

Clunie, D. (2006). *DICOM Standard Status*. Retrieved from: http://www.dclunie.com/dicom-status/status.html

Cormack, A. M. (1963). Representation of a function by its line integrals with some radiological applications. *Journal of Applied Physics*, *34*, 2722-2727.

Cormode, D. P., & Fayad, Z. A. (2011). Nanoparticle contrast agents for CT: their potential and the challenges that lie ahead. *Imaging in Medicine, 3*(3), 263-266.

Cormode, D. P., Roessl, E., Thran, A., Skajaa, T., Gordon, R. E., Schlomka, J. P., Fuster, V., Fisher, E. A., Mulder, W. J., Proksa, R., & Fayad, Z. A. (2010). Atherosclerotic plaque composition: analysis with multicolor CT and targeted gold nanoparticles. *Radiology. 256*(3), 774-782.

De Feyter, P. J., Serruys, P. W., Nieman, K., Mollet, N., Cademartiri, F., van Geuns, R. J., Slager, C., van der Steen, A. F. W., Krams, R., Schaar, J. A., WVielopolski, P., Pattnama, P. M. T., Arampatzis, A., van der Lugt, A., Regar, E., Ligthart, J., & Smits, P. (2003). Imaging of coronary atherosclerosis and identification of the vulnerable plaque. *Netherlands Heart Journal*, *11*(9), 347-358.

De Kamp, R. A., Epstein, F. H., Catana, C., Tsui, B. M. W., & Ritman, E. L. (2010). Small animal molecular imaging methods. *Journal of Nuclear Medicine, 51*(1), 18S-32S.

De Weert, T. T., Ouhlous, M., Meijering, E., Zondervan, P. E., Hendriks, J. M., Van Sambeek, M. R., Dippel, D. W., Van der Lugt, A. (2006). In vivo characterization and quantification of atherosclerotic carotid plaque components with multidetector computed tomography and histopathological correlation. *Arteriosclerosis Thrombosis and Vascular Biology*, *26*(10), 2366-2372.

Dewey, M. (2010). Cardiac CT. In M. Dewey & J. Geleijns (Eds), *Physics background and radiation exposure*. (pp. 61). Springer.

Dierick, M., Masschaele, B., & Hoorebeke, L. V. (2004). Octopus, a fast and user-friendly tomographic reconstruction package developed in labview. *Measurement Science and Technology*, *15*(7), 1366.

Doesburg, R. M. N., Clyne, M. N., Van Leeuwen, D., Cook, N. J., Butler, P. H., & Butler, A. P. H. (2009). *Fast Ethernet Readout for Medipix Arrays with MARS-CT*. Paper presented at IEEE Nuclear Science Symposium & Medical Imaging Conference, Orlando, Florida, USA.

Du, L. Y., Umoh, J., Nikolov, H. N., Pollmann, S. I., Lee, T. Y., & Holdsworth, D. W. (2007). A quality assurance phantom for the performance evaluation of volumetric micro-CT systems. *Physics in Medicine and Biology*, *52*, 7087-7108.

Elliott, J.C., & Dover, S.D. (1982). X-ray microtomography. *Journal of Microscopy, 126*, 211-213.

Faruqi, A. R. (2009). Principles and prospects of direct high resolution electron image acquisition with CMOS detectors at low energies. *Journal of Physics: Condensed Matter, 21*(31), 314004. doi:10.1088/0953-8984/21/31/314004

Fayad, Z. A., & Fuster, V. (2000). Characterisation of atherosclerotic plaques by magnetic resonance imaging. *Annals of the New York Academy of Sciences, 902,* 173-186.

Feldkamp, L. A., Davis, L. C., & Kress, J. W. (1984). Practical cone-beam algorithm. *Journal of the Optical Society of America A, 1*(6), 612-619.

Feuerlein, S., Roessl, E., Proksa, R., Martens, G., Klass, O., Jeltsch, M., Rasch, V., Brambs, H. J., Hoffmann, M. H. K., & Schlomka, J. P. (2008). Multi-energy photon counting k-edge imaging: Potential for improved luminal depiction in vascular imaging. *Radiology, 249*(3), 1010-1016.

Firsching, M., Butler, A. P., Scott, N., Anderson, N. G., Michel, T., & Anton, G. (2009). Contrast agent recognition in small animal CT using the Medipix2 detector. *Nuclear Instruments and Methods in Physics Research A, 607*(1), 179-182.

Firsching, M., Giersch, J., Niederlohner, D., & Anton, G. (2004, October). A method for stoichiometric material reconstruction with spectroscopic X-ray pixel detectors. Proceedings of IEEE Nuclear Science Symposium Conference Record, 2004.

Flannery, B. P., Deckman, H. W., Roberge, W. G., & D'Amico, K. L. (1987). Three-dimensional x-ray microtomography. *Science, 237*, 1439-1444.

Fleischmann, D., & Boas, F. E. (2011). Computed tomography-old ideas and new technology. *European Radiology, 21,* 510-517.

Flohr, T. G., McCollough, C. H., Bruder, H., Petersilka, M., Gruber, K., Suss, C., Grasruck, M., Stierstorfer, K., Krauss, B., Raupach, R., Primak, A. N., Kuttner, A., Achenbach, S., Becker, C., Kopp, A., & Ohnesorge, B. M. (2006). First performance evaluation of a dual source CT (DSCT) system. *European Radiology, 16,* 256-268.

Fornaini, A., Boerkamp, T., de Oliveira, R., & Visschers, J. (2003). A multichip board for x-ray imaging in building technology. *Nuclear Instruments Methods in Physics Resrach Section A, 509,* 206-212.

Fornaini, A., Boerkamp, T., De Oliveira, R., & Visschers, J. L. (2004). A tiled array of hybrid pixel detectors for x-ray imaging. *IEEE Transactions on Nuclear Science, 51*(4), 1824-1828.

Frallicciardi, P. M. (2009a). *Single Photon Counting X-Ray Micro Imaging of Biological Samples* (Ph.D thesis). Università degli Studi di Napoli "Federico II", Naples, Italy.

Frallicciardi, P. M., Jakubek, J. Vavrik, D., & Dammer, J. (2009b). Comparison of single-photon counting and charge integrating detectors for x-ray high resolution imaging of small biological objects. *Nuclear Instruments and Methods in Physics Research Section A, 607*(1)*,* 221-222.

Fuster, V., Fayad, Z. A., & Badimon, J. J. (1999). Acute coronary syndromes: Biology. *Lancet, 353*(12), SII5-SII9.

Gaemperli, O., & Kaufmann, P. A. (2010). Multimodality cardiac imaging. *Journal of Nuclear Cardiology, 17*(1)*,* 4-7.

Gamble, M. (2010). *Study finds CT scan use in emergency rooms tripled over decade*. Retrieved from http://www.beckershospitalreview.com/hospital-management-administration/study-finds-ct-scan-use-in-ers-tripled-over-decade.html

Gimenez, E. N., Manaeuski, D., Mac Raighne, A., Parkes, C., Bates, R., O'Shea, V., Fleta, C., Pellegrini, G., Lozano, M., Alianelli, L., Sawhney, K. J. S., Marchal, J., & Tartoni, N. (2011). 3D Medipix2 detector characterisation with a micro-focused x-ray beam. *Nuclear Instrumentation Methods in Physics Research A*, *633*(1) S114-S116.

Giattina, S. D., Courtney, B. K., Herz, P. R., Harman, M., Shortkroff, S., Stamper, D. L., Liu, B., Fujimoto, J. G., Brezinski, M. E. (2006). Assessment of coronary plaque collagen with polarization sensitive optical coherence tomography (PS-OCT). *International Journal of Cardiology*, *107*(3), 400.

Glagov, S., Bassiouny, H. S., Giddens, D. P., & Zarins, C. K. (1995). Pathobiology of plaque modeling and complication. *The Surgical Clinics of North America*, *75*(4), 545-556.

Goldman, L. W. (2007). Principles of CT and CT technology. *Journal of Nuclear Medicine Technology. 35*(3), 115-128.

Gordon, R. (1985). Industrial applications of computed tomography and NMR imaging: An OSA Topical Meeting. *Applied Optics*, *24(*23), 3948-3949.

Graser, A., Johnson, T. R., Hecht, E. M., Becker, C. R., Leidecker, C., Staehler, M., Stief, C. G., Hildebrandt, H., Godoy, M. C., Finn, M. E., Stepansky, F., Reiser, M. F., & Macari, M. (2009). Dual-energy CT in patients suspected of having renal masses; can virtual nonenhanced images replace true nonenhanced images? *Radiology*, *252,* 433-440.

Gui, J. B., Hu, Z. L., & Zhou, Y., (2009). Technology development of micro-CT with high spatial resolution. *Computerised Tomography Theory and Applications, 18*(2), 106-116.

Guidera, M. (2010). *Dramatic rise in MRI, CT use in emergency departments raise questions*. Retrieved from http://www.hopkinsmedicine.org/news/media/releases/dramatic_rise_in_mri_ct_use_in_emergency_departments_raise_questions

Gutstein, D. E., & Fuster, V. (1999). Pathophysiology and clinical significance of atherosclerotic plaque rupture. *Cardiovascular Research*, *41*(2), 323-333.

Halpern, E. J. (2011). *Clinical cardiac CT: Anatomy and Function*. Pennsylvania, USA: Thieme Medical Publishers Inc.

Harding, G., & Tischler, R. (1986). Dual-energy Compton scatter tomography. *Physics in Medicine and Biology*, *31*(5), 477.

Hardy, T. L., Koch, J., & Lassiter, A. (1983). Computer graphics with computerised tomography for functional neurosurgery. *Applied Neurophysiology, 46*, 217-226.

Hardy, T., & Koch, J. (1982). Computer-assisted stereotactic surgery. *Applied Neurophysiology, 45*, 396-398.

Hatsukami, T. S., Ross, R., Polissar, N. L., & Yuan, C. (2000). Visualization of fibrous cap thickness and rupture in human atherosclerotic carotid plaque in vivo with high resolution magnetic resonance imaging. *Circulation, 102,* 959-964.

Hay, D. (2004). Cardiovascular Disease in New Zealand. A Summary of Recent Statistical Information. National Heart Foundation of New Zealand.

Herman, G. T. (1979). Correction for beam hardening in computed tomography. *Physics in Medicine and Biology*, *24*(1), 81.

Herman, G. T. (1980). Image reconstruction from projection. *The Fundamentals of Computerised Tomography,* (pp. 40-54). New York: Academic Press.

Hoffman, U., & Butler, J. (2005). Noninvasive detection of coronary atherosclerotic plaque by multi-detector row computed tomography. *International Journal of Obesity, 2*(5), 46-53.

Holdsworth, D. W., & Thornton, M. M. (2002). Micro-CT in small animal and specimen imaging. *Trends Biotechnology, 20*(8), S34-S39.

Holdsworth, D. W., Drangova, M., & Fenster, A. (1993). A high-resolution XRII-based quantitative volume CT scanner. *Medical Physics, 20*, 449-62.

Hounsfield, G. N. (1973). Computerised transverse axial scanning (tomography). Part 1. Description of system. *The British Journal of Radiology, 46*, 1016-1022.

Hsieh, J. (2003). *Computed tomography: principles, design, artifacts and recent advances* (pp. 31-34). United States of America: SPIE.

Hu, Z., Zou1, J., Gui, J., Rong, J., Li1, Y., & Zheng, H. (2010). Geometric calibration method based micro-CT system for small-animal imaging. *IEEE, 15*(4), 1-4.

Huda, W. (2002). Dose and image quality in CT. *Pediatric Radiology, 32,* 709-713.

Hyafil, F., Cornily, J., Feig, J., Gordon, R., Vucic, E., Amirbekian, V., Fisher, E., Fuster, V., Feldman, L., & Fayad, Z. (2007). Noninvasive detection of macrophages using a nanoparticulate contrast agent for computed tomography. *Nature Medicine, 13*(5), 636-641.

JCGM (2008). Evaluation of measurement data guide to the expression of uncertainty in measurement JCGM 100: 2008 (GUM 1995 with minor corrections). Technical report, JCGM: BIPM, IEC, IFCC, ILAC, ISO, IUPAC, IUPAP and OIML.

Johnson, T. R., Krauss, B., Sedlmair, M., Grasruck, M., Bruder, H., Morhard, D., Fink, C., Weckbach, S., Lenhard, M., Schmidt, B., Flohr, T., Reiser, M. F., & Becker, C. R. (2007). Material differentiation by dual-energy CT: initial experience. *European Radiology, 17*(6), 1510-1517.

Judy, P., Balter, S., Bassano, D., McCullough, E., Payne, J., & Rothenberg, L. (1977). AAPM report No. 1 phantoms of performance evaluation and quality assurance of CT scanner. Chicago, Illinois: AAPM.

Kachelrieß, M. (2008). Micro-CT. *Handbook of Experimental Pharmacology,* (185 Pt 1), 23-52.

Kak, A. C., & Slaney, M. (1988). Principles of Computerised Tomographic Imaging. Philadelphia: SIAM.

Kalender, W. A. (2001). Computed Tomography, (volume 12). Publicis Corporate Publishing, Erlangen.

Kalender, W. A. (2005). *Computed tomography: Fundamentals, system technology, image quality, applications*. Germany: Publicis MCD Verlag.

Kalender, W. A., Hebel, R., & Ebersberger, J. (1987). Reduction of CT artifacts caused by metallic implants. *Radiology, 164*(2), 576-577.

Kalender, W. A., Perman, W. H., Vetter, J. R., & Klotz, E. (1986). Evaluation of a prototype dual-energy computed tomographic apparatus I. Phantom studies. *Medical Physics. 13,* 334-339.

Kelcz, F., Joseph, P. M., & Hilal, S. K. (1979). Noise considerations in dual energy CT scanning. *Medical Physics*, *6*, 418-425.

Khoury, R., Bonissent, A., Cl´emens, J. C., Meessen, C., Vigeolas, E., Billault, M., & Morel, C. (2009). A geometrical calibration method for the PIXSCAN micro-CT scanner. *Journal of Instrumentation, 4*(P07016), 1-6. doi:10.1088/1748-0221/4/07/P07016.

Kiessling, F. (2011). Small animal imaging: Basic and practical guide. In M. Schafers, K. Tiemann, M. Kuhlmann, L. Slegger, K. Schafers & S. Hermann (Eds.), *Imaging in cardiovascular research* (pp. 449-472). Berlin, Heidelberg: Springer-Verlag.

Kim, H. K., Lee, S. C., Cho, M. H., Lee, S. Y., & Cho, G. (2005). Use of a flat-panel detector for microtomography: A feasibility study for small-animal imaging. *IEEE Transactions on Nuclear Science*, *52*(1), 193-198.

Knollmann, F., Ducke, F., Krist, L., Kertesz, T., Meyer, R., Guski, H., & Felix, R. (2008). Quantification of atherosclerotic coronary plaque components by submillimeter computed tomography. *International Journal of Cardiovascular Imaging, 24*(3), 301-310.

Kooi, M. E., Cappendijk, V. C., Cleutjens, K. B. J. M., Kessels, A. G. H., Kutslaar, P. J. E. H. M., Borgers, M., Frederik, P. M., Daemen, M. J. A. P., & van Engelshoven, J. M. A. (2003). Accumulation of ultra small super paramagnetic particles of iron oxide in human atherosclerotic plaques can be detected by in vivo magnetic resonance imaging. *Circulation, 107,* 2453-2458.

Kullo, I. J., Edwards, W. D., Schwartz, R. S. (1998). Vulnerable plaque: pathobiology and clinical implications. *Annals of Internal Medicine, 129*,1050-1060.

Landis, E. N., & Keane, D. T. (2010). X-ray microtomography. *Materials Characterisation, 61,* 1305-1316.

Langheinrich, A. C., Kampschulte, M., Crobmann, C., Moritz, R., Rau, W. S., Bohle, R. M., & Ritman, E. L. (2009). Role of computed tomography voxel size in detection and discrimination of calcium and iron deposits in atherosclerotic human coronary artery specimens. *Journal of Computer Assisted Tomography, 33*(4), 517-522.

Langheinrich, A. C., Michniewicz, A., Sedding, D. G., Lai, B., Jorgensen, S. M., Bohle, R. M., & Ritman, E. L. (2007). Quantitative x-ray imaging of intraplaque hemorrhage in aortas of ApoE-/-/LDL-/- double knockout mice. *Investigative Radiology, 42*(5), 263-273.

Larose, E., Yeghiazarians, Y., Libby, P., Yucel, E. K., Aikawa, M., Kacher, D. F., Aikawa. E., Kinlay, S., Schoen, F. J., Selwyn, A. P., Ganz, P. (2005). Characterisation of human atherosclerotic plaques by intravascular magnetic resonance imaging. *Circulation*, *112*(15), 2324-2331.

Ledley, R. S., Di Chiro, G., Luessenhop, A. J., Twigg, H. L. (1974). Computerised transaxial x-ray tomography of the human body. *Science*, *186*(4160), 207-212.

Lee, S. C., Kim, H. K., Chun, I. K., Cho, M. H., Lee, S. Y., & Cho, M. H. (2003). A flat panel detector based micro-CT: Performance evaluation for small animal imaging. *Physics in Medicine and Biology, 48*(24), 4173-4185.

Lemacks, M., Kappadath, S., Shaw, C., Liu, X., & Whitman, G. (2002). A dual-energy subtraction technique for microcalcification imaging in digital mammography-A signal-to-noise analysis. *Medical Physics*, *29*, 1739.

Li, H., Zhang, H., Tang, Z., & Hu, G. (2008). Micro-computed tomography for small animal imaging: Technological details. *Progress in Natural Science, 18*, 513-521.

Libby, P. (2009) Atherosclerosis Imaging: A Biological and Clinical Perspective, in Novel Techniques for Imaging the Heart: Cardiac MR and CT. In M. F. Di Carli and R. Y. Kwong (Eds.). Oxford, UK: Wiley-Blackwell Ltd. doi:10.1002/9781444300598.ch17.

Lima, J. A., Desai, M. Y., Steen, H., Warren, W. P., Gautam, S., & Lai, S. (2004). Statin induced cholesterol lowering and plaque regression after 6 months of magnetic resonance imaging-monitored therapy. *Circulation, 110,* 2336-2341.

Lin, P., Beck, T., Borras, C., Cohen, G., Jucius, R., Kriz, R., Nickoloff, E., Rothenberg, L., Strauss, K., Villafana, T., Cacak, R. K., Gray, J. E., Hangartner, T. N., Hendrick, R. E., & Rossi, R. P. (1993). *Specification and acceptance testing of computed tomography scanners* [Report]. AAPM.

Little, W. C., Constantinescu, M., Applegate, R. J., Kutcher, M. A., Burrows, M. T., Kahl F. R., & Santamore, W. P. (1988). Can coronary angiography predict the site of a subsequent myocardial infarction in patients with mild-to-moderate coronary artery disease?. *Circulation, 78*, 1157-1166.

Liu, X., Yu, Lifeng, Primak, A. N., & McCollough, C. H. (2009). Quantitative imaging of element composition and mass fraction using dual-energy CT: Three-material decomposition. *Medical Physics, 36*(5), 1602-1609.

Llopart, X., Campbell, M., San Segundo, D., Pernigotti, E., & Dinapoli, R. (2002). Medipix2, a 64k pixel read out chip with 55 μm square elements working in single photon counting mode. *IEEE Transactions on Nuclear Science*, *49*(5), 2279-2283.

Llopart, X., & Campbell, M. (2003). First test measurements of a 64 k Pixel readout chip working in single photon counting mode. *Nuclear Instruments Methods in Physics Resrach Section A, 509,* 157-163.

Llopart, X., Campbell, M., Segundo, D. S., Pernigotti, E., & Dinapoli R. (2002). Medipix2: A 64-k pixel readout chip with 55-μm square elements working in single photon counting mode. *IEEE Transactions on Nuclear Science*. *49*(5), 2279-2283.

Luu, Y., Lublinsky, S., Ozcivici, E., Capilla, E., Pessin, J., Rubin, C., and Judex, S. (2009). In vivo quantification of subcutaneous and visceral adiposity by microcomputed tomography in a small animal model. *Medical Engineering and Physics*, *31*(1), 34-41.

Mahnken, A. H., Stanzel, S., & Heismann, B. (2009). Spectral rhoZ-projection method characterisation of body fluids in computed tomography: ex vivo experiments. *Academic Radiology*, *16*, 763-769.

Manos, D. (2011). *CT scans up, hospital admissions down, study says*. Retrieved from http://www.healthcareitnews.com/news/study-ct-scans-hospital-admissions-down

Marchal, J. (2010). Theoretical analysis of the effect of charge-sharing on the detective quantum efficiency of single photon counting segmented silicon detectors. *Journal of Instrumentation*, *5*, P01004.

MARS. (2011). *Quality Assurance Protocol: Geometrical Alignment.* (Report version 1). Christchurch, New Zealand.

Marshall, W. H., Jr., Alvarez, R. E., & Macovski, A. (1981). Initial results with pre-reconstruction dual energy computed tomography (PREDECT), *Radiology,140,* 421-430.

Marshall, W., Hall, E., Doost-Hoseini, A., Alvarez, R., Macovski, A. & Cassel, D. (1984). An implementation of dual energy CT scanning. *Journal of Computer Assisted Tomography, 8,* 745-749.

Matter, C. M., Stuber, M., & Nahrendorf, M. (2009). Imaging of the unstable plaque: how far have we got?. *European Heart Journal*. *30*(21): 2566-2574.

McNitt-Gray, M. (2006). Tradeoffs in Image Quality and Radiation Dose for CT. *Medical Physics*, *33,* 2154.

Medcyclopaedia (2011). W.C Roentgen and the discovery of x-rays. Retrieved from http://www.medcyclopaedia.com/library/radiology/chapter01.aspx

Medipix. (2011). *Medipix.* Retrieved from http://medipix.web.cern.ch/MEDIPIX/.

Melzer, T. R., Cook, N. J., Butler, A. P., Watts, R., Anderson, N., Tipples, R., & Butler, P. H. (2008). Spectroscopic biomedical imaging with the Medipix2 detector. *Australasian Physical and Engineering Sciences in Medicine, 31*(4)*,* 300-306.

Mikulec, B., Campbell, M. Heijne, E., Llopart, X., & Tlustos, L. (2003). X-ray imaging using single photon processing with semiconductor pixel detectors. *Nuclear Instruments and Methods in Physics Research Section A, 511*(1-2)*,* 282-286.

Millner, M. R., McDavid, W. D., Waggener, R. G., Dennis, M. J., Payne, W. H., & Sank, V. J. (1979). Extraction of information from CT scans at different energies. *Medical Physics, 6*(1):70-71.

Mintz, G. S., Nissen, S. E., Anderson, W. D., Bailey, S. R., Erbel, R., Fitzgerald, P. J., Pinto, F. J., Siegel, R. J., Tuzcu, E. M. & Yock, P. G. (2001). American college of cardiology clinical expert consensus document on standards for acquisition, measurement and reporting of intravascular ultrasound studies (IVUS). A report of the American College of Cardiology task force on clinical expert consensus documents. *Journal of the American College of the Cardiology, 37*(5)*,* 1478-1492.

Mitschke, M. (2006). *Evaluation of different sensor materials for the Medipix x-ray detectors* (Ph.D thesis). University Erlangen-Nürnberg.

Munch, B., Trtik, P., Marone, F., & Stampanoni, M. (2009). Stripe and ring artifact removal with combined wavelet-fourier filtering. *Optics Express*, *17*(10), 8567-8591.

Nair, A., Kuban, B. D., Tuzcu, E. M., Schoenhagen, P., Nissen, S. E., & Vince, D. G. (2002). Coronary plaque classification with intravascular ultrasound radiofrequency data analysis. *Circulation, 106,* 2200-2206.

National Heart Foundation of New Zealand. (2007). General Statistics. National Heart Foundation of New Zealand. Wellington. Retrieved from: www.nhf.org.nz/index.asp?pageID=2145831169

Nissen, S. E., & Yock, P. (2001). Intravascular ultrasound: novel pathophysiological insights and current clinical applications. *Circulation, 103,* 604-616.

Nissen, S. E., Tuzcu, E. M., Schoenhagen, P., Brown, B. G., Ganz, P., Vogel, R. A., Crowe, T., Howard, G., Cooper, C. J., Brodie, B., Grines, C. L., & DeMaria, A. N. (2004). Effect of intensive compared with moderate lipid-lowering therapy on progression of coronary atherosclerosis: a randomised controlled trial. *Journal of the American Medical Association, 291*(9), 1071-1080.

Nobelprize. (1979). *The Nobel Prize in Physiology or Medicine 1979*. Retrieved from http://www.nobelprize.org/nobel_prizes/medicine/laureates/1979/press.html

Noo, F., Clackdoyle, R., Mennessier, C., White, T. A., & Roney, T. J. (2000). Analytic method based on identification of ellipse parameters for scanner calibration in cone-beam tomography. *Physics in Medicine and Biology*, *45*(11), 3489-3508.

OECD. (2011). *OECD Health Data 2011*. Retrieved from http://www.oecd.org/els/health/data

Ohta, S., Lai, E. W., Morris, J. C., Bakan, D. A., Klaunberg, B., Cleary, S., Powers, J. F., Tischler, A. S., Abu-Asab, M., Schimel, D., & Pacak, K. (2006). Micro-CT for high-resolution imaging of ectopic pheochromocytoma tumors in the liver of nude mice. *International Journal of Cancer, 119*(9), 2236-2241.

Oliver, T. B., Lammie, G. A., Wright, A. R., Wardlaw, J., Patel, S. G., Peek, R., Ruckley, C. V., & Collie, D. A. (1999). Atherosclerotic Plaque at the Carotid Bifurcation: CT Angiographic Appearance with Histopathologic Correlation. *American Journal of Neuroradiology,20*(5), 897-901.

OpenLearn LabSpace. (2005). Imaging in Medicine. Retrieved from http://labspace.open.ac.uk/mod/resource/view.php?id=417927

Pasterkamp, G., Falk, E., Woutman, & H., Borst, C. (2000). Techniques characterising the coronary atherosclerotic plaque: Influence on clinical decision making? *Journal of the American College of Cardiology, 36*(1), 13-21.

Paulus, M. J., Gleason, S. S., Kennel, S. J., Hunsicker, P. R., & Johnson, D. K. (2000). High resolution x-ray computed tomography: an emerging tool for small animal cancer research. *Neoplasia*, *2*, 62-70.

Paulus, M. J., Sari-Sarraf, H., Gleason, S. S., Bobrek, M., Hicks, J. S., Johnson, D. K., Behel, J. K., Thompson, L. H., & Allen, W. C. (1999). A new x-ray computed tomography system for laboratory mouse imaging. *IEEE Transaction on Nuclear Science, 46*(3)*,* 558-564.

Pavlicek, W., Panse, P., Hara, A., Boltz, T., Paden, R., Yamak, D., Licato, P., Chandra, N., Okerlund, D., Dutta, S., Bhotika, R., & Langan, D. (2010). Initial use of fast switched dual energy CT for coronary artery disease. *Proceedings of SPIE*, *7662*, 76221V. doi:10.1117/12.844859.

Pellegrini, G., Maiorino, M., Blanchot, G., Chmeissani, M., Garcia, J., Lozano, M., Martinez, R., Puigdengoles, C., & Ullan, M. (2007). Direct charge sharing observation in single-photon counting pixel detector. *Nuclear Instruments and Methods in Physics Research Section A*, *573*(1-2), 137-140.

Pennicard, D., Marchal, J., Fleta, C., Pellegrini, G., Lozano, M., Parkes, C., Tartoni, N., Barnett, D., Dolbnya, I., Sawhney, K., Bates, R., O'Shea, V., & Wright, V. (2010). Synchrotron tests of a 3D Medipix2 x-ray detector. *IEEE Transaction Nuclear Science*, *57*, 387-394.

Perilli, E., Baruffaldi, F., Visentin, M., Bordini, B., Traina, F., Cappello, A., & Viceconti, M. (2007). MicroCT examination of human bone specimens: effects of polymethylmethacrylate embedding on structural parameters. *Journal of MicroscopyOxford*, *225*(2), 192-200.

Peters, T. M. (1974). Spatial Filtering to improve Transverse Tomography. *IEEE Transactions on Biomedical Engineering*, *21*(3), 214-219.

Peters, T. M. (2006). Image-guidance for surgical procedures. *Physics in Medicine and Biology, 51,* R505-R540. doi:10.1088/0031-9155/51/14/R01.

Peters, T. M., Clark, J. A., Olivier, A., Marchand, E. P., Mawko, G., Dieumegarde, M., Muresan, L. V., & Ethier, R. (1986). Integrated stereotaxic imaging with CT, MR imaging and digital subtraction angiography. *Radiology*, *161*, 821-826.

Primak, A. N., Fletcher, J. G., Vrtiska, T. J. (2007). Noninvasive differentiation of uric acid versus non-uric acid kidney stones using dual-energy CT. *Academic Radiology*, *14*, 1441-1447.

Protocol Database. (2011). *Histology & IHC Protocols*. Retrieved from http://www.ihcworld.com/protocol_database.htm

Radon, J. (1917). Über die Bestimmung von Funktionen durch ihre Integral werte längsgewisser Mannigfaltigkeiten. Ber. Vor Sächs. Akad. Wiss. *69*, 262-277 (English

translation available: Radon, J. (1986). On determinations of functions from their integral values along certain manifolds. *IEEE Transaction on Medical Imaging, MI5*(4), 170-176.

Ramachandran, G. N., & Lakshminarayanan, A. V. (1971). Three dimensional reconstruction from radiographs and electron micrographs: application of convolutions instead of Fourier transforms. *Proceedings of the National Academy of Sciences of USA, 68*(9), 2236-2240.

Ritman, E. L. (2004). Micro-computed tomography-current status and developments. *Annual Review of Biomedical Engineering, 6,* 185-208.

Ritman, E. L. (2007). Small animal CT - Its difference from and impact on clinical CT. *Nuclear Instrument Methods in Physics Research A, 580*(2), 968-970.

Robb, R. A. (1982). X-ray computed tomography: From basic principles to applications. *Annual Review of Biophysics and Bioengineering, 11*, 177-201.

Rodgers, C., D. (1996). Information content and optimisation of high spectral resolution measurements. Proceedings of SPIE, 2830, pp. 136-147. doi:10.1117/12.256110

Roentgen, W. C. (1896). On a new kind of rays. *Nature*, *53*(1369), 274-276.

Roessl, E., & Proksa, R. (2007). K-edge imaging in x-ray computed tomography using multi-bin photon counting detectors. *Physics in Medicine and Biology, 52*(15), 4679-4696.

Roessl, E., Brendel, B., Martens, G., Proksa, R., Schmidt, F., Thran, A., & Schlomka, J-P. (2009). *Energy-Sensitive, Photon-Counting Computed Tomography: Opportunities and Technological Challenges* [PowerPoint Slides]. Anaheim, California.

Romer, T. J., Brennan, J. F., Puppels, G. J., Zwinderman, A. H., van Duinen, S. G., van der Laarse, A., van der Steen, A. F., Bom, N. A., & Bruschke, A. V. (2000). Intravascular ultrasound combined with Raman spectroscopy to localize and quantify cholesterol and calcium salts in atherosclerotic coronary arteries. *Arteriosclerosis Thrombosis and Vascular Biology, 20*(2), 478-483.

Ronaldson, J. P., Walsh, M., Nik, S. J., Donaldson, J., Doesburg, R. M. N., van Leeuwen, D., Ballabriga, R., Clynee, M. N., Butlera, A. P. H., & Butler, P. H. (2011a). Characterisation of Medipix3 with the MARS readout and software. *Journal of Instrumentation*, *6*(C01056), d oi:10.1088/1748-0221/6/01/C01056

Ronaldson, J. P., Zainon, R., Butler, A. P., & Butler, P. H. (2011b, October). *Performance of MARS-CT using Medipix3 for spectral imaging of soft-tissue*. Paper presented at the Nuclear Science Symposium, Valencia, Spain.

Ronaldson, J. P., Zainon, R., Sedayo, A., Scott, N. J. A, Butler, A. P. B., Butler, P. H., & Anderson, N. G. A. (2011c, December). *Towards quantifying the composition of soft-tissue by spectral CT imaging with Medipix3.* Paper presented at the Radiological Society of North America Meeting, Chicago, USA.

Ross, R. (1999). Atherosclerosis--an inflammatory disease. *The New England Journal of Medicine, 340*(2), 115-126.

Ross, W., Cody, D. D., & Hazle, J. D. (2006). Design and performance characteristics of a digital flat-panel computed tomography system. *Medical Physics*, *33*(6), 1888-1901.

Rougee, A., Picard, C., Ponchut, C., & Trousset, Y. (1993). Geometrical calibration of x-ray imaging chains for three-dimensional reconstruction. *Computer Medical Imaging Graph*. *17*, 295-300. doi: 10.1016/0895-6111(93)90020-N.

RSNA. (2010). *CT scans growing in popularity for hospital visits*. Retrieved from http://www.hcplive.com/articles/CT-Scans-Growing-in-Popularity-for-Hospital-Visits

Rudd, J. H. F, Davies, J. R., & Weissberg, P. L. (2005). Imaging of atherosclerosis - can we predict plaque rupture? *Trends in Cardiovascular Medicine, 15*(1), 17-24.

Rutherford, R. A., Pullan, B. R., & Isherwood, I. (1976a). Measurement of effective atomic number and electron density using an EMI scanner. *Neuroradiology, 11*(1):15-21.

Rutherford, R. A., Pullan, B. R., & Isherwood, I. (1976b). X-ray energies for effective atomic number determination. *Neuroradiology*, *11*(1):23-28.

Schaar, J. A., Muller, J. E., Falk, E., Virmani, R., Fuster, V., Serruys, P. W., Colombo, A., Stefanadis, C., Casscells, S. W., Moreno, P. R., Maseri, A., & Van Der Steen, A. F. W. (2004). Terminology for high risk and vulnerable coronary artery plaques. *European Heart Journal, 25*(12), 1077-1082.

Schladitz, K. (2011). Quantitative micro-CT. *Journal of Microscopy*, *243*(2), 111-117.

Schlomka, J. P., Roessl, E., Dorscheid, R., Dill, S., Martens, G., Istel, T., Baumer, C., Herrmann, C., Steadman, R., Zeitler, G., Livne, A., & Proksa, R. (2008). Experimental feasibility of multi-energy photon counting k-edge imaging in pre-clinical computed tomography. *Physics in Medicine and Biology, 53*(15)*,* 4031-4047.

Seibert, J. A. (2004). X-ray imaging physics for nuclear medicine technologists. Part 1: Basic principles of x-ray production. *Journal of Nuclear Medicine Technology*, *32*(3), 140.

Seibert, J. A., & Boone, J. M. (2005). X-ray imaging physics for nuclear medicine technologists. Part 2: X-ray interactions and image formation. *Journal of Nuclear Medicine Technology*, *33*(1), 3-18.

Shikhaliev, P. M. (2008). Computed tomography with energy-resolved detection: A feasibility study. *Physics in Medicine and Biology, 53*(5), 1475-1495.

Shikhaliev, P. M., & Fritz, S. G. (2011). Photon counting spectral CT versus conventional CT: comparative evaluation for breast imaging application. *Physics in Medicine and Biology, 56*(7), 1905-1930.

Shikhaliev, P. M., Xu, T., & Molloi, S. (2005). Photon counting computed tomography: concept and initial results. *Medical Physics, 32*, 427.

Smith, P. R., Peters, T. M., & Bates, R. H. T. (1973). Image Reconstruction from Finite Numbers of Projections. *Journal of Physics, A 6*, 361.

Sommer, W. H., Johnson, T R., Becker, C. R., Arnoldi, E., Kramer, H., Reiser, M. F., & Nikolaou, K. (2009). The value of dual-energy bone removal in maximum intensity projections of lower extremity computed tomography angiography. *Investigative Radiology*, *44*, 285-292.

Stanton, L. (1969). Basic Medical Radiation Physics (New York: Meridith).

Stary, H. C., Chandler, B., Dinsmore, R. E., Fuster, V., Glagov, S., Insull, W., Rosenfeld, M. E., Schwartz., C. J., Wagner, W. D., & Wissler, R. W. (1995). A definition of advanced types of atherosclerotic lesions and a histological classification of atherosclerosis. *Circulation, 92*(5), 1355-1374.

Stauber, M., & Muller, R. (2008). Micro-computed tomography: a method for the non-destructive evaluation of the three-dimensional structure of biological specimens. *Methods in Molecular Biology, 455,* 273-292.

Stefanadis, C., Diamantopoulos, L., Vlachopoulos, C., Tsiamis, E., Dernellis, J., Toutouzas, K., Stefanadi, E., & Toutouzas P. (1999). Thermal heterogeneity within human atherosclerotic coronary arteries detected in vivo: a new method of detection by application of a special thermography catheter. *Circulation, 99,* 1965-1971.

Stolzmann, P., Scheffel, H., Rentsch, K., Schertler, T., Frauenfelder, T., Leschka, S., Sulser, T., Marincek, B., & Alkadhi, H. (2008). Dual-energy computed tomography

for the differentiation of uric acid stones: ex vivo performance evaluation. *Urol Res, 36*(3-4), 133-138.

Sun, Y., Hou, Y., Zhao, F., & Hu, J. (2006). A Calibration Method for Misaligned Scanner Geometry in Cone-beam Computed Tomography. *NDT & E International, 39*(6), 1-4.

Swinton, A. A. C. (1896). Roentgen Photograms. *Nature*, *53*, 340.

Tan, K. T., & Lip, G. Y. H. (2008). Imaging of the unstable plaque. *International Journal of Cardiology, 127*(2), 157-165.

Thomas, K. E. (2011). CT utilisation - trends and developments beyond the United States' borders. *Pediatric Radiology*, *41* (Suppl 2), S562-S566. doi:10.1007/s00247-011-2101-8.

Tlustos, L. (2005). *Performance and limitations of high granularity single photon processing X-ray imaging detectors* (Ph.D thesis). Atominstitut der Österreichischen Universitäten.

Tran, D. N., Straka M., Ross, J. E., Napel, S., & Fleischmann, D. (2009). Dual-energy Ct discrimination of iodine and calcium: experimental results and implications for lower extremity CT angiography. *Academic Radiology*, *16*, 160-171.

U.S. Department of Health and Human Services (2010). *Computed Tomography (CT).* Retrieved from http://www.fda.gov/RadiationEmittingProducts/RadiationEmittingProductsandProcedures/MedicalImaging/MedicalX-Rays/ucm115317.htm

Uotani, K., Watanabe, Y., Higashi, M., Nakazawa, T., Kono, A. K., Hori, Y., Fukuda, T,, Kanzaki, S., Yamada, N., Itoh, T., Sugimura, K., & Naito, H. (2009). Dual-energy CT head bone and hard plaque removal for quantification of calcified carotid stenosis: utility and comparison with digital subtraction angiography. *European Radiology*, *19*(8), 2060-2065.

Vetter, J. R., Perman, W. H., Kalender, W. A., Mazess, R. B., & Holden, J. E. (1986). Evaluation of a prototype dual-energy computed tomographic apparatus II. Determination of vertebral bone mineral content. *Medical Physics, 13*(3)*,* 340-343.

Van Gils, M. J., Vukadinovic, D., van Dijk, A. C., Dippel, D. W., Niessen, W. J., van der Lugt, A. (2012). Carotid Atherosclerotic Plaque Progression and Change in Plaque Composition Over Time: A 5-Year Follow-Up Study Using Serial CT Angiography. *American Journal of Neuroradiology*, *33*(7), 1267-1273.

Von Smekal, L., Kachelriess, M., Stepina, E., & Kalender, W. A., (2004). Geometric misalignment and calibration in cone-beam tomography. *Medical Physics*, *31*(12), 3242-3266. doi: 10.1118/1.1803792.

Walsh, M. F., Opie, A. M. T., Ronaldson, J. P., Doesburg, R. M. N., Nik, S. J., Mohr, J. L., Ballabriga, R., Butler, A. P. H., & Butler, P. H. (2011). First CT using Medipix3 and the MARS-CT-3 spectral scanner. *Journal of Instrumentation, 6,* C01095.

Wang, J., Garg, N., Duan, X., Leng, S., Yu, L., Liu, Y., Parker, K., Ritman, E. L., Kantor, B., & McCollough, C. H. (2010). Non-invasive Detection of Iron as a New Marker of Unstable Plaques using Dual-energy CT and a New Porcine Plaque Model. *Circulation*, 122, A19849.

Wang, X., Meier, D., Mikkelsen, S., Maehlum, G. E., Wagenaar, D. J., Tsui, B. M. W., Patt, B. E., & Frey, E. C. (2011a). Micro-CT with energy-resolved photon counting detectors. *Physics in Medicine and Biology, 56*(9)*,* 2791-2816.

Wang, X., Meier, D., Taguchi, K., Wagenaar, D. J., Patt, B. E., & Frey, E. C. (2011b). Material separation in x-ray CT with energy resolved photon-counting detectors. *Medical Physics, 38*(3), 1534-1546.

Watt, J., Davidson, D.W., Johnston, C., Smith, C., Tlustos, L., Mikulec, B., Smith, K. M., & Rahman, M. (2003). Dose reductions in dental X-ray imaging using Medipix. *Nuclear Instruments and Methods in Physics Research A*, *513*, 65-69.

Wermes, N. (2003). Pixel detectors for particle physics and imaging applications. *Nuclear Instruments Methods in Physics Research Section A, 512,* 277-288.

Willekens, I., Buls, N., Lahoutte, T., Baeyens, L., Vanhove, C., Caveliers, V., Deklerck, R., Bossuyt, A., & de Mey, J. (2010). Evaluation of the radiation dose in micro-CT with optimisation of the scan protocol. *Contrast Media & Molecular Imaging*, *5*(4), 201-207.

World Health Organisation. (2011). *Cardiovascular disease.* Retrieved from http://www.searo.who.int/LinkFiles/Non_Communicable_Diseases_CVD-fs.pdf

Yabushita, H., Bouma, B. E., Houser, S. L., Aretz, H. T., Jang, I. K., Schlendorf, K. H., Kauffman, C. R., Shishkov, M., Kang, D. H., Halpern, E. F., & Tearney, G. J. (2002). Characterisation of human atherosclerosis by optical coherence tomography. *Circulation, 106,* 1640-1645.

Yamamoto, S, McWilliams, J., Arellano, C., Marfori, W., Cheng, W., Mcnamara, T., Quinones-Baldrich, W. J., & Ruehm, S. G. (2009). Dual-energy CT angiography of pelvic and lower extremity arteries: dual-energy bone subtraction versus manual bone subtraction. *Clinical Radiology*, *64*(11), 1088-1096.

Yang, K., Kwan, A. L., Miller, D. F., & Boone, J. M. (2006). A geometric calibration method for cone beam CT systems. *Medical Physics, 33*(6), 1695-1706. doi: 10.1118/1.2198187.

Yuan, C., Mitsumori, L. M., Ferguson, M. S., Polissar, N. L., Echelard, D., Ortiz, G., Small, R., Davies, J. W., Kerwin, W. S., & Hatsukami, T. S. (2001). In vivo accuracy of multispectral magnetic resonance imaging for identifying lipid rich necrotic cores and intraplaque hemorrhage in advanced human carotid plaques. *Circulation, 104*(17), 2051-2056.

Yuan, C., Oikawa, M., Miller, Z., & Hatsukami, T. (2006). MRI of carotid atherosclerosis. *Journal of Nuclear Cardiology*, *15*(2), 266-275.

Zainon, R., Butler, A. P. H., Cook, N. J., Butzer, J., Schleich, N., de Ruiter, N., Tlustos, L., Clark, M. J., Heinz, R., & Butler, P. H. (2010a). Construction and operation of MARS-CT scanner. *Internetworking Indonesia Journal, 2*(1), 3-10.

Zainon, R., Cook, N. J., Gieseg, S. P., Butler, A. P. H, & Butler, P. H. (2010c). *Spectroscopic imaging of excised plaques*. Paper presented at Canterbury Health Research Poster Expo, Christchurch, New Zealand.

Zainon, R., Cook, N., Butler, A. P., Gieseg, S. P., Anderson, N. G., Buckenham, T. M., Shelkov, G., Tlustos, L., Roake, J. A., & Butler, P. H. (2010b). High resolution multi-energy CT imaging of atherosclerotic plaque. *New Zealand Medical Journal, 23*(1319), 97.

Zainon, R., Dufreneix, S., Nik, S. J., de Ruiter, N., Cook, N. J., Hurrell, M., Gieseg, S. P., Butler, A. P. H., & Butler, P. H. (2009). *Spectroscopic x-ray computed tomography imaging of plaque and arteries using the Medipix detector*. Paper presented at New Zealand Institute of Physics Conference, Christchurch, New Zealand.

Zainon, R., Ronaldson, J. P., Butler, A. P., & Butler, P. H. (2011). *Establishing a linear basis for quantifying material composition using spectral computed tomography*. Paper presented at the World Congress on Technology and Engineering: Bioinformatics and Biomedical Engineering Conference, Shanghai, China.

Zhang, X., Tian, J., Feng, J., Zhu, S., & Yan, G. (2009). An anatomical mouse model for multimodal molecular imaging. Proceedings of the 31st Annual International Conference of the IEEE Engineering in Medicine and Biology Society, Minneapolis, Minnesota, USA, 2-6 September 2009 pp. 5817-5820.

Zhu, S., Tian, J., Yan, G., Qin, C., & Feng, J. (2009). Cone beam micro-CT system for small animal imaging and performance evaluation. *Journal of Biomedical Imaging*, *2009*, 1-9.

Zwergera, A., Faulera, A., Fiederle, M., Jakobs, K. (2007). Medipix2: Processing and measurements of GaAs pixel detectors. *Nuclear Instruments and Methods in Physics Research A,* 576, 23-26.